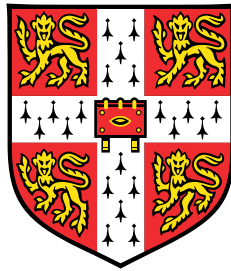


Mathematical modelling of asymmetrical metal rolling processes



Jeremy John Minton

Supervised by Dr E. J. Brambley

Department of Applied Mathematics and Theoretical Physics
University of Cambridge

This dissertation is submitted for the degree of
Doctor of Philosophy

Mathematical Modelling of Asymmetrical Metal Rolling Processes

Jeremy John Minton

This thesis explores opportunities in the mathematical modelling of metal rolling processes, specifically asymmetrical sheet rolling. With the application of control systems in mind, desired mathematical models must make adequate predictions with short computational times. This renders generic numerical approaches inappropriate.

Previous analytical models of asymmetrical sheet rolling have relied on ad hoc assumptions about the form of the solution. The work within this thesis begins by generalising symmetric asymptotic rolling models: models that make systematic assumptions about the rolling configuration. Using assumptions that apply to cold rolling, these models are generalised to include asymmetries in roll size, roll speed and roll-workpiece friction conditions. The systematic procedure of asymptotic analysis makes this approach flexible to incorporating alternative friction and material models. A further generalisation of a clad-sheet workpiece is presented to illustrate this. Whilst this model was formulated and solved successfully, deterioration of the results for any workpiece inhomogeneity demonstrates the limitations of some of the assumptions used in these two models.

Attention is then turned to curvature prediction. A review of workpiece curvature studies shows that contradictions exist in the literature; and complex non-linear relationships are seen to exist between asymmetries, roll geometry and induced curvature. The collated data from the studies reviewed were insufficient to determine these relationships empirically; and neither analytical models, including those developed thus far, nor linear regressions are able to predict these data. Another asymmetric rolling model is developed with alternative asymptotic assumptions, which shows non-linear behaviour over ranges of asymmetries and geometric parameters. While quantitative curvature predictions are not achieved, metrics of mechanisms hypothesised to drive curvature indicate these non-linear curvature trends may be captured with further refinement.

Finally, coupling a curved beam model with a curvature predicting rolling model is proposed to model the ring rolling process. Both of these parts are implemented but convergence between them is not yet achieved. By analogy this could be extended with shell theory and a three-dimensional rolling model to model the wheeling process.

Preface and Acknowledgements

The following constitutes my own work and any work resulting from collaboration is listed below and stated explicitly in the text. This work, nor any part, is substantially the same as any work I have submitted, or is being concurrently submitted, for a degree or diploma or other qualification at the University of Cambridge or any other University or similar institution.

Chapter 2 is based on work published in the *International Journal of Mechanical Sciences*, Minton et al. (2016). The work comprising Chapters 2 and 4 to 6 has also been submitted and presented at national and international conferences; in particular, Chapter 4 will be presented at the *International Conference on the Technology of Plasticity 2017*, Minton et al. (2017).

I would like to thank my friends and family for their support throughout this process. It also goes without saying that I thank my supervisor, Dr. E. J. Brambley, for his guidance and support, but I am particularly grateful to have worked with him over the past four years. He has been an inspiration and consistently encouraged me towards thorough and thoughtful science. Dr. C. J. Cawthorn also deserves thanks for many discussions, particularly while developing the rolling models presented in Chapter 2 and Chapter 3. Finally, a thanks to my editors, P. Heron, M. Kingston, R. Pearson and E. Unwin, for their herculean effort reading numerous drafts.

This work was supported by the Royal Society of New Zealand and the Cambridge Trust through the Rutherford Foundation PhD Scholarship. I am also grateful to Jesus College and the Department of Applied Mathematics and Theoretical Physics for supporting my attendance of several national and international conferences.

Table of contents

List of figures	ix
List of tables	xiii
1 Introduction	1
1.1 Sheet rolling	2
1.1.1 Asymmetric rolling	9
1.2 Ring rolling	10
1.3 English wheel	12
1.4 Governing equations	13
1.4.1 Material models	14
1.4.2 Friction models	17
1.5 Modelling approaches	22
2 Asymmetric rolling	25
2.1 Introduction	26
2.2 Model formulation	28
2.2.1 Non-dimensionalisation	30
2.3 Solution	33
2.3.1 Leading-order solution	33
2.3.2 Comparison with an existing slab model	37
2.3.3 Correction terms	37
2.4 Numerical simulations	38
2.5 Results and discussion	39
2.5.1 Numerical comparison over varying asymmetries	39
2.5.2 Numerical comparison over varying non-dimensional parameters	41
2.5.3 Numerical comparison of stress and strain fields	47

2.5.4	Computational time comparison	50
2.5.5	Application to hardening material	50
2.5.6	Alternative friction models	52
2.6	Conclusion	52
3	Clad-sheet rolling	57
3.1	Introduction	57
3.2	Model formulation	58
3.3	Solution	62
3.4	Numerical simulations	64
3.5	Results and discussion	65
3.5.1	Distributions	67
3.6	Conclusion	71
4	Curvature prediction	75
4.1	Literature review	75
4.1.1	Experiments	76
4.1.2	Numerics	81
4.1.3	Analytical models	88
4.2	Numerical comparison	90
4.2.1	Data collection	91
4.2.2	Initial observations	94
4.2.3	Linear regressions models	97
4.2.4	Lasso regression models	101
4.2.5	Non-parametric regression	103
4.3	Analytical models	103
4.3.1	Comparison to the Markowski et al. (2003) simulation results	107
4.4	Hybrid methods	107
4.5	Conclusion	109
5	Thick-sheet rolling	111
5.1	Introduction	111
5.2	Alternative asymptotic assumptions	115
5.3	Results	118
5.3.1	Stress and strain fields	119
5.3.2	Force and torque predictions	119

5.3.3	Curvature predictions	122
5.4	Concluding remarks	123
6	Ring rolling	125
6.1	Introduction	125
6.2	Curved beam models	128
6.3	Extended slab model	130
6.4	Coupling	135
6.5	Conclusion and further work	137
6.5.1	Dynamics	138
6.5.2	English wheel	138
7	Conclusion and further work	143
	References	149
A	Asymmetric rolling asymptotic correction	161
B	Clad-sheet rolling asymptotic correction	167
C	Statistical method	173
C.1	Data exploration	173
C.2	Linear regression	176
D	<i>ABAQUS</i> simulations	185
D.1	Simulation configurations	185
D.1.1	Three-dimensional symmetric and asymmetric rolling	186
D.1.2	Two-dimensional asymmetric rolling	188
D.1.3	Clad-sheet rolling	191
D.1.4	Ring rolling	193
D.2	Mesh convergence	194
D.3	Post-processing	198
D.4	Transients control	199
D.5	Friction behaviour	201

List of figures

1.1	Examples of sheet rolling.	4
1.2	A diagram of sheet rolling.	5
1.3	A diagram of characteristic velocity, shear and pressure in rolling.	6
1.4	An illustration of the key assumption in Orowan (1943)	7
1.5	A photograph of a ring rolling machine in operation.	11
1.6	A photograph of an English wheel in use.	13
1.7	Coulomb friction effect on stress.	19
1.8	Relative-slip friction effect on stress.	20
1.9	Friction factor effect on stress.	20
1.10	Karabin et al. (1990) friction effect on stress.	22
2.1	An illustration of the idealised two-dimensional rolling model.	29
2.2	An illustration of the cross-shear region.	36
2.3	Roll force and torque predictions over the asymmetries.	40
2.4	Neutral point predictions over varying roll speed asymmetry.	42
2.5	Roll force and torque predictions over μ_t , δ and r	44
2.6	Absolute error of roll force and torque predictions.	45
2.7	Relative error of roll force and torque predictions.	46
2.8	Stress fields for the leading order, asymptotic and simulated solutions.	48
2.9	Strain rate fields for the leading order, asymptotic and simulated solutions.	49
2.10	Roll pressure and roll shear predictions through the roll gap.	49
2.11	Hardening curve for carbon steel type material.	51
2.12	Roll force and torque predictions for a hardening material.	51
2.13	Leading order stress fields for alternative friction models.	53
3.1	An illustration of idealised clad-sheet rolling geometry.	59
3.2	Roll force and torque over cladding compositions.	66

3.3	Cross sections of Figure 3.2	68
3.4	Stress fields for the asymptotic and numerical solutions.	69
3.5	Strain rate fields for the asymptotic and numerical solutions.	70
3.6	Position, normal stress and tangential stress of the cladding interface.	72
4.1	The digitised data by parameter.	95
4.2	The digitised data by publication.	96
4.3	Trends by regression of asymmetric terms.	98
4.4	Trends by regression of asymmetric by non-asymmetric terms.	98
4.5	Trends by regression of asymmetric and cubed asymmetric by non-asymmetric terms.	99
4.6	Trends by regression of asymmetric and cubed asymmetric by non-asymmetric terms with a p-value over 1×10^{-4}	100
4.7	Lasso regression coefficients for decreasing λ	102
4.8	Trends from the Dewhurst et al. (1974) model.	104
4.9	Trends from the Salimi et al. (2002) model.	105
4.10	Curvature predictions of the Markowski et al. (2003) results by all models.	108
5.1	Shear stress fields from Chapter 2 and Chapter 3.	112
5.2	Shear stress fields assorted simulations.	113
5.3	Numerical and thin-sheet asymptotic shear stress fields for varying δ	114
5.4	Numerical and thick-sheet asymptotic shear stress fields for varying δ	120
5.5	Numerical and thick-sheet asymptotic stress and strain fields.	121
5.6	Roll force and torque predictions over the asymmetries.	122
5.7	Curvature and curvature indicators for the Markowski et al. (2003) results.	124
6.1	A diagram of the ring rolling process.	126
6.2	Illustrative results of the Timoshenko et al. (1925) curved beam model.	131
6.3	Illustrative results of the extended slab model.	134
6.4	A diagram of the roll gap of curved sheet rolling.	136
C.1	Histogram and box plot of the digitised curvature data.	174
C.2	Q-Q plot of the digitised curvature data.	174
C.3	Scatter matrix of the digitised curvature data.	175
C.4	Residuals from regression over the asymmetric terms.	177
C.5	Residuals from regression over the asymmetric by non-asymmetric terms.	179

C.6	Residuals from regression over the asymmetric and cubed asymmetric by non-asymmetric terms with p-value over 1×10^{-4}	183
D.1	Example of symmetric rolling mesh used in simulation.	187
D.2	Example of asymmetric rolling mesh used in simulation.	189
D.3	Example of clad-sheet rolling mesh used in simulation.	192
D.4	Example of the ring rolling mesh used in simulation.	194
D.5	Convergence study for three-dimensional explicit model.	195
D.6	Convergence study for the two-dimensional explicit model.	196
D.7	Convergence study for the two-dimensional implicit model.	197
D.8	Normal and tangential stress and relative-slip on the roll surfaces. . . .	202
D.9	Tangential stress and relative-slip against normal stress on the roll surfaces.	203

List of tables

2.1	Initial parameter sets for varying parameter comparison	39
4.1	Experimental curvature literature summary	79
4.2	Numerical curvature literature summary	83
4.3	Assumed friction ratios	92
4.4	Assumed material values	93
4.5	Penalty multiplier value for non-zero coefficients	102
C.1	Linear regression coefficients for the asymmetric terms	176
C.2	Linear regression coefficients for the asymmetric by non-asymmetric terms	178
C.3	Linear regression coefficients for the asymmetric and cubed asymmetric by non-asymmetric terms	181
C.4	Linear regression coefficients for the asymmetric and cubed asymmetric by non-asymmetric terms with p-value less than 1×10^{-4}	182
D.1	Parameters for three-dimensional symmetric rolling	186
D.2	Parameters for two-dimensional asymmetric rolling	188
D.3	Parameters for two-dimensional asymmetric rolling	191

Chapter 1

Introduction

Global steel consumption was projected to exceed 2 Gt in 2017¹ and global aluminium production reached nearly 60 Mt in 2016². Production of metals generally involves four stages: ore extraction, surface or underground mining, or digging of ore sands; smelting, chemical or thermal processing of ores into pure metals; casting, the shaping of metal by pouring molten metal into molds; and forming, the shaping of the metal workpiece by mechanical means; and machining. Numerous forming processes are employed and many products undergo more than one of these during manufacturing. Consequently, a few processes are common between most metal products. For example, in excess of 99% of steel and around half of aluminium undergoes rolling at some point in the production process (Allwood et al., 2012). Innovations in these key processes have the potential for huge reductions in emissions and cost, and improvements in quality and throughput.

Until automation occurred during the industrial revolution, manufacturing relied on skilled artisans hand producing individual items. Product creation was then divided into many small steps for mechanisation or greater labourer specialisation; machine-based manufacturing pushed artisan workmen out of mainstream manufacturing. Machines are now able to accomplish nearly every step of most manufacturing processes, increasing speed and ensuring high reliability.

Recently, manufacturing management strategies, such as *just-in-time* manufacturing, and recent market trends for bespoke components have increased the demand for flexible, yet still automated processes. Computer numerical control (CNC) machines have met

¹www.steelbb.com/files/PDFDownloads/Eurostrategy%20Outlook_2017_Report_orderform.pdf accessed 2017/05/04

²www.minerals.usgs.gov/minerals/pubs/commodity/aluminum/mcs-2017-alumi.pdf accessed 2017/05/04

that demand and are now commonplace in additive and subtractive manufacturing: 3D printing and milling as respective examples. Development in forming automation has not followed suit due to a dependence on part-specific tooling: the need for specific tools in many processes like dies for deep drawing or custom profiled rolls for profiled rolling. Consequently, most forming processes remain open loop and rely on many repetitions to find viable operating conditions. This will not satisfy demand for more bespoke, higher quality products; lower energy consumption or material waste; and resilience to higher variability of raw material from recycled metals. This continues to motivate research into these century old processes, including this work.

Analytical models, predominantly asymptotic models, of asymmetric rolling have been studied: thin-sheet asymptotic models for asymmetric rolling in Chapter 2 and clad-sheet rolling in Chapter 3, statistical and existing methods in literature for curvature prediction in Chapter 4, a thick-sheet asymptotic model for asymmetric rolling in Chapter 5, and a slab method for ring rolling with a brief discussion of the English wheel in Chapter 6. But first, a general introduction to rolling processes and the equations which govern them.

1.1 Sheet rolling

Sheet rolling is the process of reducing the thickness of a workpiece, a flat metal sheet, by passing it between two rolls separated by less than the current thickness. Rolling is performed in many different regimes but is generally categorised into hot rolling, cold rolling and foil rolling. Hot rolling, Figure 1.1a, is when the workpiece is rolled above the recrystallisation temperature to prevent hardening. This process typically occurs during rough rolling: the reduction of large workpieces, such as cast ingots, to an appropriate size for subsequent forming. Some finished products are produced with hot rolling including thick-sheet metal, I-beams, vehicle frames, building materials and other items with simple cross-sections and rough surface finishes. Cold rolling, Figure 1.1b, is when the workpiece is rolled below the recrystallisation temperature. Deformation heating may still cause the workpiece to far exceed room temperature, but recrystallisation temperatures can be much higher again: as much as 540°C for low carbon steel. Work hardening is a by-product of this and can be as much as 20% with 50% reduction in thickness. Reduction is limited during cold rolling but cold rolling produces a better surface finish than hot rolling. It is typically used for the final rolling passes so workpieces are often thinner to begin with. Cold rolled products include

metal furniture, computer hardware, metal drums and other thinner sheet metals. Foil rolling is also a room temperature process but the workpieces are thinner again. It is usually characterised by extremely high pressures and elastic roll deformation. As the name suggests, metal foils are the products of foil rolling.

For each of these processes there can also be a range of roll configurations. To ensure sufficient rigidity of the working rolls, two-roll configurations can be reinforced with a single set of backup rolls in a four-roll configuration, or with two sets of backup rolls in a six-roll configuration, or with even more in cluster configurations. These are chosen to minimise span-wise deflection that results in span-wise variation of workpiece thickness. Sometimes the rolls can be reversed to pass the workpiece forward and back for incremental reductions. Three-high roll configurations pass workpieces forward and back passes on the top and bottom of the middle roll. Time is saved without the delay of stopping the rolls and bringing them up to speed in the opposite direction; although, raising and lowering the workpiece between the roll gaps adds machine complexity. Tandem mills set up multiple rolling stands in series and the workpiece feeds from one stand into the next. This increases throughput at the expense of process complexity from the forward and back tension coupling between the stands.

It is worth introducing relevant terminology and geometry before explaining the key dynamics of rolling. The workpiece half-thickness, roll radii, and entrance velocity are all self evident, labelled \hat{h}_0 , $\hat{R}_{t/b}$ and \hat{U}_0 in Figure 1.2 respectively. The contact points, or tri-junctions, are the four intercepts between the workpiece and the rolls. The roll gap is the region between the two rolls where the workpiece is gripped by the rolls, the shaded region in Figure 1.2, and the roll gap length is the horizontal length of this region, taken as the horizontal distance between the workpiece contact points on the roll, \hat{l} in Figure 1.2. The amount the workpiece thickness is reduced is the gauge, Δh and the fractional change in the workpiece thickness, $\frac{\Delta h}{h_0}$, is called the reduction. This distinction will not be important in this work as both values are equivalent after non-dimensionalising vertically by the initial workpiece half-thickness.

Within the roll gap, the pressure ramps up from the entrance due to friction pulling the workpiece into the roll gap. Towards the end of the roll gap the pressure must ramp down again to match conditions outside the roll gap. The result is a characteristic pressure hill. To better understand the physics of this, first consider conservation of mass and the coarse approximation of plug-like flow. The material of the workpiece is forced to move faster as the distance between the rolls decrease; the surface velocity is marked as a solid line in panel (b) of Figure 1.3. Contrast this with the roll surface



(a) Hot rolling at Thyssenkrupp Steel mill in Bochum, Germany. Photograph credit: Uwe Niggemeier.



(b) Semi-disassembled cold rolling mill. Photograph source: SMS group

Fig. 1.1 Examples of sheet rolling.

which maintains a constant velocity, marked as a dashed line on the same panel. The intersection of these lines indicates the existence of a point, points, or region at which the direction of relative-slip and hence friction changes. This is called the neutral point, labelled \hat{x}_n in Figure 1.3. The opposing directions of friction act to squeeze the material towards the neutral point, building the pressure from both ends to a maximum at the neutral point. This is the mechanism forming the pressure hill. It is established by experiment and borne out in all rolling models presented in the literature.

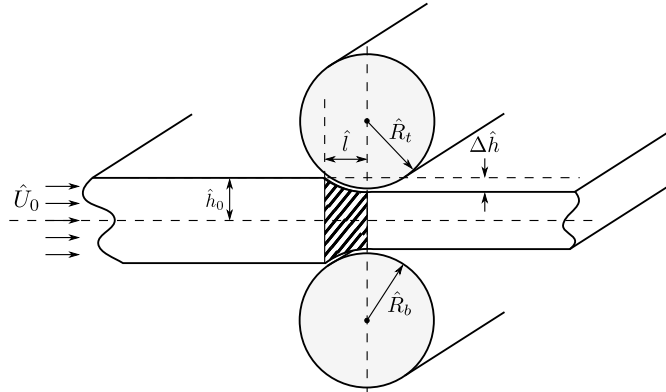


Fig. 1.2 A diagram of rolling illustrating the relevant parameters of two-dimensional geometry. This includes the workpiece half-thickness, \hat{h}_0 ; the roll radii, $\hat{R}_{t/b}$, the workpiece inlet velocity, \hat{U}_0 ; the roll gap length, \hat{l} ; and the gauge, $\Delta\hat{h}$.

Possibly contrary to intuition, the position of the neutral point depends predominantly on the balance of end forces on the workpiece. An end tension, or compression, would be balanced by the neutral point shifting to decrease, or increase, the friction in that direction. Applying tension to both ends would not have this effect, rather decrease the pressure throughout the entire roll gap.

By considering rolling in this way, extrusion and drawing are special cases of rolling: the roll velocities are zero and large entry compressions or exit tensions respectively move the neutral point to the entry contact point. In the general case, the rolls are not stationary and moderate end forces leave the neutral point away from the ends of the roll gap.

Modelling of rolling began in early twentieth century Germany with notable publications including Siebel (1924), Karman (1925) and Siebel et al. (1927). These each present a variation of a slab model: a model that determines the roll pressure and roll shear through the roll gap by applying a force balance to each vertical element, or slab, of the workpiece. This assumes no through-thickness variation of internal stresses, no internal shear and that the workpiece is at yield on the roll surfaces. Some experimental results support the validity of these assumptions; however, there is no rigorous basis for them and the limits of validity have not been thoroughly explored. Despite this, slab models are being developed and extended to more diverse applications, applications such as asymmetric rolling where shear is likely to be more significant.

The next major contribution came from Orowan (1943) in which an approximate model that incorporates shear is presented. Horizontal and vertical force balances

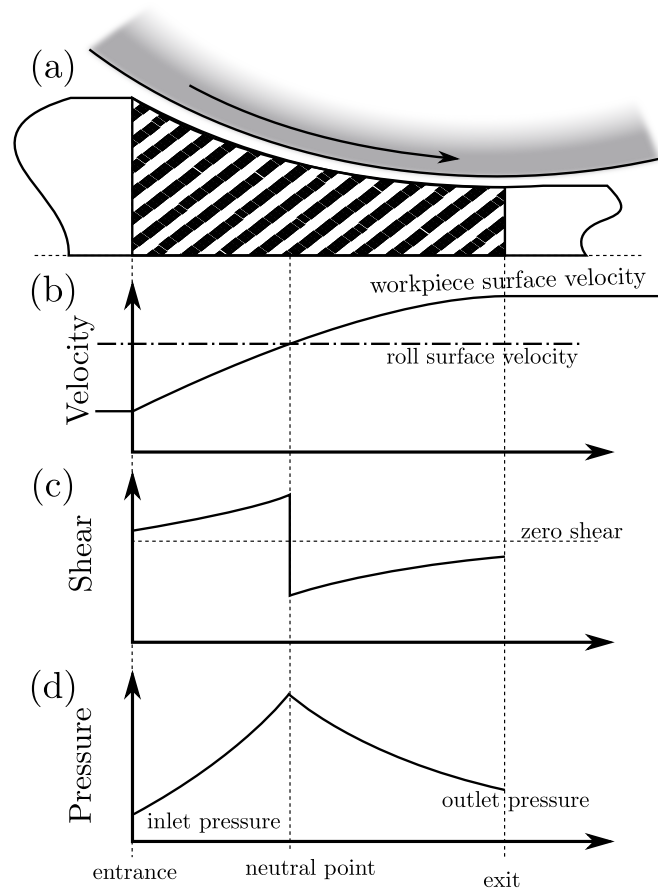


Fig. 1.3 A diagram of rolling (a), and characteristic plots of velocity (b); shear (c); and pressure (d), on the workpiece-roll interface. This illustrates the direction change of the interfacial relative-slip; the resulting change in sign of shear; and the characteristic pressure hill this mechanism produces. The neutral point, \hat{x}_n , is the point of zero relative-slip.

are closed by assuming that, locally, the solution can be approximated by Nadai's compressing wedge solution (Nadai, 1931). By considering a vertical element of material, marked by the lines $A - A'$ and $B - B'$ in Figure 1.4, and assuming this region is in dynamic equilibrium, the net forces on the dashed lines must equal the net forces on the solid lines. By this argument $A - A'$ can be deformed to the circumference of a circle perpendicularly intersecting the rolls and $B - B'$ can be deformed to a wedge of the circumference $A - A'$. The Nadai (1931) solution is then applied to this new geometry which closes the force balance for each vertical element.

Despite Orowan's claims to eliminate ad hoc assumptions from the analysis, the validity of this model relies on the assumption that the forces of a vertical slab are equivalent to those of a wedge. First, this equivalence has not been verified

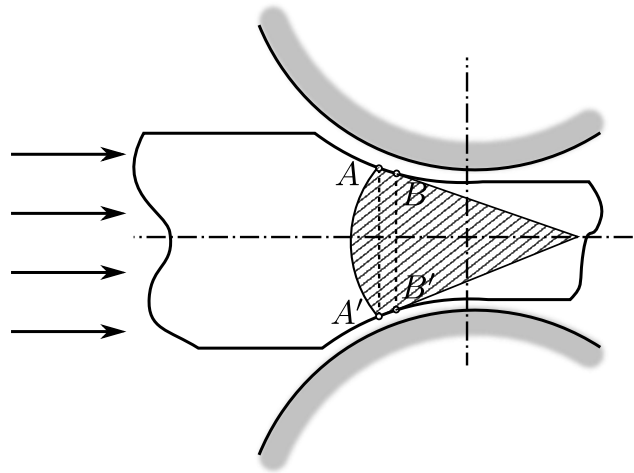


Fig. 1.4 Diagram indicating the approximation of a vertical elemental, $A - A' - B' - B$, to a compressing wedge solution (shaded) used by Orowan (1943) to close the force balance on each vertical element.

experimentally, numerically or analytically, especially for shallow angle wedges; and secondly, the compressing wedge solution used, although exact, can only be found for flow toward the wedge apex, limiting the correctness to the inlet side of the neutral point. Despite these inaccuracies, this solution has generally been adopted as a benchmark and is widely used by industry although with parameters empirically fitted for different set-ups. Some developments since then include Orowan et al. (1946), D. R. Bland et al. (1948) and D. Bland et al. (1948), which extend Orowan's original work to incorporate tensions or to simplify the calculation process with additional assumptions.

Slip-line theory has also been applied to symmetric rolling in two publications: Alexander (1955) and Collins (1969). These develop sticking models and the latter is limited to a qualitative discussion of the results due to no computation having been attempted on account of the model's complexity.

Hartley et al. (1989) provides the first review of rolling which predominantly covers these classical models as well as experimentation and some early finite element models.

More recently, asymptotic analysis has been applied to some metal forming applications. Asymptotic analysis exploits systematic assumptions of scale to find a rigorous yet tractable approximation, as opposed to simplifications through ad hoc assumptions of unknown error and limitation. It was first utilised in metal forming in 1987 by R. E. Johnson. Having transferred these techniques from modelling creep in glaciers,

he considers conical extrusion of a power-law rate hardening elasto-plastic material with Coulomb friction and neglected inertia. The asymptotic limit is quite elegant in that it considers deviation from a plug flow, making the solution valid for either low friction or shallow dies. One or both of these assumptions form the basis of all following asymptotic methods in extrusion and rolling. For example, Govindarajan et al. (1991) consider shallow die extrusion of a porous, compressible material.

A series of papers apply these same techniques to sheet rolling with R. E. Johnson as a common author. The first of these is Smet et al. (1989), followed three years later by R. E. Johnson et al. (1992). The former applies an almost identical process to that of R. E. Johnson (1987) while also neglecting elasticity and, of course, accounting for the neutral point, which is not present in extrusion. The latter paper makes a number of additional simplifications to progress further towards a closed form solution; the workpiece is modelled as a rigid material with arbitrary plastic behaviour and the rolls and workpiece interaction is modeled as a friction factor.

A similar formulation in Domanti et al. (1995) re-introduces Coulomb friction, while assuming the ratio of maximum pressure to yield stress is large and the reduction is small. Unfortunately, the first of these requires compressive end conditions and the latter, due to the coupling between reduction, roll gap length and sheet thickness, restricts the valid geometry considerably.

Finally, using a relative-slip friction model and strain-rate dependent constitutive equations, Cherukuri et al. (1997) solves the governing equations to a single ODE assuming only a small aspect ratio. This is repeated for small, medium and large friction then again with no-slip conditions.

Asymptotic models of three-dimensional effects and spread are considered in R. E. Johnson (1991) and Domanti et al. (1994). The former has a rare comparison to finite element simulations and experimental results. Asymptotic analysis has also been used for stability analysis of ‘chatter’ in R. E. Johnson (1994b); a multiple scales analysis of work roll heat transfer in R. E. Johnson et al. (1998); and a model for roller deformation in Langlands et al. (2002). A review of modelling methods applied to rolling is presented in Domanti et al. (1998) although no comparison of results is made.

Many numerical studies have been performed since they began in 1972 with Alexander (1972). Notably, Venter, R. D and Abd-Rabbo, A (1980) and Venter et al. (1980) develop numerical implementations of the Orowan (1943) solution. Finite element simulations have since become the most popular technique and several reviews exist including Montmitonnet et al. (1991) and Montmitonnet (2006), in which 34 and 25

publications of finite element simulations of rolling have been reviewed respectively. It is, in fact, included as an example problem in the commercial finite element package, *ABAQUS*, ‘Example Problems Manual’ (Dassault Systemes, 2012b). This ubiquity is a result of the analytical models failing to generalise to a range of materials and geometry without reformulation. Despite this, the computational time of Finite element modelling (FEM) remains long, too long for integration with control systems. The results from these investigations are also difficult to transfer or generalise; the process of constructing and solving these simulations is often repeated in independent studies for very similar set-ups.

1.1.1 Asymmetric rolling

Asymmetry can arise during the rolling process in a variety of ways including asymmetric roll sizes, roll speeds or roll-workpiece interfaces; asymmetric material properties from hardening or temperature variation; and asymmetric end conditions. These may manifest unintentionally through machine wear, material imperfections or poorly designed heating; or be intentionally exploited to simplify machine design such as single drive stands, reduce energy consumption by maximising shear strain or improve product quality by increasing strain hardening.

The rolling of inhomogeneous sheets, specifically clad or bi-metallic sheets, is another instance of asymmetry. The bonding of sheets can occur during the rolling processes and so both bonded and unbonded sheets have been studied in literature as well as the transition between the two. Composite sheets can also reduce the required total force and torque of rolling compared to homogeneous sheets, which improves efficiency. Other configurations such as tri-metallic, or sandwich sheet, rolling also exists.

Like symmetric rolling, the pressure hill and the position of the neutral point are key dynamics of asymmetrical rolling. This is complicated by the asymmetry because the neutral points on each roll surface are not generally vertically coincident. This leads to a region, termed the cross-shear region, between the neutral points in which the traction forces act in opposite directions. The cross-shear region has a high, fairly uniform shear stress through-thickness as opposed to the other sections where shear is zero near the centre-line. The cross-shear region is also characterised by a truncation of the apex of the pressure hill: the horizontally opposing traction forces do not squeeze the workpiece in this region. This provides an explanation for the reduced roll force

and torque required in asymmetric rolling. The high shear is also likely the explanation for increased work hardening.

Two key areas of interest in asymmetrical rolling are the prediction of the roll gap strain field to predict micro-structural evolution and the prediction of the induced curvature.

Analytical modelling has included a range of solutions. Modified slab models (Chekmarev et al., 1956; Y. Hwang et al., 1993; Kennedy et al., 1958; Mischke, 1996; Sauer et al., 1987) have been incrementally developed to include more asymmetries and even curvature predictions (Aboutorabi et al., 2016; Gudur et al., 2008; Qwamizadeh et al., 2011; Salimi et al., 2002). Upper-bound methods (M. M. Kiuchi et al., 1986; D. Pan et al., 1982) and slip-line methods (Collins et al., 1975; Dewhurst et al., 1974) have also been applied, with some making curvature predictions.

Both slab models (Afrouz et al., 2015; Y. M. Hwang et al., 1996a,b; S. Pan et al., 2008; Qwamizadeh et al., 2013, 2014; Wang et al., 2015) and upper-bound methods (Maleki et al., 2013; Pishbin et al., 2010; Shintani et al., 1992) have also been employed to study clad-sheet rolling with some extending curvature prediction to this area (Y. Hwang et al., 1996b; Lee et al., 2015; Qwamizadeh et al., 2014). The behaviour at the composite interfaces, including slipping, bonding and bond breaking, is an additional consideration for rolling composite workpieces (S. C. Pan et al., 2006; Yong et al., 2000).

Asymptotic analysis has been applied to modelling asymmetric rolling once (R. E. Johnson, 1994a).

A more in-depth discussion of homogeneous asymmetric rolling begins Chapter 2 and a more in-depth discussion of clad rolling begins Chapter 3. Specific attention is also given to curvature and curvature prediction in Chapter 4.

1.2 Ring rolling

Ring rolling is another variation of rolling, shown in Figure 1.5. Instead of a flat sheet, a closed ring is rolled to reduce its profile width. A pair of vertical rolls are used, the unpowered inner roll is called the mandrel and the powered outer roll is called the work roll. The thinning of the ring results in growth of the ring's diameter and profile height. A second pair of horizontal rolls, called the axial rolls, are used to limit this growth in profile height. Unpowered guide rolls are also commonly used to ensure the ring remains centred on the work roll and mandrel.



Fig. 1.5 A ring being rolled by a D53K CNC radial axial Ring Rolling Machine. On the left, the ring is pinched between the work roll outside and the mandrell inside. On the right, two horizontal conical rolls prevent vertical growth. Two unpowered guide rolls are also visible on the left, either side of the work roll. As the ring increases in diameter, the left and right sets of rolls are moved apart.

There are a number of key differences between ring rolling and sheet rolling. Most obviously, the joined workpiece couples the end conditions of the roll gap. Forces and, more significantly, moments that otherwise would not be balanced with free sheets, are supported by this coupling. Secondly, the characteristic reduction is small and the roll gap aspect ratio is large; the opposite of many sheet rolling regimes. A corollary of small reduction is that a single workpiece will undergo many rotations while being formed, which increases the significance of work hardening during the process. Finally, the workpiece width is comparatively small so edge effects may be considerably more significant than sheet rolling. In fact, axial rolls are required due to profile height increases in some cases, indicating a plane stress condition.

Three considerations of product quality include circularity, coaxiality and flatness. These are measures of uniformity in local curvature, profile width and profile height respectively. Two more considerations during processing are centrality, the distance between the ring centre and the line of symmetry of the rolls; and slip, how much the work roll surface slips on the workpiece or, in terms of asymmetrical rolling, the position of the neutral point in the roll gap. The three measures of product quality will always be of importance as tolerances for each will be specified by the product

application, whereas centrality and slip are only of interest in so far as they have proven useful to ensure successful process design.

Current areas of development in ring rolling include controlling circularity to produce elliptical or other polygonal shapes; more complex profile control, such as forming non-rectangular cross-sections; and flexible profile forming, such as forming L-shapes of different proportions with a single tool set.

Analytical models of ring rolling fall into two categories: models of the roll gap only (Hawkyard et al., 1973; Lin et al., 1997; Parvizi et al., 2014, 2011; Zamani, 2014) or mass conservation models of the ring evolution (Berti et al., 2015; Guo et al., 2011; Xu et al., 2012). This has been in the interest of process design (Berti et al., 2015) or control (Hua et al., 2016). Other areas of research in ring rolling include profile ring rolling (Akcan, 2009; Zhou et al., 2014), curvature control (Arthington et al., 2016) and strain estimation (Quagliato et al., 2016). Existing literature is discussed in more detail in Chapter 6.

1.3 English wheel

The English wheel, or the wheeling machine, is an unpowered manufacturing tool that entered mainstream use in the early 1900s. It consists of a 'C' shaped frame mounting rolls at either end with a variable separation. By rolling regions of a sheet metal workpiece by hand, local thinning occurs, which causes out of plane deformation. Figure 1.6 pictures an English wheel and illustrates the frame, top roll and its use, although the lower roll cannot be seen beneath the workpiece.

This comparatively slow and manual process lost popularity as production volumes increased. Today it has been relegated to artisan workshops for custom part production and no instances of automation are known to the author. The English wheel has not only avoided automation, but no studies or models could be found of the process. This leaves some open questions regarding the regime that occurs within the roll gap, whether the plastic region is limited to the roll gap and whether bending from out of plane boundary forces contributes to the formation of curvature. The framework for a model of the English wheel is presented in Section 6.5.2 as well as further discussion of these points.



Fig. 1.6 A doubly curved sheet being rolled with an Eastwood English Wheel. Photograph by Nick Capinski.

1.4 Governing equations

Like any continuum mechanics problem, these processes are described with three sets of equations: kinetics, compatibility/kinematics, and constitutive laws. Newton's second law governs kinetics,

$$\nabla \cdot \hat{\sigma} = \hat{\rho} \hat{\mathbf{a}}, \quad (1.1)$$

where $\hat{\sigma}$ is the stress tensor, $\hat{\rho}$ is the density, $\hat{\mathbf{a}}$ is the acceleration and hats here, and throughout this document, denote dimensional quantities. For the applications considered in this work inertia is negligible and so acceleration terms will be ignored unless stated explicitly otherwise.

The kinematics can be satisfied most easily by considering deformation as a continuous velocity field such that

$$\frac{\partial \hat{\epsilon}_{ij}}{\partial \hat{t}} = \frac{1}{2} \left(\frac{d\hat{v}_i}{d\hat{x}_j} + \frac{d\hat{v}_j}{d\hat{x}_i} \right), \quad (1.2)$$

where $\hat{\epsilon}_{ij}$ is the ij^{th} term in the strain tensor, \hat{v}_i is the velocity in the i^{th} direction, \hat{x}_i is the basis vector in the i^{th} direction and \hat{t} is time.

The constitutive laws can be defined as some function of stress, strain, strain-rate, temperature or other external factors which might affect material properties,

$$\frac{\partial \hat{\epsilon}_{xx}}{\partial \hat{t}} = f_{xx}(\hat{\sigma}, \hat{\epsilon}, \frac{\hat{\epsilon}}{\hat{t}}, \dots) \quad (1.3)$$

$$\frac{\partial \hat{\epsilon}_{yy}}{\partial \hat{t}} = f_{yy}(\hat{\sigma}, \hat{\epsilon}, \frac{\hat{\epsilon}}{\hat{t}}, \dots) \quad (1.4)$$

$$\frac{\partial \hat{\epsilon}_{xy}}{\partial \hat{t}} = \frac{\partial \hat{\epsilon}_{yx}}{\partial \hat{t}} = f_{xy}(\hat{\sigma}, \hat{\epsilon}, \frac{\hat{\epsilon}}{\hat{t}}, \dots) \quad (1.5)$$

$$(1.6)$$

where f_{ij} is a function determined by the constitutive law. A wide range of functions could be applied here and an appropriate choice must be made considering the functions' form and accuracy for the application. Possibilities are discussed in the next section.

These relations must be closed with a suitable set of boundary conditions, typically contact laws. There are numerous friction models that form the required contact laws so some discussion of these models is provided in Section 1.4.2.

1.4.1 Material models

The constitutive, or material, law must relate the displacements and the stresses within the material. Many material models exist to describe different physical phenomena or satisfy particular analytical properties. This section is structured around the phenomena captured by constitutive laws in solid mechanics and each is discussed in the context of rolling processes.

Plasticity

Plasticity can be described as the permanent deformation of a material and is, clearly, essential for modelling any forming process. Plasticity is defined by a yield condition which, if satisfied, allows the material to deform irreversibly according to a flow rule for each tensor element. The flow rules are typically in terms of strain increments that define the mode of plastic deformation. The flow parameter then defines the magnitude of plastic deformation such that compatibility is enforced without exceeding the yield condition.

Some flow rules can be related to the yield condition by defining the plastic strain increment vector as normal to the yield surface. These flow rules are called associative flow rules; compared to non-associative flow rules which violate this normality relation.

Associative flow rules have been shown to be accurate for metals but not soils and rocks.

One common example of a set of associative flow rules are the Levy-Mises equations which are associated with the von-Mises yield condition. These can be written for plane strain, without elasticity or hardening, as

$$\begin{aligned}\frac{\partial \hat{u}}{\partial \hat{x}} &= \hat{\lambda} \hat{s}_{xx}, \\ \frac{\partial \hat{v}}{\partial \hat{y}} &= \hat{\lambda} \hat{s}_{yy}, \\ \frac{\partial \hat{u}}{\partial \hat{y}} + \frac{\partial \hat{v}}{\partial \hat{x}} &= 2\hat{\lambda} \hat{s}_{xy}\end{aligned}\quad (1.7)$$

$$\text{and } \hat{s}_{xx}^2 + \hat{s}_{yy}^2 + 2\hat{s}_{xy}^2 = 2\hat{k}^2 \quad (1.8)$$

respectively, where $\hat{\lambda}$ is the time differential of the flow parameter; (\hat{u}, \hat{v}) are the horizontal and vertical velocity components respectively; \hat{s}_{ij} is the ij^{th} deviatoric stress, $\hat{s}_{ij} = \hat{\sigma}_{ij} + \hat{p}$; \hat{p} is pressure; and, \hat{k} is the yield stress in shear.

The use of equality in equation (1.8) imposes a state of plastic deformation. If this were an inequality, the left hand side less than the right, then $\hat{\lambda} = 0$ would be enforced to eliminate plastic deformation and, without elasticity, amounts to solid body motion.

Equation (1.8) implies an elliptic yield surface, which is both analytically appealing and has been shown to more accurately describe metals than, say, the Tresca yield condition. The inclusion of hardening would depend on the material being modelled as some metals undergo considerable hardening where others do not. Neglecting elasticity is also acceptable where plastic deformation is orders of magnitude larger than elastic deformation. Rigid perfect plasticity with an elliptical yield surface is therefore a reasonable choice to model the rolling processes.

Elasticity

Elasticity can be described as the reversible deformation of a material. It occurs above and below yield and is usually assumed to be additive with plastic deformation, that is $\hat{\epsilon} = \hat{\epsilon}^e + \hat{\epsilon}^p$ where $\hat{\epsilon}$, $\hat{\epsilon}^e$ and $\hat{\epsilon}^p$ are the total, elastic and plastic strains respectively.

Linear, isotropic elasticity is expressed as the generalised Hooke's law,

$$\hat{\epsilon} = \frac{1 + \nu}{\hat{E}} \hat{\sigma} - \frac{\nu}{\hat{E}} \text{tr}(\hat{\sigma}) \mathbf{I} \quad (1.9)$$

where ν is Poisson's ratio and \hat{E} is the elastic modulus.

Differentiating in time and using the Jaumann objective stress rate gives a rate form for easier comparison to the plastic equations,

$$\begin{aligned} \frac{\partial \hat{u}}{\partial \hat{x}} &= \frac{1 + \nu}{\hat{E}} \left(\hat{u} \frac{\partial \hat{s}_{xx}}{\partial \hat{x}} + \hat{v} \frac{\partial \hat{s}_{xx}}{\partial \hat{y}} \right) + \frac{1 + 3\nu}{\hat{E}} \left(\hat{u} \frac{\partial \hat{p}}{\partial \hat{x}} + \hat{v} \frac{\partial \hat{p}}{\partial \hat{y}} \right) - \frac{1 + \nu}{\hat{E}} \left(\frac{\partial \hat{u}}{\partial \hat{y}} - \frac{\partial \hat{v}}{\partial \hat{x}} \right) \hat{s}_{xy} \\ \frac{\partial \hat{v}}{\partial \hat{y}} &= \frac{1 + \nu}{\hat{E}} \left(\hat{u} \frac{\partial \hat{s}_{yy}}{\partial \hat{x}} + \hat{v} \frac{\partial \hat{s}_{yy}}{\partial \hat{y}} \right) + \frac{1 + 3\nu}{\hat{E}} \left(\hat{u} \frac{\partial \hat{p}}{\partial \hat{x}} + \hat{v} \frac{\partial \hat{p}}{\partial \hat{y}} \right) + \frac{1 + \nu}{\hat{E}} \left(\frac{\partial \hat{u}}{\partial \hat{y}} - \frac{\partial \hat{v}}{\partial \hat{x}} \right) \hat{s}_{xy} \\ \text{and } \frac{\partial \hat{u}}{\partial \hat{y}} + \frac{\partial \hat{v}}{\partial \hat{x}} &= 2 \frac{1 + \nu}{\hat{E}} \left(\hat{u} \frac{\partial \hat{s}_{xy}}{\partial \hat{x}} + \hat{v} \frac{\partial \hat{s}_{xy}}{\partial \hat{y}} \right) + \frac{1 + \nu}{\hat{E}} \left(\frac{\partial \hat{u}}{\partial \hat{y}} - \frac{\partial \hat{v}}{\partial \hat{x}} \right) (\hat{s}_{xx} - \hat{s}_{yy}). \end{aligned} \quad (1.10)$$

Linear elasticity is widely accepted as accurate for metals undergoing small deformations. The elastic modulus is typically three orders of magnitude larger than the yield stress so plastic deformation quickly begins to dominate once the material reaches yield.

Hardening

Hardening can be described as the expansion of the yield surface as a result of other changes in the material. It can occur in response to a range of factors but is commonly connected to strain or strain-rate.

Strain hardening, also called work hardening or cold working, increases the yield stress depending on the accumulated strain, or the strain path, of the material. Strain-rate hardening increases the materials' resistance to plastic deformation as deformation occurs more quickly making the yield stress a function of the plastic flow rate.

For example, the von-Mises yield condition is modified here to incorporate strain-rate hardening. Using a new variable $\hat{\Omega}$, for

$$\hat{s}_{xx}^2 + \hat{s}_{yy}^2 + 2\hat{s}_{xy}^2 = 2\hat{\Omega}, \quad (1.11)$$

The yield stress is made dependent on the plastic flow rate, $\hat{\lambda}$, by choosing a power law relation, such as

$$\frac{\hat{\lambda}}{\hat{\lambda}_0} = \left(\frac{\hat{\Omega}}{\hat{k}} \right)^{n-1}.$$

Cherukuri et al. (1997) made the dimensionally inconsistent choice $\hat{\lambda}_0 = (\hat{k})^{n-1}$ for the associated flow rule

$$\begin{aligned} \frac{\partial \hat{u}}{\partial \hat{x}} &= \hat{\Omega}^{n-1} \hat{s}_{xx}, \\ \frac{\partial \hat{v}}{\partial \hat{y}} &= \hat{\Omega}^{n-1} \hat{s}_{yy} \\ \text{and } \frac{\partial \hat{u}}{\partial \hat{y}} + \frac{\partial \hat{v}}{\partial \hat{x}} &= 2\hat{\Omega}^{n-1} \hat{s}_{xy}, \end{aligned} \quad (1.12)$$

Both strain hardening and strain-rate hardening can be used to increase accuracy of a yield condition. Each are significant for certain types of metals and both have been used in rolling models (Cherukuri et al., 1997; Smet et al., 1989).

Other Phenomena

The yield stress can be made dependent on a wide range of other factors by modifying equation (1.8) to make \hat{k} a function of any number of additional variables. One example, relevant to hot forming processes, is temperature. Other, less relevant examples, could include chemical state, compaction or the local magnetic field. Often this additional dependence will be the source of coupling between the deformation equations and other dynamics such as temperature diffusion, chemical reactions or electro-magnetic state.

There also exists kinematic hardening, or more generally anisotropic hardening, as hardening of a material does not necessarily occur uniformly in every direction. Kinematic hardening is when the yield surface translates; that is, hardening in one direction results in softening in another and is known as the Bauschinger effect.

1.4.2 Friction models

With a complete set of governing equations, it remains to define boundary conditions and close the system. Surface contact occurs throughout manufacturing and provides the necessary conditions.

Normal forces are satisfied with a no-penetration condition; however, traction forces are less obvious and continue to be the subject of research in tribology and other areas. There are many traction models available so several of the most common are discussed here. Numerous other models exist with increasing complexity, particularly for high temperature and lubricated conditions. Despite many models existing, there is a scarcity of experimental work to determine their validity for rolling. Mamalis

(1975) and Ghobrial (1989) appear to be two of the few experimental works that approach this subject, although tangentially. Photo-elastic rolls (Ghobrial, 1989) or a pin load cell/membrane method (Mamalis, 1975) are used to measure the roll pressure distribution, which could be used, with an analytical or numerical model, to fit a friction model. More direct measurement appears to be an enormous experimental challenge and so has not been investigated further. This being the case, the additional complexity of other models is unlikely to add additional insight or accuracy and so only these general models are considered in this work.

Coulomb friction

Coulomb friction is widely used. It is the assumption that the friction force is proportional to the normal pressure,

$$\hat{\boldsymbol{\tau}} = -\mu \mathbf{n} \cdot \hat{\boldsymbol{\sigma}} \cdot \mathbf{n} \frac{\Delta \hat{\mathbf{u}}}{|\Delta \hat{\mathbf{u}}|} \quad (1.13)$$

where $\hat{\boldsymbol{\tau}}$ is the tangential surface traction, μ is a constant dimensionless friction coefficient, \mathbf{n} is the unit normal vector to the contact surface, $\hat{\boldsymbol{\sigma}}$ is the stress tensor and $\Delta \hat{\mathbf{u}}$ is the relative-slip velocity vector of the plastic material past the surface. It has been applied to static and slipping friction problems, although coefficient values are very different between these regimes. It is generally considered accurate over mid-range traction forces and saturation will be reached at high pressures, ultimately when the yield condition is reached with shear alone.

Figure 1.7 illustrates the result of this friction model in an asymptotic model of symmetric rolling assuming a thin-sheet and low friction, following a method similar to Cherukuri et al. (1997). There is a discontinuity in the shear stress at the neutral point, which produces a corner at the apex of the pressure hill. The discontinuity aside, this model produces the pressure hill characteristic of rolling.

Relative-slip friction

Relative-slip friction is specifically a slipping model as it assumes the friction force is proportional to the velocity difference between the surfaces in contact,

$$\hat{\boldsymbol{\tau}} = -\hat{\kappa} \Delta \hat{\mathbf{u}} \quad (1.14)$$

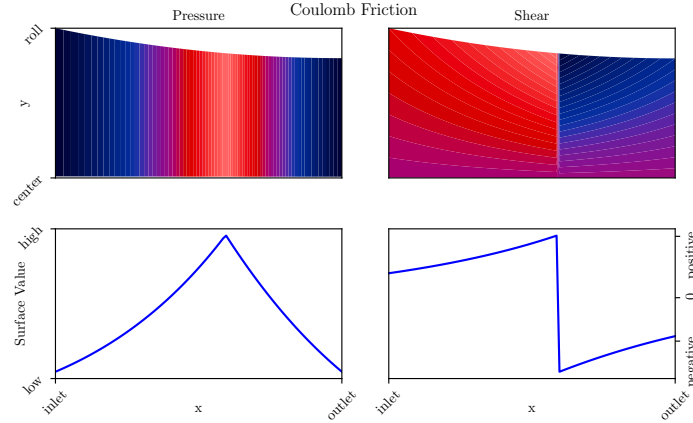


Fig. 1.7 Illustrative example of pressure and shear stress field and respective values on the roll surface for rolling with Coulomb friction assuming low friction and a small roll gap aspect ratio.

where \hat{k} is a constant friction coefficient with dimensions newton seconds per meter cubed. It predicts zero traction for static contact and exceeds the yield stress at high slip rates, which provide obvious bounds to its validity.

Figure 1.8 illustrates this friction model in the same context as Figure 1.7. The apex of the pressure hill is smoothed as there is no discontinuity around the sign change of shear. The maximum shear is predicted at the workpiece-roll contact points, which is not generally considered to be true.

Friction factor

Friction factor is the assumption that friction forces are constant at some fraction of the yield stress,

$$\hat{\tau} = -m\hat{k} \frac{\Delta \hat{u}}{|\Delta \hat{u}|} \quad (1.15)$$

where m is a constant dimensionless factor, typically taken as 1 and always between 0 and 1 inclusive.

Friction factor models become accurate as others saturate and so are applicable to high friction regimes. This makes them attractive for hot rolling models. They are also attractive for their simplicity and for not further coupling the governing equations when used in conjunction with a constant yield stress, \hat{k} .

Figure 1.9 illustrates the effect of this friction model and, comparing with Figure 1.7, looks very similar to Coulomb friction. The shear discontinuity and sharp pressure hill apex are both present. There is still a slight change in shear stress throughout the

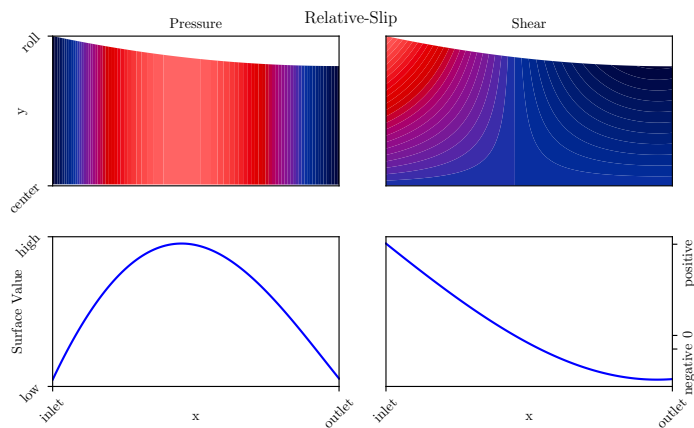


Fig. 1.8 Illustrative example of pressure and shear stress field and respective values on the roll surface for rolling with relative-slip friction assuming low friction and a small roll gap aspect ratio.

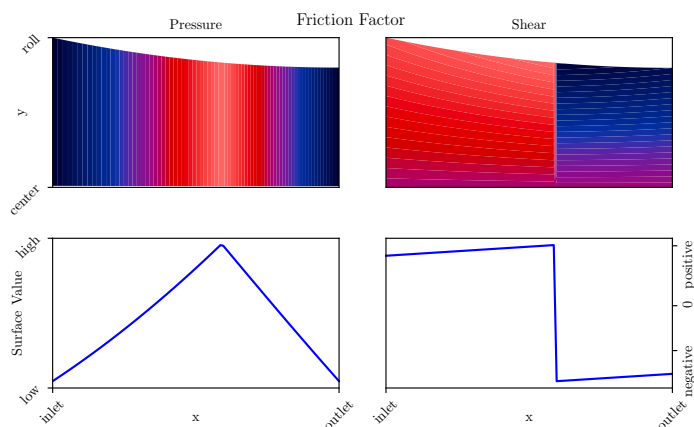


Fig. 1.9 Illustrative example of pressure and shear stress field and respective values on the roll surface for rolling with a factor friction model assuming low friction and a small roll gap aspect ratio.

roll gap as the plot shows shear stress, not surface traction, so the shape of the roll contributes. Therefore, the pressure hill is slightly concave, although not as pronounced as with the Coulomb friction model.

No-slip contact

The no-slip condition is another obvious friction choice, specifying the boundary material displacements to be equal, rather than specifying surface forces. That is

$$\hat{\mathbf{u}} = \hat{\mathbf{U}} \quad (1.16)$$

where $\hat{\mathbf{u}}$ is the velocity of one surface and $\hat{\mathbf{U}}$ is the velocity of the other. For rigid perfectly-plastic, and other materials, this will leave the stresses undetermined and so the associated stress condition is a friction factor model where $m = 1$. No-slip would be appropriate for sticking conditions or very high friction situations such as hot rolling.

Transitional models

Considering the relative regions of accuracy for the preceding models, it is unsurprising that some models propose transitioning from one friction condition to another. For example, Friction factor when Coulomb or relative-slip friction models saturate is an obvious choice to prevent the yield condition being exceeded. This is commonly used in finite element implementations.

Other models transition between friction definitions on a more ad hoc basis to exploit the model most accurate for each circumstance. One example of this type of model is presented in Karabin et al. (1990).

$$\hat{\tau} = |\hat{\tau}| \frac{\Delta \hat{\mathbf{u}}}{|\Delta \hat{\mathbf{u}}|}$$

$$\text{where } |\hat{\tau}| = \min \left(\hat{\mu} \psi^l (\mathbf{n} \cdot \hat{\boldsymbol{\sigma}} \cdot \mathbf{n})^m, \hat{k} \right)$$

$$\text{and } \psi = \min \left(\frac{|\Delta \hat{\mathbf{u}}|}{\hat{\Delta}_v}, 1 \right) \quad (1.17)$$

where $\hat{\mu}$, $\hat{\Delta}_v$, l and m are all constants.

Letting $l = 1$ and $m = 1$, this formulation will behave like relative-slip at low slip speeds, when $\psi < 1$. It will then transition to a Coulomb model at higher speeds, when $\psi = 1$ and $|\hat{\tau}| = \hat{\mu} \mathbf{n} \cdot \hat{\boldsymbol{\sigma}} \cdot \mathbf{n}$. Finally, before exceeding the yield condition, it will transition to a friction factor model with coefficient of unity, $|\hat{\tau}| = \hat{k}$. Note that the

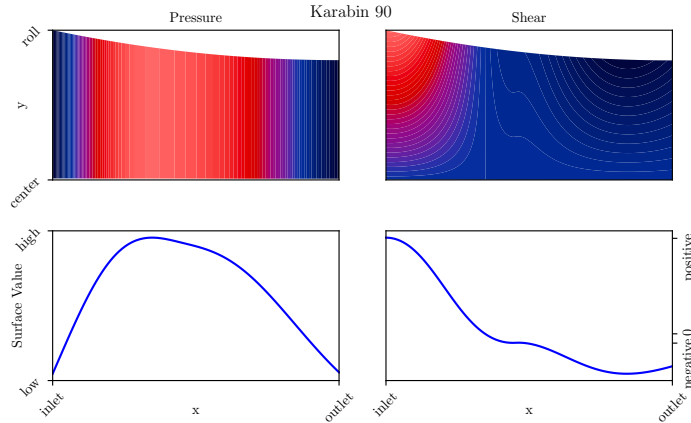


Fig. 1.10 Illustrative example of pressure and shear stress field and respective values on the roll surface for rolling with the Karabin et al. (1990) friction model assuming low friction and a small roll gap aspect ratio. $\Delta_v = 0.2U_{\text{roll}}$, $m = 2$, $l = 2$ and $\mu = 0.3$.

position of this first transition relies on a non-physical parameter, $\hat{\Delta}_v$, which must be fitted. The powers l and m are also fitting parameters. Fitting more parameters requires more experimentation of the process being modelled, which may or may not be feasible.

Figure 1.10 illustrates this model. The results look quite strange but show some desirable characteristics. No discontinuity occurs, which presents a big advantage over Coulomb or friction factor models. The transition between signs also occurs more quickly than the relative-slip model and the maximum and minimum shear is moved within the roll gap, which characteristically agrees with observed behaviour. While illustrative, this example could be made to match experimental results with the additional fitting parameters.

More transitional models of increasing complexity exist such as Wanheim et al. (1978); however, as discussed in the introduction to this section, these are unlikely to add insight or value to this discussion and hence are omitted.

1.5 Modelling approaches

Given a set of governing equations to describe each of these processes a range of techniques can be employed to derive usable information. Finite element simulations provide a versatile means of approximating complete solutions of complex geometries and are hence used widely. The obvious drawback of finite element analysis is the computational time and the limited transferability of understanding from one solution

to others. At the cost of generality, approximate analytical solutions can overcome both of these challenges. These take longer to develop and hence are applied less widely. The approximations are made either on an ad hoc basis or systematically. Both must be verified for accuracy and validity; however, this is generally easier for the latter. Regression modelling can also produce models that evaluate quickly; however, ensuring valid results requires exhaustive experiments or simulations of the regime of interest and so is an expensive approach.

Considering the broader objective of this work, to develop control systems, which requires reliable predictions in real-time or faster, finite element analysis is inappropriate. A range of mathematical approaches, specifically asymptotic analysis, and some regression modelling will be the basis of this investigation. They are faster solutions that can be made sufficiently accurate within specific regimes. It is also hoped that using these approaches will generate new insights into the underlying dynamics of forming to inform process design and innovation.

Ideally both numerical and experimental validation would be conducted; however, this was not feasible so only finite element analysis is used. This has the advantage of limiting possible deviation between analytical and numerical solutions to a limited set of assumptions as the governing equations used in the simulations are known. The drawback is, of course, that the accuracy of these governing equations to model the problem physics will remain unquantified in this work.

Chapter 2 presents an asymptotic model of sheet rolling with asymmetry included in the roll sizes, roll speeds and interfacial friction conditions. It is developed by exploiting two assumptions: that the workpiece is thin and that the effect of friction is weak. Chapter 3 extends this model to include a composite workpiece of two bonded materials by solving for a free boundary denoting the interface of the two materials. Curvature is a key property to be predicted in either of these applications and so a review of curvature prediction is presented in Chapter 4. This includes a qualitative review of numerical and experimental literature investigating curvature; a statistical analysis of the results presented in these publications; and a comparison of analytical models that predict curvature. An asymptotic model with alternative assumptions is proposed in Chapter 5 to model thick-sheet rolling and capture more of the non-linear behaviour observed in the previous chapter. Chapter 6 concludes the substantive chapters with a framework for applying predictive curvature models to the ring rolling processes and, by analogy, to the English wheel.

Chapter 2

Asymmetric rolling

An analytical model for asymmetric rolling is presented, which includes asymmetry in roll friction, roll size and roll speed, for a rigid, perfectly-plastic thin-sheet deformed with Coulomb friction. This model is solved asymptotically, based on the systematic assumptions that both the roll gap aspect ratio and the friction coefficient are small. The leading order solution is shown to be consistent with an existing slab model (Y. Hwang et al., 1993); additional detail is then derived by looking to higher orders. The leading and higher order solution are compared with finite element simulations, and the results are used to determine the practically valid range of the analytical model. Within this region, it gives good quantitative predictions of the force and torque results produced by finite element simulations. It also approximates through-thickness variation of stress and strain, all with orders of magnitude shorter computation times than the finite element counter parts. This also validates the ad hoc assumptions made when deriving the previous slab model.

The model is formulated in Section 2.2. The choice of material and friction models is used to illustrate the asymptotic process; following this procedure, solutions could be found for any of the friction or material models used in the asymptotic rolling literature (Cawthorn, Minton et al., 2016; Cherukuri et al., 1997; Domanti et al., 1995; R. E. Johnson et al., 1992; Smet et al., 1989). This model is non-dimensionalised for six non-dimensional groups: the aspect ratio, δ and the friction coefficient, μ , which are both assumed to be small; and the sheet reduction r ; the ratio of roll sizes; the ratio of roll speeds; and the ratio of roll-workpiece frictions, which are all considered to be of order one. The asymptotic solution is developed in Section 2.3 and is validated against the commercial finite element package *ABAQUS/Explicit* (Dassault Systemes, 2012a) through a range of asymmetries and parameters in Section 2.5. An abridged

version of this chapter has been published in the International Journal of Mechanical Science (Minton et al., 2016).

2.1 Introduction

The mechanical simplicity of a single driven roll configuration was appealing in industry, which first motivated investigations into asymmetric rolling (Zorowski et al., 1963). Process efficiency gains, improved workpiece quality and reduced maintenance requirements are several reasons this area of research continues to be active. Curvature is also desirable to produce a wider range of products or eliminate product imperfections.

Experimental investigations into asymmetrical rolling predominantly investigate the resulting workpiece curvature. This is thoroughly reviewed in Chapter 4 so will not be repeated here; however, some studies also report results of roll force and torque. W. Johnson et al. (1966a,b) establish the correlation between roll speed asymmetry and the torque ratio and attribute this to the changing position of neutral points. D. Pan et al. (1982) identifies that this same asymmetry produces a drop in total roll force. Ghobrial (1989) is also notable for the use of a photo-elastic roll material to ascertain stress distributions throughout the rolls. The change in friction direction and cross-shear were able to be visualised, and a higher peak roll pressure was observed for the smaller roll under roll radii asymmetry.

Like experimental studies, many finite element method studies of asymmetrical rolling investigate curvature, also reviewed in Chapter 4; however, the stress and strain field results provide valuable insight. Shivpuri et al. (1988) illustrates the region of yield for speed asymmetry by plotting the equivalent plastic strain field. Horizontal stress fields for asymmetric friction in Richelsen (1997) show the pressure hill as well as oscillations through the roll gap. Markowski et al. (2003) shows a reduction in total roll force as the roll size asymmetry is increased. A rapid reduction occurs for small asymmetries and a gradual reduction continues for asymmetries beyond this point. The ratio of roll torques varies uniformly with increasing asymmetric roll size. Akbari Mousavi et al. (2007) verifies that both the total roll force and torque decreases with asymmetric roll speed. Contact stresses are also shown and present a pressure hill, distinct neutral points and a cross shear region. More recent work has investigated the effects of increased shear due to asymmetry on microstructural behaviour induced by asymmetry (Pesin et al., 2014).

Analytical modelling of asymmetrical rolling has included a range of approaches; the most popular being to modify symmetric rolling slab models. This began with Y. Hwang et al. (1993), in which through-thickness variation of stress was neglected to justify an average of the top and bottom friction forces used in the differential equation for pressure. This model captures the region of cross shear, which is the dominant effect in asymmetric rolling. Subsequent variations include: Mischke (1996) uses an alternative origin to consider non-vertically aligned contact points on the inlet; Y. Hwang et al. (1997) reformulates the original Y. Hwang et al. (1993) model with constant shear friction; Salimi et al. (2002) applies assumptions about through-thickness stresses to generate curvature predictions; Salimi et al. (2004) is worthy of note as it introduces vertical force and moment balances to resolve horizontal stress on the top and bottom surface and the vertically averaged shear stress through the roll gap; Gudur et al. (2008) applies the curvature prediction of Salimi et al., 2002 to estimate friction coefficients; Qwamizadeh et al. (2014) assumes a quadratic through-thickness shear profile; and Aboutorabi et al. (2016) assumes a free surface profile as an alternative to assuming vertically aligned entry contact points. The original slab models are based on ad hoc assumptions that are not validated thoroughly, making the assumptions of these subsequent models increasingly questionable. This seems particularly relevant for the more recent works which include greater asymmetry, but are still used to predict curvature.

Alternative techniques have included upper-bound methods (Y. Hwang et al., 1996a; M. Kiuchi et al., 1987) and slip-line methods (Collins et al., 1975; Dewhurst et al., 1974). The upper-bound method assumes a parametrised compatible strain field and minimises the energy of deformation to determine the parameters of this field. Specifically, the strain field used in Y. Hwang et al. (1996a) is a nozzle flow with quadratic profile and rigid body motion outside of the roll gap. The slip-line method solves for the slip-lines, lines parallel to the directions of principal stress, from compatibility conditions and assumptions of the form of the slip-line field. The earlier slip-line model (Dewhurst et al., 1974) applies assumptions valid for symmetric rolling to derive a closed form solutions. These are elegant but limited in validity to weak asymmetries. The latter (Collins et al., 1975) achieves more generality by exploiting a sophisticated matrix formulation of slip-line problems (Dewhurst et al., 1973). This requires optimising twelve variables, which are reported to cause convergence challenges. Both slip-line models assume sticking friction.

Both these methods predict roll force and torque; curvature; the roll contact points; and the yield region, but require a priori knowledge or assumptions about the form of the solution. This hinders the development of these models for other geometries, materials and friction behaviours, meaning they have seen less attention in recent years. The accuracy of curvature prediction for all of these models is specifically examined in Chapter 4.

Results from the experimental and numerical publications have been used for validation in some of these publications. Quantifying the accuracy of a given model and the parameter regions of validity is essential to ensure a model can be used reliably. Simulations can be exploited more to provide this thorough validation.

Asymptotic analysis has only been applied to asymmetric rolling by R. E. Johnson (1994a) where asymmetries were considered for the friction coefficients and roll speeds. The friction coefficient was assumed to be an order of magnitude larger than the roll gap aspect ratio, which is not representative of many thin-sheet processes that are predominantly cold rolling. Roll size may also be necessary to capture the complete dynamics of the process, indicated by experiments (W. Johnson et al., 1966a,b) and simulations (Knight et al., 2003, 2005). These studies have also shown dependence of curvature direction on geometry.

2.2 Model formulation

Plane-strain is assumed because it is valid away from the workpiece edges for sufficiently wide workpieces. This means Figure 2.1 captures the extent of the model. The rolls are vertically aligned and the workpiece is fed horizontally. The initial workpiece half thickness is \hat{h}_0 and the length of the roll gap is \hat{l} , giving the roll gap aspect ratio as $\delta = \hat{h}_0/\hat{l}$. The material model is taken to be rigid perfectly-plastic; that is, no elasticity and no hardening. It was also assumed that plastic deformation occurs everywhere within the roll gap and the yield region has vertical boundaries between the contact points at the entry and exit, marked as the hashed region in Figure 2.1. These assumptions are typical of existing slab and asymptotic models of rolling. Strictly, assuming horizontally aligned contact points, or vertical boundaries to the plastic region, imposes specific combinations of bending and shear end conditions for a given asymmetry. It has been shown experimentally, though, that the bending effects from non-extreme end conditions can be neglected (Salimi et al., 2002).

Using carets to denote dimensional quantities, \hat{p} , \hat{s}_{ij} , \hat{u} , \hat{v} , $\hat{\lambda}$ and \hat{k} are defined as the pressure, ij^{th} deviatoric stress, horizontal velocity, vertical velocity, flow rate parameter and yield stress respectively. Also, $\hat{h}_{t/b}(\hat{x})$ is the roll surface, applicable to both top and bottom rolls and $\hat{F}_{\text{in/out}}$ are the end tensions, per unit width, applied to the workpiece, applicable to the upstream and downstream workpiece.

The upstream velocity of the workpiece is denoted as \hat{u}_0 , although it is not possible to specify this value independently of the roll velocities. Consequently, \hat{u}_0 is taken as an undefined characteristic velocity for the purpose of non-dimensionalisation and its value is determined later from the roll velocities.

2.2.1 Non-dimensionalisation

Vertical distances are scaled with the initial workpiece half-thickness, \hat{h}_0 , and horizontal distances with the length of the roll gap, \hat{l} . The aspect ratio, $\delta = \hat{h}_0/\hat{l}$, is assumed to be small. The friction is also assumed to be small, $\mu_{t/b} = O(\delta)$, so a normalised friction coefficient is defined as $\beta = \mu_b/\delta = O(1)$. This leaves δ as the sole small parameter.

Using the scaling choice of Cherukuri et al. (1997), the shear stress scales with the friction coefficient and yield stress, $\hat{s}_{xy} = \delta\beta\hat{k}s_{xy}$. The scaling used in Domanti et al. (1995), $\hat{s}_{xy} = \beta\hat{k}s_{xy}$, was also considered; however, this requires either small reductions or end compression to make the stress balance consistent.

The scaling for longitudinal deviatoric stress is chosen to balance the yield condition and the scaling for pressure is chosen to balance the horizontal force balance: $\hat{s}_{xx} = \hat{k}s_{xx}$ and $\hat{p} = (\hat{s}_{xy0}/\delta)p$, where \hat{s}_{xy0} is the characteristic shear stress defined above as $\delta\beta\hat{k}$. Velocities are scaled by the upstream workpiece velocity and to balance incompressibility: $\hat{u} = \hat{u}_0u$ and $\hat{v} = \delta\hat{u}_0v$. Finally, the scaling for the flow rate is chosen to balance the horizontal flow equation: $\hat{\lambda} = \lambda\frac{\hat{u}_0}{\hat{k}\hat{l}}$.

Armed with these definitions,

$$\begin{aligned} \hat{x} &= \hat{l}x & \hat{h} &= \hat{h}_0h & \hat{y} &= \hat{h}_0y \\ \hat{s}_{xx} &= \hat{k}s_{xx} & \hat{s}_{xy} &= \delta\beta\hat{k}s_{xy} & \hat{p} &= \beta\hat{k}p \\ \hat{u} &= \hat{u}_0u & \hat{v} &= \delta\hat{u}_0v & \hat{\lambda} &= \lambda\frac{\hat{u}_0}{\hat{k}\hat{l}}, \end{aligned} \quad (2.1)$$

we are now able to determine the non-dimensional governing equations,

$$-\beta \frac{\partial p}{\partial x} + \frac{\partial s_{xx}}{\partial x} + \beta \frac{\partial s_{xy}}{\partial y} = 0 \quad (2.2)$$

$$-\beta \frac{\partial p}{\partial y} - \frac{\partial s_{xx}}{\partial y} + \delta^2 \beta \frac{\partial s_{xy}}{\partial x} = 0 \quad (2.3)$$

$$\frac{\partial u}{\partial x} = \lambda s_{xx} \quad (2.4)$$

$$\frac{\partial u}{\partial y} + \delta^2 \frac{\partial v}{\partial x} = 2\delta^2 \beta \lambda s_{xy} \quad (2.5)$$

$$\frac{\partial u}{\partial x} + \frac{\partial v}{\partial y} = 0 \quad (2.6)$$

$$\text{and } s_{xx}^2 + \delta^2 \beta^2 s_{xy}^2 = 1, \quad (2.7)$$

where incompressibility is used in favour of the vertical flow rate and, from plane-strain, $-s_{xx}$ in favour of s_{yy} .

Similarly, the velocity boundary conditions are

$$v(x, h_t) = u(x, h_t) \frac{dh_t}{dx}, \quad (2.8a)$$

$$v(x, h_b) = u(x, h_b) \frac{dh_b}{dx}. \quad (2.8b)$$

Plug flow, which is verified by the leading order velocity solution in the next section, confirms the existence of a single neutral point on each roll as described in Chapter 1. Given this phenomenon, the directional Coulomb friction coefficients are more simply described as constant on either side of each neutral point: $0 < x < x_{nt/nb}$ and $x_{nt/nb} < x < 1$ where x_{nt} and x_{nb} are the top and bottom neutral points. Hence, in addition to non-dimensionalising with the bottom roll friction coefficient, the friction coefficients are defined piecewise to eliminate surface slip from the problem formulation,

$$\gamma_t = \begin{cases} \frac{\mu_t}{\mu_b} & : x < x_{nt} \\ -\frac{\mu_t}{\mu_b} & : x > x_{nt} \end{cases} \quad \text{and} \quad \gamma_b = \begin{cases} -1 & : x < x_{nb} \\ 1 & : x > x_{nb} \end{cases}. \quad (2.9)$$

This allows the shear boundary conditions to be expressed as

$$\begin{aligned}
s_{xy}(x, h_t) &= \gamma_t (\beta p(x, h_t) + s_{xx}(x, h_t)) + \frac{2}{\beta} s_{xx}(x, h_t) \frac{dh_t}{dx} \\
&+ \delta^2 \left[\gamma_t (\beta p(x, h_t) + s_{xx}(x, h_t)) \left(\frac{dh_t}{dx} \right)^2 \right. \\
&\quad \left. + s_{xy}(x, h_t) \left(\left(\frac{dh_t}{dx} \right)^2 - 2\beta \gamma_t \frac{dh_t}{dx} \right) \right]
\end{aligned} \tag{2.10a}$$

$$\begin{aligned}
s_{xy}(x, h_b) &= \gamma_b (\beta p(x, h_b) + s_{xx}(x, h_b)) + \frac{2}{\beta} s_{xx}(x, h_b) \frac{dh_b}{dx} \\
&+ \delta^2 \left[\gamma_b (\beta p(x, h_b) + s_{xx}(x, h_b)) \left(\frac{dh_b}{dx} \right)^2 \right. \\
&\quad \left. + s_{xy}(x, h_b) \left(\left(\frac{dh_b}{dx} \right)^2 - 2\beta \gamma_b \frac{dh_b}{dx} \right) \right]
\end{aligned} \tag{2.10b}$$

The end force and velocity conditions are also non-dimensionalised as

$$F_{\text{in/out}} = \int_{h_b}^{h_t} -\beta p + s_{xx} dy, \tag{2.11}$$

where $\hat{F}_{\text{in/out}} = F_{\text{in/out}} (\hat{h}_t - \hat{h}_b) \hat{k}$, and

$$2 = \int_{h_b(0)}^{h_t(0)} u(0, y) dy. \tag{2.12}$$

Note that, due to the choice of scaling, the small parameter, δ , occurs as δ^2 only. This suggests that the subsequent asymptotic solution will be a good approximation whilst δ^2 is small, rather than when δ is small as previously thought. This is borne out later when the first order correction is found to have no contribution and second order terms must be used to make a correction to the leading order.

Finally, it is useful to define the workpiece height through the roll gap as $\Delta h(x) = h_t(x) - h_b(x)$ and the total roll friction acting to the left as $\Delta \gamma = \gamma_t(x) - \gamma_b(x)$.

2.3 Solution

To conduct an asymptotic analysis, an expansion is sought for each of the variables, u , v , s_{ij} , p and λ of the form

$$A(x, y) = A^{(0)}(x, y) + \delta A^{(1)}(x, y) + \delta^2 A^{(2)}(x, y) + O(\delta^3). \quad (2.13)$$

Assuming δ is sufficiently small, powers of δ are considered orthogonal so like terms are collected and solved successively, starting from low orders of δ .

2.3.1 Leading-order solution

Neglecting terms of order δ and smaller, the governing equations are reduced to

$$-\beta \frac{\partial p^{(0)}}{\partial x} + \frac{\partial s_{xx}^{(0)}}{\partial x} + \beta \frac{\partial s_{xy}^{(0)}}{\partial y} = 0, \quad (2.14)$$

$$-\beta \frac{\partial p^{(0)}}{\partial y} - \frac{\partial s_{xx}^{(0)}}{\partial y} = 0, \quad (2.15)$$

$$\frac{\partial u^{(0)}}{\partial x} = \lambda^{(0)} s_{xx}^{(0)}, \quad (2.16)$$

$$\frac{\partial u^{(0)}}{\partial y} = 0, \quad (2.17)$$

$$\frac{\partial u^{(0)}}{\partial x} + \frac{\partial v^{(0)}}{\partial y} = 0, \quad (2.18)$$

$$\text{and } s_{xx}^{(0)2} = 1, \quad (2.19)$$

with boundary conditions

$$s_{xy}^{(0)}(x, h_t(x)) = \gamma_t \left(\beta p^{(0)}(x, h_t) + s_{xx}^{(0)} \right) + \frac{2}{\beta} s_{xx}^{(0)}(x, h_t) \frac{dh_t}{dx}, \quad (2.20a)$$

$$s_{xy}^{(0)}(x, h_b(x)) = \gamma_b \left(\beta p^{(0)}(x, h_b) + s_{xx}^{(0)} \right) + \frac{2}{\beta} s_{xx}^{(0)}(x, h_b) \frac{dh_b}{dx}, \quad (2.20b)$$

$$v^{(0)}(x, h_t(x)) = \frac{dh_t(x)}{dx} u^{(0)}(x, h_t(x)), \quad (2.21a)$$

$$v^{(0)}(x, h_b(x)) = \frac{dh_b(x)}{dx} u^{(0)}(x, h_b(x)), \quad (2.21b)$$

$$\int_{h_b(0)}^{h_t(0)} -\beta p^{(0)}(0, y) + s_{xx}^{(0)}(0, y) dy = F_{\text{in}}, \quad (2.22a)$$

$$\int_{h_b(1)}^{h_t(1)} -\beta p^{(0)}(1, y) + s_{xx}^{(0)}(1, y) dy = F_{\text{out}}, \quad (2.22b)$$

$$\text{and } \int_{h_b(x)}^{h_t(x)} u^{(0)}(x, y) dy = 2. \quad (2.23)$$

Equation (2.17) indicates that the leading order horizontal velocity is vertically homogeneous so enforcing conservation of mass to each vertical element of the workpiece gives

$$u^{(0)} = \frac{2}{\Delta h(x)}. \quad (2.24)$$

Equation (2.19) can be solved to give $s_{xx}^{(0)} = -s_{yy}^{(0)} = \pm 1$. $s_{yy}^{(0)} = -1$ is chosen to ensure the rolls remain in compression when $p^{(0)} < 1/\beta$, hence,

$$s_{xx}^{(0)} = -s_{yy}^{(0)} = 1. \quad (2.25)$$

Substituting these results into equation (2.16) gives

$$\lambda^{(0)} = \frac{1}{s_{xx}^{(0)}} \frac{du^{(0)}}{dx} = -\frac{2}{\Delta h^2} \frac{d\Delta h}{dx}. \quad (2.26)$$

Then integrating equation (2.18) and using the velocity boundary conditions, equation (2.21), gives

$$v^{(0)} = - \int_{h_b(x)}^{h_t(x)} \frac{du^{(0)}}{dx} dy = \frac{2}{\Delta h^2} \left(h_t \frac{dh_b}{dx} - h_b \frac{dh_t}{dx} + y \frac{d\Delta h}{dx} \right). \quad (2.27)$$

Equation (2.15) shows that the pressure is homogeneous through-thickness so applying the stress results to equation (2.14) and integrating in y gives

$$s_{xy}^{(0)} = \frac{dp^{(0)}}{dx} y + K(x). \quad (2.28a)$$

Assuming known shear conditions on $y = h_t$ and $y = h_b$ gives the general forms

$$\frac{dp^{(0)}}{dx} = \frac{s_{xy}^{(0)}(x, h_t(x)) - s_{xy}^{(0)}(x, h_b(x))}{h_t(x) - h_b(x)} \quad (2.28b)$$

$$\text{and } K(x) = \frac{h_t(x)s_{xy}^{(0)}(x, h_b(x)) - h_b(x)s_{xy}^{(0)}(x, h_t(x))}{h_t(x) - h_b(x)}. \quad (2.28c)$$

The stress boundary conditions, equation (2.20), applied to equation (2.28b) produces an ordinary differential equation (ODE) for pressure,

$$\frac{dp^{(0)}}{dx} = \frac{1}{\Delta h(x)} \left(\Delta \gamma(x) (\beta p^{(0)} + 1) + \frac{2}{\beta} \frac{d\Delta h(x)}{dx} \right). \quad (2.29)$$

The pressure at the entrance and exit are determined from the workpiece force end conditions, equation (2.22), as

$$p^{(0)}(0) = \frac{1}{\beta} \left(s_{xx}^{(0)}(0) - \frac{F_{\text{in}}}{\Delta h(0)} \right) \quad \text{and} \quad p^{(0)}(1) = \frac{1}{\beta} \left(s_{xx}^{(0)}(1) - \frac{F_{\text{out}}}{\Delta h(1)} \right). \quad (2.30)$$

This defines both boundary conditions for the ODE, equation (2.29); however, the discontinuous nature of $\Delta \gamma$ means that equation (2.29) must be solved in three sections, as shown in Figure 2.2: the entrance region ($0 < x < \min(x_{nb}, x_{nt})$); between the neutral points ($\min(x_{nb}, x_{nt}) < x < \max(x_{nb}, x_{nt})$); and the exit region ($\max(x_{nb}, x_{nt}) < x < 1$).

The locations of the neutral points, x_{nt} and x_{nb} , are determined to ensure pressure continuity and the correct roll surface speed ratio. x_{nt} and x_{nb} are the locations where, by definition, the surface velocity equals the roll velocity, hence the speed ratio of these points must equal the roll surface speed ratio as illustrated in panel (b) of Figure 2.2.

The characteristic velocity, \hat{u}_0 is then chosen to satisfy the magnitude of the roll surface speeds. This is analogous to choosing the constant of integration marked in panel (c) of Figure 2.2.

Finding the neutral points is implemented with a bounded numerical solver. One of the two neutral points is solved for the correct relative speed ratio at the neutral points while the second neutral point is solved in this calculation as the intercept of the pressure integrals to ensure continuity. This was implemented using *MATLAB*'s 'ODE Events' functionality (MathWorks, 2015).

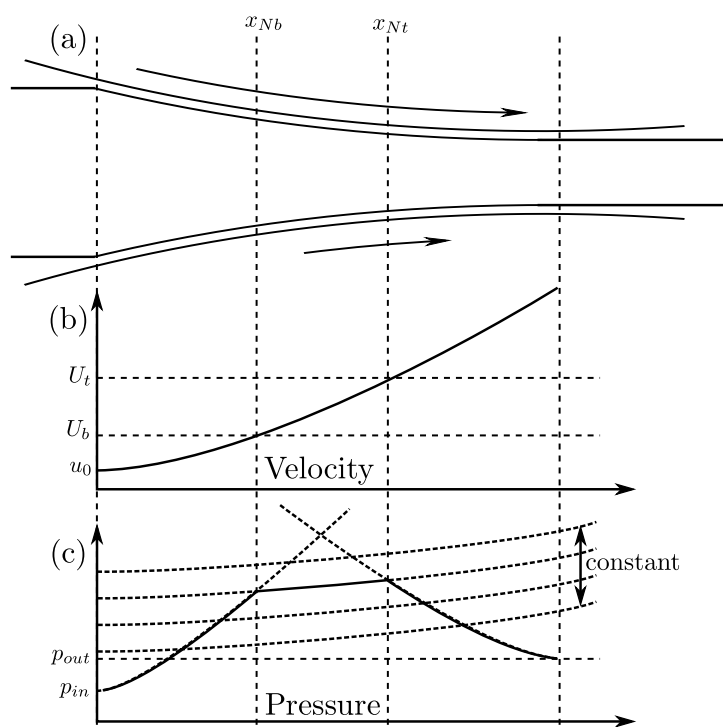


Fig. 2.2 A schematic of the rolling process marking the differences in roll velocity and neutral points (a); a plot of the characteristic surface velocity curve (b); and a plot of the characteristic pressure with alternative velocity-scale curves as dashed lines (c).

Once equations (2.28b) and (2.28c) have been solved for $p^{(0)}$ and $K(x)$, substitution reveals the shear stress to be

$$s_{xy}^{(0)}(x, y) = \frac{\beta p^{(0)}(x) + 1}{\Delta h(x)} (\Delta \gamma(x)y + (h_t(x)\gamma_b(x) - h_b(x)\gamma_t(x))) + \frac{2}{\beta \Delta h(x)} \left(\frac{d\Delta h(x)}{dx} y + \left(h_t \frac{dh_b}{dx} - h_b \frac{dh_t}{dx} \right) \right), \quad (2.31)$$

which completes the leading order solution.

2.3.2 Comparison with an existing slab model

Extracting the surface pressure and surface shear from this leading order solution is equivalent to employing a slab model; this particular solution is equivalent to equation (10) in Y. Hwang et al. (1993) if small reductions are assumed. Y. Hwang et al. (1993) approximates the horizontal coordinate with an expansion of the tangent function, $x = \tan(\omega) \simeq \omega + \omega^3/3$ where ω is the angular coordinate from the origin at a roll centre, to solve much of this in closed form. This also means the neutral point search is reduced to numerically inverting an algebraic equation; however, this approximation is only valid in the limit of small reductions.

While this agreement validates the assumptions made in Y. Hwang et al. (1993), the rigour of the present method offers further benefits. The explicit style of the assumptions in an asymptotic analysis makes the validity of the method easier to establish. For example, neglecting the shear stress contributions in the yield criterion at leading order is a consequence of assuming small friction coefficients so we can, in principle at least, determine the range of friction coefficients for which accuracy is ensured. Another benefit is being able to solve for correction order to improve accuracy and potentially reveal additional phenomena.

2.3.3 Correction terms

After solving the leading order solution, subsequent higher order terms of δ can be solved iteratively. The same solution process is required at each order with additional forcing terms from lower orders. The absence of order δ terms in the governing equations or boundary conditions mean that this order is solved to be identically zero. This shows why the existing slab models have been generally successful at predicting roll

force and torque; given their ad hoc assumptions are correct, they achieve accuracy to $O(\delta^2)$.

Further accuracy can still be achieved by repeating this process with terms of $O(\delta^2)$. The correction terms increase the through-thickness resolution of the solution. In practice each variable raises an order as a polynomial in y with each correction. As a result, horizontal velocity, pressure, longitudinal deviatoric stresses and the flow parameter become quadratic in y and vertical velocity and shear stress become cubic. Velocity also becomes dependent on the stress distribution so material properties and friction behaviours affect the strain field.

For brevity the derivation of this correction has been relegated to Appendix A.

2.4 Numerical simulations

The present model was compared to numerical simulations. The commercial finite element package *ABAQUS* was used with a model modified from an explicit two-dimensional rolling model with *CPE4R* elements presented in Section 1.3.11 of the ‘*ABAQUS* Example Problems Manual’ (Dassault Systemes, 2012b). Symmetry was broken by adding a second roll and the initialisation was modified so the rolls closed onto the stationary workpiece instead of feeding the workpiece into the roll gap with a non-zero initial velocity. Further discussion of the simulation configuration, including a mesh convergence study, is provided in Appendix D.

The first simulation set used a material close to rigid perfect-plastic so the asymptotic modelling assumptions are matched as closely as possible. This was to compare the accuracy of the asymptotic assumptions. The yield stress in shear was set to 173.2MPa with no hardening effects. *ABAQUS* cannot support rigid behaviour so the elastic modulus and Poisson’s ratio were set as high as feasible: 200GPa and 0.45 respectively.

The symmetric base case was a 10mm strip thinned by 12% with 2.5m radius rolls; this roll size is realistic when approximating curvature of rolls flattened slightly from pressure. The friction coefficients were taken to be 0.1 and roll surface speeds to be 1.2ms^{-1} . This gave non-dimensional values δ , r and μ , of 0.091, 0.12 and 0.1 respectively.

From this configuration, the properties of the top roll were varied to achieve the desired ratios of top to bottom friction coefficient, surface speed and roll size. It is worth noting that δ varied with the roll size as the workpiece thickness was held constant.

Table 2.1 Initial parameter sets for varying parameter comparison

Name	(μ_b, δ, r)	μ_t/μ_b	\hat{R}_t/\hat{R}_b	\hat{U}_t/\hat{U}_b
Symmetric	(0.1, 0.1, 0.25)	1.0	1.0	1.0
Friction	(0.1, 0.1, 0.25)	0.9	1.0	1.0
Size	(0.1, 0.1, 0.25)	1.0	0.9	1.0
Speed	(0.1, 0.1, 0.25)	1.0	1.0	0.95
Combo 1	(0.1, 0.1, 0.25)	1.0	0.95	0.95
Combo 2	(0.1, 0.1, 0.25)	0.9	1.1	0.95

A second set of simulations were made to observe the performance over a range of the parameters: specifically, varying the friction magnitude, aspect ratio and reduction. One of these dimensionless parameters was varied while the others were held constant. This means two geometric parameters may vary simultaneously; for example, the roll size was reduced as the reduction was increased to ensure the aspect ratio remained constant. Six different sets of initial parameters, as specified in Table 2.1, were used.

The lower roll surface speed and initial half-thickness were 1.2ms^{-1} and 0.005m respectively. The material parameters used were further from perfect plasticity than the previous example to improve computation time but were observed to have minimal effect on the solutions: Poisson's ratio of 0.35, elastic modulus of 100 GPa, and a yield shear stress of 100MPa.

2.5 Results and discussion

This section presents the comparison between the numerical simulations and asymptotic solution for varying asymmetries, several cross sections of non-dimensional parameters. Comparisons of stress and strain fields, computational time and a hardening material approximation are also given.

2.5.1 Numerical comparison over varying asymmetries

Results from the leading and second order asymptotic solution for the first set of simulations described in Section 2.4 are plotted in Figure 2.3 with the numerical simulation results.

The trends of the roll force and torque as each ratio is varied are captured well by the asymptotic solution. The median error was 0.85MN and 0.007MNm for the force and torque respectively with maximum errors of 2.25MN and 0.28MNm occurring for

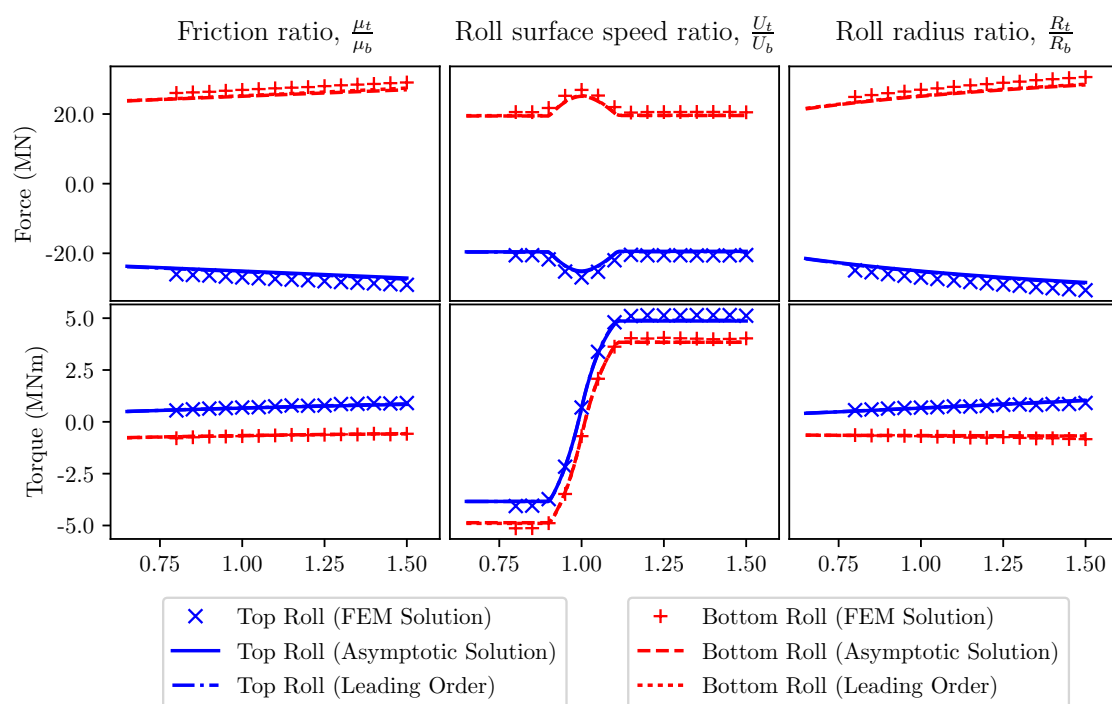


Fig. 2.3 Roll force (top) and torque (bottom) as the top roll is varied to achieve the ratio of roll characteristics: friction (left), speed (middle) and size (right). The other parameters used are $(\hat{h}_0, \hat{R}_b, r, \mu, \hat{k}) = (0.01\text{m}, 2.5\text{m}, 0.12, 0.1, 173\text{MPa})$.

asymmetric speeds where the magnitudes vary the most. Considering characteristic force and torque values of 25MN and 1.0MNm, these median values correspond to less than 3.5% error. There is minimal difference between the leading order and corrected asymptotic solutions, which is expected given it is accurate to $O(\delta^2)$. The discrepancies with the numerical results can most likely be attributed to elastic effects, which are neglected in the asymptotic model but incorporated in the simulations. This will allow the position of the contact points to vary, due to compressibility, which varies the length of the contact surface on these rolls. Given the high normal pressures this will have small but consistent contributions to the roll force and torque calculations.

The most phenomenologically interesting trend in both cases is the drop in force and transition in direction of torque as the roll speed ratio varies. Figure 2.4 makes it clear that this trend stems from the movement of the neutral points from one side of the roll gap to the other.

A region of sticking often occurs between the roll and workpiece denoted by the error bars in Figure 2.4. In this region the shear stress smoothly changes direction and the workpiece drops below yield which may be a consequence of elasticity or a static friction model. This is discussed more in Appendix D.5.

Figure 2.4 shows that the force and torque plateaus where the neutral point reaches the end of the roll gap. The asymptotic solution predicted the location of the neutral point in all cases with similar accuracy to that observed in Figure 2.4, although the neutral point varies little while friction or roll size ratios are varied.

In the case of large roll speed asymmetry, when a neutral point has reached an end of the roll gap, the assumption of Coulomb friction renders any further speed asymmetry inconsequential. The speed of the process, expressed by the velocity scaling, is then determined only by the non-slipping roll, which does not give a unique solution. Elastic effects in the finite element simulations mean both roll speeds contribute until both neutral points have reached opposite ends of the roll gap. This explains the discrepancy between the numerical and asymptotic solutions of the left hand neutral point for asymmetric speeds below 0.9 and above 1.15, shown in Figure 2.4

2.5.2 Numerical comparison over varying non-dimensional parameters

The roll force, roll torque and neutral points from the ‘Combo 2’ simulations are presented in Figure 2.5. The remaining five parameter sets defined in Table 2.1 exhibit

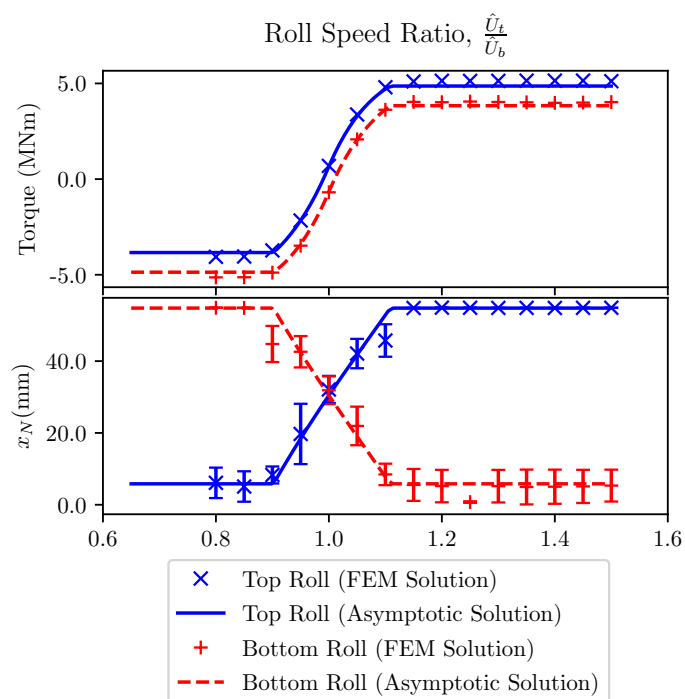


Fig. 2.4 Roll torque (top) and neutral point (bottom) as the top roll speed is varied for the ‘perfectly plastic’ material. Error bars indicate the finite length of sticking between the rolls and workpiece. The other parameters used are $(\hat{h}_0, \hat{R}_b, \hat{U}_b, r, \mu, \hat{k}) = (0.01\text{m}, 2.5\text{m}, 1.2\text{ms}^{-1}, 0.12, 0.1, 173\text{MPa})$. Error bars indicate the finite length of sticking between the rolls and workpiece.

similar trends so are illustrated by way of absolute error of roll force and torque in Figure 2.6.

The finite element simulations failed to reach a steady state when δ exceeded 0.3 as the rolls slipped without deforming the workpiece. This is reflected by the asymptotic model as both boundary conditions cannot be satisfied with pressure continuity indicating a physical limit of the process.

For larger friction coefficients, typically $\mu_b \geq 0.3$, the asymptotic solution broke down: terms began to ‘jump order’. That is, correction terms became as large as leading order terms, which is a clear sign that the premise of separating orders in the asymptotic analysis is invalid. This is unsurprising considering the small friction assumption is violated in these cases.

Given these caveats, the asymptotic solution behaves as one would intuitively expect and captures most of the trends exhibited by the simulations within the presented parameter ranges, aside from one major exception: the clear deviation of roll torque for increasing friction coefficient. Figure 2.6 shows that this error only occurs in parameter sets with asymmetric roll speeds. The widening sticking regions around the neutral points in the simulations, observed in Section 2.5.1, may be driving this error. Sticking would smooth the surface shear sign change and, hence, minimise the severe effects the cross-shear region has on the roll torque observed with the asymptotic model. The increasing error with friction coefficient appears linear and is unsurprising considering the friction coefficient is assumed to be small.

Variation due to changes in aspect ratio or reduction are well-captured by our model above $\delta = 0.05$ and $r \approx 0.15$. The poor agreement for small reduction may result from the workpiece falling below yield, as indicated by the widening sticking zone. The lower reduction rate would be insufficient for plasticity to penetrate the workpiece thickness resulting in significant elastic contributions.

For small δ , force and torque are generally larger in magnitude so the larger absolute error is not too concerning. This is confirmed with Figure 2.7, which presents relative error and shows the convergence of an asymptotic solution. This convergence plateaus at very small δ as the simulations began to lose accuracy and the large relative errors are a consequence of the very small magnitudes at larger δ . The convergence may also perform better if μ is reduced with δ as the assumption is made that these are of comparable size. The noisy results of the top roll torque will be a consequence of how the neutral point is chosen, discussed above.

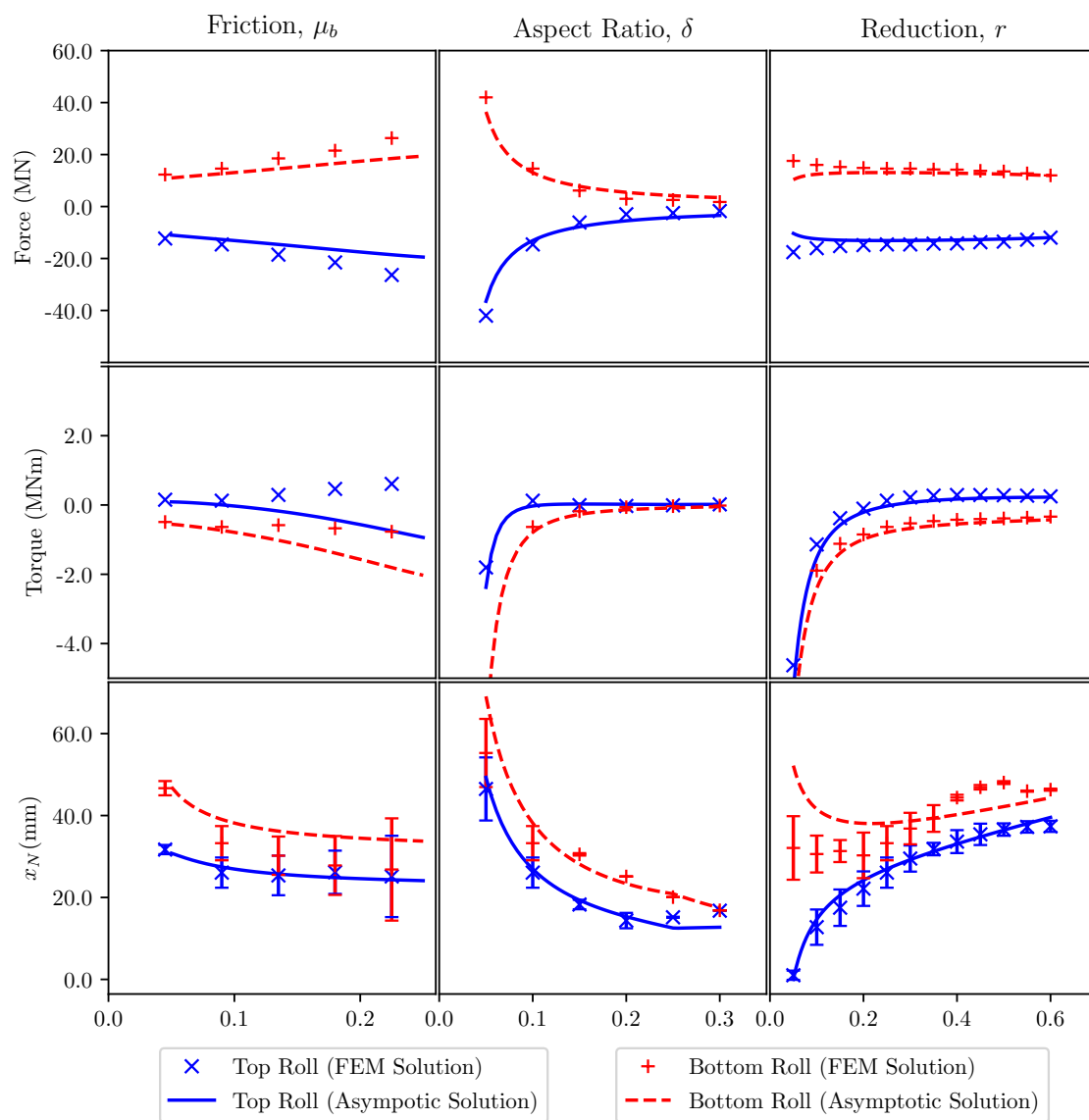


Fig. 2.5 Roll force (top), roll torque (middle) and neutral point (bottom) as the bottom friction magnitude (left), aspect ratio (middle) and reduction (right) were varied for the ‘Combo 2’ parameter set in Table 2.1. Error bars indicate the finite length of sticking between the rolls and workpiece.

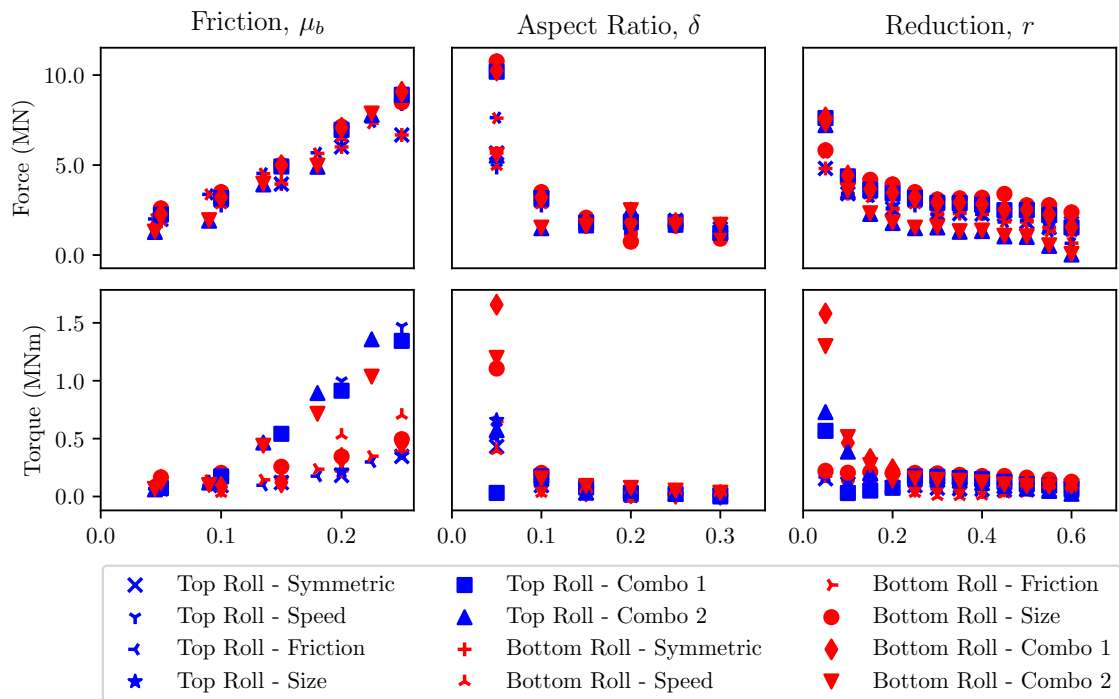


Fig. 2.6 Absolute error in roll force (top) and torque (bottom) between the asymptotic solution and simulation results as the bottom friction magnitude (left), roll gap aspect ratio (middle) and reduction (right) were varied for each of the parameter sets in Table 2.1.

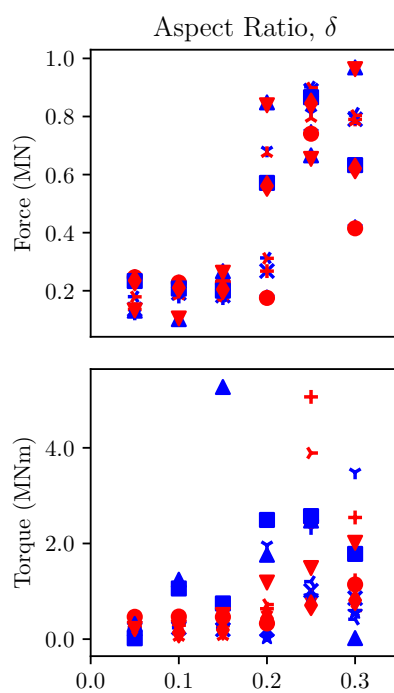


Fig. 2.7 Relative error in roll force (top) and torque (bottom) between the asymptotic solution and simulation results as the bottom roll gap aspect ratio is varied for each of the parameter sets in Table 2.1.

2.5.3 Numerical comparison of stress and strain fields

Referring to Figure 2.3, it is clear that the correction terms make little difference to the force and torque predictions. Nevertheless, the qualitative accuracy is increased by including higher order terms. This is evident when plotting the stress distributions and velocity fields between leading and correction order solutions, as shown in Figure 2.8 and Figure 2.9 respectively. The ‘Combo 2’ asymmetries and parameters from Table 2.1 have been used.

As discussed in Section 2.3.3, each variable gains additional through-thickness resolution from the corrected asymptotic solution. Although all solutions now exhibit top-bottom asymmetry, this is most pronounced for the horizontal velocity, pressure and longitudinal deviatoric stresses, which are homogeneous in y at leading order. Both velocities gain dependence on the leading order shear stress fields via equation (3.5), which results in discontinuities at the neutral points. These discontinuities are a necessary consequence of Coulomb friction without elasticity or smoothing at low relative-slip speeds. It is interesting to note that the leading order velocity solution is independent of the stress state, including the friction model used. This casts doubt on the analogous slab solutions being used for curvature predictions, discussed further in Chapter 4.

The trends of the numerical pressure, horizontal stress and horizontal velocity fields are generally captured by the asymptotic solution. The shear stress and vertical velocity fields exhibit oscillations, or a series of lobes, through the length of the roll gap. This behaviour has not been described within the literature and so further investigation was conducted, which is presented in Chapter 5.

These stress and strain fields can be used to determine the pressure and traction between the workpiece and the roll. These results are presented in Figure 2.10 and show good agreement for both roll pressure and traction. The good match of the roll pressure validates the assumption that elasticity can be neglected within the roll gap; however, the early drop off at the entrance and exit suggest it is relevant in determining accurate roll gap boundaries. These lesser values could also explain the force and torque discrepancy hypothesised earlier. Smoothed friction transition on both roll surfaces and oscillations of the stress lobes are observed but are characteristic of stress field discrepancies discussed previously. The latter is less significant here as the magnitude of the oscillations are smaller at the workpiece edges compared to the centreline.

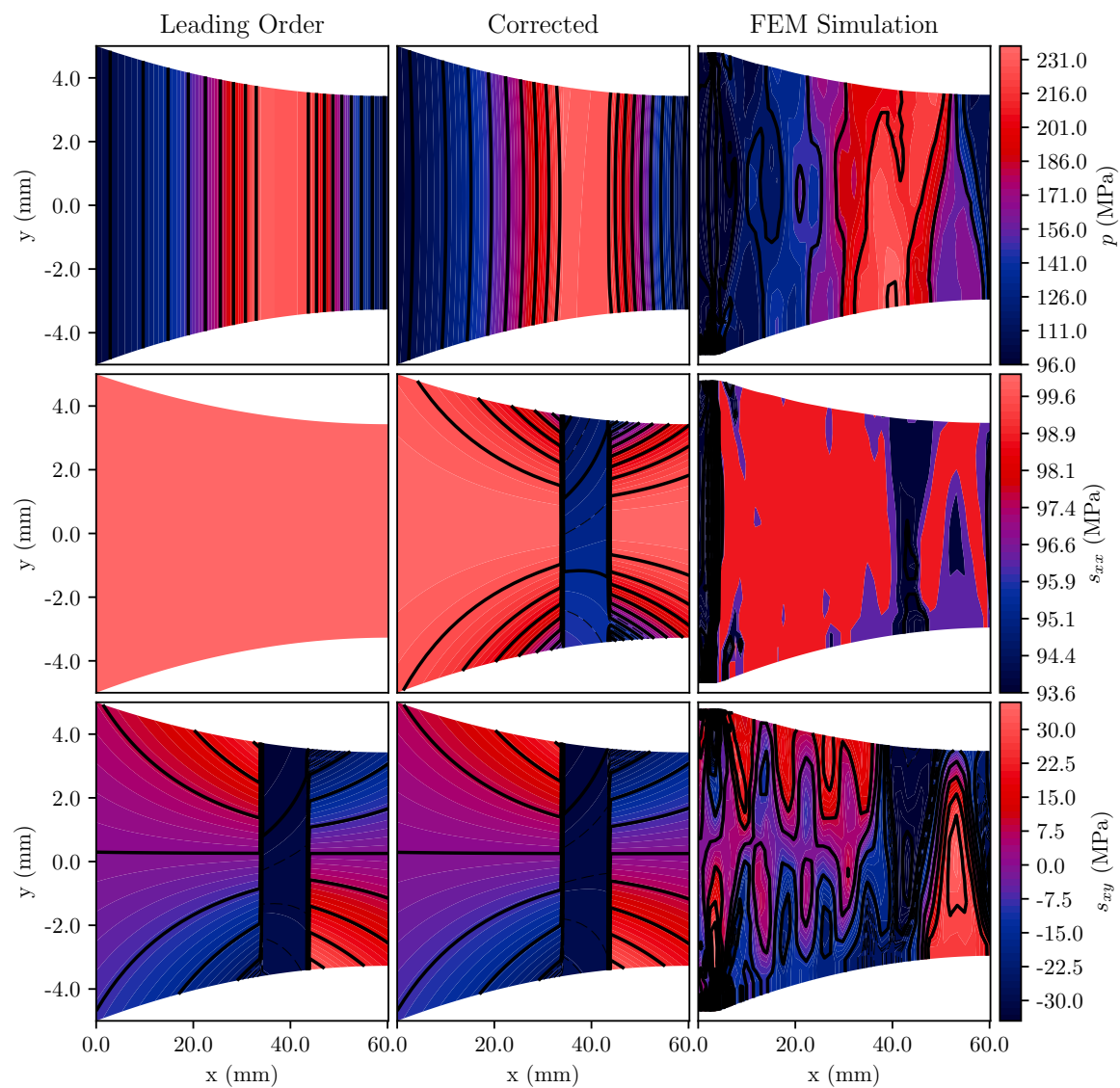


Fig. 2.8 Pressure (top), horizontal deviatoric stress (middle) and shear stress (bottom) fields for the ‘Combo 2’ parameter set, $(\mu_b, \delta, r, \mu_t/\mu_b, \hat{R}_t/\hat{R}_b, \hat{U}_t/\hat{U}_b) = (0.1, 0.1, 0.25, 0.9, 1.1, 0.95)$, from the leading order asymptotic model (left) and corrected asymptotic model (centre) and finite element simulations (right). Dashed contours of finer resolution, 0.8MPa, illustrate the behaviour within the cross-shear region.

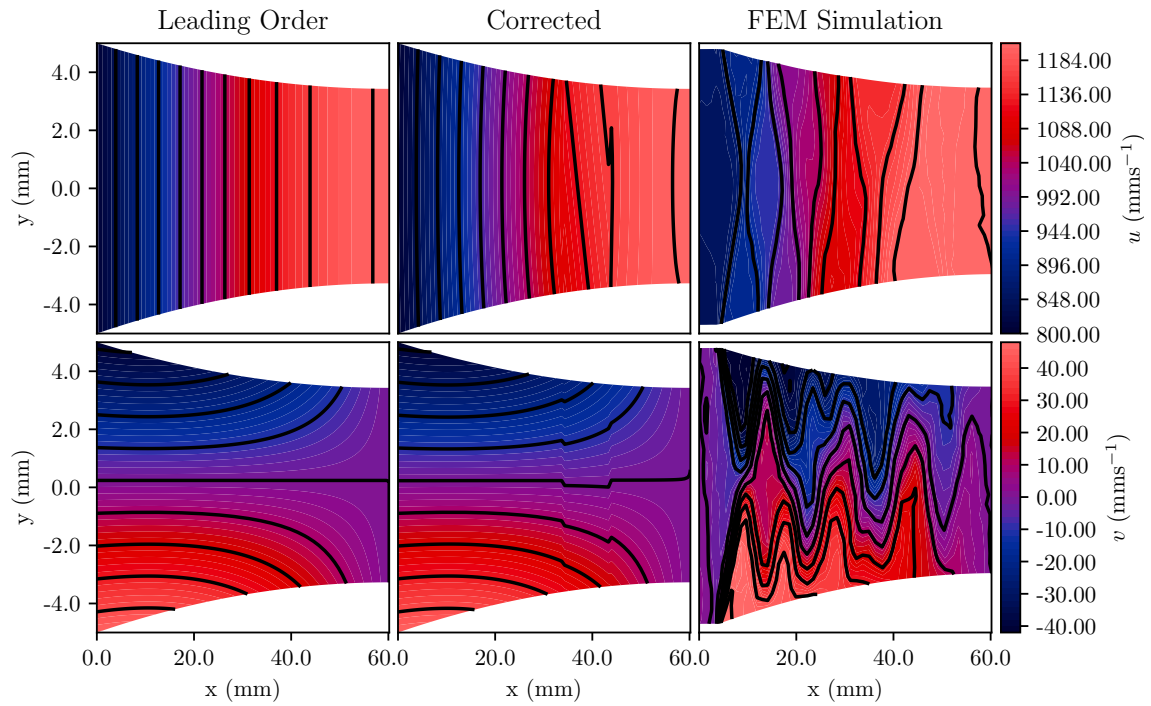


Fig. 2.9 Horizontal (top) and vertical (bottom) velocity fields for the ‘Combo 2’ parameter set from the asymptotic model; leading order (left) and corrected solution (right).

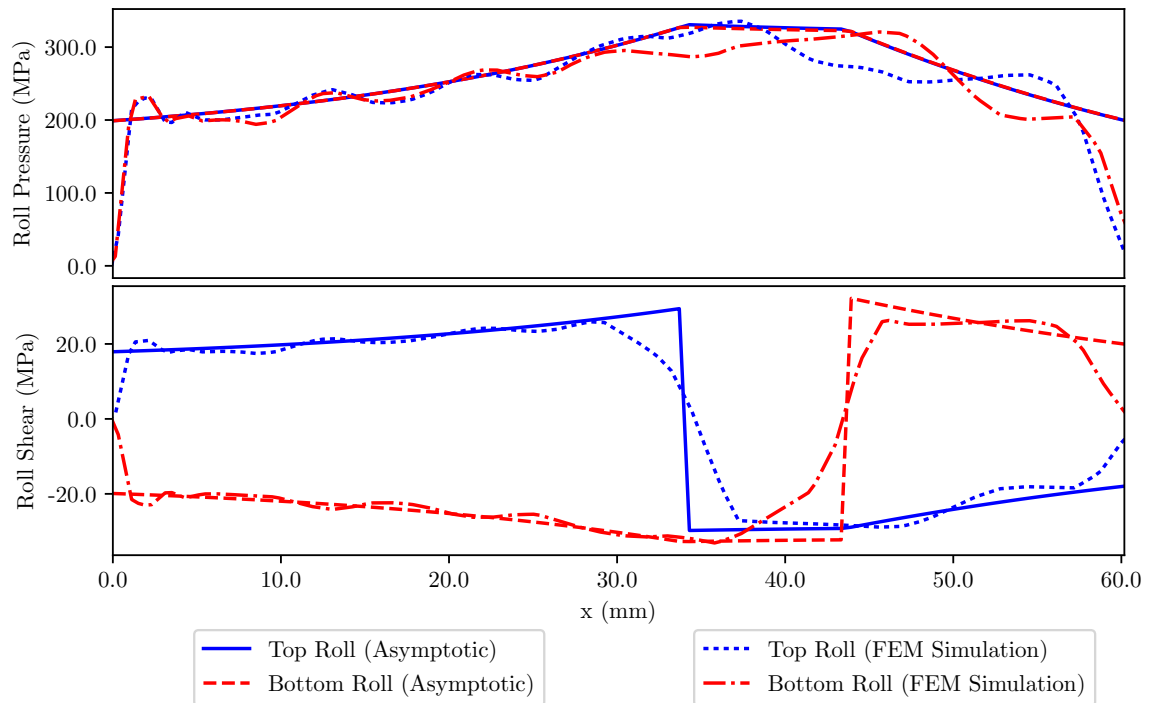


Fig. 2.10 Roll pressure (top) and roll shear (bottom) for the ‘Combo 2’ parameter set from the corrected asymptotic model and finite element simulations.

2.5.4 Computational time comparison

The asymptotic solutions presented here, implemented in *MATLAB* (MathWorks, 2015), were computed in less than one fifteenth of the time the *ABAQUS* (Dassault Systemes, 2012a) finite element solutions were computed. More typical increases in speed were of the order of one thousand fold.

Further, the second order correction comes at a small additional cost to the leading order; finding the neutral point consumes the majority of the computation time. The leading order solution typically required around 20 seconds whereas the second order correction typically required around one second¹. This being the case, significant increases in speed could be achieved by using prior knowledge of the neutral point and to apply parallelisation. Applications that make repeated calculations under similar conditions, such as control, lend themselves to this approach as smaller time increments lead to faster convergence. Real-time computation could be feasible under these conditions and higher accuracy could be achieved with comparatively small improvements in processing power.

2.5.5 Application to hardening material

Proper treatment of a hardening material would require the reformulation of the model with an alternative yield condition and the rework of the asymptotic analysis. In the interest of a quick comparison, an ad hoc approximation is made: the yield stress is selected to correspond to the mean accumulated effective strain produced by the current model. This is compared to simulations of a hardening material based on carbon steel. Specifically, an elastic modulus of 180GPa; Poisson's ratio of 0.27; and shear yield stress specified in Figure 2.11 are used.

The trends of the roll force and torque, shown in Figure 2.12, deteriorate only slightly compared to the perfect plastic shown in Figure 2.3 over asymmetry ratios between 0.8 and 1.5. The median errors become 0.17MN and 0.05MNm with maximum errors of 2.84MN and 0.48MNm. Considering higher characteristic force and torque values of 40MN and 2.0MNm, these median values still indicate errors below 3%. If this accuracy were insufficient more could be achieved with proper treatment of the appropriate material law.

¹Solutions computed on an Intel i5 3.4GHz quad-core with 32GB RAM.

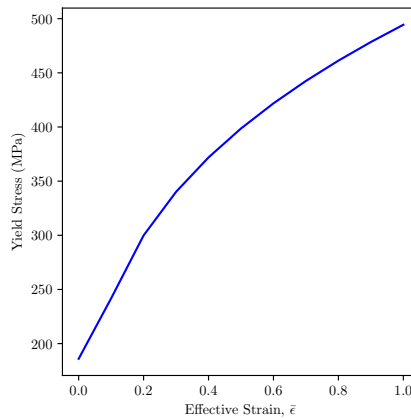


Fig. 2.11 Yield shear stress against effective strain for carbon steel used to compare the present model with *ABAQUS* simulations. An elastic modulus of 180GPa and Poisson's ratio of 0.27 were also used.

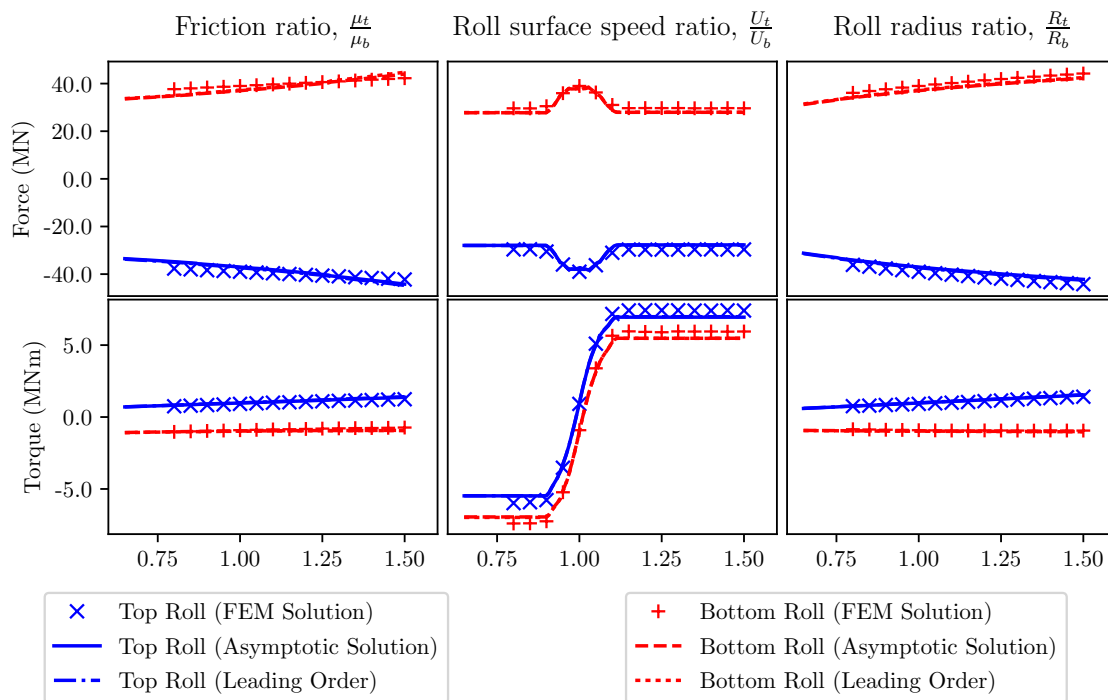


Fig. 2.12 Roll force (top) and torque (bottom) as the top roll is adjusted to vary the ratio of roll characteristics: friction (left), speed (middle) and size (right). The other parameters used are $(\hat{h}_0, \hat{R}_b, r, \mu, \nu, \hat{E}, \hat{k}) = (0.01\text{m}, 2.5\text{m}, 0.12, 0.1, 180\text{GPa}, 0.27, 186\text{MPa to } 494\text{MPa})$.

2.5.6 Alternative friction models

Proper treatment can also be given to other modelling assumptions, particularly friction models. To illustrate this, two alternative friction models have been implemented to leading order. Each uses the same procedure followed in Section 2.3 with surface traction terms, the first term on the right hand side of equation (2.20), replaced with the appropriate friction model.

The leading order stress fields of these solutions are presented in Figure 2.13. The deviatoric stress is unaffected by friction at leading order and so is homogeneous in all three cases. The pressure is homogeneous through the thickness and so the behaviour discussed in Section 1.4.2 remains relevant here, only with the addition of the cross-shear region. The friction factor is characteristically similar to Coulomb friction only less concave and relative-slip friction smooths both shear sign changes rendering the cross-shear region almost indistinct.

The implementation used here can accommodate any friction model that depends on uncoupled properties and abides by the low friction assumption. This covers most common friction models and illustrates how this work can be modified to incorporate further tribology research in rolling.

2.6 Conclusion

A model for asymmetric rolling of rigid-perfect plastic sheets under Coulomb friction has been presented and solved asymptotically to a piece-wise ordinary differential equation. This was achieved via the systematic assumptions that the aspect ratio, δ , and the friction coefficient, μ , are small.

The leading order solution agrees with one of the many slab models (Y. Hwang et al., 1993) for predicting roll force and torque in the limit of small reduction, an assumption not needed by the method presented here. This gives confidence to the ad hoc assumptions made to derive that slab model by formalising the assumptions required to achieve these solutions. Correction terms of $O(\delta^2)$, rather than $O(\delta)$, help to explain why this and other slab models perform so well in practice.

The $O(\delta^2)$ correction still offers new predictions of the through-thickness variation of each stress and strain component. This qualitative refinement has a relatively minor effect on the force and torque predictions; however, it gains significance when modelling

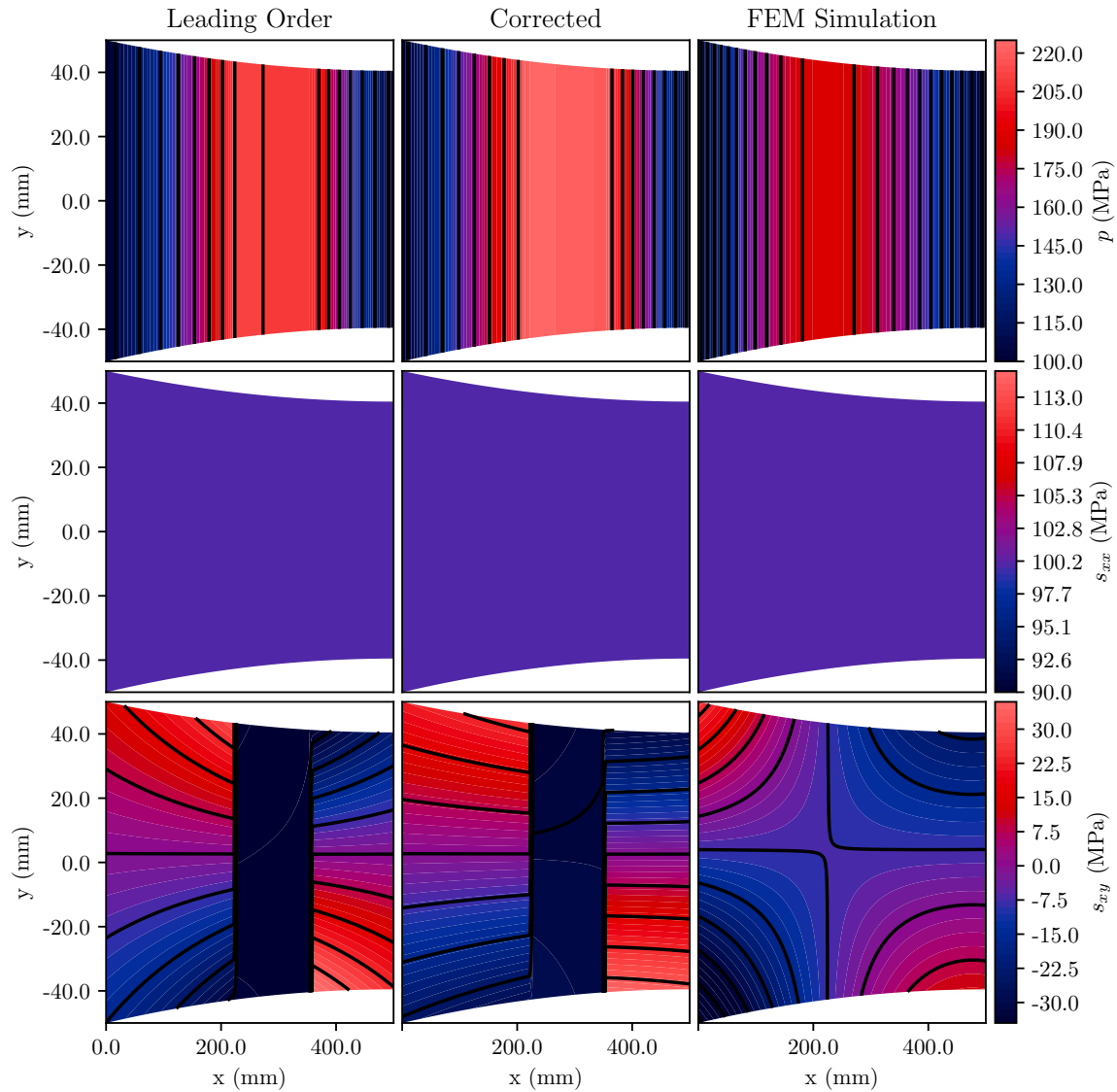


Fig. 2.13 Leading order solutions for pressure (top) and shear stress fields (bottom) for Coulomb friction (left), friction factor (middle) and relative-slip friction (right). The 'Combo 2' asymmetries and geometry with 100MPa yield stress were used. Bottom friction coefficients of 0.11, 0.3 and 1.0 ($\hat{u}^{(0)}(\hat{l}) - \hat{u}^{(0)}(0)$) were used for each model respectively. Leading order pressure is vertically homogeneous, deviatoric stress and both strain fields remain identical to the Coulomb case shown in Figure 2.8 and Figure 2.9.

hardening effects, such as R. E. Johnson et al. (1992), or if consideration must be made of the material micro-structure, such as modelling dynamic recrystallisation.

The asymptotic solution was compared to finite element simulations in the most comprehensive validation of an asymmetric rolling model to date. The asymptotic model captures most trends present in the simulated force, torque and neutral point variation while taking orders of magnitude less time to compute. Specifically, it was confirmed that the model performs well within the region where $0.1 \leq \delta \leq 0.3$; $0.15 \leq r \leq 0.6$; $\mu_b \leq 0.1$; and asymmetries of roll size, speed and friction between 0.8 and 1.5. Outside these limits, thin-sheet asymptotic and slab models should be used with extreme care. In particular, for $\mu_t \geq 0.3$ the solution was found to ‘jump order’, indicating that it should be considered invalid.

The geometric regime compared here corresponds to thin-sheet rolling - for example, a 4mm sheet reduced by 25% with a 0.5m effective roll radius. The material assumptions are applicable to materials with minimal hardening and high elastic modulus compared to the yield stress, such as lead, mild steel and some aluminium alloys. The tolerance for hardening can be extended by considering the strain predictions to modify the yield stress, as presented in Section 2.5.5; however, including hardening in the model formulation would be a more rigorous approach in these circumstances.

Degradation of the solution quality may stem from regions where the workpiece sticks to the roll surfaces. In the simulations, this results in the material falling below yield in the cross-shear region, which affects torque predictions. Although the cross-shear region is captured in the asymptotic model, the rigid plastic assumption renders it incapable of resolving these sub-yield regions.

The numerics, Figure 2.5 in particular, also capture an oscillation in the position of the bottom neutral point as the reduction is varied. This may be related to the change in the sign of curvature observed in other studies (Chekmarev et al., 1956; Knight et al., 2003, 2005). If so, this would indicate that for a model to robustly predict curvature through reduction variations, it would require greater phenomenological detail than the present asymptotic or previous slab models.

Future work could incorporate more realistic materials. Although work hardening was approximated by modifying the yield stress based on the mean effective strain with this model, the asymptotic method could be used to provide a rigorous treatment for this or other hardening behaviours, like Smet et al. (1989); R. E. Johnson et al. (1992); Domanti et al. (1995); or Cherukuri et al. (1997). Further, incorporating elasticity and sub-yield behaviour may capture trends missed by the present model, although

this poses a significant modelling challenge. Modelling elasticity may also solve the discontinuities at the entrance and exit as well as the neutral points. Incorporating roll deformation could also improve predictions for foil rolling, another regime this model is applicable to.

Finally, the prediction of curvature has been attempted by several authors (Aboutorabi et al., 2016; Farhatnia et al., 2011; Gong et al., 2010; Gudur et al., 2008; Qwamizadeh et al., 2011; Salimi et al., 2002) and the same methods could be applied to this asymptotic model. The detail gained here could also underpin future, more systematic, curvature predictions to capture the oscillations discussed above. Curvature trends, and methods of curvature prediction, are discussed further in Chapter 4.

Chapter 3

Clad-sheet rolling

An asymptotic model of sandwich sheet rolling, symmetric rolling of composite plates, was developed in collaboration with Dr Chris Cawthorn and has been published in Cawthorn, Minton et al. (2016). The interface between the surface and inner material was modelled as a free surface and is the first use of this technique in asymptotic rolling models. A variation of that model is presented in this chapter, extending the asymmetric model of Chapter 2, or Minton et al. (2016), to model the rolling of a bi-metallic workpiece, known as clad-sheet rolling, by applying this free boundary approach. This model is consistent with the asymmetric model in the limit of a homogeneous workpiece.

This model has been implemented in *Python* and verified against finite element simulations using the *ABAQUS/Explicit* finite element package (Dassault Systemes, 2012a). Under any workpiece inhomogeneity, good agreement was found for roll force but poor agreement for roll torque.

The model formulation is presented in Section 3.2 and then solved in Section 3.3. Section 3.4 provides details of the finite element analysis used to validate this model and the validation itself presented Section 3.5.

3.1 Introduction

Composite metal sheets are formed from multiple layers of bonded metal plates. Bi-metallic, or clad-sheets, specifically involve two bonded plates. Extensive applications exist for clad-sheets because material properties are able to be combined; for example corrosion resistance, tensile strength or electrical conductance. These sheets are manufactured by rolling multiple homogeneous sheets together, either bonded or

unbonded, to produce a product of the correct gauge. Unbonded sheets can undergo bonding during the rolling process and then can undergo subsequent rolling to achieve the desired thickness.

In literature, both bonded and unbonded clad-sheet rolling are investigated with experiments (Eizadjou et al., 2008; Y. Hwang et al., 1996b), numerics (Maleki et al., 2013; Shintani et al., 1992) and analytical modelling. The analytical models are extensions of models for homogeneous asymmetric rolling. These fall into two major categories: slab models (Afrouz et al., 2015; Y. M. Hwang et al., 1996a,b; S. Pan et al., 2008; Qwamizadeh et al., 2013, 2014; Wang et al., 2015) and upper-bound methods (Y. Hwang et al., 1996b; Maleki et al., 2013; Pishbin et al., 2010; Shintani et al., 1992). In addition, some models predict bond formation during rolling (S. C. Pan et al., 2006; Yong et al., 2000); symmetric tri-layer, or sandwich rolling (Manesh et al., 2005; Tzou et al., 2003); and curvature (Lee et al., 2015; Qwamizadeh et al., 2014; Shintani et al., 1992), which is specifically investigated in Chapter 4

No asymptotic model has yet been proposed to model clad-sheet rolling. This application seems like a natural extension of the work presented in Chapter 2, especially in context of the asymptotic sandwich sheet rolling model in Cawthorn, Minton et al. (2016). Combining treatment of asymmetry from Minton et al. (2016) and the free boundary treatment of the material interface from Cawthorn, Minton et al. (2016), this work presents such a model.

3.2 Model formulation

The clad model is formulated assuming rigid perfect-plasticity for both metals and Coulomb friction for the roll-workpiece interfaces. Assumptions of small roll gap aspect ratio and small friction coefficient are exploited to make an asymptotic expansion. Many similarities exist between the work here and the previous chapter; the assumptions, governing equations and choice of boundary conditions are consistent between both models. The extension here is a free boundary within the workpiece which models the interface of the two materials. This boundary is assumed to be bonded, although a slipping friction or evolution law could be used to model unbonded or bonding sheets.

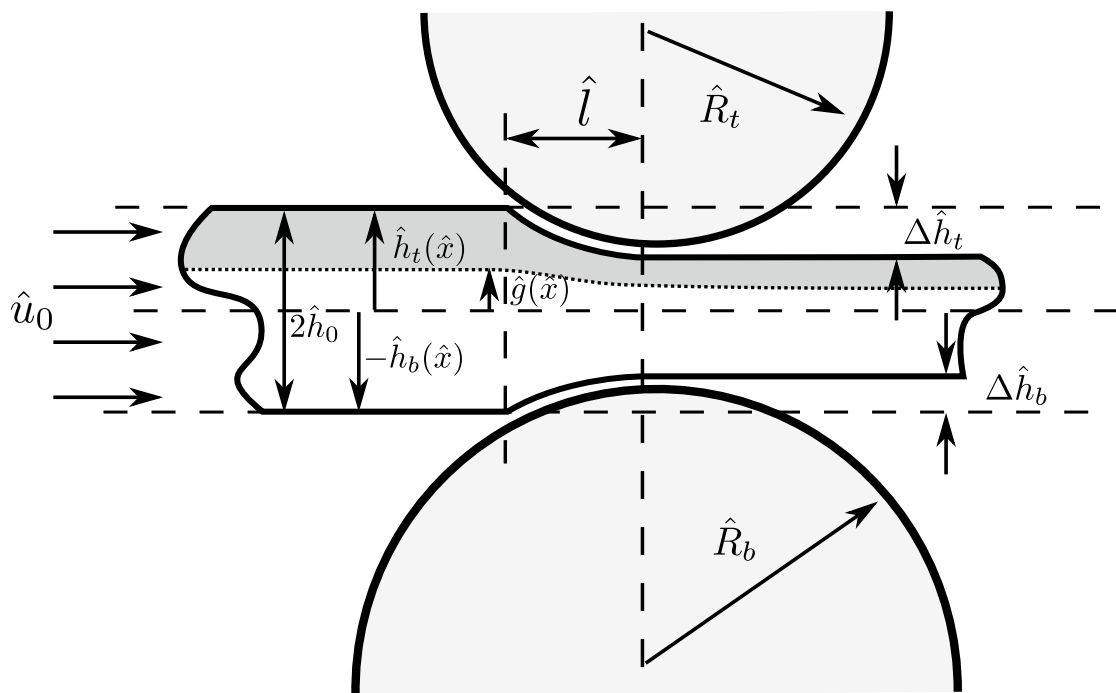


Fig. 3.1 An illustration of idealised clad-sheet rolling geometry.

The variables for the material below the interface are denoted with capital variables, for example the yield stress for the upper material is \hat{k} and the yield stress for the lower material is \hat{K} . The relevant variables are non-dimensionalised as follows.

$$\begin{aligned}
\hat{x} &= \hat{l}x & \hat{h} &= \hat{h}_0h & \hat{y} &= \hat{x}_0y & \hat{g} &= \hat{h}_0g \\
\hat{s}_{xx} &= \hat{k}s_{xx} & \hat{s}_{xy} &= \delta\beta\hat{k}s_{xy} & \hat{S}_{xx} &= \hat{k}S_{xx} & \hat{S}_{xy} &= \delta\beta\hat{k}S_{xy} \\
\hat{p} &= \beta\hat{k}p & \hat{u} &= \hat{u}_0u & \hat{P} &= \beta\hat{k}P & \hat{U} &= \hat{u}_0U \\
\hat{v} &= \delta\hat{u}_0v & \hat{\lambda} &= \lambda\frac{\hat{u}_0}{\hat{k}\hat{l}} & \hat{V} &= \delta\hat{u}_0V & \hat{\Lambda} &= \Lambda\frac{\hat{u}_0}{\hat{k}\hat{l}}
\end{aligned} \tag{3.1}$$

where \hat{p} , \hat{s}_{xx} , \hat{s}_{xy} , \hat{u} , \hat{v} and $\hat{\lambda}$ are the pressure, horizontal deviatoric stress, shear stress, horizontal velocity, vertical velocity and flow rate parameter respectively; \hat{g} is the vertical position of the interface from the centre-line; \hat{h}_0 , \hat{l} and \hat{u}_0 are marked in Figure 3.1; \hat{k} is the yield stress; $\beta = \mu_b/\delta$ and $\delta = \hat{h}_0/\hat{l}$.

Using this and the plane-strain condition, the non-dimensionalised governing equations become

$$-\beta\frac{\partial p}{\partial x} + \frac{\partial s_{xx}}{\partial x} + \beta\frac{\partial s_{xy}}{\partial y} = 0 \qquad -\beta\frac{\partial P}{\partial x} + \frac{\partial S_{xx}}{\partial x} + \beta\frac{\partial S_{xy}}{\partial y} = 0 \tag{3.2}$$

$$-\beta\frac{\partial p}{\partial y} - \frac{\partial s_{xx}}{\partial y} + \delta^2\beta\frac{\partial s_{xy}}{\partial x} = 0 \qquad -\beta\frac{\partial P}{\partial y} - \frac{\partial S_{xx}}{\partial y} + \delta^2\beta\frac{\partial S_{xy}}{\partial x} = 0 \tag{3.3}$$

$$\frac{\partial u}{\partial x} = \lambda s_{xx} \qquad \frac{\partial U}{\partial x} = \Lambda S_{xx} \tag{3.4}$$

$$\frac{\partial u}{\partial y} + \delta^2\frac{\partial v}{\partial x} = 2\delta^2\beta\lambda s_{xy} \qquad \frac{\partial U}{\partial y} + \delta^2\frac{\partial V}{\partial x} = 2\delta^2\beta\Lambda S_{xy} \tag{3.5}$$

$$\frac{\partial u}{\partial x} + \frac{\partial v}{\partial y} = 0 \qquad \frac{\partial U}{\partial x} + \frac{\partial V}{\partial y} = 0 \tag{3.6}$$

$$s_{xx}^2 + \delta^2\beta^2s_{xy}^2 = 1, \qquad S_{xx}^2 + \delta^2\beta^2S_{xy}^2 = K^2, \tag{3.7}$$

using, as a consequence of plane strain, $-s_{xx}$, $-S_{xx}$ and the incompressibility condition in favour of s_{yy} , S_{yy} and the vertical flow rule.

The top and bottom roll boundary conditions, specifically no penetration and Coulomb friction, are defined as,

$$v(x, h_t) = u(x, h_t) \frac{dh_t}{dx}, \quad (3.8a)$$

$$V(x, h_b) = U(x, h_b) \frac{dh_b}{dx}, \quad (3.8b)$$

and

$$\begin{aligned} s_{xy}(x, h_t) = & \gamma_t (\beta p(x, h_t) + s_{xx}(x, h_t)) + \frac{2}{\beta} s_{xx}(x, h_t) \frac{dh_t}{dx} \\ & + \delta^2 \left[\gamma_t (\beta p(x, h_t) + s_{xx}(x, h_t)) \left(\frac{dh_t}{dx} \right)^2 \right. \\ & \left. + s_{xy}(x, h_t) \left(\left(\frac{dh_t}{dx} \right)^2 - 2\beta \gamma_t \frac{dh_t}{dx} \right) \right] \end{aligned} \quad (3.9a)$$

$$\begin{aligned} S_{xy}(x, h_b) = & \gamma_b (\beta P(x, h_b) + S_{xx}(x, h_b)) + \frac{2}{\beta} S_{xx}(x, h_b) \frac{dh_b}{dx} \\ & + \delta^2 \left[\gamma_b (\beta P(x, h_b) + S_{xx}(x, h_b)) \left(\frac{dh_b}{dx} \right)^2 \right. \\ & \left. + S_{xy}(x, h_b) \left(\left(\frac{dh_b}{dx} \right)^2 - 2\beta \gamma_b \frac{dh_b}{dx} \right) \right] \end{aligned} \quad (3.9b)$$

where

$$\gamma_t = \begin{cases} \frac{\mu_t}{\mu_b} & : x < x_{nt} \\ -\frac{\mu_t}{\mu_b} & : x > x_{nt} \end{cases} \quad \text{and} \quad \gamma_b = \begin{cases} -1 & : x < x_{nb} \\ 1 & : x > x_{nb} \end{cases}. \quad (3.10)$$

The material interface, $g(x)$, is defined from the centreline, like $h_t(x)$ and $h_b(x)$, but is solved for using volume conservation,

$$\begin{aligned} \int_{g(0)}^{h_t(0)} u(0, y) dy &= \int_{g(x)}^{h_t(x)} u(x, y) dy \\ \int_{h_b(0)}^{g(0)} U(0, y) dy &= \int_{h_b(x)}^{g(x)} U(x, y) dy. \end{aligned} \quad (3.11)$$

To ensure continuity at this interface velocities are defined to be equal,

$$u(x, g(x)) = U(x, g(x)) \quad \text{and} \quad v(x, g(x)) = V(x, g(x)), \quad (3.12)$$

and similarly, to ensure forces balance, the surface tractions are defined to be equal,

$$\begin{aligned}\beta\tau_s &= \frac{1}{1 + \delta^2 g'^2} \left(-2g' s_{xx} + \beta s_{xy} (1 - \delta^2 g'^2) \right) \\ &= \frac{1}{1 + \delta^2 g'^2} \left(-2g' S_{xx} + \beta S_{xy} (1 - \delta^2 g'^2) \right) = \beta T_s\end{aligned}\quad (3.13a)$$

$$\begin{aligned}\text{and } \tau_n &= \beta p (1 + \delta^2 g'^2) + s_{xx} (1 - \delta^2 g'^2) + \delta^2 \beta s_{xy} g' \\ &= \beta P (1 + \delta^2 g'^2) + S_{xx} (1 - \delta^2 g'^2) + \delta^2 \beta S_{xy} g' = T_n\end{aligned}\quad (3.13b)$$

where τ_s and τ_n are the tangential and normal traction forces on the interface and derivatives in x are denoted with primes.

The end force and velocity conditions are also non-dimensionalised to be

$$F_{\text{in/out}} = \int_g^{h_t} -\beta p + s_{xx} dy + \int_{h_b}^g -\beta P + S_{xx} dy, \quad (3.14)$$

where $\hat{F}_{\text{in/out}} = F_{\text{in/out}} (\hat{h}_t - \hat{h}_b) \hat{k}$, and

$$2 = \int_{g(0)}^{h_t(0)} u(0, y) dy + \int_{h_b(0)}^{g(0)} U(0, y) dy. \quad (3.15)$$

It is also convenient to define the workpiece height throughout the roll gap, $\Delta h(x) = h_t(x) - h_b(x)$, and the total roll friction acting on a vertical element of the workpiece, $\Delta\gamma = \gamma_t(x) - \gamma_b(x)$.

3.3 Solution

A feature of assuming the workpiece is a thin-sheet, shared with slab models, is that the material properties have no effect on determining leading order velocity profiles. Consequently, with velocity continuity across the interface, the horizontal and vertical velocities remain unchanged from the homogenous asymmetric case,

$$u^{(0)} = U^{(0)} = \frac{2}{\Delta h(x)} \quad (3.16)$$

$$v^{(0)} = V^{(0)} = - \int_{h_b(x)}^{h_t(x)} \frac{du^{(0)}}{dx} dy = - \int_{h_b(x)}^{h_t(x)} \frac{dU^{(0)}}{dx} dy = \frac{2}{\Delta h^2} \left(h_t \frac{dh_b}{dx} - h_b \frac{dh_t}{dx} + y \frac{d\Delta h}{dx} \right). \quad (3.17)$$

Using these solutions, the leading order position of the interface can be solved to ensure mass conservation of each material,

$$g^{(0)}(x) = \frac{1}{\Delta h(0)} (g(0)\Delta h(x) + h_b(x)h_t(0) - h_t(x)h_b(0)). \quad (3.18)$$

Unsurprisingly, this is a stream-line of the velocity field. The yield condition gives the longitudinal deviatoric stresses for each material,

$$s_{xx} = -s_{yy} = 1 \quad \text{and} \quad S_{xx} = -S_{yy} = K. \quad (3.19)$$

These give flow rate parameters of

$$\lambda^{(0)} = -\frac{2}{\Delta h^2} \frac{d\Delta h}{dx} \quad \text{and} \quad \Lambda^{(0)} = -\frac{2}{K\Delta h^2} \frac{d\Delta h}{dx}. \quad (3.20)$$

The vertical force balance shows that leading order pressure is independent of y . The interfacial boundary condition then shows

$$P^{(0)} = p^{(0)} + \frac{s_{xx}^{(0)}(x, g^{(0)}(x)) - S_{xx}^{(0)}(x, g^{(0)}(x))}{\beta} \quad (3.21)$$

$$\text{and} \quad \frac{dP^{(0)}}{dx} = \frac{dp^{(0)}}{dx}. \quad (3.22)$$

The horizontal force balance is integrated between h_b and g and then between g and h_t for

$$\frac{dp^{(0)}}{dx} = \frac{s_{xy}^{(0)}(x, h_t) - s_{xy}^{(0)}(x, g^{(0)})}{h_t(x) - g^{(0)}(x)} \quad \text{and} \quad \frac{dP^{(0)}}{dx} = \frac{S_{xy}^{(0)}(x, g^{(0)}) - S_{xy}^{(0)}(x, h_b)}{g^{(0)}(x) - h_b(x)}. \quad (3.23)$$

Eliminating $g^{(0)}(x)$ from equation (3.22) and equation (3.23) gives

$$\frac{dp^{(0)}}{dx} \Delta h = s_{xy}^{(0)}(x, h_t) - S_{xy}^{(0)}(x, h_b) - (s_{xy}^{(0)}(x, g^{(0)}) - S_{xy}^{(0)}(x, g^{(0)})) \quad (3.24)$$

which can be solved with the interfacial boundary condition for

$$\begin{aligned} \frac{dp^{(0)}}{dx} \Delta h &= \gamma_t (\beta p^{(0)} + s_{xx}^{(0)}) + \frac{2}{\beta} s_{xx}^{(0)} \frac{dh_t}{dx} - \gamma_b (\beta P^{(0)} + S_{xx}^{(0)}) - \frac{2}{\beta} S_{xx}^{(0)} \frac{dh_b}{dx} \\ &\quad - \frac{2}{\beta} \frac{dg^{(0)}}{dx} (s_{xx}^{(0)} - S_{xx}^{(0)}) \end{aligned} \quad (3.25)$$

where the homogeneity in $s_{xx}^{(0)}$ and $S_{xx}^{(0)}$ has been used to simplify. This can be further simplified, using equation (3.21), to

$$\frac{dp^{(0)}}{dx} \Delta h = \Delta \gamma (\beta p^{(0)} + s_{xx}^{(0)}) + \frac{2}{\beta} \left(s_{xx}^{(0)} \frac{h_t(0) - g^{(0)}(0)}{\Delta h(0)} + S_{xx}^{(0)} \frac{g^{(0)}(0) - h_b(0)}{\Delta h(0)} \right) \frac{d\Delta h}{dx}.$$

which is an ODE for the leading order pressure, $p^{(0)}$. With the solution of this, the shear stress solution can be determined from the indefinite integral of the horizontal force balance, and both boundary conditions, as

$$\begin{aligned} s_{xy}^{(0)} &= \frac{dp^{(0)}}{dx} (y - h_t) + \gamma_t (\beta p^{(0)} + s_{xx}^{(0)}) + s_{xx}^{(0)} \frac{2}{\beta} \frac{dh_t}{dx} \\ \text{and } S_{xy}^{(0)} &= \frac{dP^{(0)}}{dx} (y - h_b) + \gamma_b (\beta P^{(0)} + S_{xx}^{(0)}) + S_{xx}^{(0)} \frac{2}{\beta} \frac{dh_b}{dx}. \end{aligned} \quad (3.26)$$

Correction order

The rigour of the asymptotic method allows refinement to these solutions by iteratively solving the governing equations at higher orders of δ . Analogous to the homogeneous asymmetric case, and other thin-sheet asymptotic models, the $O(\delta)$ terms are solved to be identically zero and terms of $O(\delta^2)$ must be considered to refine the solution. Solutions to this order are included in Appendix B. These corrections bring increased resolution through-thickness with the polynomial form of each variable raising an order in y . The strain field also becomes dependent on the leading order stress field and hence material properties from the cladding.

3.4 Numerical simulations

The commercial finite element package *ABAQUS* (Dassault Systemes, 2012a) was used to simulate the clad rolling process and assess the quality of the model presented here. An implicit finite element solver was used to simulate a workpiece. The workpiece was made of two-dimensional plane-strain elements, *CPE4R*, and the rolls were circular rigid analytic surfaces. Since the unsupported alignment of the workpiece and the rolls was unknown a priori, the simulation was run so the rolls closed on a stationary workpiece before they began to rotate to avoid numerical errors caused by inconsistencies in the imposed initial conditions.

Static stress analysis was used since the process is considered pseudo-steady state and inertia can be neglected, To further reduce shocks, pressure over-closure was included in the Coulomb friction surface interactions and smooth amplitude changes were applied to the roll closure rate and the initial spin up of the roll rotations.

The geometry was defined by a 5mm workpiece that was reduced by 20% in a roll gap with rolls giving an aspect ratio of 0.1. The ultimate length of the workpiece was 2000mm and approximately 50% of this length was rolled in the course of the simulation. The workpiece is modelled with 18 elements through-thickness and 360 lengthwise. Friction coefficients of 0.1 were used for the workpiece-roll interactions on both the upper and lower surface. The final roll surface speed was 1.2ms^{-1} although this should have no impact with the assumed lack of inertia, .

Cladding was incorporated by defining two sections, each assigned materials of different yield stress. Node locations were chosen so that a row of nodes lay on the clad interface and no element lay across the interface. The material properties were chosen to match the asymptotic modelling assumptions as closely as possible. No hardening effects were included and a homogeneous isotropic yield stress was chosen for each section of the plate. *ABAQUS* is unable to simulate rigid-plastic materials so an elastic modulus and Poisson's ratio of 100GPa and 0.30 were used. The yield stress of the top material was 100MPa in shear and the bottom yield stress was varied to ensure $\frac{\hat{K}}{\hat{k}} = K$ for specified values of K .

Further detail of this finite element model, including a mesh convergence study, can be found in Appendix D.

3.5 Results and discussion

It can be seen that analytically this model reduces to the homogeneous asymmetric rolling model presented in Chapter 2, when $g_0 = \pm 1$ or when $K = 1$, as these cases correspond to no cladding. The discussion provided there remains valid for this model in these cases.

This section will focus on the accuracy of the new asymmetry of non-homogenous workpieces, where $g_0 \neq \pm 1$ and $K \neq 1$. Comparisons are made between the asymptotic model presented and numerical simulations described in the previous section. Figure 3.2 shows the force and torque results as the yield stress ratio is varied between 0.65 and 1.55 and as the thickness ratio is varied over its entire range.

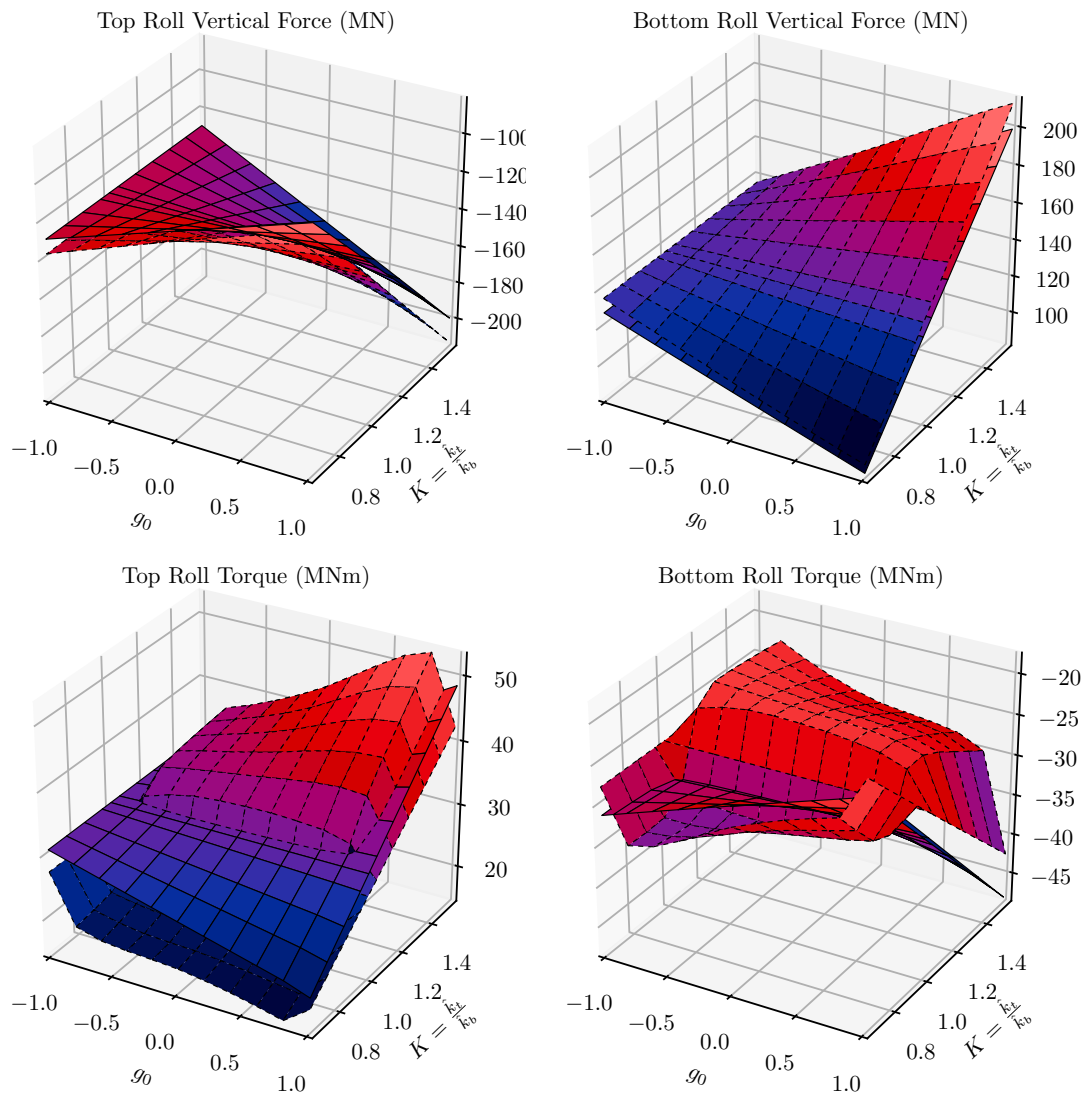


Fig. 3.2 Roll force and torque as the cladding parameters are varied for the asymptotic (solid wire frame) and finite element (dashed wire frame) solutions. The roll set-up is otherwise symmetric with parameters: $(\hat{h}_0, \delta, r, \mu, \hat{k}) = (0.05, 0.1, 0.20, 0.1, 100\text{MPa})$.

Agreement is good for $g_0 = \pm 1$ and $K = 1$. The results are constant for $g_0 = -1$ as the upper material forms the entire workpiece, rendering the value of K irrelevant. Similarly, the results are also constant when $K = 1$ because the lower material is identical to the upper material. The force and torque scale linearly with K for $g_0 = 1$ as the lower material forms the entire workpiece, producing a yield stress scaling of the previous homogenous case discussed. All these trends also occur for the numerical results and the accuracy is comparable with the findings of the previous chapter.

The asymptotic roll force and torque predictions could generally be described as an interpolation of the homogenous cases. Pressure is the dominant contribution to the roll force and torque predictions and, at leading order, the gradient differs from the homogenous case in the frictionless term only, which is now the average of deviatoric stresses.

This interpolation behaviour is reflected in the numerical force predictions such that the relative error of the asymptotic model does not rise above 6.5%. The numerical torque predictions exhibit a more complex behaviour, however. Any of the simulations conducted with inhomogeneity show an almost constant shift away from an interpolation between the homogenous cases. Figure 3.3 is a cross-section of Figure 3.2 and clearly illustrates this. The analytical model does not capture this behaviour so the roll torque for the higher-yield side is underestimated and the roll torque for the lower-yield side is overestimated. Relative error of torque predictions rise to over 50%, although the median errors remain around 12.5%. The small thicknesses at which this jump occurs could suggest a boundary layer effect that is not captured by the asymptotic model. An alternative hypothesis is that elasticity causes residual stresses that curve both the deformed and undeformed workpiece, which was observed in the simulations but is not modelled in the rigid perfectly-plastic asymptotic model. This short-coming would be predicted to arise in all slab-models and most upper-bound models also.

3.5.1 Distributions

The stress and strain distributions, Figures 3.4 and 3.5, exhibit many of the same features as the asymmetric distributions. The leading order is seen to have resulted in a slab-like solution. The constant deviatoric longitudinal stresses are constant in each material section; through-thickness pressure is constant with a jump at the material interface; and a linearly varying through-thickness shear stress with no apparent jump at the material interface. The strain distributions are identical to the asymmetric

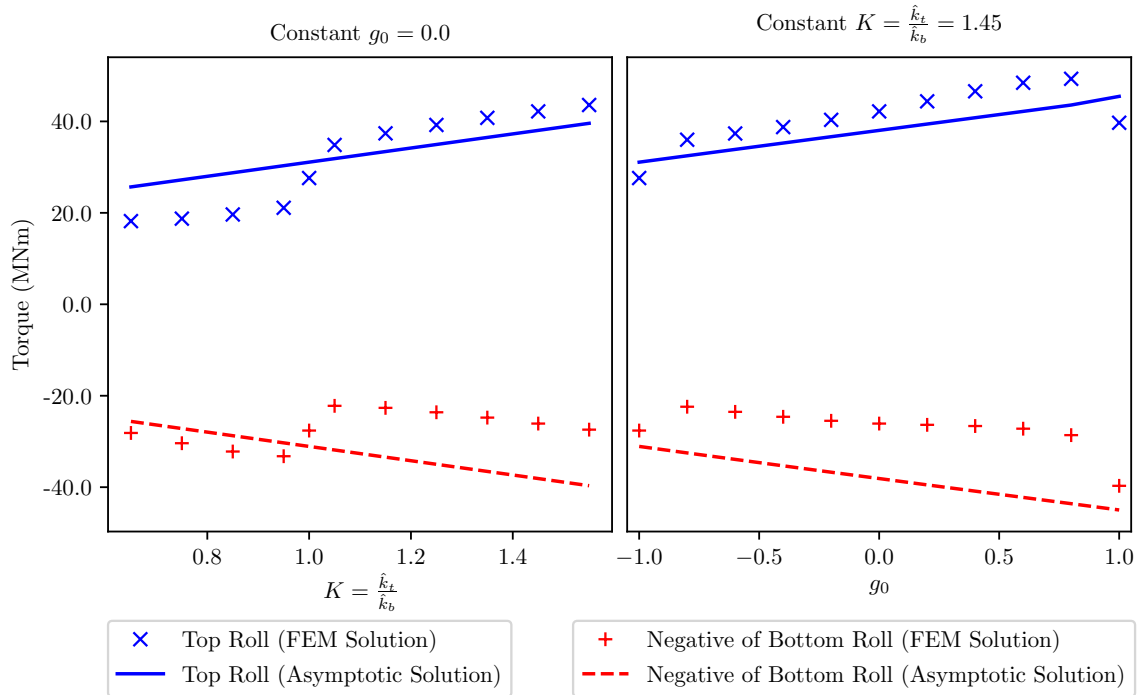


Fig. 3.3 Cross sections of Figure 3.2

rolling model at this order because the effect of stress distributions only feature in strain solutions at the correction order.

The correction order refines the through-thickness distributions indicating higher pressures at the roll surfaces than the centre of the workpiece, lower deviatoric stress at the roll surfaces than the centre of the workpiece and no visible change to the shear stress. The strain distributions develop small discontinuities at the material interface.

Lobes dominate the numerical shear results and are echoed in the other numerical stress results. These were also observed for the asymmetric rolling simulations and are more thoroughly investigated in Chapter 5.

Looking past this, the pressure hill and value of horizontal deviatoric stress agrees with the asymptotic solution. Both velocity fields are also in reasonable agreement past a short entrance region. This entrance region shows elastic bending of the unworked material such that the workpiece does not enter the roll gap horizontally. This is why the workpiece thickness appears thinner in the numerical solution and why there is a uniform positive vertical velocity at the entrance.

The complete stress field allows stress predictions along the material interface, which provides useful information about how the bond is affected by the process. For example, determining the necessary bond strength from the maximum shear stresses

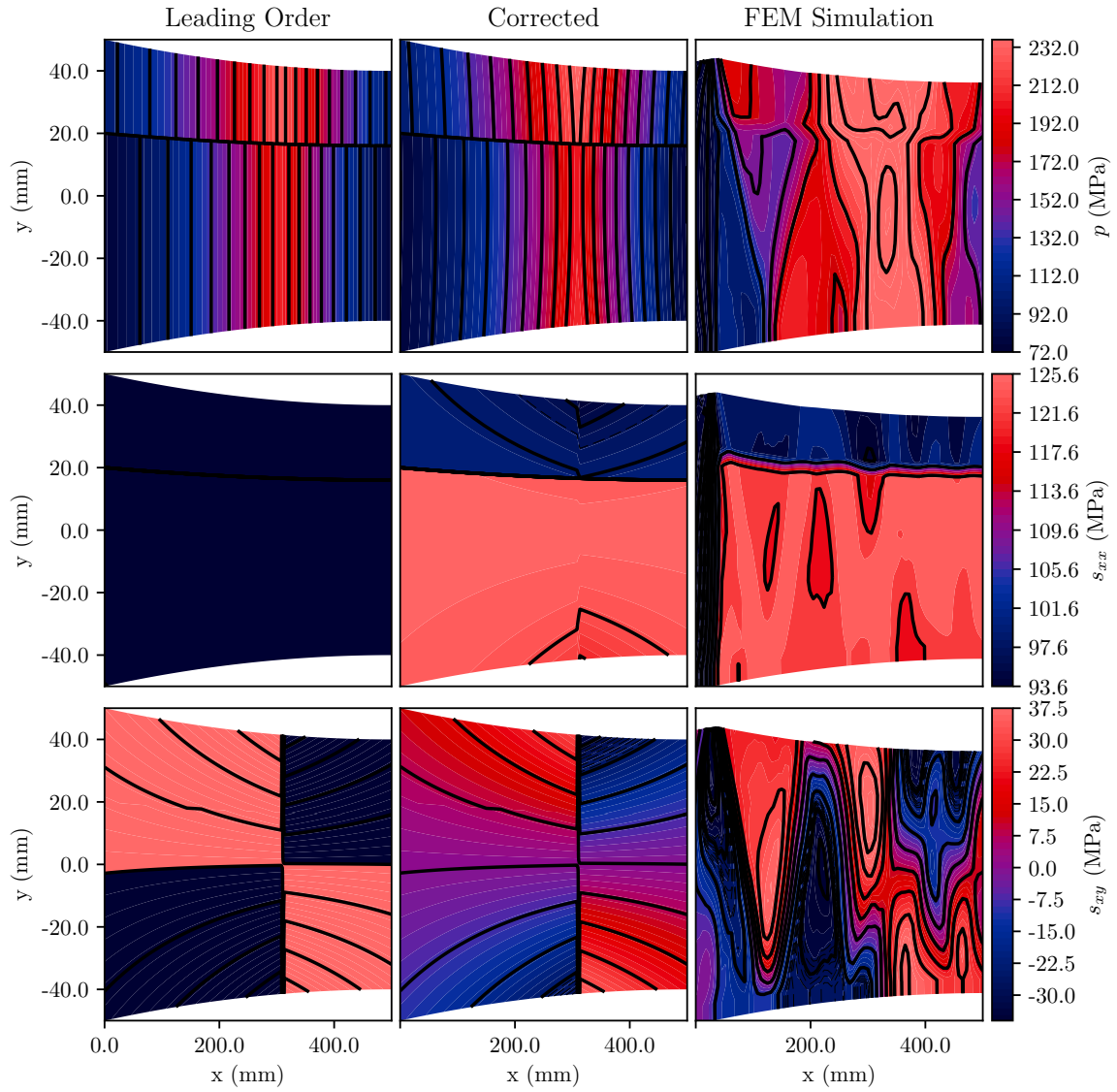


Fig. 3.4 Pressure (top), horizontal deviatoric stress (middle) and shear stress (bottom) fields from the asymptotic model leading order (left) corrected solution (centre) and finite element simulations (right) for $g_0 = 0.4$ and $K = 1.25$. The roll set-up is otherwise symmetric with parameters: $(\hat{h}_0, \delta, r, \mu, \hat{k}) = (0.05, 0.1, 0.20, 0.1, 100\text{MPa})$.

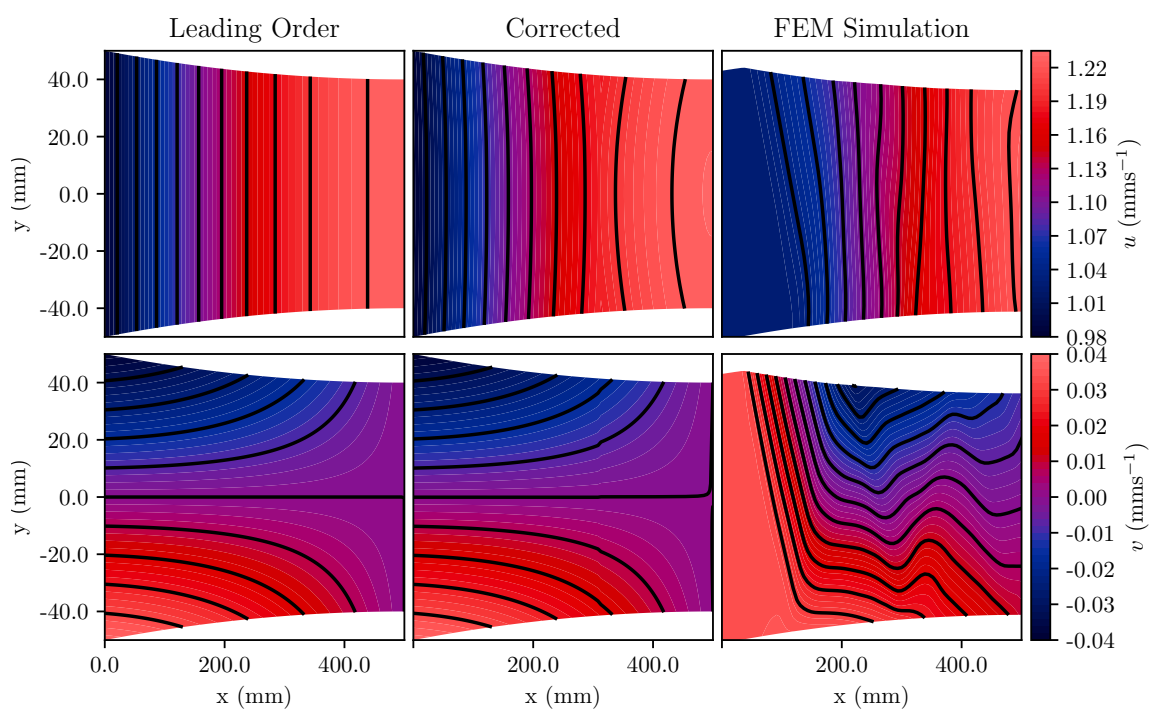


Fig. 3.5 Horizontal (top) and vertical (bottom) velocity fields from the asymptotic model leading order (left) corrected solution (centre) and finite element simulations (right) for a symmetric rolling configuration with a clad workpiece of $g_0 = 0.4$ and $K = 1.25$. The roll set-up is otherwise symmetric with parameters: $(\hat{h}_0, \delta, r, \mu, \hat{k}) = (0.05, 0.1, 0.20, 0.1, 100\text{MPa})$.

on this interface. The position of the bonded interface is predicted very well except for a small discrepancy around the inlet; the normal force on the interface is predicted well; but the tangential force on the interface is predicted poorly. These are shown in Figure 3.6. The position discrepancy at the inlet is likely a consequence of the angled entry of the workpiece and is of little concern. The inaccuracies in the interfacial forces are a reflection of the inaccuracies in the entire stress field, specifically the shear oscillations, or lobes. As these oscillations often dominate the value to be predicted, the present model would not be sufficient for this application. Further refinement would be needed to provide quantitative information about the bonded interface during clad rolling.

3.6 Conclusion

Asymptotic analysis was used to derive a model for clad rolling under the assumptions of perfect rigid plasticity, a small roll gap aspect ratio and weak Coulomb friction. This is an extension of the model presented in Chapter 2 as the same scaling assumptions and asymmetries are used here. The solution procedure involves solving the location of both neutral points to ensure leading order pressure continuity. With Coulomb friction, this gives a piecewise ODE for pressure. Both the stress and strain fields are closed form solutions in terms of the pressure.

This model was verified against finite element simulations for varying thickness and yield stress ratios. The roll force prediction was found to have reasonable accuracy across the entire parameter range investigated; however, the roll torque predictions lost accuracy for any amount of inhomogeneity in the workpiece. This suggests a significant phenomenon of the clad rolling processes, perhaps elastic curvature, is not captured by the present model. Shear stress lobes are also present in the finite element simulations used here but absent from the asymptotic solution. The magnitudes of these lobes are sufficiently large that they determine the bonding strength required between the layers. Reducing or eliminating the shear lobes might, therefore, be practically relevant for rolling weakly bonded metals. The lobe phenomenon is discussed further in Chapter 5. Unsurprisingly the asymptotic solution is much faster to compute than the finite element solution.

Further developments to this model could be made as discussed in the concluding remarks of Chapter 2 for the homogeneous asymmetric case; however, the significant roll torque discrepancy for any amount of workpiece inhomogeneity should be the focus

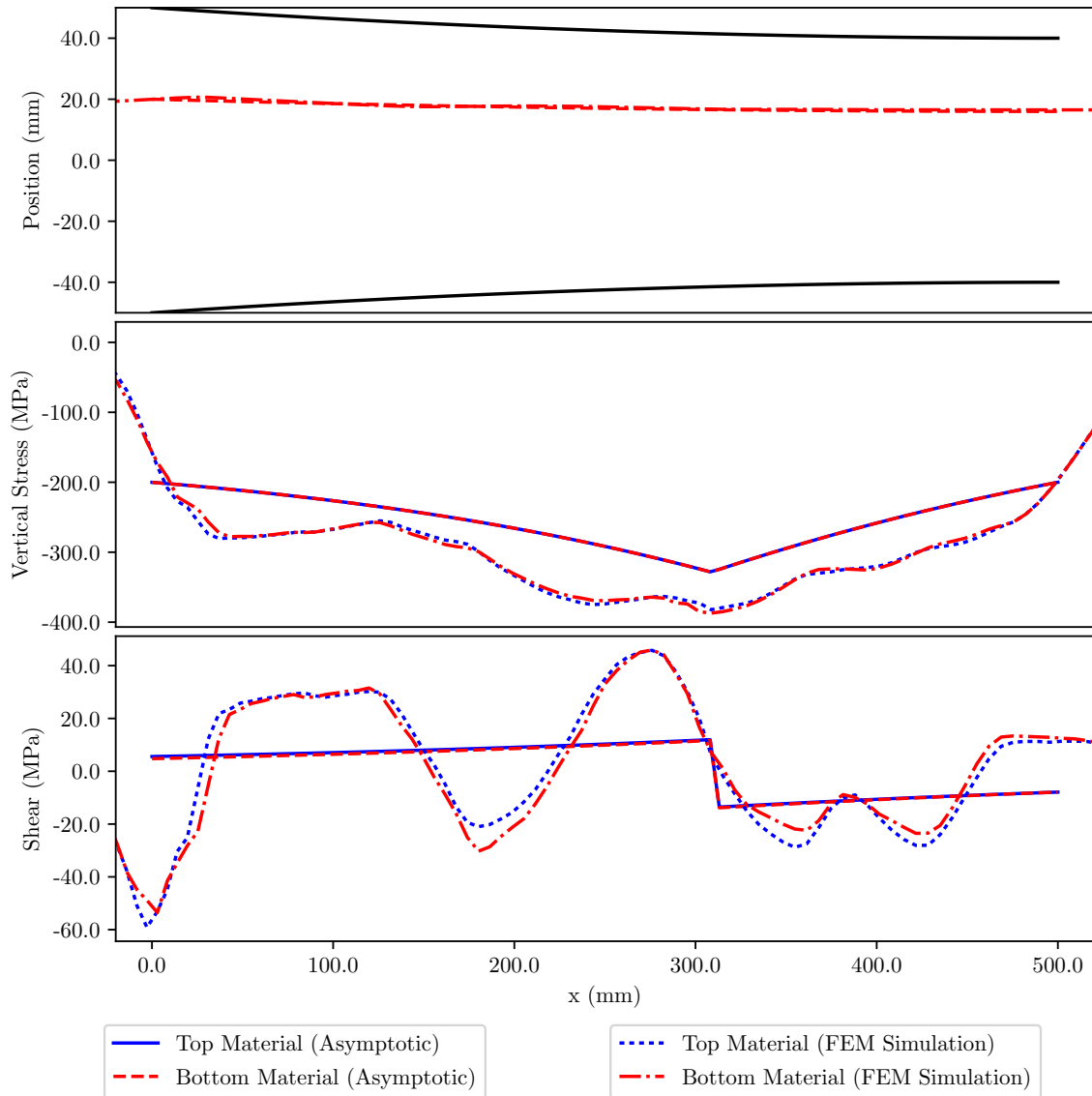


Fig. 3.6 Material interface position (top) and the normal (centre) and tangential (bottom) forces across the material interface for a clad workpiece of $g_0 = 0.5$ and $K = 1.25$. The roll set-up is otherwise symmetric with parameters: $(\hat{h}_0, \delta, r, \mu, \hat{k}) = (0.05, 0.1, 0.20, 0.1, 100\text{MPa})$.

of any future development of this model. This likely would lead to investigating the effects of elasticity and residual stresses on inducing curvature.

Chapter 4

Curvature prediction

Curvature is an important consideration in the operation of asymmetric rolling as it must fall within mill tolerances for successful operation and within product tolerances for quality assurance. To more clearly ascertain the trends between induced curvature and other parameters of a rolling configuration, the studies in this area were reviewed, digitised and statistically analysed. The qualitative review, presented in Section 4.1, revealed contradictions in the literature. In Section 4.2, regression modelling is performed on the digitised data. While no regression model was constructed that could accurately predict curvature, evidence was gained for which factors in the problem are significant. Strong interaction is shown between the roll size asymmetry and other geometric factors and significant dependence on material properties is found. Finally, Section 4.3 provides some numerical comparison of curvature prediction models presented in literature. None of the implemented models capture the non-linearities observed in the digitised data. This work is to be presented at the International Conference on Technology of Plasticity 2017 and initial results have been published in the conference proceedings (Minton et al., 2017).

4.1 Literature review

Experimental investigations into curvature can be dated back to at least 1956 and attempts to model this process to 1963. Despite this long history there are few generally applicable rules to describe the phenomenological trends relating workpiece curvature to the rolling mill configuration. There appear to be unacknowledged correlations between factors, which are missed by many studies that vary only a single parameter. Similarly,

many of the analytical models are validated with a small number of experimental data and are untested in general mill configurations.

Previous studies are summarised here to collate observed trends and to clarify correlations between factors where possible. Section 4.1.1 and Section 4.1.2 review the experimental and numerical literature by giving conclusions synthesised from observed trends, followed by Table 4.1 and Table 4.2, which summarise the set-ups and results of each publication reviewed.

Before studies are compared, the definition and measurement of curvature requires some consideration. Jeswiet et al. (1998) provides a discussion on this and enumerates some approaches with a critique of each. Curvature is a local property and is non-linearly related to most aspects of the rolled workpiece geometry. The differences in curvature measures often reduce to how the length of the workpiece is averaged. Later studies more explicitly consider averaging and which regions to include to target leading edge behaviour, but this could equally be used to exclude leading edge effects. Jeswiet et al. (1998) ultimately decides to use a peculiar measure of curvature: taking the height above the horizontal over the horizontal component of the worked length. This is a flawed measure as it is dependent on the length of the workpiece. A better choice might be to average local curvatures, which could be non-dimensionalised against several parameters. The workpiece thickness, initial or final, seems the most obvious as curvature and thickness are the only local intrinsic geometric properties of a two-dimensional workpiece. This is the definition of curvature adopted here, with the initial workpiece thickness used for ease.

4.1.1 Experiments

Some of the earliest studies provide the most comprehensive experiments; it is a shame the age often renders them unavailable or published exclusively in German, Russian or Japanese. Later work becomes dominated by numerical investigations, reviewed in the next section, and experimental work is often conducted only to validate such numerical models (Fu et al., 2012; Y. Hwang et al., 1999). Despite these limitations, twelve papers presenting experimental work have been reviewed and are summarised in Table 4.1. From these, loose qualitative conclusions can be drawn about curvature, including:

- Curvature is towards the roll with faster peripheral velocity for small roll surface speed asymmetries, but the opposite for larger asymmetries.

- Curvature is towards the smaller roll for small reductions and the larger roll for large reductions.
- Surface roughness affects curvature; however, the direction is dependent on reduction.
- Curvature is non-linearly related to reduction with a maximum curvature related to the roll gap ratio.

The non-specific nature of these conclusions is representative of the body of work. Most studies examine trends in a single asymmetry over a few rolling configurations, which often leads to conclusions contradicting other studies, of limited validity, and unrepresentative of broader trends. Once multiple asymmetries are introduced the convoluted effects become less predictable, rendering these conclusions entirely inadequate. This becomes clear in publications such as W. Johnson et al. (1966b) where the descriptions of trends are vague in terms of geometrical dependence.

A number of other, potentially significant, experimental considerations are also not widely discussed. Such considerations are related to the geometry of the workpiece. Insufficiently wide workpieces, compared to thickness, could result in edge effects dominating the behaviour. Conclusions drawn from studies such as Buxton et al. (1972) and W. Johnson et al. (1966a,b), which have small ratios, should be cautiously applied to plane strain rolling. Similarly, overly short workpieces may be dominated by end effects (Buxton et al., 1972; Kennedy et al., 1958). Unfortunately, without understanding the physics that drive curvature it is not possible to reason the extent of end effects and this has not yet been established experimentally. The roll gap aspect ratio is another consideration never explicitly discussed in these publications. It is well understood that thin and thick-sheet rolling, characterised by small (Pospiech, 1987) and large (Buxton et al., 1972; Dewhurst et al., 1974; Jeswiet et al., 1998; W. Johnson et al., 1966a,b; Kennedy et al., 1958) roll gap aspect ratios respectively, are distinct regimes that behave differently. Comparison between these sets of studies may, therefore, not be valid.

Smooth dry rolls slip unpredictably (Buxton et al., 1972) which adds experimental uncertainty to the process as transitions between sticking and slipping friction regimes significantly change the effect of friction. Care must be taken when measuring force, torque and curvature to identify if a transition has occurred. Despite many of these studies working within this regime (Jeswiet et al., 1998; W. Johnson et al., 1966a), Buxton et al. (1972) is the only one of these publications to identify this behaviour.

Lastly, Tanaka et al. (1969) concludes that smaller Young's modulus produces greater curvature. Unfortunately, many studies do not characterise the material behaviour, rendering them directly incomparable.

Further to considerations of experimental design, few papers discuss the mechanism that produces curvature. Chekmarev et al. (1956) is a notable exception in which a hypothesis of two independent mechanisms is proposed: friction pushes material against the faster roll through the roll gap more quickly so the workpiece curves away from the faster roll; and simultaneously, the smaller roll produces a bigger reduction so the workpiece is pushed away from the smaller roll. This hypothesis was rejected, however, as experiments performed in the same paper do not support it; the aggregated conclusions presented here do not generally support it either.

Table 4.1 Summary of Experimental Investigations into Curvature

Reference	Geometry	Material	Controlled Variables	Key Results	Notes
Chekmarev et al. (1956)	10-35x45mm workpiece; 87.5-105mm radius rolls; 10-70% reduction	Aluminium; lead and steel	Roll size; reduction; initial thickness	Curvature is towards the small roll under small reductions and towards the large roll under large reductions forming a cubic type curve. Initial thickness influences the shape of this curve. Asymmetric roll size with equal surface speed did not change this trend.	Originally published in Russian; British Library Translation, R.T.S. 8939.
Kennedy et al. (1958)	63x146-178mm workpiece; 380mm radius rolls; 25% reduction	Hot steel	Roll speed ratio; torque ratio	Roll speed asymmetry has more effect on curvature than roll torque. Roll speed asymmetry affects curvature for both transient and steady-state rolling. A linear relationship exists between speed ratio and curvature but with different slopes for each set-up.	Both torque and speed regulated set-ups used.
W. Johnson et al. (1966a)	6x25x150mm workpiece; 16-29mm radius rolls; 13-48% reduction	Tellurium lead	Roll size; roll speed; reduction	Curvature is towards the slower roll. Curvature varies over reduction with some finite maximum value.	Conference paper.
W. Johnson et al. (1966b)	6x25x150mm workpiece; 16-29mm radius rolls; 13-48% reduction	Tellurium lead	Roll size; roll speed; reduction; roll surface finish	Curvature is not always towards the slower roll, generally increases with greater reduction and decreases with rougher rolls. Curvature direction changes at specific reductions, with increasing roughness at small reductions and is dependent on roll speed.	Continues from W. Johnson et al. (1966a).
Tanaka et al. (1969)	2-high mill	Brass	Roll size	Curvature is towards the smaller roll. Curvature is greater for lower Young's modulus.	Strong asymmetry wrapped the workpiece around roll so no trend could be identified.

Reference	Geometry	Material	Controlled Variables	Key Results	Notes
Buxton et al. (1972)	20x38x152mm workpiece; 70mm radius rolls; 25% reduction	Standard hard plasticine	Roll speed; entry angle	For given angle of entry curvature is proportional to roll speed ratio. Slip can affect curvature.	Specifically investigates leading edge bending.
Dewhurst et al. (1974)	3-8x51x152mm workpiece; 72-75mm radius rolls; 20-40% reduction	Commercially pure lead	Roll size; roll speed; initial workpiece thickness	A relationship between reduction and roll gap aspect ratio is presented that predicts maximum strip curvature. Near this, curvature is towards the larger/faster roll for small asymmetries.	Results compared qualitatively well with a slip-line model.
Pospiech (1987)	25.5x0.92x150mm workpiece; 57mm radius roll; 6-73% reduction	99.9% pure annealed aluminium	Roll roughness; lubrication	Surface finish and lubrication can affect curvature. Curvature only changes sign with increasing reductions under some circumstances.	Quantitative results were not presented.
Jeswiet et al. (1998)	3x32x305mm workpiece; 51mm radius roll; 20-55% reduction	3003 aluminium	Roll speed; reduction	Increasing speed asymmetry increases curvature but curvature direction depends on reduction.	Also compared to FEM.
Y. Hwang et al. (1999)	3.2-6.0x80x300mm workpiece; 105mm radius roll; 5-35% reduction	Aluminium A1050P-H16; aluminium A1050P-F	Roll size with fixed angular velocity; reduction; initial thickness	Curvature is towards the smaller/slower roll for small reductions and towards the larger/faster roll for large reductions.	Presented as validation of FEM.
Fu et al. (2012)	8mm workpiece thickness; 90mm roll radius; 10-12.5% reduction	7150 aluminium	Roll speed ratio; angle of entry	Angle of entry changes curvature direction.	Presented as validation of FEM.
Li et al. (2016)	5x60x200mm workpiece; 50mm roll radius; 30,50% reduction	AA1060 aluminium	Roll speed ratio; angle of entry; reduction	A roll speed ratio can be found to produce zero curvature for a given reduction and angle of entry.	Studied microstructural change.

4.1.2 Numerics

Numerical studies of curvature began as early as 1988; however, these early investigations were focused on validating finite element methods against experimental results. Since then, numerous studies have been conducted to investigate many aspects of curvature, including the effect of roll size, roll speed, friction, temperature gradients, reduction, aspect ratio and combinations of the above. Twenty of these studies have been summarised in Table 4.2.

Many of the same trends found in the experimental literature arise from numerical studies. The comparatively low cost of simulations, compared to experiments, means numerical studies have investigated many more parameters than the experimental studies. Aggregated conclusions from these works are summarised by:

- Curvature is towards the faster (J. Yang et al., 2017) or the slower (Shivpuri et al., 1988) roll depending on the roll gap aspect ratio (Knight et al., 2003, 2005; Yoshii et al., 1991) and reduction (Harrer et al., 2003; Y. Hwang et al., 1999; Knight et al., 2003, 2005; Philipp et al., 2007). Small roll gap aspect ratios curve towards the slower roll and larger roll gap aspect ratios curve towards the faster roll (Knight et al., 2005; Salganik et al., 2014); and greater surface speed asymmetry produces greater curvature magnitude (Fu et al., 2012; Harrer et al., 2003; Philipp et al., 2007).
- Curvature is towards the larger (Farhat-Nia et al., 2006) or the smaller (Dvorkin et al., 1997) roll depending on the roll gap aspect ratio (Farhat-Nia et al., 2006) and the workpiece reduction (Y. Hwang et al., 1999; Knight et al., 2003); although neither parameter has been seen to change the sign of curvature in a single study.
- Considering constant ratios of angular velocity, curvature has been observed towards the smaller/slower roll for small reductions and towards the larger/faster roll for large reductions (Lu et al., 2000); and, towards the larger/faster roll for small reductions and towards the smaller/slower roll for large reductions (Kawałek, 2004).
- Curvature is towards the roll with higher friction (Y. Hwang et al., 1999; Knight et al., 2003; Richelsen, 1997; Yoshii et al., 1991) or the roll with lower friction (Dvorkin et al., 1997). Curvature doesn't change direction with roll gap aspect ratio (Anders et al., 2012) or reduction (Y. Hwang et al., 1999); although, some value of reduction produces maximum curvature (Richelsen, 1997) and

curvature magnitude increases with increasing asymmetric friction ratio (Anders et al., 2012).

- Curvature is towards the colder surface of the workpiece (Dvorkin et al., 1997).
- Feed offset can induce curvature in otherwise symmetric rolling (Dvorkin et al., 1997; Seo et al., 2016).
- Curvature is dependent on material properties (Markowski et al., 2003).

Compared to experimental studies, numerical methods also provide unprecedented detail about what is occurring within the workpiece, which has been used to investigate hypotheses and propose more refined curvature mechanisms. The first of these proposed that curvature is driven by a growing region of cross-shear. Akbari Mousavi et al. (2007) discusses this explicitly and shows that it is, at best, insufficient; comparing the cross-shear region from surface shear stress plots with curvature shows no correlation. Akbari Mousavi et al. (2007) went on to hypothesise that curvature is driven by horizontal plastic strains and the mechanism acts like an Euler-Bernoulli beam. This is also incomplete as curvature, in some configurations, can be predominantly driven by shear (Richelsen, 1997).

Anders et al. (2012) presents a comprehensive study of a non-dimensional parameter space. One recurring trend of the results is peak curvature for given roll geometry, where the initial to final thickness ratio and initial thickness over roll radius are used as geometric parameters, but even this general trend was not universal. Regardless, the plots provide useful reference for future studies; unfortunately, the author was unable to provide the data for subsequent analysis. Yoshii et al. (1991) is also worth noting for their evidence based discussion of curvature mechanisms. Features of the stress and strain fields are used to explain the observed curvature results, specifically formation of larger effective strain under the smaller or larger roll depending on the roll gap aspect ratio.

Table 4.2 Summary of Numerical Investigations into Curvature

Reference	Geometry	Material & Friction	Numerical Implementation	Controlled Variables	Key Results	Notes
Shivpuri et al. (1988)	2.5" workpiece; 3.8" radius roll; 25% reduction	Elastic-plastic material with power-law strain hardening; friction factor	Explicit time stepping; 1120 triangular plane-strain elements	Roll speed	FEM matches experimental results from Kennedy et al. (1958): curvature is towards the slower roll.	Impact force reduction factor used on entry. 90 elastic elements used for the rolls.
Yoshii et al. (1991)	10-100mm workpiece thickness; 574mm radius rolls; 10-30% reduction	Rigid-perfectly plastic; Coulomb friction	320 elements; non-steady state	Roll speed ratio; friction ratio; reduction; initial thickness; temperature gradient	Curvature is towards the slower roll for thin-sheets and the opposite for thick-sheets. Curvature towards the faster roll is due to deformation along the slower roll near the exit; curvature towards the slower roll is due to deformation along most of the faster roll. Curvature is towards the side of larger friction and towards the side of lower temperature.	Torsional vibration model of the driving system included in simulation. Experiments were conducted to validate the FEM.
Dyja et al. (1994)	4-10mm workpiece thickness; 500mm radius roll; 5-20% reduction	Huber-Mises rigid plasticity; non-linear relative-slip friction	Coupled plastic flow and diffusion equations. Solver described in Pietrzyk et al. (1991).	Roll rotation; friction coefficients; angle of entry; reduction	No conclusions drawn.	No meshing information provided. Curvature is not quantified.
Dvorkin et al. (1997)	2.75-112.21mm workpiece thickness; 320-408mm roll radius; 18-40% reduction	Temperature dependent, rigidly-perfect plasticity; friction factor with transition smoothing	Explicit Eulerian plane-strain formulation; based on the flow formulation and the pseudo-concentrations technique	Roll radius ratio; friction ratio; temperature profile; feed offset	Curvature is towards the smaller, lower friction or colder side of the workpiece. Curvature is in the same direction as feed offset.	<i>METFOR</i> software package used.

Reference	Geometry	Material & Friction	Numerical Implementation	Controlled Variables	Key Results	Notes
Richelsen (1997)	0.12 aspect ratio; 10-60% reduction	Aluminium as elastic-viscoplastic; Wanheim et al. (1978) friction model	Explicit time stepping with rate tangent modulus method; 1764 quadrilateral elements each with four triangular linear plane-strain elements	Roll friction; reduction	Curvature is towards the higher friction roll and larger friction asymmetry induces larger curvature. Maximum curvature occurs at 30% reduction.	
Y. Hwang et al. (1999)	6-10mm workpiece thickness; 93-105mm roll radius; 5-30% reduction	Unspecified material behaviour; yield limited Coulomb friction	Plane-strain explicit solver with dynamic remeshing; 500 element workpiece; steady-state termination conditions	Roll speed ratio; roll radius ratio; friction ratio; reduction	Curvature changes sign with reduction for asymmetric size and speed but not friction. Curvature is towards the roll with higher friction.	DEFORM software package used and validated with experiments.
Lu et al. (2000)	5-10mm workpiece thickness; 72.5-204mm rolls; 20-40% reduction	Elastic-plasticity with strain hardening; Coulomb friction	Central difference time stepping; 368 4-node, bilinear, reduced integration, hourglass controlled, plane-strain elements	Roll radius with fixed angular velocity; reduction	Increasing initial thickness increases curvature towards the smaller/slower; increasing reduction increases curvature towards the larger/faster. Curvature changes sign as the roll size increases and thin-sheet curvature is more sensitive to roll size.	Rolls modelled with 179 2-node, linear rigid elements.
Knight et al. (2003)	54.22 and 206mm workpiece thickness; 600mm radius roll; 10-40% reduction	High-temperature low-carbon steel as elastic-plasticity with strain-rate and temperature dependence; sticking Coulomb friction	Explicit time stepping; 800 4-node, bilinear, reduced integration, plane-strain elements	Friction ratio; roll speed ratio; average roll speed; average friction; through-thickness temperature gradient; reduction	Curvature is towards the higher friction roll, but curvature from asymmetric roll speed depends on the roll gap aspect ratio and reduction where the aspect ratio can change the direction of curvature	The reversing rougher of Corus, Port Talbot, hot mill used to test proposed zero curvature regime.

Reference	Geometry	Material & Friction	Numerical Implementation	Controlled Variables	Key Results	Notes
Markowski et al. (2003)	2.22-3.13mm workpiece thickness; 670mm roll; 10-25% reduction	Rigid-plastic with strain, strain-rate and temperature dependence; unspecified friction	Steady-state Eulerian FEM; unspecified discretisation	Roll radius ratio	Curvature is dependent on the roll asymmetry, aspect ratio, relative roll size and material properties.	Complete set-up included in Pietrzyk et al., 1991. The ELROLL software package was used.
Harrer et al. (2003) and Philipp et al. (2007)	28-150mm workpiece thickness; 500mm roll radius; 0-60% reduction	Structural steel S235JRG2 at 1000°C as elasto-plastic with modified Hansel and Spittel stress function; yield limited Coulomb friction	2D implicit time stepping FEM; Unknown number of CPE4 (4-node plane strain) elements.	Roll speed ratio; reduction	Curvature is towards the faster roll for small reductions and towards the slower roll for large reductions. The reduction where the curvature changes direction increases with sheet thickness. Very thick-sheets do not change curvature direction. Larger velocity asymmetry and thinner sheets produce greater curvature.	Qualitative review included. The <i>ABAQUS/Standard</i> software package used.
Kawałek (2004)	2.1-8.3mm workpiece thickness; 320-660mm rolls; 7-40% reduction	Steel as perfect-plasticity with strain-rate and temperature dependence; friction unspecified		Roll size with fixed angular velocity; reduction; workpiece thickness	Curvature is towards the larger/faster roll for small reductions. Curvature increases with larger asymmetry and smaller reductions.	Unspecified numerical method and discretisation but ELROLL and FORGE2 software packages used.
Knight et al. (2005)	54.2-206mm workpiece thickness; 10-40% reduction; 60mm roll radius	Elastic-plasticity with strain, strain-rate and temperature dependence; Coulomb friction	Explicit time stepping; ~800 (geometry dependent) 4-node, bilinear, reduced integration, plane-strain elements	Initial thickness; reduction	Thick-sheets increase curvature with reduction, medium sheets peak curvature and thin-sheets curvature direction changes. Curvature is towards the slower roll with small reductions and towards the faster roll with large reductions. Friction has a bigger influence for curvature towards the faster roll.	Fixed asymmetric roll speed of 0.95. <i>ABAQUS/Explicit</i> software package used.

Reference	Geometry	Material & Friction	Numerical Implementation	Controlled Variables	Key Results	Notes
Farhat-Nia et al. (2006)	5mm thickness; 50-100mm roll radius; 12-40% reduction	Aluminium strip as elastic plasticity with von-Mises yield and isotropic strain-hardening; Coulomb friction	Arbitrary Lagrangian-Eulerian 2D FEM; 800 4-node quadrilateral elements	Roll size; roll speed; reduction	Curvature is towards the larger roll with a maximum at a given aspect ratio; a direction change occurs for some roll geometries and speed ratios.	Generalised ALE code developed by Gadala et al. (2000)
Akbari Mousavi et al. (2007)	2x80mm workpiece; 105mm roll radius; 13-37% reduction	Aluminium 1050P as elastic-plasticity with power-law strain hardening; friction factor limited Coulomb friction	3D explicit time stepping FEM	Roll speed ratio	Curvature is towards the surface with less normal plastic strain. Curvature does not necessarily increase with a larger cross-section region. Curvature also depends on the roll gap aspect ratio.	Discretisation was unspecified. <i>ABAQUS/Explicit</i> software package used; experimental and analytical validation with Y. Hwang et al. (1997)
Anders et al. (2012)	Presented non-dimensionally	Rigid plastic with von Mises yield and associated flow rule; yield limited Coulomb friction	Isoparametric quadrilateral plane-strain elements with linear shape functions	Friction; roll speed; reduction; roll gap aspect ratio	Asymmetric velocity has a stronger affect on curvature than asymmetric friction but is more dependent on geometry, changing the curvature direction in some cases. Comprehensive figures of curvature as roll gap geometry is varied for a range of asymmetries.	Presents a dimensional analysis argument. MARC/MENTAT software package used.
Fu et al. (2012)	200-300x3000mm workpiece thickness; 263.5-412.5mm roll radius; 6-25% reduction	7150 aluminium alloy at 410°C as elasto-plastic material with empirical strain-rate and work hardening; sticking limited Coulomb friction	Four-node plane-strain full integration workpiece elements; rigid analytic rolls and roll table	Roll speed ratio; roll radius; reduction; initial thickness; angle of entry	Curvature increases then decreases with angle of entry. The effect of entry angle depends on workpiece thickness and roll size. Larger velocity asymmetry or larger reduction increases curvature.	MARC/MENTAT software package used. Validated by experiments.

Reference	Geometry	Material & Friction	Numerical Implementation	Controlled Variables	Key Results	Notes
Hao et al. (2013)	2mm workpiece thickness; 240-288mm roll radius; 10-40 % reduction	Q235 Steel as elastic-plasticity with strain hardening; yield limited Coulomb friction	Explicit dynamic, ALE FEM; 4-node bilinear, reduced integration, hourglass controlled, plane-strain elements	Roll size with constant angular velocity; reduction	The cross-shear region increases with roll surface speed ratio. An asymmetric roll size/surface speed exists to produce zero curvature for a given reduction.	<i>ABAQUS/Explicit</i> software package used. Rolls are linear discrete rigid elements. Experimental validation of the model and zero curvature configuration included.
Salganik et al. (2014)	8-50mm workpiece thickness; 575mm radius rolls; 5-40% reduction	Low alloy steel at 800-1000°C as visco-plastic; friction factor		Speed ratio; temperature; initial thickness	Curvature is towards the slower roll for thin-sheets and towards the faster roll for thick-sheets. Temperature and thickness were also found to be factors.	Numerical method and workpiece discretisation unspecified and rigid rolls. <i>DEFORM</i> software package used.

4.1.3 Analytical models

The first publication, found in this review, to predict curvature was Tanaka et al. (1969). This is a semi-empirical model for roll indentation, from which a quadratic distribution of longitudinal residual stress and then curvature is estimated. This paper was published in the Journal of Japanese Institute of Metals and, unfortunately, no translation has been found. Since this, models based on one of three different methods have been proposed; the slip-line method, the upper-bound method and slab approximations.

Slip-line models

Slip line models have been applied to model rolling as early as 1955 (Alexander, 1955). Complex phenomena can be captured with comparatively few calculations, suitable for human and early computers; however, a priori knowledge is required to specify the form of the slip-lines. Two slip-line models of asymmetric rolling (Collins et al., 1975; Dewhurst et al., 1974) were presented before popularity in this area faded. The increasing complexity of these models made further developments increasingly unwieldy. They are also limited to plane-strain, quasi-static processes involving rigid plastic materials.

Dewhurst et al. (1974) generalizes from a symmetric rolling model that was shown to be accurate for specific combinations of reduction and roll gap aspect ratio. A closed form solution of curvature was derived using compatibility conditions in the model but this model is only valid for small asymmetries around this reduction-aspect ratio curve.

Collins et al. (1975) presents a more general slip-line solution. It is formulated using a matrix technique developed, with a *FORTRAN* implementation, in Dewhurst et al. (1973). This technique expands the radius of curvature of each slip-line as a power series in the angular coordinate. A matrix is formed from the relations between slip lines. The rolling problem is then defined by this set of linear equations which must be solved numerically to satisfy twelve force balance and compatibility conditions. This model shows curvature changing sign with varying roll size ratio and roll speed ratio, the only analytical model that does so. It was compared to results from Chekmarev et al. (1956) and produces reasonable quality predictions.

Upper-bound models

The first use of an upper-bound model for curvature prediction was M. Kiuchi et al. (1987). Roll size ratio, roll speed ratio and the workpiece angle of entry were included parameters. Shivpuri et al. (1988) reports that this model agrees well with experimental results over asymmetric roll sizes (Nakajima, 1980, 1984) but poorly over asymmetric roll speed ratios (Dewhurst et al., 1974; W. Johnson et al., 1966a,b).

Y. M. Hwang et al. (1996b) also used an upper-bound model to predict curvature. The flow field is determined by specifying a quadratic stream function within the roll gap and matching this to a stream function of uniform flow. The upper-bound is minimised against three parameters; the flow rate, one of the inlet contact points and a parameter characterising the inner flow. Results are presented over varying roll size ratios showing better agreement than the slip-line model of Dewhurst et al., 1974.

Slab models

Since slab models were first used to predict curvature, in 2002, no fewer than five variations have been published. Generally, these models use assumptions of through-thickness stress or strain distributions to approximate full strain fields, from which predictions of curvature are made using further assumptions about the curvature mechanism.

Salimi et al. (2002) presents the first of these models: a modified slab model that solves a differential equation for the roll pressure on slab elements. Friction factor and the yield condition make this sufficient to solve for the roll-workpiece interface stress distribution. Averaging, with an additional weighting parameter, between the interface and centre-line shears determines the effective stress field of the top and bottom halves of the workpiece. Some justification for the value of this coefficient is provided for a linear through-thickness shear distribution. Curvature is then predicted as the sum of two curvature mechanisms: mean shear strain through the roll gap and differential longitudinal strain between the top and bottom halves of the plate. A comparison was made to results from Buxton et al. (1972); Kennedy et al. (1958); and Shivpuri et al. (1988).

Gudur et al. (2008) presents a model similar to this: curvature is calculated identically to Salimi et al. (2002) but differential equations for average shear elements, pressure on the top surface and pressure on the bottom surface are solved as a system, which allows for asymmetric roll sizes. Strain-hardening behaviour is included and

friction is chosen to be the transition model from Wanheim et al., 1978. The shear stress distribution was taken to be linear, eliminating the additional parameters of Salimi et al. (2002). The curvature model performs well against results from Shivpuri et al. (1988); Y. Hwang et al. (1997); and Salunkhe (2006). This model is then used in an inverse problem: predicting the friction coefficients from observed curvature.

Gong et al. (2010), like Salimi et al. (2002), derives a single differential equation for horizontal stress through the roll gap using Coulomb friction. A roll torque estimate is then made for the top and bottom rolls and the resulting moment balance is satisfied with a moment assumed to be applied to the outlet workpiece. This model is appealing as it is dependent on both the yield stress and Young's modulus, factors known to be relevant from the previous review sections, but is questionable as elastic bending is assumed to be the sole mechanism of curvature. It is not compared to numerical or experimental results.

Qwamizadeh et al. (2011) presents a model similar to Gudur et al. (2008), except with Coulomb friction, no hardening behaviour and a more complex through-thickness shear profile. The form of the shear stress is assumed to be quadratic through-thickness, where the three coefficients are chosen to satisfy the yield stress condition on the top and bottom surfaces and the mean shear stress from the differential equations.

Farhatnia et al. (2011) presents a model including a hardening elastic-plastic material and a friction factor law. Three differential equations are solved explicitly for the shear force, the mean tension in the strip and the bending moment. Curvature was calculated from the same two mechanisms presented in Salimi et al. (2002), only the axial component was calculated from elastic and plastic deformations due to bending moments. Curvature results were not compared to simulation or experiment.

Aboutorabi et al. (2016) attempts to treat non-vertically aligned contact points in a manner similar to the work presented in Chapter 6. A differential equation is solved with a flat free surface and no traction force over an inlet region where the workpiece contacts one roll only. The curvature calculation includes an additional bending to the two mechanisms identified by Salimi et al. (2002) due to the region with a free surface. This matches moderately well to finite element simulations presented in this study.

4.2 Numerical comparison

It is clear from the previous section that the relationship between the rolling configuration and curvature is complex and existing analytical models have not been

validated over very large parameter spaces. A qualitative description of the observed trends is insufficient due to the interaction between parameters. This has resulted in contradictory conclusions from studies on this subject. The data from fifteen studies have been digitised and collectively analysed to reconcile these conclusions, provide a more holistic view of the process and identify key parameters or interactions that drive curvature.

To improve comparability, the curvatures are non-dimensionalised by the workpiece thickness throughout the following analysis. Workpiece thickness was chosen because it is the only other local and intrinsic dimension in plane-strain rolling.

4.2.1 Data collection

Digitisation was conducted using an online application¹ after digitally extracting the figures from each publication. The publications used were those that included sufficient detail to reproduce the work; those not specifying sufficient detail to determine the workpiece thickness, roll gap aspect ratio, workpiece reduction, friction ratio, roll speed ratio, roll size ratio, yield stress and Young's modulus were omitted. Many publications did not quantify the curvature results, present the quantified values, or provide the detail required so ultimately only four papers with experimental results (Buxton et al., 1972; Dewhurst et al., 1974; W. Johnson et al., 1966a,b) and eleven papers with numerical results (Akbari Mousavi et al., 2007; Farhat-Nia et al., 2006; Hao et al., 2013; Kawalek, 2004; Knight et al., 2003, 2005; Lu et al., 2000; Philipp et al., 2007; Shivpuri et al., 1988; J. Yang et al., 2017) were digitised for a total of 1130 data points.

Workpiece-roll surface friction model

There is no obvious comparison between friction metrics. Friction factor and Coulomb friction coefficients require a pressure estimate and yield stress to compare and experimental studies typically report surface roughness, which has even greater dependence on unknown parameters such as the roll material and workpiece surface finish.

This problem is made easier by considering a ratio of friction effects only. Friction factor and Coulomb friction coefficients are non-dimensional making a ratio of these meaningful. Yield limited Coulomb friction, transitioning to friction factor when Coulomb friction exceeds the yield condition, complicates a simple ratio and is common with simulations. The ratio of Coulomb friction coefficients will be used for this work

¹www.arohatgi.info/WebPlotDigitizer/app/

as friction is rarely limited in cold rolling and the friction factor model is often used in hot rolling simulations.

Surface roughness remains a challenge as the relation between surface roughness and friction effects is highly non-linear. It would be possible to treat each experimental configuration of friction as a categorical variable, which would effectively fit a friction coefficient to each group of data; however, the limited size of this dataset makes this approach susceptible to overfitting given the large number of configurations. This would be especially egregious if material properties are treated similarly.

A more systematic solution can be found for most cases as force and torque results are often also presented. The inverse of analytical models for torque can be used to estimate friction coefficients (Gudur et al., 2008). Specifically, the slab model presented in Salimi et al. (2002) was used to determine friction factor coefficients. The coefficients derived from each torque data point of a given experimental configuration were averaged for final coefficients before taking the ratio.

Table 4.3 Assumed friction ratios

Paper (Roll roughness top/bottom in μm)	Friction ratio estimate
W. Johnson et al. (1966a) (0.43/0.025)	2.5
W. Johnson et al. (1966b) (0.64/0.43)	1.77
W. Johnson et al. (1966b) (3.05/0.43)	4.17

Ultimately, this process was only applied to W. Johnson et al. (1966a) and W. Johnson et al. (1966b) as Jeswiet et al. (1998) did not present torque results and other works have symmetric friction conditions. The ratio of friction coefficients used for each case are presented in Table 4.3. These results seem reasonable: the magnitudes are congruent with the simulation data and the non-linearity discussed previously means non-monotonicity is plausible. Of course, the quality of these results depends on the accuracy and sensitivity of the torque predictions over the range of parameters within the regression. This is difficult and time consuming to determine so these values are used knowing the impact this may have on the regression.

Material model parameterisation

A similar issue arose for estimating material parameters: materials are difficult to compare when strain rate hardening, work hardening and temperature dependence are significant. An ideal approach would be to estimate the effective yield stress within the roll gap; however, there is insufficient information in each publication to reconstruct

the experiments with this detail, even if the computation were feasible. Parameterising hardening curves alleviates the need for computation but results in excessive parameters for the regression and overfitting. Alternatively, workpiece material could be treated as a categorical variable; however, this also faces the issue of overfitting.

The parameter space was reduced by taking the ratio of yield stress and Young's modulus, which is dimensionally justified. A nominal yield stress value was chosen for the hardening materials and values were chosen from available datasets for studies where only the material name was given. These are specified in Table 4.4 where E is the Young's modulus and σ_{eff} is the effective yield stress, converted to shear in the table.

Table 4.4 Assumed material values

Paper	Material Name	$\sigma_{\text{eff}}/\sqrt{3}$ (MPa)	E (GPa)
W. Johnson et al. (1966a)	Tellerium lead	$8.66e6$ ¹	14.0 ²
W. Johnson et al. (1966b)	Tellerium lead	$8.66e6$ ¹	14.0 ²
Buxton et al. (1972)	Plasticine	0.88	0.003 ³
Dewhurst et al. (1974)	Pure commercial lead	8.08 ⁴	13.8 ⁵
Collins et al. (1975)	Steel	62.1 ⁵	200 ⁶
Shivpuri et al. (1988)	Mild steel	62.1 ⁵	200.0 ⁵
Lu et al. (2000)	Steel C15	98.2	550.0 ⁶
Knight et al. (2003)	Low carbon steel	43.3	76.0
Markowski et al. (2003)	Steel 05XA	115.0 ⁷	200.0 ⁷
Kawałek (2004)	110-coded grade steels	115.5 ⁷	200.0 ⁷
Knight et al. (2005)	Hot low carbon steel	34.6	76.0
Farhat-Nia et al. (2006)	Unspecified	29.0	68.0
Philipp et al. (2007)	Steel S235JRG2	19.2	985.0 ⁸
Akbari Mousavi et al. (2007)	Aluminium 1050P	72.2 ¹	71.0 ¹
Hao et al. (2013)	Q235 Steel	138.6	210.0
J. Yang et al. (2017)	Aluminium AA7050	155.0	70.0

¹ www.azom.com² www.ascelibrary.org³ Sofouoglu and Rasty, (2000). Flow behavior of Plasticine used in physical modeling of metal forming processes. Tribology International.⁴ www.ila-lead.org⁵ www.wikipedia.com⁶ www.matbase.com⁷ www.matweb.com⁸ www.steel-grades.com

Many of the materials have a wide range of values for both the yield stress and Young's modulus. This will result in noise within the results of the statistical analysis and produce a poorer fit for any regression.

Logging asymmetric parameters and material properties

The three asymmetric parameters: roll radius ratio, roll speed ratio and surface friction ratio; are presented as ratios in most literature. This places the symmetric case at unity and obfuscates the vertical symmetry of the process. Logging each asymmetric ratio moves the symmetric case to zero and captures the vertical symmetry as an anti-symmetric function in these three variables.

The form of the other parameters are less obvious. The ratio of yield stress to Young's modulus and the roll gap aspect ratio could also be logged as ratios; it is unclear if the inverse of either group should be used instead. Similarly, the reduction could be expressed as a ratio of inlet to outlet thicknesses, $1 - r$. Logging this ratio has the added appeal of zero reduction, causing zero curvature, also being at the origin.

4.2.2 Initial observations

Plotting these results provides rudimentary insight into the underlying trends. Curvature against each of the three asymmetries is plotted in Figure 4.1 with the two geometric and one material parameters indicated by colour. Curvature towards the slower roll is the only trend that can be discerned from these plots. A trend of curvature towards the smaller roll might also be present but this is not a strong trend. It also appears that reduction might be able to reverse curvature under all three asymmetries and the roll gap aspect ratio could increase curvature from roll surface speed ratios and friction ratios.

A clear set of extreme curvature values are also apparent. These correspond to low yield stress to Young's modulus ratios from plasticine experiments. It is initially unclear whether these data should be excluded as outliers; their extreme curvature values could distort the analysis, but including them could increase the parameter range and improve accuracy. Ultimately, the plasticine data were included as regression models that included the material parameter reasonably accounted for them without dramatically altering any trends.

Figure 4.2 presents the data by publication and grouped by studies that investigate the asymmetry on the horizontal axis. The extreme curvature values can be identified as the results of Buxton et al. (1972). These experiments were the only non-metal experiments, which explains the unusual behaviour of these data. This figure also reveals some more detailed trends, such as non-linearity in the roll radius ratio and a strong interaction between the surface speed ratio and another parameter, found

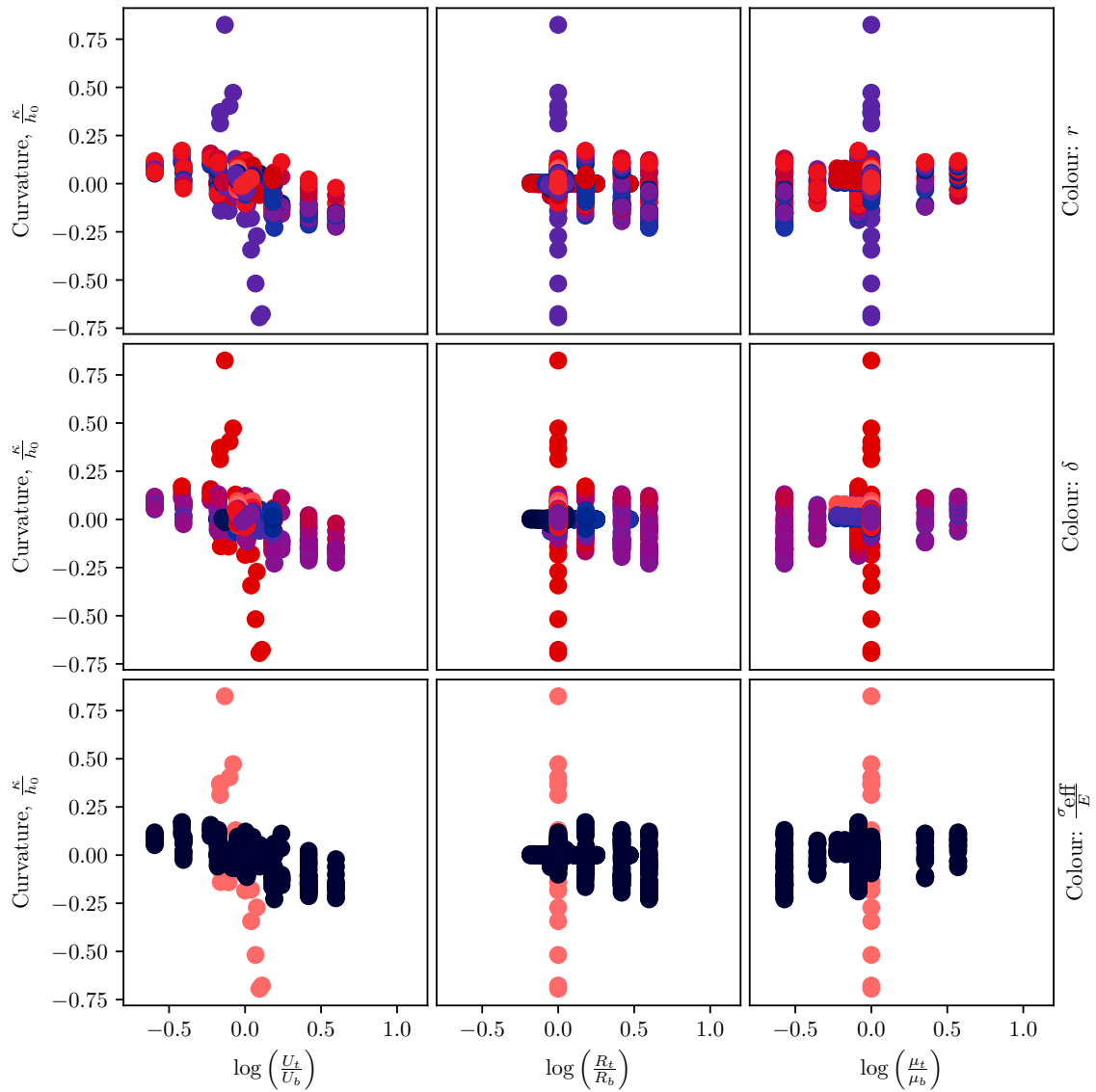


Fig. 4.1 Digitised curvature results against roll surface speed ratio (left), roll radius ratio (centre) and friction ratio (right) with colour indicating reduction (top), roll gap aspect ratio (centre) or the yield stress to Young's modulus ratio (bottom).

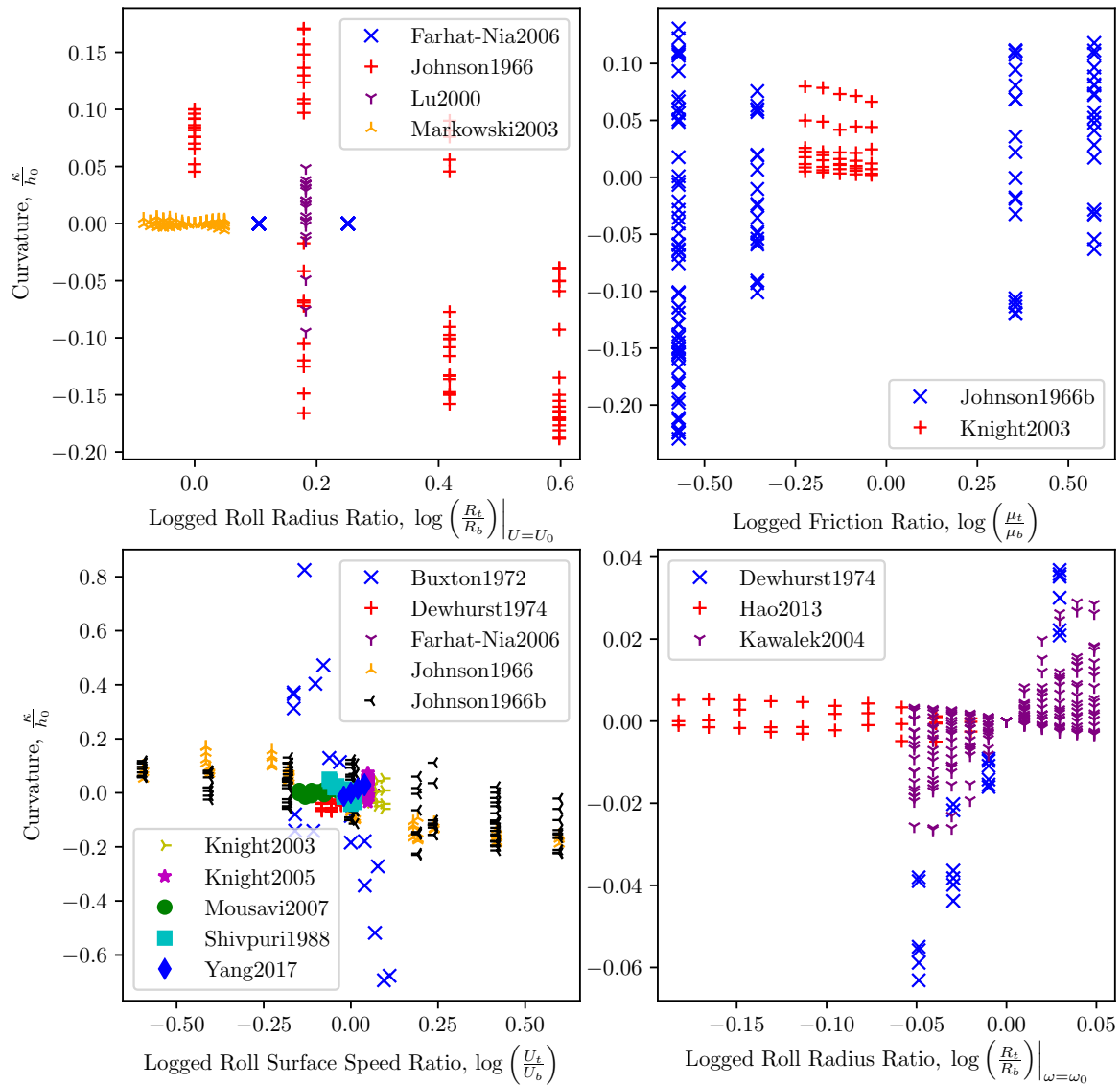


Fig. 4.2 Digitised curvature results against roll size ratio with fixed surface speed (top left), friction ratio (top right), roll surface speed ratio (bottom left) and roll size ratio with fixed rotation rate (bottom right), and grouped by publication.

to be reduction, in Knight et al. (2003). Unfortunately, most of the trends involving interacting parameters only present in individual studies, which may lead to the same contradictions found in the qualitative review.

Statistical analyses are performed in the following sections to find trends that unify these individual studies and gain more insight about the overall behaviour of curvature.

4.2.3 Linear regressions models

Linear regression is applied to these data with generally poor results; however, some qualitative insight can be gained from the process.

The inherent vertical symmetry is exploited in all the regression models; only taking terms with odd powers of the logged asymmetric ratios and setting the constant to zero ensures the correct anti-symmetric response in these three terms.

The simplest possible model that satisfies this condition regresses over the three logged asymmetries. As expected, this model performs very poorly and captures none of the non-linearity. Example trends of this model over each asymmetry are presented in Figure 4.3. The other parameters used are indicative of the values found in the digitised data. The error bars denote the magnitude of the residuals of the model with the digitised data, which show the errors are far greater than the predicted curvature. The adjusted R-squared value, the percent of variation in the data explained by the model adjusted for the complexity of the model, is 0.40, which corroborates the poor performance of this model. This is unsurprising given the known complexity of the problem, such as the outlier dataset, Buxton et al. (1972), depending so significantly on the material parameter.

A layer of complexity is added by multiplying each asymmetry by the material parameter, the roll gap aspect ratio and the reduction. This increases the adjusted R-squared value to 0.52 with only twelve degrees of freedom. Figure 4.4 shows similar trends to Figure 4.3, only the friction asymmetry trend is inverted, and some noticeably reduced residuals.

Logged non-asymmetric terms, including the log of one minus the reduction, were also tested. Marginally worse results were produced so the unlogged terms continue to be used for the following models.

Cubic asymmetric terms were then introduced to account for the strong non-linear behaviour observed in the literature review and initial observations. This model, illustrated in Figure 4.5, shows non-linearity, noticeably smaller residuals and an adjusted R-squared value of 0.68. However, this model fits 49 degrees of freedom so is

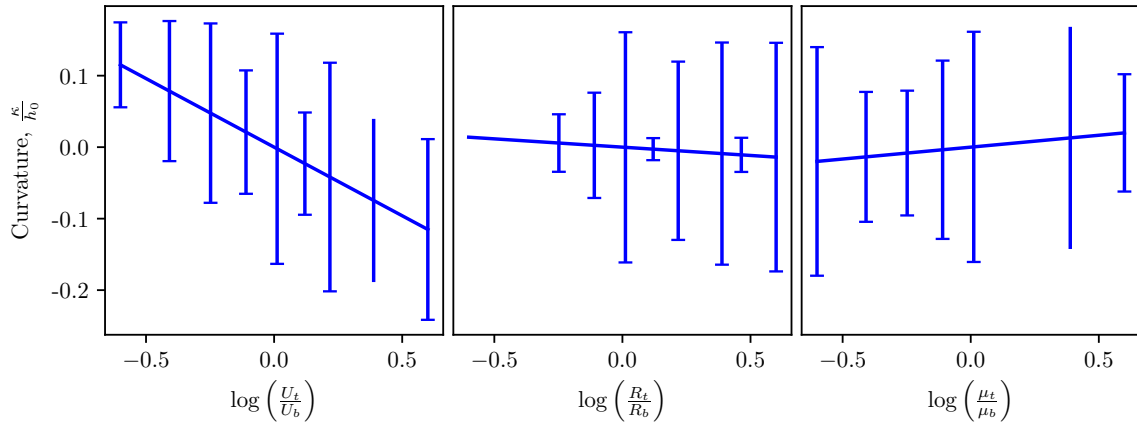


Fig. 4.3 Curvature predictions by the regression model with linear asymmetric terms only. The error bars denote the magnitude of residuals of this model. The rolling set-up is defined by $(\delta, r, \frac{\sigma_Y}{E}) = (0.3, 0.2, 0.00056)$ and asymmetries in roll surface speed (left), roll size (centre) and friction (right).

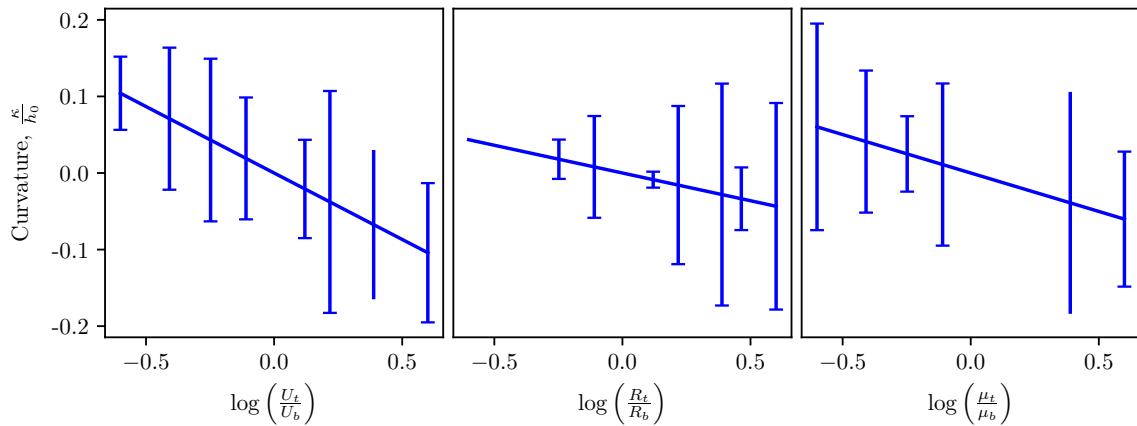


Fig. 4.4 Curvature predictions by the regression model with linear asymmetric terms multiplied by the material parameter, roll gap aspect ratio and reduction. The error bars denote the magnitude of residuals of this model. The rolling set-up is defined by $(\delta, r, \frac{\sigma_Y}{E}) = (0.3, 0.2, 0.00056)$ and asymmetries in roll surface speed (left), roll size (centre) and friction (right).

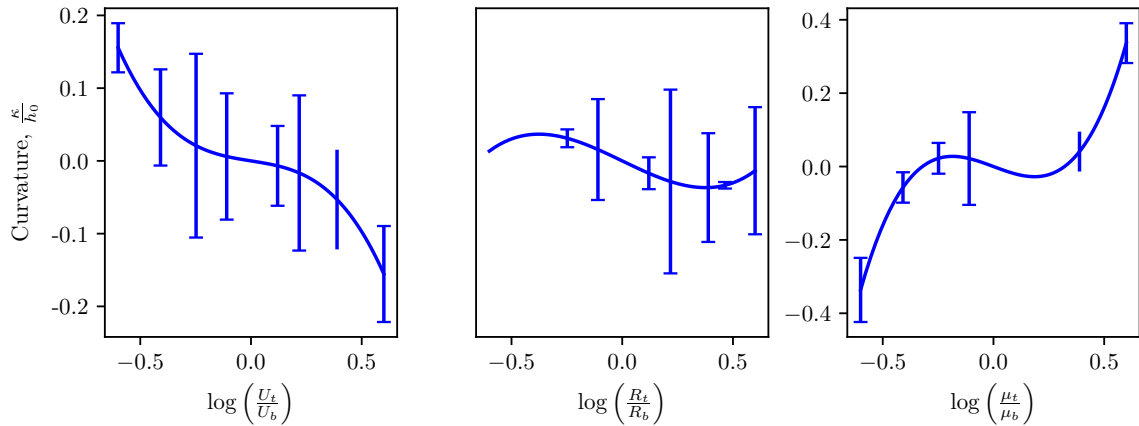


Fig. 4.5 Curvature predictions by the regression model with linear and cubic asymmetric terms multiplied by the material parameter, roll gap aspect ratio and reduction. The error bars denote the magnitude of residuals of this model. The rolling set-up is defined by $(\delta, r, \frac{\sigma_Y}{E}) = (0.3, 0.2, 0.00056)$ and asymmetries in roll surface speed (left), roll size (centre) and friction (right).

likely to be overfitted, fitted to the specific data and not the underlying trend due to insufficient data for the model's degrees of freedom.

Other models, using selected subsets of the cubic terms, were also tried but none performed noticeably better than the others, indicating that any individual term is not capturing the underlying trend significantly more than the others. This supports the overfitting hypothesis.

One final model was produced to capture the maximum variation in the data with the fewest number of parameters. This was achieved by incrementally eliminating terms from the previous model with the greatest probability of its coefficient being zero, p-value. After each term was removed, the regression was rerun and another term removed until all the terms had probabilities of being zero of less than 0.01%. The resulting model had an adjusted R-squared value of 0.65 with fifteen degrees of freedom. The trends and residuals are presented in Figure 4.6 and the final form of

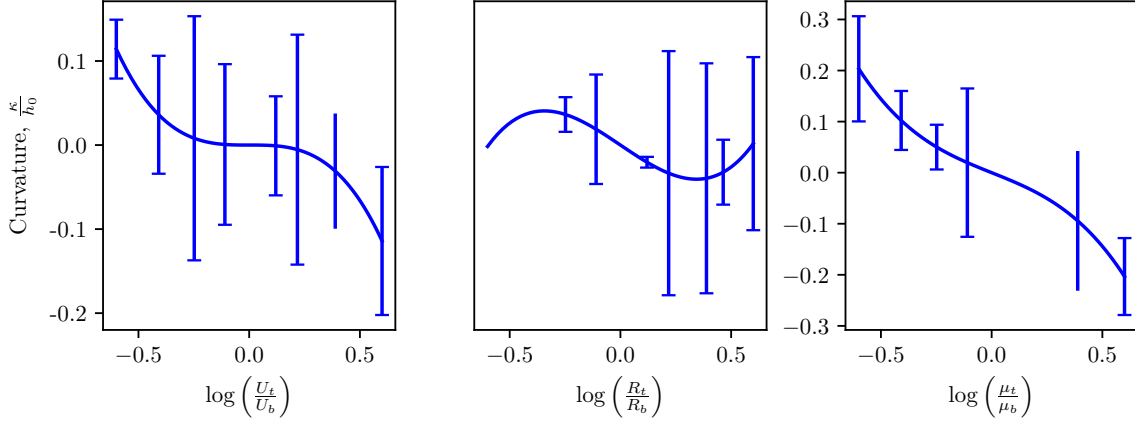


Fig. 4.6 Curvature predictions by the regression model with linear and cubic asymmetric terms multiplied by the material parameter, roll gap aspect ratio and reduction where the probability of the associated coefficient being zero is less than 0.01%. The error bars denote the magnitude of residuals of this model. The rolling set-up is defined by $(\delta, r, \frac{\sigma_Y}{E}) = (0.3, 0.2, 0.00056)$ and asymmetries in roll surface speed (left), roll size (centre) and friction (right).

the regression is

$$\begin{aligned}
\kappa = & A_0 \log\left(\frac{\mu_t}{\mu_b}\right) + A_1 \log\left(\frac{R_t}{R_b}\right) + A_2 \frac{\sigma_Y}{E} \log\left(\frac{\mu_t}{\mu_b}\right) + A_3 \delta \log\left(\frac{R_t}{R_b}\right) + A_4 \delta \left(\log\left(\frac{R_t}{R_b}\right)\right)^3 \\
& + A_5 \delta \left(\log\left(\frac{U_t}{U_b}\right)\right)^3 + A_6 r \log\left(\frac{R_t}{R_b}\right) + A_7 \log\left(\frac{R_t}{R_b}\right) \left(\log\left(\frac{\mu_t}{\mu_b}\right)\right)^2 \\
& + A_8 \delta \log\left(\frac{R_t}{R_b}\right) \left(\log\left(\frac{\mu_t}{\mu_b}\right)\right)^2 + A_9 \delta \log\left(\frac{R_t}{R_b}\right) \left(\log\left(\frac{U_t}{U_b}\right)\right)^2 \\
& + A_{10} \delta \log\left(\frac{U_t}{U_b}\right) \left(\log\left(\frac{R_t}{R_b}\right)\right)^2 + A_{11} r \log\left(\frac{R_t}{R_b}\right) \left(\log\left(\frac{U_t}{U_b}\right)\right)^2 \\
& + A_{12} \frac{\sigma_Y}{E} \log\left(\frac{R_t}{R_b}\right) \left(\log\left(\frac{\mu_t}{\mu_b}\right)\right)^2 + A_{13} r \log\left(\frac{U_t}{U_b}\right) \left(\log\left(\frac{R_t}{R_b}\right)\right)^2 \\
& + A_{14} \frac{\sigma_Y}{E} \log\left(\frac{R_t}{R_b}\right) \left(\log\left(\frac{U_t}{U_b}\right)\right)^2 + A_{15} r \log\left(\frac{\mu_t}{\mu_b}\right) \log\left(\frac{R_t}{R_b}\right) \log\left(\frac{U_t}{U_b}\right) \quad (4.1)
\end{aligned}$$

While this model is still likely to be overfitted, it is reasonable to assume that the terms that remain indicate trends which may be significant to the problem.

This model should not be used for prediction, but does indicate a noteworthy parameter space. This is useful for guiding future investigations and model validation.

This equation can be rearranged to provide different insights. Specifically, it can be seen that there is strong interaction between the three geometric variables: reduction, roll gap aspect ratio and the roll radius ratio.

For example, $(r + \delta) \left(\log \left(\frac{R_t}{R_b} \right) + \log \left(\frac{U_t}{U_b} \right) \log \left(\frac{R_t}{R_b} \right)^2 + \log \left(\frac{U_t}{U_b} \right)^2 \log \left(\frac{R_t}{R_b} \right) \right)$ can be factored from these terms. It can also be seen that the friction ratio has less interaction than the other asymmetries but shows the greatest interaction with the material parameter.

More details of these regression models can be found in Appendix C.

4.2.4 Lasso regression models

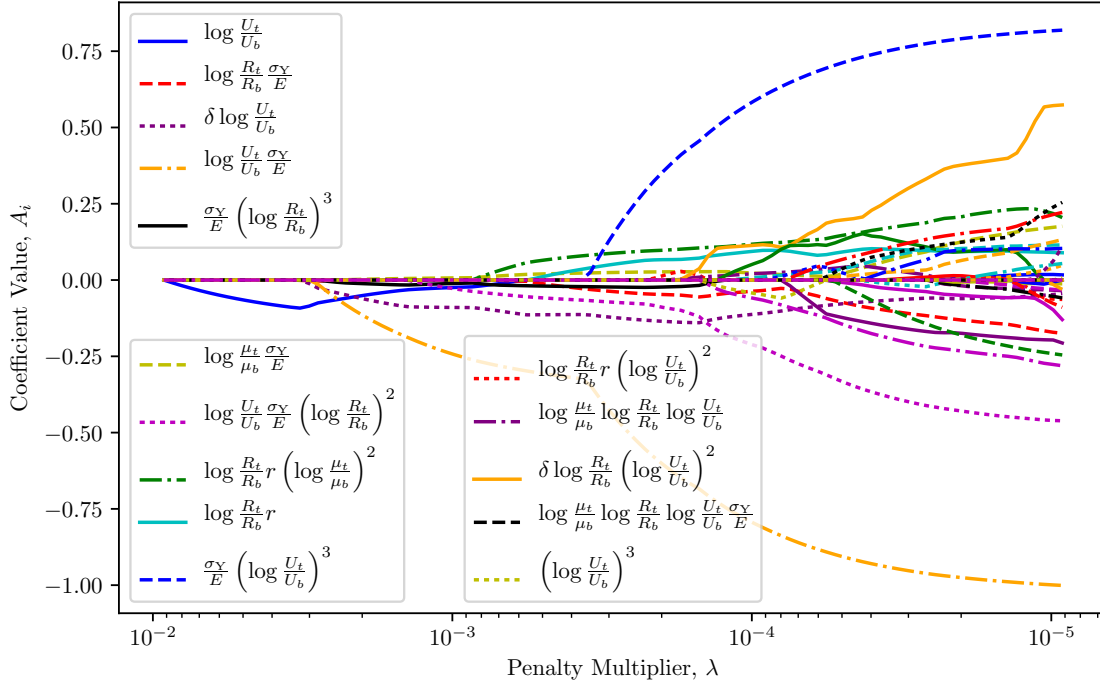
Lasso regression is a modern regression technique that penalises non-zero coefficients to discourage overfitting and perform better with fewer data points or more regressors, such as the cubic case in the previous section. It can be written in the Lagrangian form as

$$\min_{\beta \in \mathbb{R}^p} \left\{ \frac{1}{N} (y - X \cdot \beta)^2 + \lambda |\beta| \right\} \quad (4.2)$$

where y is the dependent variable, X is the vector of independent variables, β is the vector of coefficients and λ is the selected penalty to the L1 norm of the coefficient vector, $|\beta|$. Setting the multiplier to zero returns a regular regression result, but increasing it will eliminate the next least significant coefficient.

Lasso regression is commonly used with cross validation, a process of regressing over a subset of the data and checking the performance of the resulting model against the out of sample data, to find an optimal value of λ . This resulted in high values of λ and only three variables included in the regression. The performance of these models were also sensitive to the sub-set of data selected, possibly due to the structured nature of the data or the small size of the dataset. This might be resolved by manually subdividing the data to ensure both subsets are representative of the data as a whole; however, this was not undertaken as the poor regressions in the previous chapter suggest the models here would be equally poor.

An alternative use of Lasso regression is to start with a sufficiently high penalty to eliminate all variables then reduce the penalty to incrementally introduce new variables. The coefficients generated for different values of λ are plotted in Figure 4.7 and Table 4.5 shows the value of λ at which each coefficient becomes non-zero, for λ greater than 1×10^{-4} . This indicates which terms are most significant to the problem. The data for each term was normalised for this process to ensure fair penalisation. For example, without normalisation the material property, with small values, would be excluded because their large coefficient would be penalised far more than other coefficients.

Fig. 4.7 Lasso regression coefficients for decreasing λ .Table 4.5 Regressors and penalty multiplier value when the corresponding coefficient becomes non-zero for multiplier values greater than 1×10^{-4}

Regressor	λ	Regressor	λ
$\log\left(\frac{U_t}{U_b}\right)$	0.00919	$\log\left(\frac{R_t}{R_b}\right) \frac{\sigma_Y}{E}$	0.00323
$\delta \log\left(\frac{U_t}{U_b}\right)$	0.00301	$\log\left(\frac{U_t}{U_b}\right) \frac{\sigma_Y}{E}$	0.00281
$\frac{\sigma_Y}{E} \left(\log\left(\frac{R_t}{R_b}\right)\right)^3$	0.00281	$\log\left(\frac{\mu_t}{\mu_b}\right) \frac{\sigma_Y}{E}$	0.00244
$\log\left(\frac{U_t}{U_b}\right) \frac{\sigma_Y}{E} \left(\log\left(\frac{R_t}{R_b}\right)\right)^2$	0.0014	$\log\left(\frac{R_t}{R_b}\right) r \left(\log\left(\frac{\mu_t}{\mu_b}\right)\right)^2$	0.000857
$\log\left(\frac{R_t}{R_b}\right) r$	0.000526	$\frac{\sigma_Y}{E} \left(\log\left(\frac{U_t}{U_b}\right)\right)^3$	0.000346
$\log\left(\frac{R_t}{R_b}\right) r \left(\log\left(\frac{U_t}{U_b}\right)\right)^2$	0.000212	$\log\left(\frac{\mu_t}{\mu_b}\right) \log\left(\frac{R_t}{R_b}\right) \log\left(\frac{U_t}{U_b}\right)$	0.000185
$\delta \log\left(\frac{R_t}{R_b}\right) \left(\log\left(\frac{U_t}{U_b}\right)\right)^2$	0.000172	$\log\left(\frac{\mu_t}{\mu_b}\right) \log\left(\frac{R_t}{R_b}\right) \log\left(\frac{U_t}{U_b}\right) \frac{\sigma_Y}{E}$	0.000172
$\left(\log\left(\frac{U_t}{U_b}\right)\right)^3$	0.00015	$\delta \log\left(\frac{R_t}{R_b}\right)$	0.00014
$\log\left(\frac{R_t}{R_b}\right) \left(\log\left(\frac{U_t}{U_b}\right)\right)^2$	0.00013	$\log\left(\frac{\mu_t}{\mu_b}\right) r$	0.000113

These results corroborate some of the observations made at the end of the previous section. Specifically, $(r + \delta)(R + U^2R)$, $\sigma\mu$ and δR are the six terms shared between both analyses. More generally, the complex interaction of the roll radius ratio and all other parameters is borne out in this model, if not more so. Much of this relates the roll radius ratio with both other geometric factors. Contrary to the previous analysis, the material parameter shows more interaction generally; although, less interaction with the friction ratio specifically.

4.2.5 Non-parametric regression

Assorted non-parametric regression techniques were tested; including kernel regression, decision trees and neural networks. These models are particularly susceptible to overfitting given their high degrees of freedom; the current data set is likely too small. Cross validation, fitting the model to a subset of the data and checking the performance against the out-of-sample data, was used to test for overfitting. High variability in the quality of fitting to the out of sample data suggested that these models were sensitive to which data were included in the fitting and, hence, were overfitting. Further, the complexity of these models introduced other limitations: it was challenging to enforce anti-symmetry or other form into these models.

The complexity, and such poor fitting, means it is unlikely that meaningful insight can be distilled from these models. Given this, non-parametric regression techniques were not pursued further. With a large undertaking of simulations to generate more data, these could capture the non-linear trends observed but, due to their complexity, it is unlikely they could be queried in a way to infer the important dynamics that induce curvature.

4.3 Analytical models

Now that a dataset has been collected, more comprehensive assessment of the predictive power of the analytical models can be made. Two predictive models have been successfully implemented: Dewhurst et al. (1974) and Salimi et al. (2002); and several others investigated but found to have errors or insufficient detail to complete their implementation. Implementation details and plots showing predicted trends and residuals are given for both implemented models.

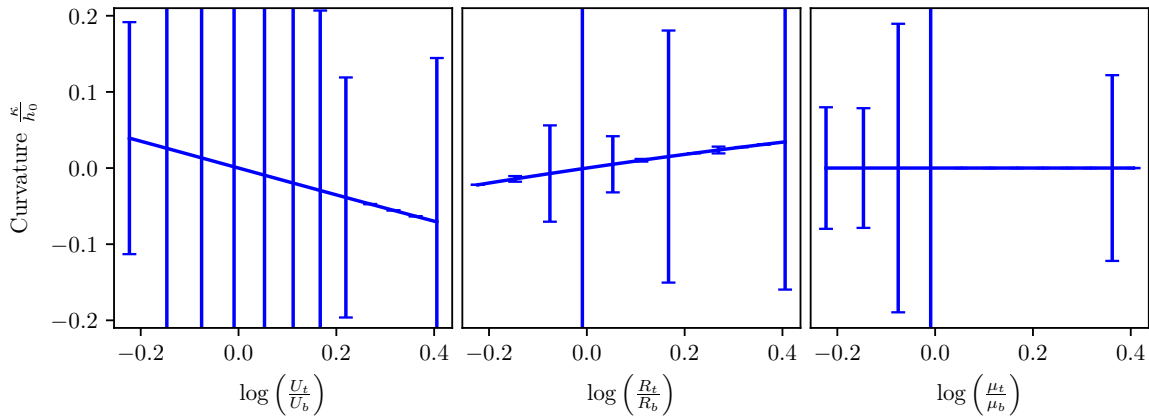


Fig. 4.8 Curvature predictions by the Dewhurst et al. (1974) model. The error bars denote the magnitude of error between this model and the digitised dataset. The rolling set-up is defined by $(\delta, r, \frac{\sigma_Y}{E}) = (0.3, 0.2, 0.00056)$ and asymmetries in roll surface speed (left), roll size (centre) and friction (right).

Dewhurst et al. (1974)

This model was easily implemented as the expression for the radius of curvature is given in closed form, specifically equation (5) (Dewhurst et al., 1974). Sticking is assumed between the workpiece and roll so the friction coefficients are unused in the model, limiting its performance on this dataset.

Figure 4.8 shows the trends and residuals of this model. The parameters are the same ones used to illustrate the regression models. The trends over the roll speed ratio agree with the various regression models; however, the trends over the roll radius ratio are generally the opposite and no curvature is predicted by asymmetric friction because of the sticking friction model. There is also no indication of non-linear trends, unsurprising given the form of this solution and the limiting range of validity.

Y. Hwang et al. (1996a)

The Y. Hwang et al. (1996a) upper-bound model was also investigated. Finding where the inner and outer flow fields intersect is a key step in solving this model as it is where the rigid flow stops and plastic deformation begins. The flow fields are determined by three parameters: a flow rate and two parameters that determine the shape of the flow field inside the roll gap. The contact position, the flow rate, and one of these two shape parameters are used to minimise the deformation power. The value of the second shape parameter is specified only by the statement from the paper, "[The second parameter]

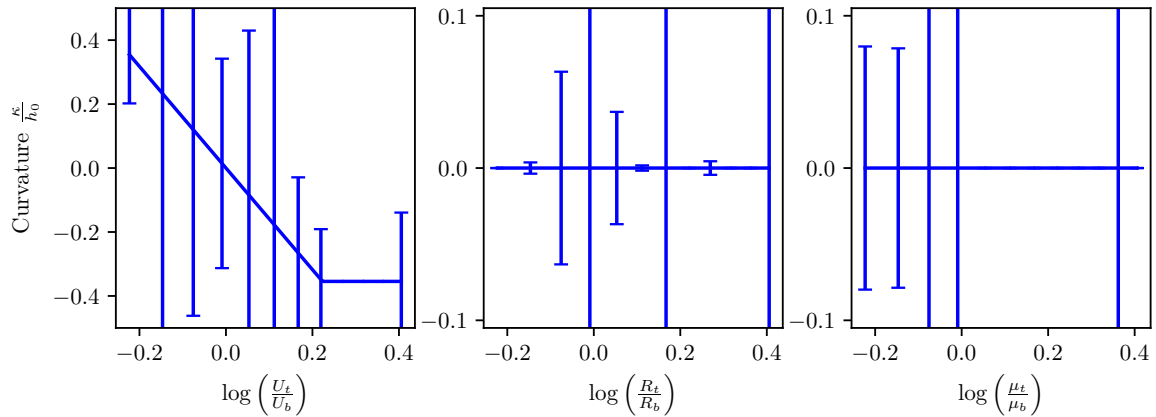


Fig. 4.9 Curvature predictions by the Salimi et al. (2002) model. The error bars denote the magnitude of error between this model and the digitised dataset. The rolling set-up is defined by $(\delta, r, \frac{\sigma_Y}{E}) = (0.3, 0.2, 0.00056)$ and asymmetries in roll surface speed (left), roll size (centre) and friction (right).

must be restricted to ensure that the rigid-plastic boundary, Γ_s , is a continuous curve." It is not clear what condition should be enforced or what value the second parameter should take to satisfy this statement. The author was contacted but was unable to provide further clarification and several obvious choices, such as zero or unity, were trialled for no angle of entry but both showed discontinuous boundaries between the flow fields.

Salimi et al. (2002)

The Salimi et al. (2002) model is a comparatively simple slab model and the solution shows similarities to the asymptotic solution presented in Chapter 2. The method of predicting curvature proposed in Salimi et al. (2002) could therefore be applied to the asymptotic models presented in this work. Unfortunately, two issues were encountered when implementing the model. First, a friction factor coefficient of unity on both roll surfaces leads to a division by zero and the resulting curvature tends to infinity in this limit. Second, it was found that Figure 11 (Salimi et al., 2002) could only be reproduced by including curvature contributions from the mean shear calculation. Contributions from the longitudinal strain terms were orders of magnitude larger. Hence, only the mean shear contributions are used throughout this document when referring to curvature predictions by the Salimi et al. (2002) model.

Figure 4.9 shows this model correctly predicting the trend direction over asymmetric roll surface speed with a plateau after some ratio, a consequence of the neutral point

behaviour. This demonstrates some non-linearity, although not as complex as that observed in the data. There is also no significant change to curvature as a result of the roll radius or friction asymmetries.

Qwamizadeh et al. (2011)

The form of the shear stress distribution in Qwamizadeh et al. (2011) is assumed to be quadratic in y , $\tau_{xy} = A(x) + yB(x) + y^2C(x)$ where $A(x)$, $B(x)$ and $C(x)$ are determined by three conditions: the top surface being at yield, the bottom surface being at yield and the mean shear determined by the differential equation. That is, equation(28),

$$\begin{aligned}\tau_{xy}|_{y=h_u} &= -\tau_u + (\sigma_u - p_u)\tan(\theta_u) \\ \tau_{xy}|_{y=h_l} &= \tau_l + (\sigma_l - p_l)\tan(\theta_l) \\ \text{and} \quad \int_{-h_l}^{h_u} \tau_x y dy &= \tau h,\end{aligned}$$

with nomenclature from the paper. Unfortunately, the friction conditions and quoted yield relation for the roll surfaces were found to result in an inconsistency. These conditions are

$$\begin{aligned}\tau_u &= m_u k \\ \tau_l &= m_l k \\ p_u &= \sigma_u + 2 \frac{-\tau_u \tan(\theta_u) + \sqrt{k^2 - \tau_u^2}}{1 + \tan^2(\theta_u)} \\ \text{and} \quad p_l &= \sigma_l + 2 \frac{\tau_l \tan(\theta_l) + \sqrt{k^2 - \tau_l^2}}{1 + \tan^2(\theta_l)}.\end{aligned}$$

Making these substitutions results in the shear stress exceeding the yield stress for high values of m ; for example, taking $m = 1$ produces $\tau_{xy} = -k(1 + 2\sin(\theta_u)\cos(\theta_u))$ on the top surface. These may be typographical errors or nomenclature confusion, but the model was not included in this study due to this confusion.

4.3.1 Comparison to the Markowski et al. (2003) simulation results

The performance of each of the implemented models, including the final linear regression model, was tested using the results of Markowski et al. (2003). These data were chosen because they are a particularly interesting set. They illustrate a transition of curvature direction over two parameters as well as a transition from linear to non-linear behaviour as reduction varies.

The predictions from each model is presented, with the original simulation data, in Figure 4.10. The regression model reasonably predicts the results for small reductions; however, the gradient change due to reduction is not captured, let alone the change from linear to non-linear behaviour. The Dewhurst et al. (1974) model predicts a gradient more correct for larger reductions and the magnitude of the curvature predictions are over ten times too small to quantitatively predict the simulated results. Finally, as expected from the previous sections, the Salimi et al. (2002) model does not predict any curvature from asymmetry in the roll radii. Clearly none of these models are able to predict curvature overall.

4.4 Hybrid methods

Given the accuracy of force and torque predictions made in Chapter 2, it would be reasonable to include this information in a regression model. Similarly, the curvature predictions from the analytical models could plausibly be included, effectively regressing over the residuals of those models. This would capture the non-linear behaviour of the models in a linear regression. For example, the plateaus caused by the neutral point reaching either end of the roll gap could be one of several trends combined in a regression model.

Force and torque are included as total force, force ratio, and torque ratio where the ratios are logged for the same reasons as the three asymmetric ratios. The predictions are made using either the Salimi et al. (2002) model or the leading order solution from Chapter 2 whether friction factor or Coulomb friction coefficients were available.

Beginning with all linear and cubic terms as well as the new force and torque terms, a model with an adjusted R-squared value of 0.78 is produced with fifty degrees of freedom. While this may seem like a large improvement, only 647 data can be used due to more parameters being required by the analytical models. It will, therefore, be more

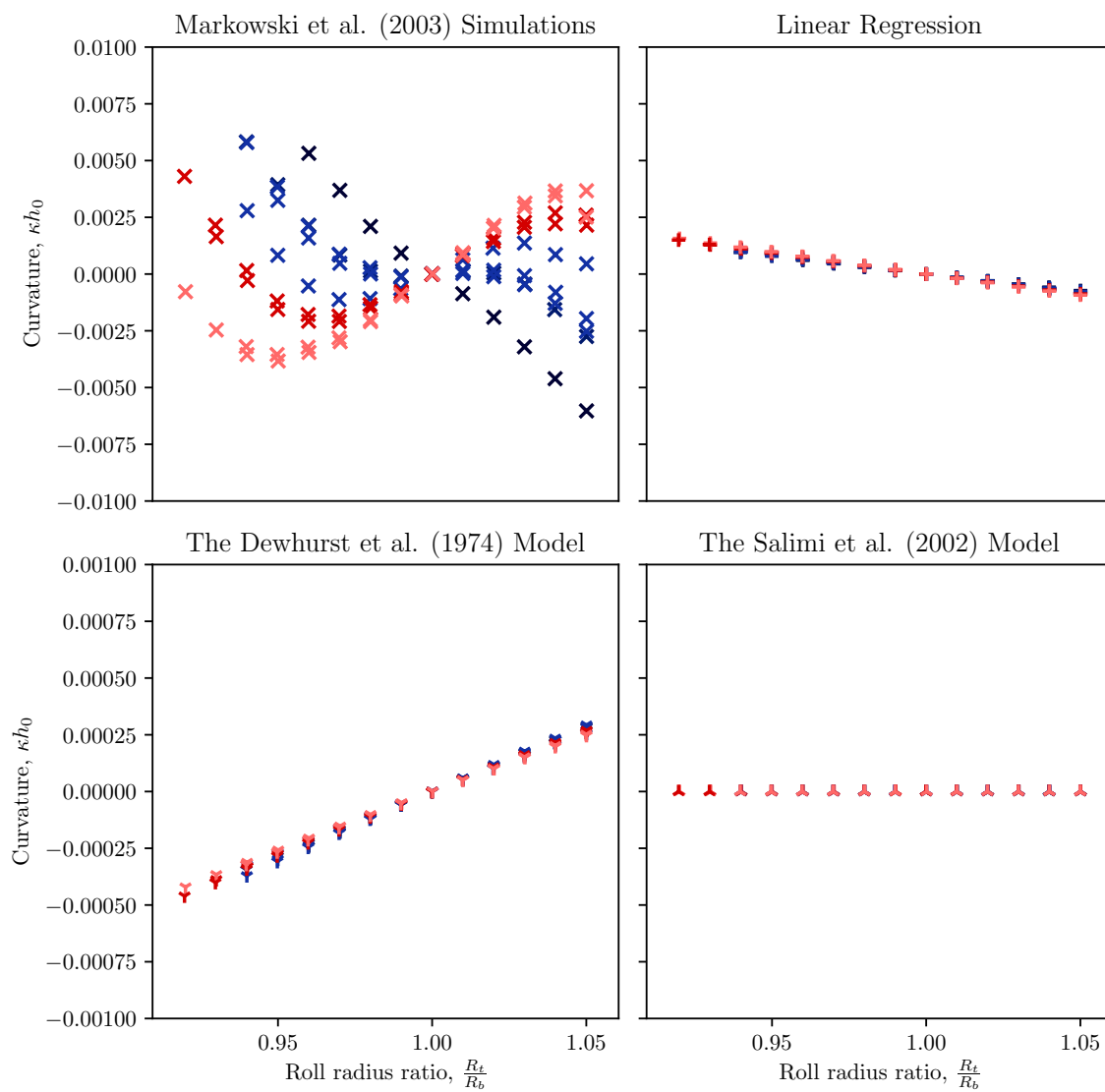


Fig. 4.10 Curvature predictions of the Markowski et al. (2003) simulated results by the reduced cubic linear regression model (top right), the Dewhurst et al. (1974) model (bottom left) and the Salimi et al. (2002) model (bottom right). Colour indicates reduction.

overfitted than the previous models. Using subsets, such as just the force and torque predictions produce very poor models, indicating that the predictive power of these parameters is not large. This is unsurprising given their inherently linear behaviour with any of the other fitting parameters.

4.5 Conclusion

At present, using currently available analytical methods, curvature cannot be robustly predicted, and care must be taken to test a range of geometric regimes and material properties before claims are made to that effect.

After an extensive review of literature investigating sheet curvature from asymmetric rolling, contradictions were found between conclusions of individual papers. These contradictions were resolved in some instances by considering other parameters, such as the dependence of curvature direction on reduction and the roll gap aspect ratio under roll surface speed asymmetries. However, in other cases no such resolution was found, such as the effects of asymmetric friction.

Data from fifteen publications were digitised and statistically modelled to try to unify these conclusions. A range of methods were considered, including linear regression, lasso regression, non-parametric regression, analytic models and hybrid methods. None of these were able to quantitatively or qualitatively predict curvature behaviour over the three asymmetric and three non-asymmetric parameters considered.

Despite these short-comings, some insight was gained that could inform future investigations or future model validation. For example, strong interaction exists between the geometric parameters and the roll radius ratio. It was also established that the material properties have a strong effect on curvature, specifically the ratio of yield stress to Young's modulus, which suggests elasticity may play a role in some cases.

Published analytical models were also investigated. Many were not able to be reproduced, due to errors in, or incomplete descriptions of, their implementations. The two that were implemented poorly reproduce the digitised dataset. Further, there is evidence that the mechanisms that produce curvature, proposed by these models, are either incorrect or incomplete. Some discussion in the literature suggests that curvature is produced by asymmetry in stresses on the roll surfaces at the outlet of the roll gap. This hypothesis requires greater investigation and has been considered further in the next chapter.

This work could benefit from a greater and more uniformly distributed data. The structure of the digitised experiments make it challenging to establish interactions that have not already been considered; however, there is good evidence to suggest that many more interactions exist than has been studied. Additionally, the concept of hybrid approaches could be explored more thoroughly. Whilst regressing over the results of analytical models proved unsuccessful, the inherent form of the analytical solutions, such as the neutral point plateau, could be exploited to motivate a more tailored regression approach.

Chapter 5

Thick-sheet rolling

Multiple lobes, or oscillations were observed in the shear stress fields of the simulated results for both asymmetric and clad-sheet rolling. These results, from Chapter 2 and Chapter 3, are reproduced in Figure 5.1 for reference. It is worth noting that these oscillations are not numerical artefacts of the simulations; they are robust to changes in the mesh and numerical solver.

This motivated consideration of alternative asymptotic assumptions, which are presented with a leading order solution of the resulting model in Section 5.2. Preliminary results, presented in Section 5.3, verify the oscillatory behaviour observed but show otherwise show mixed agreement with simulations: agreement was found with most of the stress and strain fields but force and torque predictions disagree by a factor. Some indication of non-linear curvature trends was also found. This model remains incomplete; specifically, the next order solution and determining systematic inlet boundary conditions. Discussion of these next steps is given with some concluding remarks in Section 5.4.

5.1 Introduction

The shear stress oscillations are found to be stable features and remain stationary to the rolls once steady state is reached. This phenomenon could be a feature of the numerical method, the modelling assumptions or part of the physical processes. Further simulation results are presented here to provide evidence that it is the latter of these possibilities.

This has already been observed for both explicit and implicit solvers, and dynamic and static stepping, in Chapter 2 and Chapter 3. Figure 5.2 shows the phenomenon

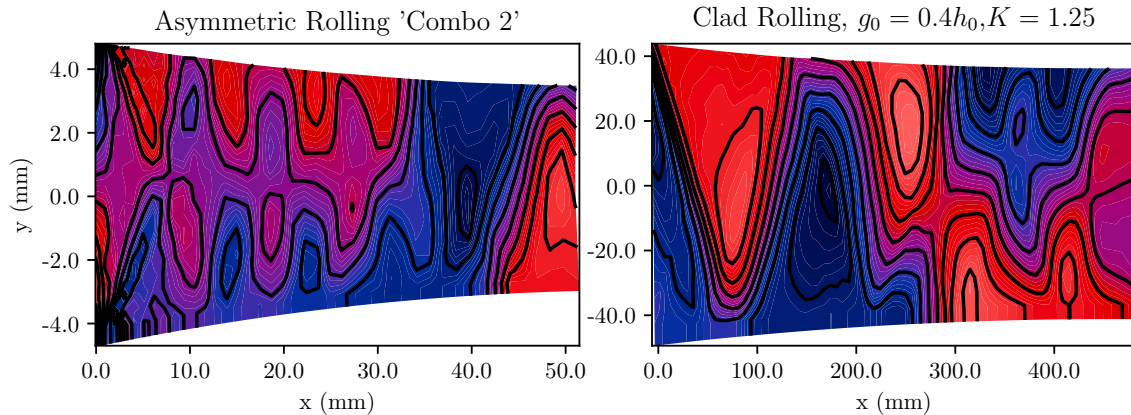


Fig. 5.1 Shear stress fields from Chapter 2 and Chapter 3.

exists with the following configurations: a work hardening material, described in Chapter 2; an implicit solver and the finest mesh included in the mesh convergence study, refer Appendix D.2; an irregular mesh; and, a three-dimensional workpiece, with and without enforced symmetry. The three-dimensional cases eliminate plane strain as the cause, the different solvers and meshes suggest it is not a numerical artefact and enforced symmetry indicates it is not vertical oscillations. Although not exhaustive, these observations indicate that it is highly likely to be a physical feature.

Further, a phenomenon in the equivalent strain rate plots, Figure 8, of Yoshii et al. (1991), shows similar patterns, although this was not discussed in that paper. This may have also been observed in Figure 8 of Richelsen (1997), a plot of the horizontal stress field.

To investigate further, simulations were completed varying each parameter, from which Figure 5.3 shows that the number of lobes is inversely proportional to the roll gap aspect ratio. The $\delta = 0.05$ case suggests that sufficiently many lobes begin to blur so no oscillations would be observable in the $\delta \rightarrow 0$ limit, which is consistent with the thin-sheet asymptotic models presented in Chapters 2 and 3. For $\delta = 1.0$, the shear stress distribution also exhibits a single sign change. This also looks like the thin-sheet asymptotic model, which might explain why this phenomenon has not been previously identified in literature.

A slip-line field of a stamp shows 45° lines from the corners of the stamp. If there were a second stamp, squeezing the material from below, these angular lines would reflect off the bottom stamp and propagate through the gap, producing lobe patterning like that seen here. Such a pattern should, therefore, be captured by the material and

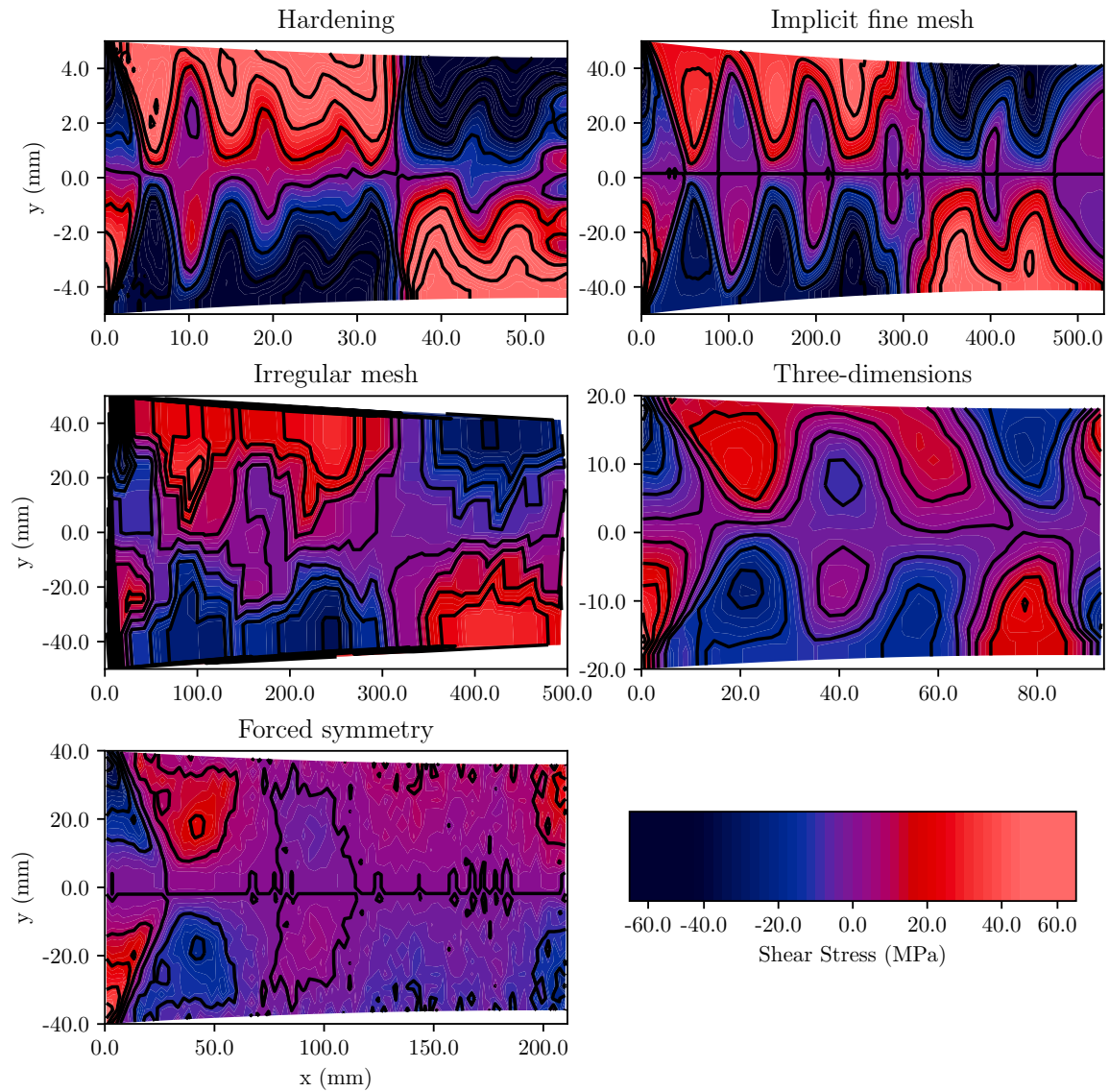


Fig. 5.2 Shear stress fields for a work hardening material, using an implicit finite element solution, using an irregular mesh, for a three-dimensional workpiece, and for the top half of a three-dimensional workpiece with a horizontal plane of symmetry. All cases are symmetric configurations with assorted parameters.

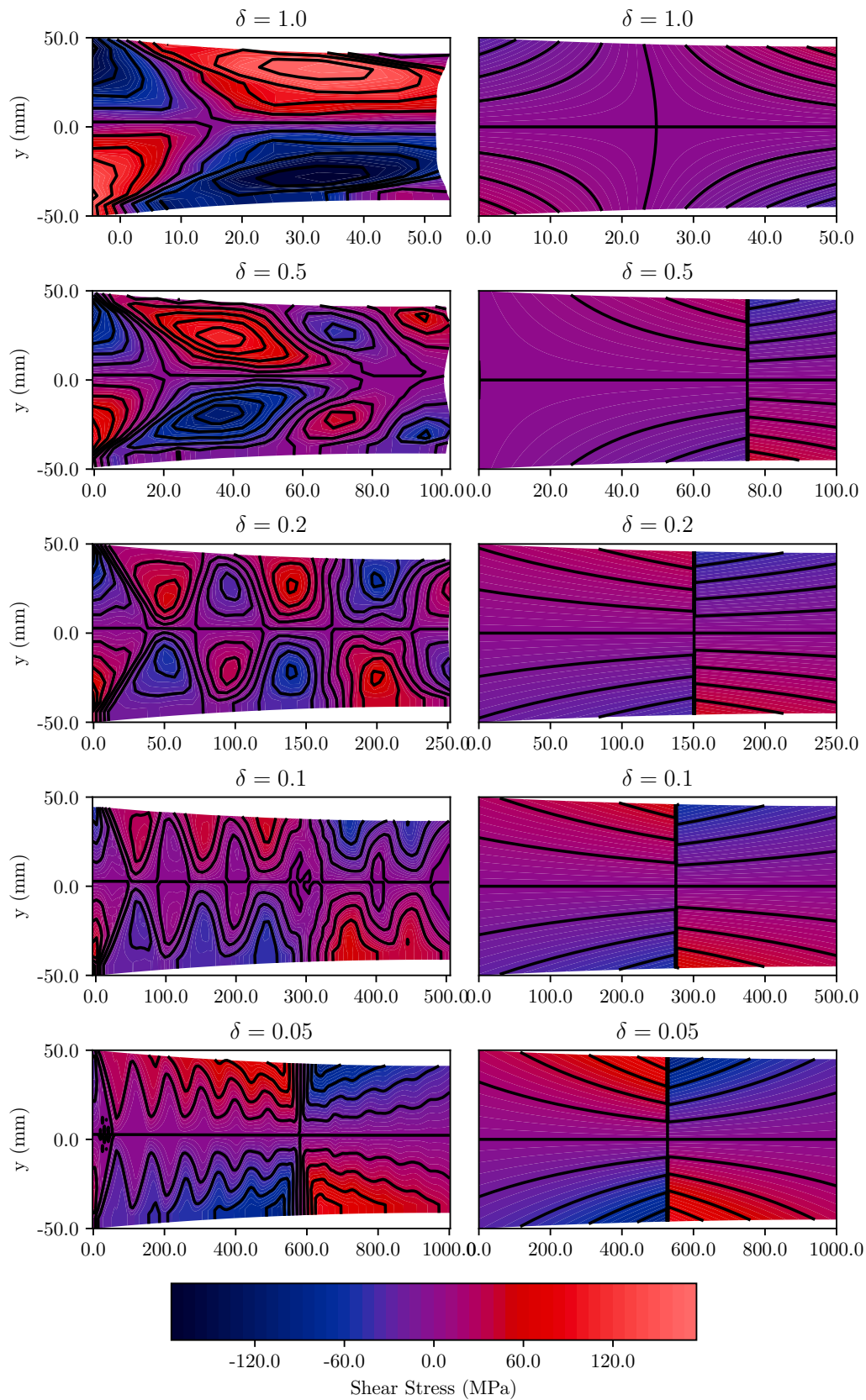


Fig. 5.3 Shear stress fields for varying δ from the finite element simulations (left) and the thin-sheet rolling model from Chapter 2(right). The other parameters used are $(\hat{h}_0, r, \mu, \hat{k}) = (0.05\text{m}, 0.2, 0.1, 173\text{MPa})$.

friction models used in Chapter 2 if the asymptotic model resolved through-thickness variation.

5.2 Alternative asymptotic assumptions

An asymptotic model is developed in this section that assumes a small reduction and small friction coefficients, but not a small roll gap aspect ratio. Similar scalings as Chapters 2 and 3 are used,

$$\begin{aligned}
 \hat{x} &= \hat{l}x & \hat{h} &= \hat{h}_0 h & \hat{y} &= \hat{h}_0 y & \frac{\partial \hat{h}}{\partial \hat{x}} &= \varepsilon \delta \frac{\partial h}{\partial x} \\
 \hat{s}_{xx} &= \hat{k} s_{xx} & \hat{s}_{xy} &= \varepsilon \hat{k} s_{xy} & \hat{p} &= \hat{k} p & \hat{\lambda} &= \lambda \varepsilon \frac{\hat{u}_0}{\hat{k} \hat{l}} \\
 & & \hat{u} &= \hat{u}_0 u & \hat{v} &= \varepsilon \hat{u}_0 v & & \\
 \gamma_t &= \begin{cases} \frac{\mu_t}{\mu_b} & : x < x_{nt} \\ -\frac{\mu_t}{\mu_b} & : x > x_{nt} \end{cases} & \gamma_b &= \begin{cases} -1 & : x < x_{nb} \\ 1 & : x > x_{nb} \end{cases}, & & & & (5.1)
 \end{aligned}$$

where the nomenclature is the same as Chapter 2 with ε taken to be the small parameter, say $\varepsilon = \mu_b$. This does not change the scaling of the stress or velocity terms; only the flow rate parameter. This produces the non-dimensional plane strain, rigid perfectly plastic governing equations

$$-\delta \frac{\partial p}{\partial x} + \delta \frac{\partial s_{xx}}{\partial x} + \varepsilon \frac{\partial s_{xy}}{\partial y} = 0, \quad (5.2)$$

$$-\frac{\partial p}{\partial y} - \frac{\partial s_{xx}}{\partial y} + \delta \varepsilon \frac{\partial s_{xy}}{\partial x} = 0, \quad (5.3)$$

$$\frac{\partial u}{\partial x} = \varepsilon \lambda s_{xx}, \quad (5.4)$$

$$\frac{\partial u}{\partial y} + \delta \varepsilon \frac{\partial v}{\partial x} = 2\delta \varepsilon^2 \lambda s_{xy}, \quad (5.5)$$

$$\delta \frac{\partial u}{\partial x} + \varepsilon \frac{\partial v}{\partial y} = 0 \quad (5.6)$$

$$\text{and } s_{xx}^2 + \varepsilon^2 s_{xy}^2 = 1. \quad (5.7)$$

with boundary conditions

$$\begin{aligned}
0 = & p(x, h_{t/b}(x)) \left(-\delta \frac{\partial h_{t/b}}{\partial x} + \frac{\delta \frac{\partial h_{t/b}}{\partial x} + \gamma_{t/b}(x)}{1 - \varepsilon^2 \delta \gamma_{t/b}(x) \frac{\partial h_{t/b}}{\partial x}} \right) \\
& + s_{xx}(x, h_{t/b}(x)) \left(\delta \frac{\partial h_{t/b}}{\partial x} + \frac{\delta \frac{\partial h_{t/b}}{\partial x} + \gamma_{t/b}(x)}{1 - \varepsilon^2 \delta \gamma_{t/b}(x) \frac{\partial h_{t/b}}{\partial x}} \right) \\
& + s_{xy}(x, h_{t/b}(x)) \left(-1 + \varepsilon^2 \delta \frac{\partial h_{t/b}}{\partial x} \frac{\delta \frac{\partial h_{t/b}}{\partial x} + \gamma_{t/b}(x)}{1 - \varepsilon^2 \delta \gamma_{t/b}(x) \frac{\partial h_{t/b}}{\partial x}} \right) \quad (5.8)
\end{aligned}$$

$$\text{and } 0 = v(x, h_{t/b}(x)) - \delta \frac{\partial h_{t/b}}{\partial x} u(x, h_{t/b}(x)). \quad (5.9)$$

Given $\varepsilon \ll 1$, each variable is expanded in terms of ε and each order of ε is considered independent. At leading order, equation (5.7) gives

$$s_{xx}^{(0)} = \pm 1 \quad (5.10)$$

where the positive sign is chosen for the same reasons given in Chapter 2. Using this solution in equations (5.2) and (5.3) shows that the leading order pressure is constant horizontally and vertically, hence

$$p^{(0)} = p_0. \quad (5.11)$$

Equation (5.5) and equation (5.6), or equation (5.4), then determine the horizontal velocity as constant,

$$u^{(0)} = u_0. \quad (5.12)$$

Considering the next order of ε , equation (5.7) gives

$$s_{xx}^{(1)} = 0 \quad (5.13)$$

and equations (5.2) and (5.3) give

$$\frac{\partial p^{(1)}}{\partial x} - \frac{1}{\delta} \frac{\partial s_{xy}^{(0)}}{\partial y} = 0 \quad (5.14a)$$

$$\text{and } \frac{\partial p^{(1)}}{\partial y} - \delta \frac{\partial s_{xy}^{(0)}}{\partial x} = 0. \quad (5.14b)$$

This wave equation set is closed with the stress boundary conditions,

$$s_{xx}^{(0)} \left(2\delta \frac{\partial h}{\partial x} + \gamma_t \right) + \gamma p^{(0)} - s_{xy}^{(0)} = 0 \quad \text{on} \quad y = h_t(x) \quad (5.15a)$$

$$\text{and} \quad s_{xx}^{(0)} \left(2\delta \frac{\partial h}{\partial x} + \gamma_b \right) + \gamma p^{(0)} - s_{xy}^{(0)} = 0 \quad \text{on} \quad y = h_b(x). \quad (5.15b)$$

Similarly, equation (5.5) and equation (5.6) give

$$\frac{\partial u^{(1)}}{\partial x} + \frac{1}{\delta} \frac{\partial v^{(0)}}{\partial y} = 0 \quad (5.16a)$$

$$\text{and} \quad \frac{\partial u^{(1)}}{\partial y} + \delta \frac{\partial v^{(0)}}{\partial x} = 0, \quad (5.16b)$$

which is the second wave equation set, closed by

$$\frac{\partial h_t}{\partial x} u^{(0)}(x, h_t(x)) - v^{(0)}(x, h_t(x)) = 0 \quad (5.17a)$$

$$\text{and} \quad \frac{\partial h_b}{\partial x} u^{(0)}(x, h_b(x)) - v^{(0)}(x, h_b(x)) = 0. \quad (5.17b)$$

Given two sets of wave equations, consider the general case,

$$\frac{d\alpha}{dx} + b \frac{d\beta}{dy} = 0 \quad (5.18a)$$

$$\text{and} \quad \frac{d\alpha}{dy} + d \frac{d\beta}{dx} = 0, \quad (5.18b)$$

which can be simplified by taking

$$\alpha(x, y) = \frac{\partial \phi}{\partial x} \quad (5.19a)$$

$$\text{and} \quad \beta(x, y) = -\frac{1}{d} \frac{\partial \phi}{\partial y} \quad (5.19b)$$

to reveal the wave equation,

$$\frac{1}{c^2} \frac{\partial^2 \phi}{\partial x^2} = \frac{\partial^2 \phi}{\partial y^2} \quad (5.20)$$

where $c^2 = \frac{b}{d}$. This has the solution of travelling waves, which form characteristics or slip-lines in this application,

$$\phi = c_1(y + cx) + c_2(y - cx). \quad (5.21)$$

Boundary conditions are required for the roll surfaces and one of the two ends. Assuming that α and β are known on the inlet boundary, $\alpha_0(y)$ and $\beta_0(y)$, and some condition is known that connects them along the roll surfaces,

$$a_0(x) + a_1(x)\alpha(x, h_{t/b}(x)) + a_2(x)\beta(x, h_{t/b}(x)) = 0, \quad (5.22)$$

conditions on c'_1 and c'_2 can be determined for the inlet boundary,

$$c'_1(y) = -\frac{1}{2} \left(\frac{\alpha_0(y)}{c} - d\beta_0(y) \right) \quad (5.23a)$$

$$\text{and } c'_2(y) = -\frac{1}{2} \left(\frac{\alpha_0(y)}{c} + d\beta_0(y) \right) \quad (5.23b)$$

valid for $y \in [h_b(0), h_t(0)]$, and, for the roll surfaces,

$$b_0(x) + b_1(x)c'_1(h_{t/b}(x) + cx) + b_2(x)c'_2(h_{t/b}(x) - cx) = 0 \quad (5.24)$$

valid for $x \in [0, l]$ and where $b_0 = a_0$, $b_1 = ca_1 - \frac{a_2}{d}$ and $b_2 = -ca_1 - \frac{a_2}{d}$. Although it would not be easy to write out a closed form solution from these boundary conditions, it is relatively straight forward to compute an analytic solution by following the slip-lines until an end condition can be applied. It is also convenient that

$$\alpha(x, y) = \frac{\partial \phi}{\partial x} = c (c'_1(y + cx) - c'_2(y - cx)) \quad (5.25a)$$

$$\text{and } \beta(x, y) = -\frac{1}{d} \frac{\partial \phi}{\partial y} = -\frac{1}{d} (c'_1(y + cx) + c'_2(y - cx)) \quad (5.25b)$$

so $\phi = c_1 + c_2$ never has to be integrated for.

5.3 Results

The development of this model remains incomplete. Correction terms should be considered for each variable to ensure all the relevant dynamics have been captured. Like the thin-sheet model, this would include stress terms only influencing the strain at the next order. Also, the pressure, shear stress and velocity must be defined along the inlet boundary, as opposed to defining constant pressure and horizontal velocity only. For the purpose of producing preliminary results, these inlets are estimated to be

either constant or linear with magnitudes matching the roll boundary conditions, but ultimately should be determined from an outer elastic problem.

Locating the neutral point is also required and the binary search used for the thin-sheet model is used here to ensure the correct average outlet pressure.

The preliminary results presented in this section are mostly for the same situations as those presented for the thin-sheet asymmetric rolling model in Chapter 2; specifically, stress and strain fields, and force and torque predictions. Proxies for curvature prediction are also presented for both the thin and thick-sheet asymptotic models and are compared to data from Markowski et al. (2003).

5.3.1 Stress and strain fields

Comparing the shear stress fields to the numerical results at the beginning of this chapter, Figure 5.4, shows that this model is able to capture the observed lobes. Both the magnitude and number of oscillations seem to be captured correctly. One notable discrepancy is the $\delta = 1.0$ case, where the sign of the top shear lobe is incorrect. This is the consequence of incorrect neutral points and indicates greater nuance in the binary search is required.

The shear and stress fields for the ‘Combo 2’ parameter set used in Chapter 2 are presented in Figure 5.5 with the numerical results from that chapter. The pressure is noisy, unlike the thin-sheet model; however, the corrected term generally exhibits a pressure hill. The horizontal deviatoric stress remains homogeneous and the shear stress shows the characteristic shear lobes, as expected from the previous results. The horizontal velocity matches well in form and magnitude; however, no oscillations are present in the vertical velocity. This is likely a consequence of the inlet velocity profile used for the model as the form of the equations for this term match the shear stress equations, hence can support the characteristic lobes also.

5.3.2 Force and torque predictions

Using the thick-sheet model, force and torque predictions are made to compare to the simulations from Chapter 2 over the three asymmetries of this model, Figure 5.6. The correct trends are captured by this model; however, there is a clear discrepancy in magnitude. This could be a consequence of the inlet boundary conditions or that this model is inaccurate for $\delta = 0.1$ and $r = 0.25$ because the assumptions made require $r \ll \delta$. The latter would not be surprising given the assumptions of this model. A

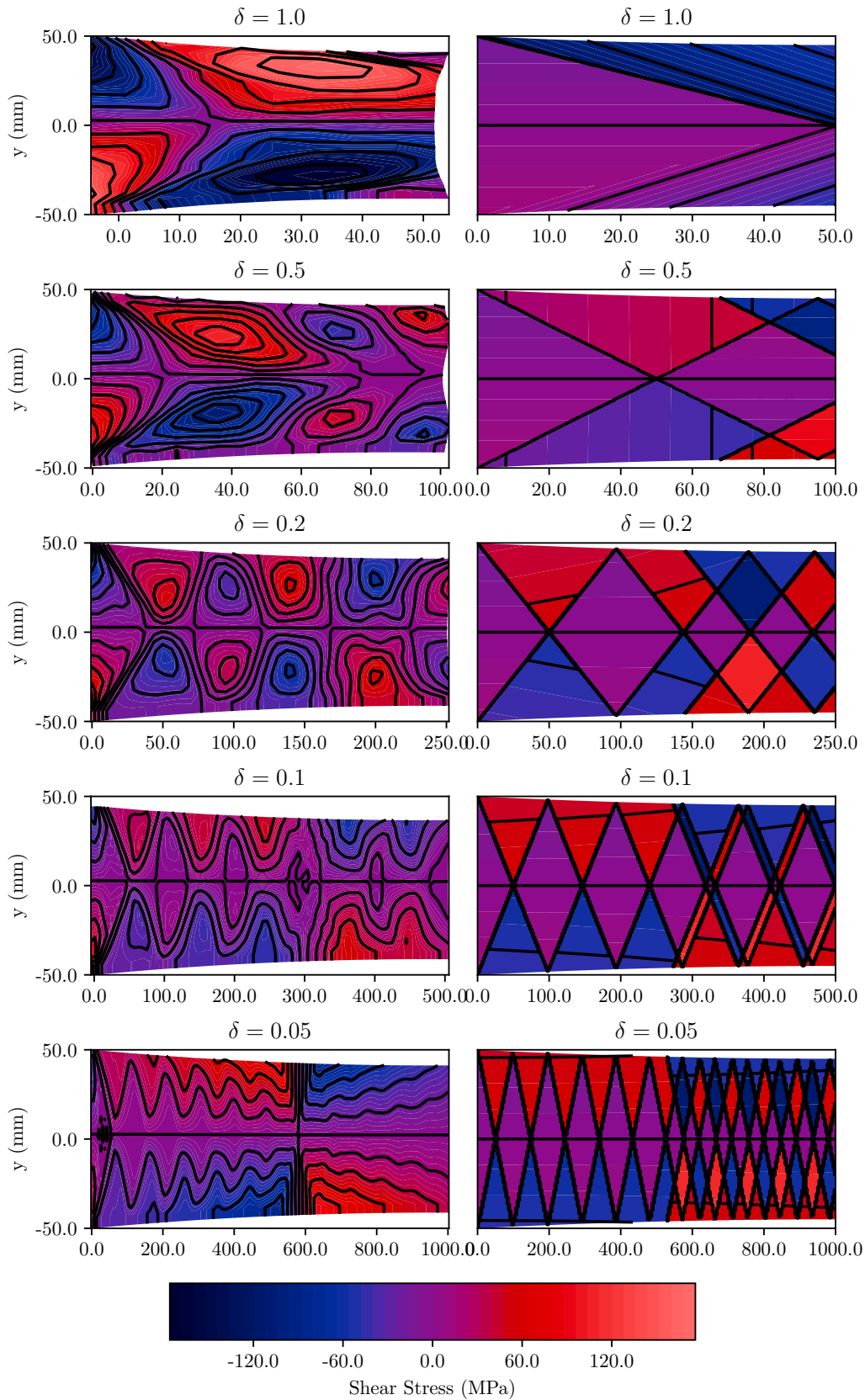


Fig. 5.4 Shear stress fields for varying δ from the finite element simulations (left) and the thick-sheet rolling model (right), both exhibiting shear lobes. The other parameters used are $(\hat{h}_0, r, \mu, \hat{k}) = (0.05\text{m}, 0.2, 0.1, 173\text{MPa})$.

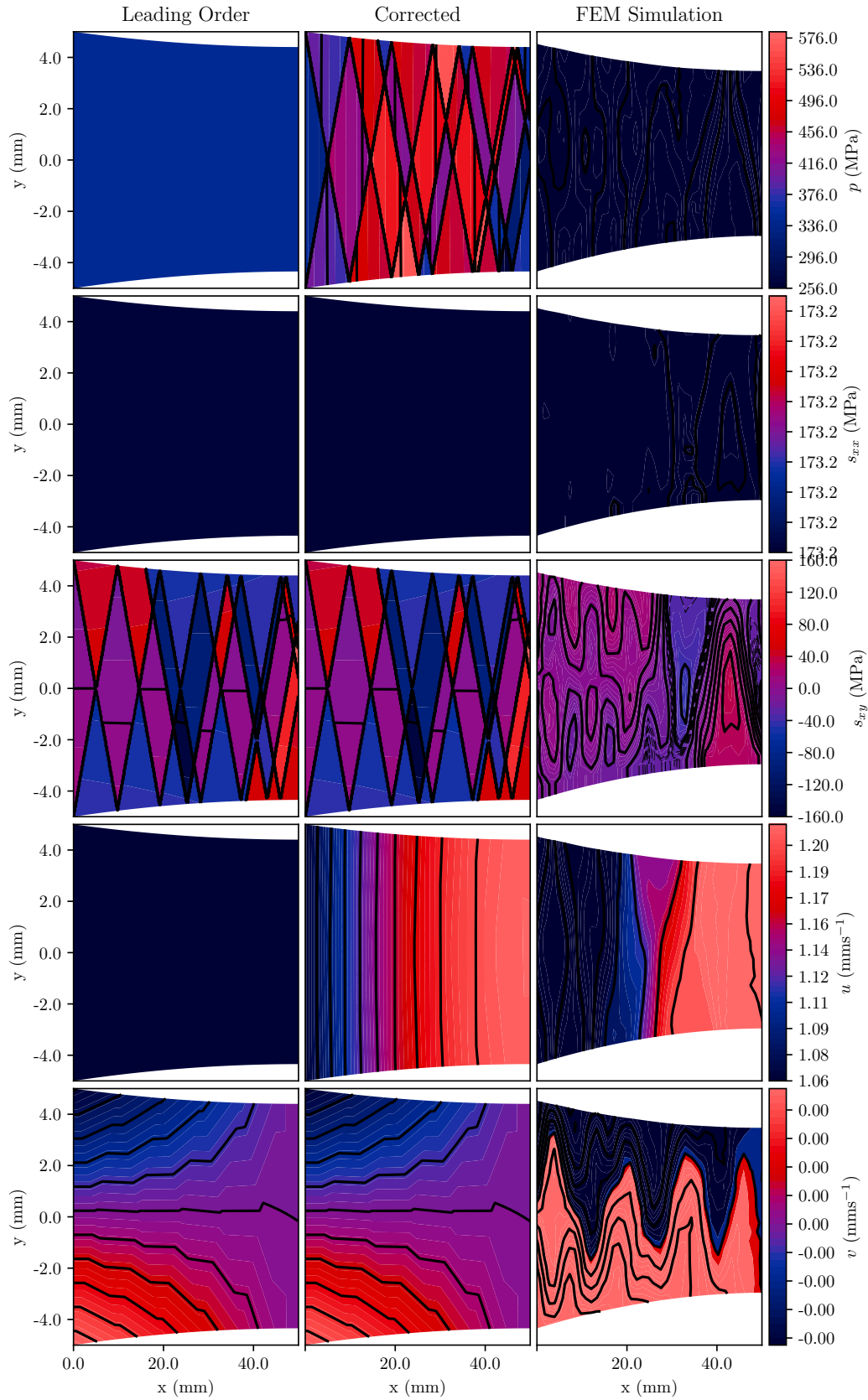


Fig. 5.5 From the top to bottom, pressure, horizontal deviatoric stress, shear stress, horizontal velocity and vertical velocity fields for the for the ‘Combo 2’ parameter set, $(\mu_b, \delta, r, \mu_t/\mu_b, \hat{R}_t/\hat{R}_b, \hat{U}_t/\hat{U}_b) = (0.1, 0.1, 0.25, 0.9, 1.1, 0.95)$, from the leading order asymptotic model (left), corrected asymptotic model (centre) and finite element simulations (right).

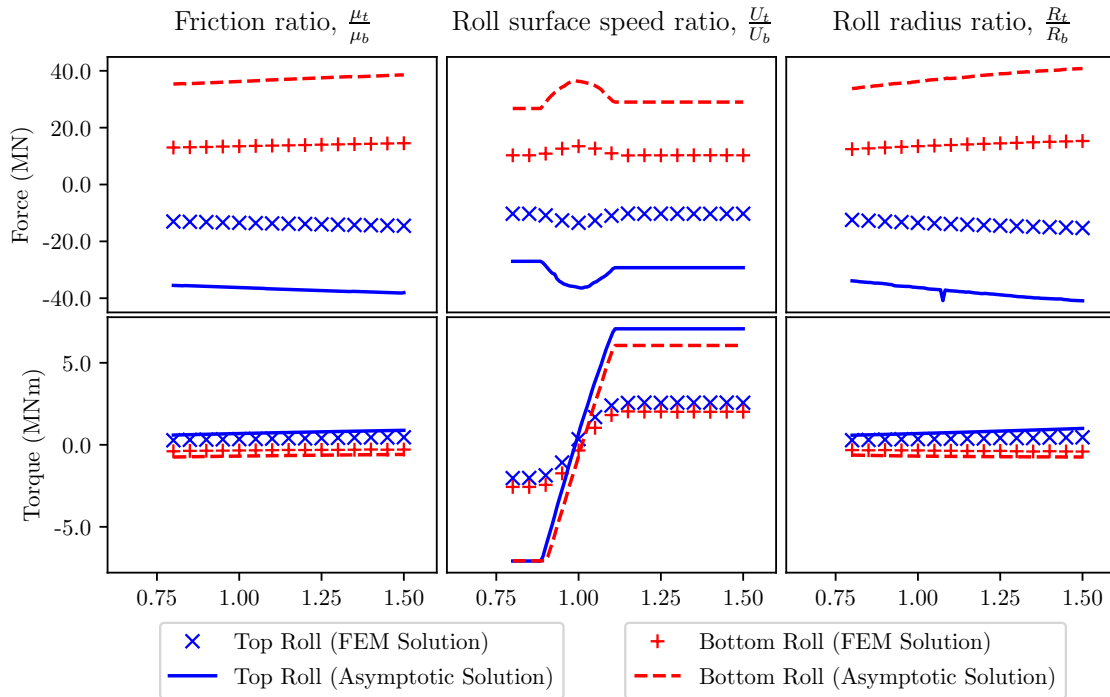


Fig. 5.6 Roll force (top) and torque (bottom) as the top roll is varied to achieve the asymmetric ratio of friction (left), speed (middle) or size (right). The other parameters used are $(\hat{h}_0, \hat{R}_b, r, \mu, \hat{k}) = (0.01\text{m}, 2.5\text{m}, 0.12, 0.1, 173\text{MPa})$.

comparison to thicker sheet simulations would be necessary to ascertain this more certainly.

5.3.3 Curvature predictions

A final comparison is made, regarding curvature prediction. While further work is required to predict curvature directly, the mean shear stress was proposed as one of two mechanisms for generating curvature in Salimi et al. (2002). The validation of the mechanism was discussed in Chapter 4. Despite these reservations, mean shear strain rate is used here as a proxy for curvature to give some indication of the behaviour of this model.

Figure 5.7 shows the curvature results of Markowski et al. (2003) and the mean shear strain rate of the thin-sheet rolling model and thick-sheet rolling model as the roll size ratio and reduction are varied. These curvature results are used because they are a clear example of the complex non-linear behaviour. This is not captured at all by the linear trends of the thin-sheet rolling model; where as, some non-linear trends are observed from the thick-sheet rolling model. While these predictions are still

quantitatively and qualitatively poor, this does show additional non-linear phenomena captured by the new model.

5.4 Concluding remarks

An asymptotic model of thick-sheet rolling is achieved by alternative scaling assumptions to the thin-sheet model presented in Chapter 2. Specifically, the small roll gap aspect ratio assumption is relaxed to a small reduction assumption. This model produces two sets of wave equations that can be solved for the first non-constant term in each variable's asymptotic expansion.

While further work is required to determine inlet boundary conditions, and higher order terms may be necessary to capture all necessary phenomena, a minimal implementation was completed to produce some initial results. These show that the numerical stress and strain fields are qualitatively predicted, particularly the characteristic shear lobes. Force and torque predictions capture the correct trends over each of the three asymmetries; however, a large discrepancy in magnitude exists. Finally, early indications for curvature prediction show the possibility of non-linear trends, unattainable with the thin-sheet rolling model, being captured. Further work is required to make direct curvature predictions from this model.

Further work is also required to determine the correct inlet profile for the pressure, shear stress and velocity. This could be achieved by matching to an elastic, mixed boundary problem around where the workpiece first contacts the roll. Such a problem has been considered by Dr Chris Cawthorn who found an analytical solution using the Weiner-Hopf method. Additional work to solve for the next order corrections could also improve accuracy and provide sufficient through-thickness resolution for direct curvature predictions.

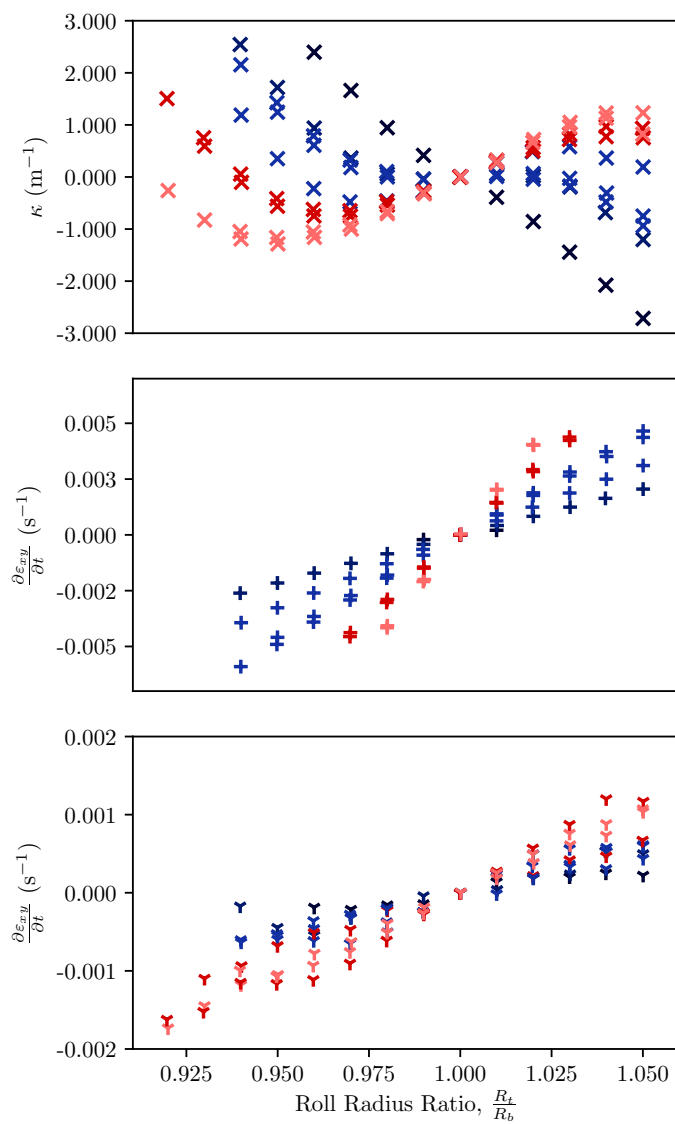


Fig. 5.7 Markowski et al. (2003) curvature results (top), mean shear strain rate of the thin-sheet rolling model (middle), and mean shear strain rate of the thick-sheet rolling model (bottom) as the roll radius ratio and reduction (colour) are varied.

Chapter 6

Ring rolling

Existing models of ring rolling seem generally inadequate due to strict assumptions regarding the circularity, how close to a circle the workpiece remains; centrality, how centred the workpiece is to the work roll and mandrel; and coaxiality, how uniform the workpiece thickness is. Prescribing these properties considerably limits how useful a model would be as these are measures to be controlled and each would indicate a failure mode of the process. An approach for modelling ring rolling is presented in this chapter that does not assume any of these three parameters. Plastic deformation only occurs within the roll gap, which allows the outer region to be modelled with a curved elastic beam model. This is presented in Section 6.2. The region between the rolls is modelled using a slab method that is extended to allow the neutral points to be horizontally misaligned and greater bending moments to be supported. While each of these models behaves as expected, nuances in the coupling between them means a complete solution has not yet been found and this work is therefore not complete. The proposed coupling and discussion of these challenges are presented in Section 6.4. The chapter concludes with some discussion about how to find a convergent coupling solver as well as ideas about how to extend this model, specifically dynamic effects are proposed for the present model in Section 6.5.1 and a model for the English wheel is proposed in Section 6.5.2.

6.1 Introduction

Ring rolling is the process of forming a ring shaped product by repeatedly passing an annular workpiece through sets of rolls. The continuous rolling results in products that are jointless and have undergone considerable work hardening. The workpiece is

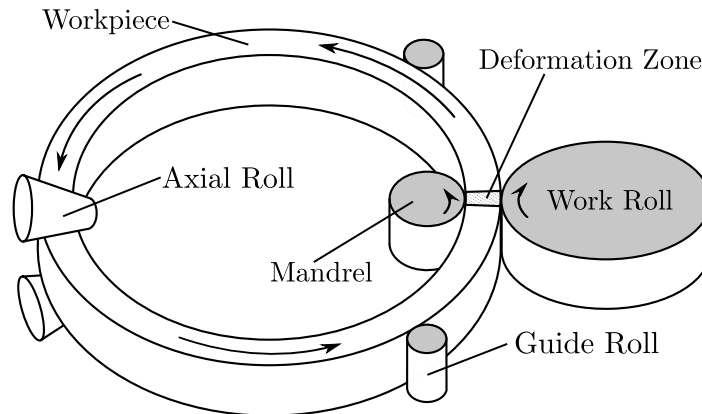


Fig. 6.1 A diagram of the ring rolling process.

typically passed through a set of horizontal and a set of vertical rolls. The majority of deformation occurs between the work roll and mandrel, marked in Figure 6.1; axial rolls, also marked in the figure, can cause further deformation, although, this typically is to prevent vertical growth of the workpiece only. Guide rolls on the outer surface of the workpiece are also common to ensure the workpiece remains centred to the work roll and mandrel.

The deformation between the work roll and mandrel is similar to asymmetric rolling. The process is driven by the same physics and can be described with the same mathematical formulation: the thickness of a workpiece is reduced by passing it through rolls of asymmetric size and rotation, which results in curvature changes that define the shape of the product. Ring rolling differs from asymmetric sheet rolling in most other ways. Obviously, the formed and unformed ends of the workpiece are joined by a ring that couples the geometry and forcing. Most of the parameters also take very different values to most asymmetrical sheet rolling configurations. The roll gap aspect ratio is typically thick, not thin; the inlet and outlet curvature is significant, not negligible; and the reduction is small, not order one. The workpiece is also deformed repeatedly, making work hardening significant. Finally, the width of the workpiece is of similar order to the thickness; height growth, the equivalent of lateral spread, is even a designed result of the process.

Many models of ring rolling have been proposed. A class of these are limited to the roll gap and are very similar to asymmetric rolling models, including slab models (Lin et al., 1997; Parvizi et al., 2011; Zamani, 2014), upper-bound models (Parvizi et al., 2014), and slip-line models (Hawkyard et al., 1973). Other models consider the kinematics of the ring to predict ring growth. Guo et al. (2011) assumes linear variation of the profile

ratio to develop a stable forming regime with constant radial growth. Xu et al. (2012) considers the ring as a curved hexahedron by assuming constant reduction of the profile dimensions. Combined with estimates of slip within the roll gap, this improves the radial expansion prediction. This line of thinking is progressed further in Berti et al. (2015), in which the ring is divided into a finite number of sections and the geometric properties of each section is determined. The geometric properties change twice per revolution: once from radial roll deformation and once from axial roll deformation. Quagliato et al. (2016) extends this model to predict the plastic strain tensor and consider hardening effects.

The objective of most research into ring riling has been to improve process control or facilitate process planning. For example, Lin et al. (1997); H. Yang et al. (2005); and Yan et al. (2007) each propose conditions on the reduction for feasible rolling above which the rolls cannot draw the ring into the roll gap. These relate friction coefficients, ring profile geometry, feed rate and rotation rate to propose operational limits. Berti et al. (2015) effectively provides a review of these findings by systematically applying analytical models and empirical rules to determine the constraints of each control variable. An alternative approach is presented in Hua et al. (2016), in which a beam model is used to determine the maximum force the guide rolls can apply before causing the workpiece to buckle.

More recently, increased sensing coverage with image processing has been used to achieve effective control without a tailored predictive model (Arthington et al., 2016). Rings with non-uniform curvature, including square and pentagonal rings, were produced with this approach. Perhaps one motivation for exploring better sensing was the limitations of existing analytical models; most assume circular and centred workpieces, which is only reasonable with sufficient guide rolls. Arthington et al. (2016) clearly demonstrates the benefits and flexibility of being able to operate ring rolling without these assumptions.

In light of this, the work presented here establishes a modelling framework of the ring rolling process that can accommodate non-circular, non-centred and non-coaxial workpieces. Ultimately, convergence was not achieved with the presented framework; however, the modelling approach described here would be of great value if the correct coupling is found.

The process is modelled as two regions, an outer elastic ring and an inner plastic region between the rolls. The outer problem is treated as a Timoshenko curved beam (Timoshenko et al., 1925), based on Castigliano's theory. The entire outer ring is

assumed to be below yield, but no other assumptions are made here beyond the beam model construction. The cross-section is taken as rectangular, but could be generalised. The inner problem is modelled as a slab model. This requires plane strain to be assumed, which is assumed in much of the published analytical work on ring rolling. This assumption has been verified using FE analysis for some configurations Berti et al. (2015) and, while height growth is significant in other configurations, it can be limited with axial rolls. Small reductions per pass make it reasonable to neglect inertia within the roll gap. Finally, the curvature and angled entry of the workpiece is significant so this model will be extended to incorporate horizontally misaligned contact points. These models are coupled through force and displacement boundary conditions.

Finally, a means of including dynamics in the outer problem is proposed in the discussion of future work of this chapter.

6.2 Curved beam models

The outer model of an elastic curved beam is a generalisation of Castigliano's Theory presented in Timoshenko et al. (1925). This model can accommodate a beam of arbitrary cross-section and of arbitrary path. It is based on Castigliano's second theorem which states that the partial derivative of the strain energy with respect to generalised forces gives the generalised displacements in the direction of that force.

An expression for the strain energy of the workpiece (Timoshenko et al., 1925) is given by

$$U = \int_{\Gamma} \left(\frac{M^2}{2RA\gamma E} + \frac{S^2}{2AE} - \frac{MS}{AER} + \frac{kQ^2}{2AG} \right) ds, \quad (6.1)$$

where S , Q and M are the longitudinal force, shear force and moment respectively; and R , A , E , G , k , γ are the radius of curvature, the cross sectional area, the elastic modulus, the shear modulus, a numerical factor and the distance between the neutral axis and centre of gravity respectively. All of these variables are defined locally so are functions of the distance along the beam, s . The terms of the integrand correspond to bending, stretching, coupled bending-stretching and shear energies respectively. According to Castigliano's second theorem, this gives

$$\delta d = \frac{\partial U}{\partial f} = \int_{\gamma} \left(\frac{\partial M}{\partial f} \left(\frac{M}{RA\gamma E} - \frac{S}{AER} \right) + \frac{\partial S}{\partial f} \left(\frac{S}{AE} - \frac{M}{AER} \right) + \frac{kQ}{AG} \frac{\partial Q}{\partial f} \right) ds \quad (6.2)$$

where δd and f are the generalised displacement and generalised force respectively.

Each of these forces can be defined in terms of a horizontal force, a vertical force and a bending moment at the position along the beam,

$$S = F_v \sin(\phi) - F_h \cos(\phi), \quad (6.3)$$

$$Q = F_h \sin(\phi) - F_v \cos(\phi) \quad (6.4)$$

$$\text{and } M = M_0 + F_v \Delta h + F_h \Delta v. \quad (6.5)$$

where F_h , F_v and M_0 are the horizontal force, vertical force and moment acting on the end of the beam; Δh and Δv are the horizontal and vertical distance to the end of the beam; and ϕ is the local angle to the horizontal.

The partial derivatives and displacements are then calculated as

$$\delta x = \frac{\partial U}{\partial F_h} = \int_{\gamma} \left(\Delta v \left(\frac{M}{RA\gamma E} - \frac{S}{AER} \right) - \cos(\phi) \left(\frac{S}{AE} - \frac{M}{AER} \right) + \sin(\phi) \frac{kQ}{AG} \right) ds, \quad (6.6)$$

$$\delta y = \frac{\partial U}{\partial F_v} = \int_{\gamma} \left(\Delta h \left(\frac{M}{RA\gamma E} - \frac{S}{AER} \right) + \sin(\phi) \left(\frac{S}{AE} - \frac{M}{AER} \right) - \cos(\phi) \frac{kQ}{AG} \right) ds \quad (6.7)$$

$$\text{and } \delta \theta = \frac{\partial U}{\partial M_0} = \int_{\gamma} \left(\frac{M}{RA\gamma E} - \frac{S}{AER} \right) ds. \quad (6.8)$$

Each of the variables must be determined locally with the following considerations:

- The radius of curvature, $R = \frac{1}{\kappa}$, and thickness, w are assumed to be known functions determined from initial conditions and the rolling process. They can vary along the length of the beam.
- The workpiece is assumed to remain rectangular, giving the cross sectional area as $A = wh$.
- E and G are both considered to be constant but could also be updated from the rolling process.
- The distance between the centre of gravity of the cross section and the neutral axis, γ , can be calculated using equations (216) and (217) of Timoshenko et al. (1925) (page 224). This assumes the width can be expressed as a function of the

distance from the centre of gravity,

$$\gamma = \frac{Rm}{1+m} \quad \text{where} \quad m = \frac{\int (w(y) \sum_{i=0}^{\infty} (y/R)^i) dy}{RA}$$

- k is a numerical factor to account for the variation in shear through the bar. It is taken to be 1.5 for rectangular bars and more discussion is provided in Section 17 of Timoshenko et al. (1925) (page 63)

The ring is discretised and linear variation of each of the variables is assumed between nodes. This is limiting with a coarse discretisation but dynamic remeshing would be straightforward to implement.

What remains are three path integrals to be evaluated. For computational ease, the path is determined from the undeformed state; an ODE evaluation using the prescribed curvature profile is sufficient. This requires the length of the beam to be known or a robust termination condition, which is determined by the model coupling.

Example results of this model are presented in Figure 6.2. Three different forces are illustrated and each shows an intuitively correct behaviour.

6.3 Extended slab model

The asymptotic rolling model developed in Chapter 2 has two short comings that limit its application in ring rolling: it assumes that the roll gap aspect ratio is small and that the contact points are vertically aligned. The latter limits bending moments supported by the roll gap and curved workpieces, which are significant in the present application. The leading order asymptotic solution, consistent with published slab models, empirically produces good force and torque predictions when the reduction is small, irrespective of the workpiece thickness. A slab model will be extended to resolve regions where the workpiece is in contact with only one roll and, hence, overcome both these limitations.

Like any asymmetric slab model, the premise is to consider a force and torque balance on each vertical element of the roll gap. By writing these balances in terms of stresses and assuming linear variation in horizontal stress through-thickness, a system

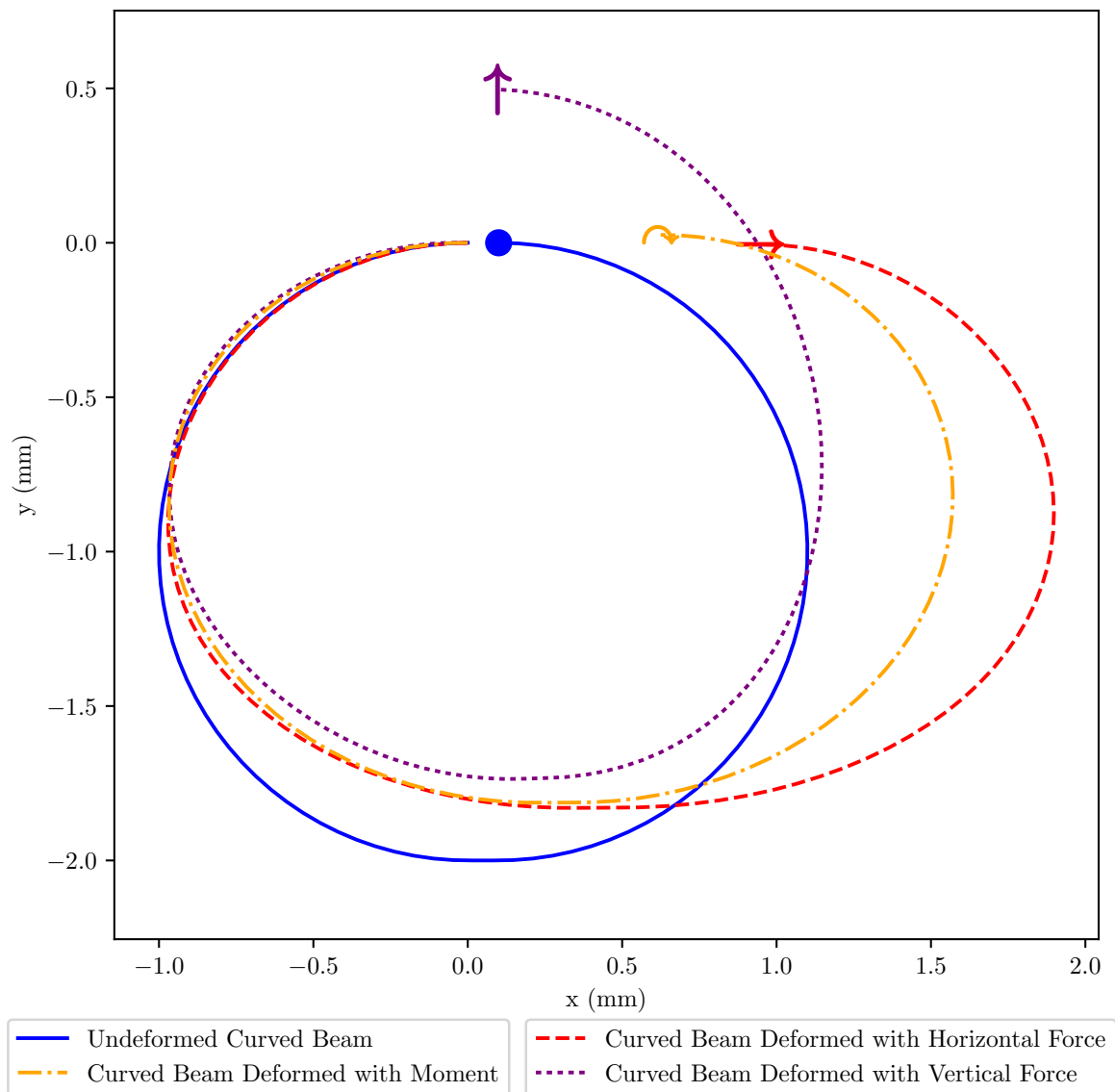


Fig. 6.2 The deflection of an example curved beam under the indicated end forces to illustrate the Timoshenko et al. (1925) curved beam model.

of ODEs in three variables can be attained,

$$\begin{aligned} \frac{d\sigma_b}{dx} = & \left((-2h_t^2 + h_th_b + h_b^2) \frac{1}{3\Delta h} \left(f_t^h + f_b^h \frac{\sigma_t + \sigma_b}{2} \frac{d\Delta h}{dx} \right) \right. \\ & + \frac{1}{6} \left(2h_t \frac{dh_t}{dx} (2\sigma_t + \sigma_b) - \left(\frac{dh_t}{dx} h_b + h_t \frac{dh_b}{dx} \right) (\sigma_t - \sigma_b) - 2h_b \frac{dh_b}{dx} (\sigma_t + 2\sigma_b) \right) \\ & \left. + \frac{f_t^v + f_b^v}{2} - f_t^h \left(h_t + \frac{dh_t}{dx} \frac{1}{2} \right) - f_b^h \left(h_b + \frac{dh_b}{dx} \frac{1}{2} \right) \right) \frac{6}{\Delta h^2}, \end{aligned} \quad (6.9)$$

$$\frac{d\sigma_t}{dx} = - \frac{f_t^h + f_b^h + \frac{\sigma_t + \sigma_b}{2} \left(\frac{d\Delta h}{dx} \right)^2}{\Delta h} - \frac{d\sigma_b}{dx} \quad (6.10)$$

$$\text{and } \frac{d\bar{\tau}}{dx} = - \frac{\bar{\tau} \frac{d\Delta h}{dx} + f_t^v + f_b^v}{\Delta h} \quad (6.11)$$

where h_t , h_b and Δh are the top roll surface, bottom roll surface and roll separation; σ_t , σ_b and $\hat{\tau}$ are the horizontal stress on the top and bottom surfaces and the shear averaged over the vertical element; and, f_t^h , f_t^v , f_b^h and f_b^v are the horizontal and vertical traction forces acting on the top and bottom of each material element respectively. The traction forces can be defined as

$$\begin{aligned} f_t^v &= \frac{\sigma_t' + \tau_t' \frac{dh_t}{dx}}{\sqrt{1 + \left(\frac{dh_t}{dx} \right)^2}}, \\ f_t^h &= \frac{-\sigma_t' \frac{dh_t}{dx} + \tau_t'}{\sqrt{1 + \left(\frac{dh_t}{dx} \right)^2}}, \\ f_b^v &= \frac{-\sigma_b' - \tau_b' \frac{dh_b}{dx}}{\sqrt{1 + \left(\frac{dh_t}{dx} \right)^2}}, \\ \text{and } f_b^h &= \frac{\sigma_b' \frac{dh_b}{dx} - \tau_b'}{\sqrt{1 + \left(\frac{dh_t}{dx} \right)^2}} \end{aligned} \quad (6.12a)$$

where σ' is the normal stress and τ' is the tangential stress on the material surface.

Rotating the stress tensor, the surface stresses can be written as

$$\sigma' = \sigma_x \sin^2(\theta) + \sigma_y \cos^2(\theta) + 2\tau \sin(\theta) \cos(\theta) \quad (6.13a)$$

$$\text{and } \tau' = (\sigma_x - \sigma_y) \sin(\theta) \cos(\theta) + \tau (\cos^2(\theta) - \sin^2(\theta)); \quad (6.13b)$$

and taking the yield condition,

$$\left(\frac{\sigma_x - \sigma_y}{2}\right)^2 + \tau^2 = k^2, \quad (6.14)$$

the following equation can be derived,

$$\begin{aligned} \tau'^2 + 2\tau' \cos^2(\theta) \frac{\tan(\theta) \left(\tau' - \sigma_x - \frac{\sigma'}{\tan(2\theta)}\right)}{4(2\sin^2(\theta) + 1)} \\ + \sin^2(\theta) \left(2\cos^2(\theta) - \sin^2(\theta)\right) \left(\frac{\tan(\theta) \left(\tau' - \sigma_x - \frac{\sigma'}{\tan(2\theta)}\right)}{4(2\sin^2(\theta) + 1)}\right)^2 \\ + k^2 \left(2\cos^2(\theta) - 1\right)^2 = 0. \end{aligned} \quad (6.15)$$

This equation is then closed with a friction law that determines τ' .

The extension, to allow the contact point to be mis-aligned, arises by assuming the free surface of the workpiece opposite the surface in contact with the roll are circular and that the surface remaining in contact stay above yield. A friction condition on each surface can express this as a four part piece-wise function,

$$\tau' = \begin{cases} 0 & \text{if } x < x_{\text{in}} \\ -\mu\sigma' & \text{if } x_{\text{in}} < x < x_{\text{n}} \\ \mu\sigma' & \text{if } x_{\text{n}} < x < x_{\text{out}} \\ 0 & \text{if } x_{\text{out}} < x \end{cases} \quad (6.16)$$

where μ is the friction coefficient; and x_{in} , x_{n} , and x_{out} are the inlet contact point, neutral point and outlet contact point respectively. The opposite sign is taken for the bottom surface.

So once four contact points, two neutral points, and one set of force end conditions have been determined this model can be quickly evaluated as a system of three ODEs Figure 6.3 illustrates an example solution, which shows significant increases in vertical forces, moments and shear stress where only one side is in contact and typical behaviour where both sides are in contact.

The contact and neutral points must be determined from other geometric and force conditions. For example, one of the two neutral points is typically determined by the roll speed ratio, like the asymptotic model; and an angle of entry and curvature of the free surface determines one of the contact points from the other. The choice of these

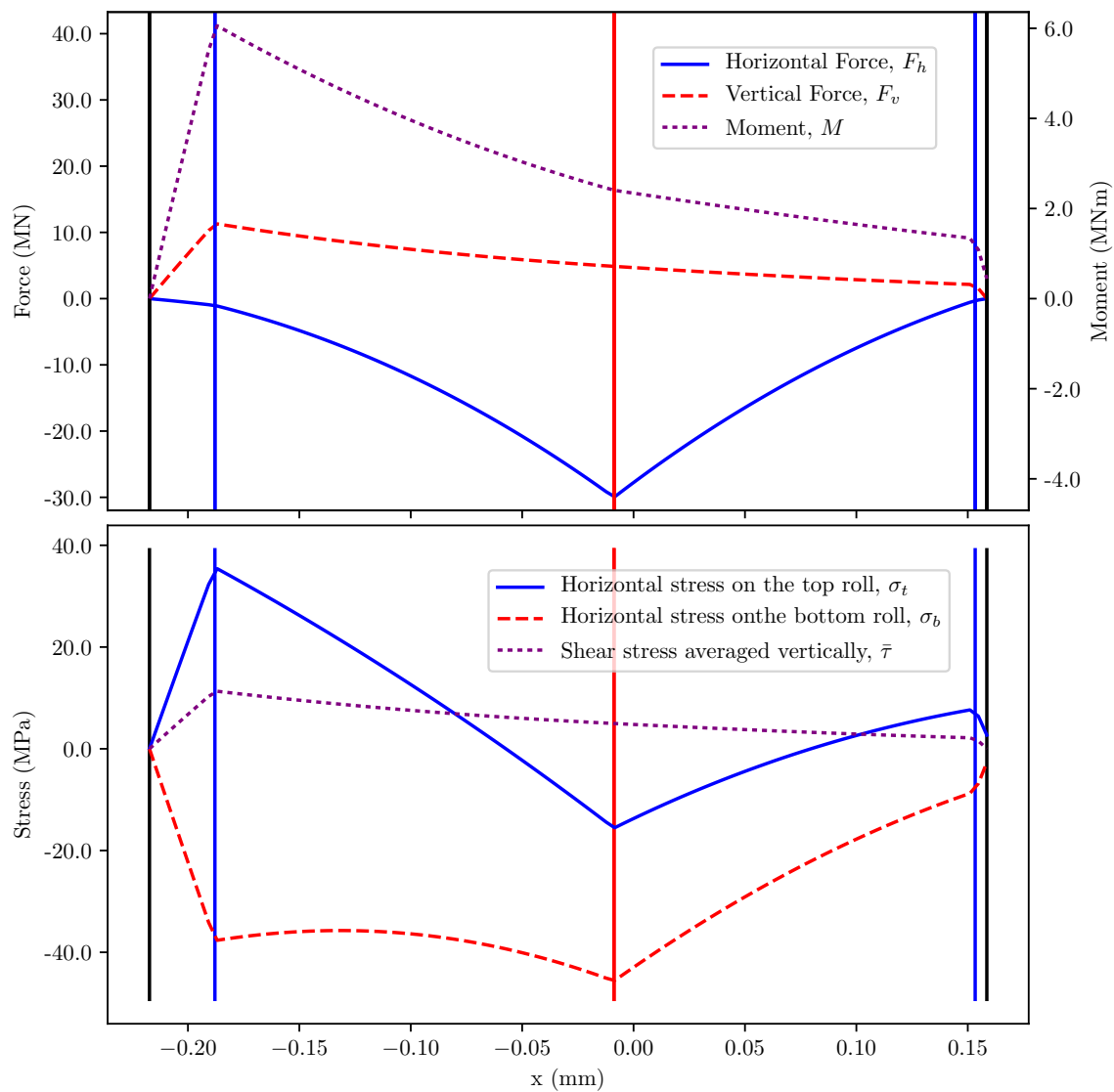


Fig. 6.3 The force and moment (top) and mean stresses (bottom) acting on vertical elements throughout the roll gap. The vertical lines indicate the contact points (black and blue) and neutral points (red). The rolling configuration is defined by $(\delta, r, k, R_t, R_b, \mu_t, \mu_b, \frac{U_t}{U_b}) = (0.01\text{m}, 0.12, 100\sqrt{3}\text{MPa}, 2.5\text{m}, 2.5\text{m}, 0.1, 0.1, 0.8)$.

conditions will be application dependent so are discussed in the context of coupling with the outer beam model in the next section.

If perfect-plasticity is assumed then both outlet contact points will be at the minimum separation between the rolls. This is the assumption used in Aboutorabi et al. (2016), which presents a model similar to that presented here. They consider rolls that are not vertically aligned, which is rotationally equivalent to the configuration considered here, less the inlet curvature. The key difference is that the Aboutorabi et al. (2016) model uses only the horizontal force balance, where this model uses moment and vertical force balances as well.

Curvature prediction with this model will be the formulation presented by Salimi et al. (2002). Aboutorabi et al. (2016) also uses this method, which makes the Aboutorabi et al. (2016) model an alternative for the framework presented here. Numerically comparing these models would be necessary to determine which is the better choice.

6.4 Coupling

The outer, curved beam model and the inner, extended slab model are coupled by both force and geometry. This coupling must provide the sufficient conditions to determine the three inlet forces, four contact points, and two neutral points of the extended slab model.

A force balance of the outer ring requires the entry and exit forces to be equal. Assuming a linear horizontal stress profile, the forces of the inner and outer models are matched for three conditions,

$$S = \Delta h(\hat{l}) \frac{\sigma_t(\hat{l}) + \sigma_b(\hat{l})}{2} = \Delta h(0) \frac{\sigma_t(0) + \sigma_b(0)}{2}, \quad (6.17)$$

$$Q = \Delta h(\hat{l}) \bar{\tau}(\hat{l}) = \Delta h(0) \bar{\tau}(0) \quad (6.18)$$

$$\text{and } M = \Delta h(\hat{l}) \frac{\sigma_t(\hat{l}) - \sigma_b(\hat{l})}{2} = \Delta h(0) \frac{\sigma_t(0) - \sigma_b(0)}{2} \quad (6.19)$$

Geometric compatibility requires matching the curvatures at both ends; the difference in the entry and exit angles; and the distance between the entry and exit. The ends of the outer beam model are taken to be on the centreline and horizontally mid-way between the two contact points. This is illustrated in Figure 6.4, where points A , C , D , and F are the contact points and points B and E are the ends of the beam model. The curvature is also taken to be the centre-line curvature of the workpiece,

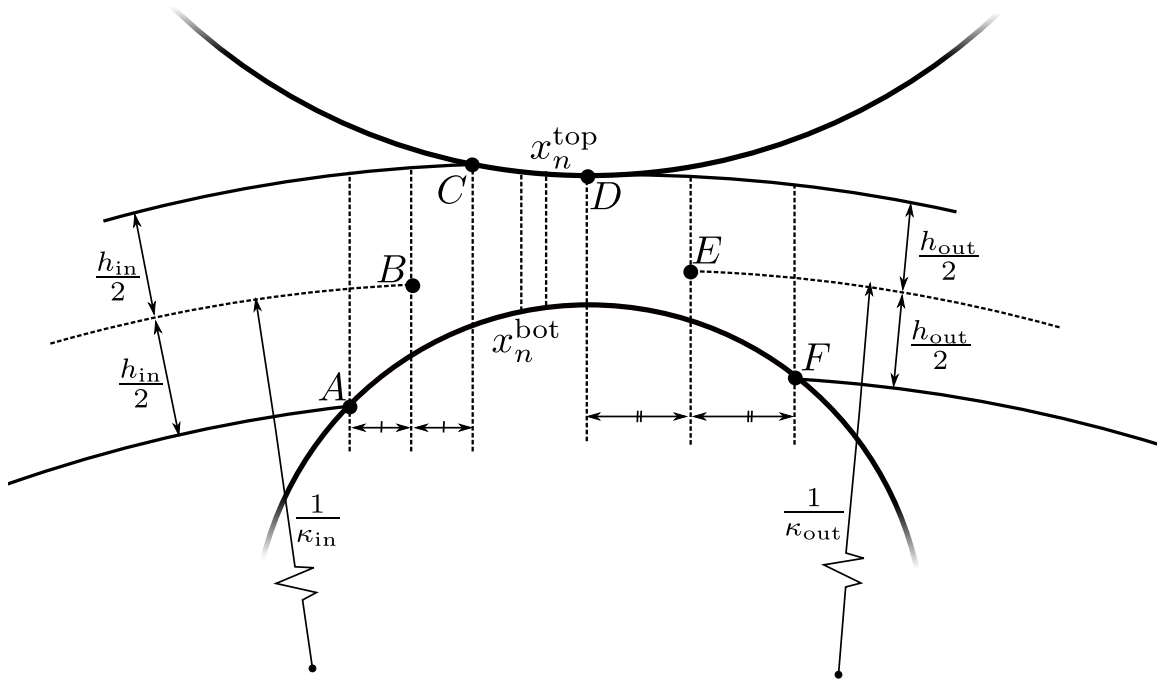


Fig. 6.4 A diagram of the geometry of the roll gap for the ring rolling processes. This illustrates the geometric compatibility of the inner and outer models.

the dotted lines from point B and E , and the free surfaces are assumed to remain circular within the inner model. The outer model, for a known set of forces, solves for the displacement between the ends, the angle difference between the ends and the curvature at each end. These geometric conditions provide three additional conditions to, say, solve for three of the contact points given the position of one.

Finally, the workpiece speed at the neutral points must match the roll surface speed ratio, determining one of the two neutral points.

This leaves two unconstrained variables. A number of approximations are plausible but it is unclear which is the best option. They include

1. Assuming perfect rigid plasticity would fix D and F to the minimum separation between the rolls, like the solution presented by Aboutorabi et al. (2016). However, the drawback is that with vertically aligned outlet conditions, no substantial bending moment or vertical force can be supported, which limits the ability to couple with the outer problem. It is also likely to be less realistic given the curved workpieces.

2. An estimate of the elastic recovery can be used to estimate the outlet thickness. Fixing one of the two outlet contact points allows the other to be determined with this condition. One such approximation, assuming vertical elastic compression only, could be $h_1(1 + E\sigma_y(x = 0)) = h_{\text{separation}}$ where h_1 is the outlet thickness, $h_{\text{separation}}$ is the roll gauge, E is Young's modulus and $\sigma_y(x = 0)$ is the vertical stress at the point of minimum separation solved as part of the slab model. This method seems like a reasonable compromise as it is able to support greater bending moments and vertical forces than the previous case. However, it has been observed in simulations that neither contact point is at the point of minimum separation so this may still be insufficient to capture the correct geometry.
3. Ideally, the position of both the outlet contact points would be determined by the model. The elastic recovery suggested previously would be one constraint; however, this leaves the system underconstrained by one constraint and no appropriate condition has been found to resolve this. It is possible that the thick-sheet model presented in Chapter 5 could be matched to a transition solution that can then be formally matched to the outer ring model.

Further to the ambiguity of the final conditions to couple these models, the sensitivity of each model makes them unsolvable using black box numerical solvers. Small displacement changes produce large force changes in the inner problem and relatively small force changes produce large displacement changes in the outer model. This has been observed using both option (1) and (2) above. Consequently, the coupled model has not been evaluated and so no further validation was achieved.

6.5 Conclusion and further work

Developing a solution method that is able to converge with the coupled models or modifying the models such that they can be solved with a black box solver are the obvious next steps. Beyond that, there are a plethora of opportunities. A longer term objective would be to include dynamics as predicting the evolution of the ring in non-stable conditions would enable considerable process innovation, discussed further in the section below.

Alternative applications of this framework could include modelling a series of rolling stands; the influence of one stand on the next could be of use in designing and controlling rolling mills. This could capture some of the new developments in

multi-stand rolling, such as snake rolling (Van Der Winden, 2005) where horizontally offset rolls with different peripheral speeds increase strains to refine grain structure and improve material properties.

By analogy, a two-dimensional version of this framework could model the English wheel process, also discussed in the following sections.

6.5.1 Dynamics

Inertia of the entire workpiece moving as a rigid body would dominate the small deflections caused by the change of shape of roll gap. Considering only displacements of the workpiece as a rigid body provides an avenue to include dynamic effects into this model. The rigid body motion of the ring will be governed by

$$\ddot{\tilde{x}} = F_{hin} + F_{hout} + \frac{M_{in}}{\tilde{y} + \Delta y_{in}} + \frac{M_{out}}{\tilde{y} + \Delta y_{out}} \quad (6.20a)$$

$$\text{and } \ddot{\tilde{y}} = F_{vin} + F_{vout} + \frac{M_{in}}{\tilde{x} + \Delta x_{in}} + \frac{M_{out}}{\tilde{x} + \Delta x_{out}} \quad (6.20b)$$

where \tilde{x} and \tilde{y} denote the centre of mass of the ring; $\Delta x_{in/out}$ and $\Delta y_{in/out}$ denote the position of the beam centreline ends; and F_{hin} , F_{hout} , F_{vin} , F_{vout} , M_{in} and M_{out} are the horizontal forces, vertical forces and moments at the inlet and outlet. The rotation of the workpiece could also be determined this way but is omitted as, once up to speed, this should not vary significantly. These equations could be solved numerically with the forcing terms from evaluating the inner model.

If successful, this model could be a major development in modelling ring rolling as the dynamics of the process have not yet been captured in an analytical model. This would support new developments of ring rolling by allowing non-circular and non-axial products to be formed. This would also facilitate the design and control of conventional ring rolling as this model could predict unstable operating regimes.

6.5.2 English wheel

The processes of wheeling, or the English wheel, is in some ways a two-dimensional rolling model and shell theory analogue to the one-dimensional slab model and beam theory ring rolling framework proposed. Ring rolling uses repeated rolling passes to locally thin and lengthen a closed beam, incrementally modifying the curvature and

size of that beam; the English wheel uses repeated rolling passes to locally thin and expand a shell, incrementally modifying the curvature of that shell.

The beginning of a model for the English wheel process is proposed here. Like the ring rolling model, an inner, plastic problem within the roll gap is considered separately from an outer elastic problem. A possible outer model is described in the following sections and some discussion of an inner model and coupling is given in a section following those.

Outer problem formulation

To model the outer plastic section, the accumulated effect of rolling will be described as pre-strains and induced curvature.

Decomposing the in-plane stress and strain into stretching and bending components, the energy density can similarly be decomposed into

$$u_s = \frac{t}{2} (\sigma_{xx} (\epsilon_{xx} - \epsilon_{x0}) + \sigma_{yy} (\epsilon_{yy} - \epsilon_{y0}) + \tau_{xy} (\gamma_{xy} - \gamma_{xy0})) \quad (6.21)$$

$$\text{and } u_b = \frac{1}{2} (M_x (\kappa_x - \kappa_{x0}) + M_y (\kappa_y - \kappa_{y0}) + 2M_{xy} (\kappa_{xy} - \kappa_{xy0})) \quad (6.22)$$

where u_s and u_b are the stretching and bending energy densities; σ_{xx} , σ_{yy} , τ_{xy} , M_x , M_y and M_{xy} are the stretching and bending stresses; and, ϵ_{xx} , ϵ_{yy} , γ_{xy} , κ_x , κ_y and κ_{xy} are the stretching and bending strains. The naughted strain variables denote the non-stressed state due to the pre-straining of rolling. Using a linear-elastic constitutive law,

$$\epsilon_{xx} - \epsilon_{x0} = \frac{1}{E} (\sigma_{xx} - \nu\sigma_{yy}), \quad (6.23)$$

$$\epsilon_{yy} - \epsilon_{y0} = \frac{1}{E} (\sigma_{yy} - \nu\sigma_{xx}), \quad (6.24)$$

$$\gamma_{xy} - \gamma_{xy0} = \frac{\tau_{xy}}{E}, \quad (6.25)$$

$$M_x = \frac{Et^3}{12(1-\nu^2)} (\kappa_x - \kappa_{x0} + \nu(\kappa_y - \kappa_{y0})), \quad (6.26)$$

$$M_y = \frac{Et^3}{12(1-\nu^2)} (\kappa_y - \kappa_{y0} + \nu(\kappa_x - \kappa_{x0})) \quad (6.27)$$

$$\text{and } M_{xy} = \frac{Et^3}{6} \kappa_{xy} \quad (6.28)$$

where t is the sheet thickness, the energy density equations can be written as

$$u_s = \frac{t}{2E} (\sigma_{xx}^2 + \sigma_{yy}^2 - 2\nu\sigma_{xx}\sigma_{yy} + \tau_{xy}^2) - \frac{t}{2E} (\sigma_{xx}\epsilon_{x0} + \sigma_{yy}\epsilon_{y0} + \tau_{xy}\gamma_{xy0}) \quad (6.29)$$

$$\text{and } u_b = \frac{Et^3}{24(1-\nu^2)} (\kappa_x^2 + \kappa_y^2 + 2\nu\kappa_x\kappa_y + 4(1-\nu^2)\kappa_{xy}^2) \\ - \frac{Et^3}{24(1-\nu^2)} (\kappa_{x0}(\kappa_x + \nu\kappa_y) + \kappa_{y0}(\kappa_y + \nu\kappa_x) + 4(1-\nu^2)\kappa_{xy0}\kappa_{xy}). \quad (6.30)$$

Minimising these energies will give equilibrium states of the shell. However, this formulation requires compatibility and equilibrium to be enforced. Compatibility requires the necessary stretching deformation for changes in Gaussian curvature and can be expressed as

$$-\Delta K = (\kappa_x\kappa_y - \kappa_{xy}^2) = \left(\frac{\partial^2\epsilon_y}{\partial x^2} + \frac{\partial^2\epsilon_x}{\partial y^2} - \frac{\partial^2\gamma_{xy}}{\partial x\partial y} \right). \quad (6.31)$$

Equilibrium is enforced by using the Airy stress function, which gives

$$\sigma_{xx} = \frac{\partial^2\varphi}{\partial y^2}, \quad (6.32a)$$

$$\sigma_{yy} = \frac{\partial^2\varphi}{\partial x^2} \quad (6.32b)$$

$$\text{and } \tau_{xy} = -\frac{\partial^2\varphi}{\partial x\partial y}. \quad (6.32c)$$

This gives the constrained optimisation problem, to minimise the energy,

minimise

$$\int_A \frac{t}{2E} \left(\left(\frac{\partial^2\varphi}{\partial y^2} \right)^2 + \left(\frac{\partial^2\varphi}{\partial x^2} \right)^2 - 2\nu \left(\frac{\partial^2\varphi}{\partial y^2} \frac{\partial^2\varphi}{\partial x^2} \right) + \left(\frac{\partial^2\varphi}{\partial x\partial y} \right)^2 \right. \\ \left. - \frac{\partial^2\varphi}{\partial y^2}\epsilon_{x0} - \frac{\partial^2\varphi}{\partial x^2}\epsilon_{y0} - \frac{\partial^2\varphi}{\partial x\partial y}\gamma_{xy0} \right) \\ + \frac{Et^3}{24(1-\nu^2)} (\kappa_x^2 + \kappa_y^2 + 2\nu\kappa_x\kappa_y + 4(1-\nu^2)\kappa_{xy}^2) \\ - \frac{Et^3}{24(1-\nu^2)} (\kappa_{x0}(\kappa_x + \nu\kappa_y) + \kappa_{y0}(\kappa_y + \nu\kappa_x) + 4(1-\nu^2)\kappa_{xy0}\kappa_{xy}) dA \quad (6.33a)$$

subject to

$$\left(\kappa_x \kappa_y - \kappa_{xy}^2\right) = \frac{1}{E} \left(3 \frac{\partial^4 \varphi}{\partial^2 x \partial^2 y} - \nu \left(\frac{\partial^4 \varphi}{\partial x^4} + \frac{\partial^4 \varphi}{\partial y^4} \right) \right), \quad (6.33b)$$

and the plate boundary conditions of zero force. This is a quadratic minimisation problem with quadratic constraints.

Outer problem solution

The constrained optimisation can be implemented using Chebyshev polynomials. A square, unit length shell is assumed and each of the variables, κ_x , κ_y and φ , are expanded using

$$U(x, y) = \sum_{i=0, j=0}^{i=N, j=M} u_{ij} T_i(2x-1) T_j(2y-1). \quad (6.34)$$

Equation (6.33a) and equation (6.33b) can be solved as a constrained problem or expressed using a Lagrange multiplier: in matrix form,

$$\begin{aligned} & \text{minimise}_{\lambda, \mu, \mathbf{x}} \\ & \mathbf{x}^T \cdot A \cdot \mathbf{x} + \lambda (\mathbf{c} \cdot \mathbf{x} - 2\mathbf{c} \cdot \mathbf{x}_0 + \mathbf{x} \cdot C \cdot \mathbf{x})^2 + \mu (\mathbf{x} \cdot B)^2. \end{aligned} \quad (6.35)$$

The minimisation of either formulation has not yet been successfully implemented.

This is due to two challenges. First, compatible solutions as initial guesses are not trivial. It may be fruitful to investigate the dual problem, optimising for compatibility given equilibrium as a condition, as the trivial zero-stress state satisfies equilibrium but not compatibility. Secondly, many local optima can exist, which represent locally stable states of the shell. Locally stable shapes may be desired as intermediate steps in a wheeling process. Unfortunately, it is not clear how to minimise either formulation to achieve a particular state, nor whether a given state is globally or locally optimal. There has been a great deal of research conducted on the topic of multiply-stable shells, such as K. A. Seffen et al. (2011), K. Seffen (2007), and Vidoli (2013), which may offer solutions to these challenges.

Some recent work has also been found that solves this problem for a different application using finite element analysis (Jones et al., 2015) over the spectral type approach presented here.

Inner problem and coupling

The other key component for this model is the inner problem which is by no means trivial. A finite element analysis of this small region could be feasible; however, it would be more desirable to construct a faster, more analytical model. Three-dimensional rolling models have been presented in literature. One example is R. E. Johnson (1991), which assumes the roll gap width is of similar size to the roll gap length and derives Poisson's equation for the horizontal velocity field. Although an appropriate scaling for wheeling and alternative boundary conditions would have to be incorporated, R. E. Johnson (1991) provides a possible means of approaching this problem.

Once an inner solution is developed, these solutions would need to be coupled then solved for each update of the shape of the workpiece as the process is incrementally stepped through.

This would be the first mathematical model of the English Wheel and provide a basis for its control and automation. This approach could also be used to model other sheet forming processes with localised deformations, spinning for example.

Chapter 7

Conclusion and further work

This thesis makes systematic progress in understanding the complex behaviour of asymmetric rolling. This includes

- asymmetric and clad-sheet asymptotic models, which illustrate a robust method of constructing thin-sheet rolling models appropriate for real-time prediction and control;
- a statistical analysis and review of studies into curvature to characterise the complex trends and gather evidence about the mechanisms driving it;
- a thick-sheet asymptotic model with new scalings to capture through-thickness variation in stress and strain fields, which could be used to optimise material evolution during the process;
- and novel frameworks for modelling ring rolling and the English wheel process, which would facilitate, for the first time in the latter case, efficient numerical control.

In retrospect, these investigations and models have advanced three main areas: the study of curvature response to rolling configurations, primarily investigated in Chapter 4 with some supporting simulation results from Chapter 5; the development of asymptotic models, primarily the three models from Chapter 2, Chapter 3 and Chapter 5; and the application of rolling models to describe other processes, specifically the concepts presented in Chapter 6 with some potential approaches arising from the model in Chapter 5.

Curvature prediction

Workpiece curvature in rolling is a long standing, significant problem as it can cause damage to the rolling machinery and stop production. Curvature control also has the potential to unlock lower-energy asymmetric processes that can produce higher-quality materials with more varied geometry. Surprisingly, it is not as well understood as one might think and the underlying physical mechanisms remain undetermined.

Contradictions were found in the literature; for example, induced curvature was observed both towards and away from the roll with higher friction coefficient. While some contradictions can be reconciled by considering additional parameters, such as reduction and roll gap aspect ratio, others remain dissonant. Data from fifteen publications were digitised to resolve these remaining contradictions and find unifying curvature trends. Despite being the largest data-set yet analysed, the resulting statistical analysis was unable to produce a robust model to predict curvature; however, it did allow insight to be gained that could prove useful to future work. Strong interaction was found between the roll radius asymmetry, the reduction and the roll gap aspect ratio, as well as significant dependence on material properties. This insight should be used to guide which parameters to consider in future studies, and what behaviours a future predictive model must exhibit.

Published analytical models were also studied. Many were not able to be reproduced due to omissions or errors in those papers and the two that were implemented, Dewhurst et al. (1974) and Salimi et al. (2002), showed only linear trends between curvature and any of the three asymmetries considered. These findings cast doubt on the proposed curvature mechanisms these works present. Evidence from the literature review suggests that curvature may instead be driven by asymmetric strains toward the exit of the roll gap; Yoshii et al. (1991) observed larger regions of strain near the exit of the roll gap, which varies with geometry and roll speed asymmetry.

The illusive trends and elusive mechanisms call for more investigation in this area and this thesis can hopefully provide a basis to inform this work. A more comprehensive analysis of analytical models may reveal phenomena and mechanisms captured by some that are missed by others; in particular, the Collins et al. (1975) model appears promising for capturing non-linear trends with varying reduction. It seems doubtful that any single model from literature will robustly predict curvature over a range of parameters; but, insights pieced together from a range of models could inform the development of a more unifying understanding. Alternatively, extensive simulations

of various rolling configurations, particularly probing the interactions discussed in Chapter 4, would provide a better dataset to repeat the study conducted here.

Asymptotic modelling of rolling

Two sets of assumptions were used to construct a number of new asymmetric rolling models with asymptotic techniques. The first uses the model formulation of Domanti et al. (1995) and the scaling presented in Cherukuri et al. (1997). Asymmetries in roll size, roll speed and roll-workpiece friction were added. The leading order solutions can be made to agree with slab models, Y. Hwang et al. (1993) for example, but additionally provide complete stress and strain field solutions. Further, asymptotic correction terms are solved to provide increased resolution to these field solutions.

The systematic nature of this method means alternative friction and material models are easily incorporated into the formulation. This includes, but is not limited to, any friction model that remains small compared to the yield stress and any material model with a yield surface dependent on strains. This has been illustrated with models of alternative friction laws and of an asymmetric clad-sheet workpiece.

Comparisons were made with finite element simulations from *ABAQUS*, the commercial finite element package. As expected from published slab models, roll force, roll torque and the neutral point position are predicted well. Also expected from the asymptotic assumptions, accuracy deteriorates as the roll gap aspect ratio or friction coefficients increase, where the latter may not have been expected from slab models. This illustrates the benefits of explicit scaling assumptions. The models presented here, and most slab models, also assume that the material throughout the roll gap has reached yield and that the contact points between the workpiece and the rolls are horizontally aligned. Any amount of clad-sheet inhomogeneity is believed to violate this last assumption resulting in poorly predicted roll torques. The leading hypothesis is that elastic strains in each layer of the sheet induce inlet curvature. This would also occur for all slab models and further illustrates the need for validation of all models in the regimes in which they are to be used.

Yet another discrepancy that illustrates the need for validation is in the shear stress and vertical velocity fields, where the simulations exhibit oscillations, or lobes, throughout the roll gap. These are not captured by the thin-sheet asymptotic models, nor by other published analytical models. In the limit of small roll gap aspect ratios, the limit in which the thin-sheet asymptotic models were derived, sufficiently many lobes merge together so that the shear strain fields agree with the thin-sheet models;

however, more complex behaviour is exhibited for roll gap aspect ratios as small as 0.1. This motivated another model with a novel set of assumptions.

This second set of asymptotic assumptions were chosen to allow through-thickness variation of stress and strain. By considering small reductions instead of a small roll gap aspect ratio, the governing equations took the form of two sets of wave equations at leading order without changing the boundary condition. A minimal implementation of this thick-sheet model captures the shear lobes observed in the numerical results, despite crude approximations defining the new inlet boundary conditions. This model also shows some indication of capturing non-linear behaviour in curvature, although further development is required to make curvature predictions directly.

This project, in collaboration with the Department of Engineering, began with the intention of constructing a demonstration rolling machine, able to apply heating, asymmetric roll drive and arbitrary end conditions. Although this became uneconomical for this project, such an endeavour would be beneficial as it could be used to find the operational limits of these models and inform which subsequent developments are important. For example, the alignment of the entry and exit of the workpiece has been shown to be important in some cases; however, these conditions remain uncharacterised. Further, these models could be directly applicable to processes like extrusion or drawing; however, validation of these extreme forcing regimes would be required.

From what is known, additional phenomena can be identified to tailor these models to specific applications. This could include

- strain or work hardening to more accurately model specific workpiece materials;
- temperature dependence and micro-structure evolution modelling to model hot rolling processes;
- elastic roll response to model the roll flattening that occurs during foil rolling;
- or, span-wise variation to capture roll deflections and to begin modelling roll forming.

While elasticity has been neglected in most of this work, owing to the yield stress being orders of magnitude smaller than the Young's modulus, it impacts rolling processes in a range of ways. For example, residual stresses induce inlet and outlet curvature as well as impact product quality: spring back changes the final thickness of the product; and a sub-yield region or compressibility may regularise the stress around

the neutral point. Unfortunately, including elasticity into models has proven difficult due to the challenges discussed in the next section. However, the new thick-sheet asymptotic model exhibits potential for matching with an elastic outer solution, which could prove a fruitful avenue of future investigation.

Rolling model applications

Assuming curvature prediction can be achieved and assuming a model similar to the Aboutorabi et al. (2016) model is such a predictor, a coupling with the Timoshenko et al. (1925) curved beam model is proposed for modelling ring rolling. While the sensitivities of both models meant the coupling could not be made to converge, it offers a framework to model ring rolling without assumptions of circularity, centrality or coaxiality, which is substantially more general than existing models. Time stepping is proposed to also incorporate dynamics into the model, which would facilitate control and tool path optimisation. More sophisticated simulations than those conducted here could provide verification of the inner and outer models independently, or insight about how they interact. Understanding the role of guide rolls and the forcing of the ring into non-central positions would also be useful for control.

With the development of a finite-width-roll model and shell theory, this framework can be extended to three-dimensions for modelling the English wheel. Investigation into the rolling regime that occurs during the English wheel process would be necessary but existing three-dimensional models could form a starting point for subsequent modelling work (Domanti et al., 1994; Karabin et al., 1993). An outer shell theory model was formulated for this application but not solved. Jones et al. (2015) presents an alternative, finite-element-type solution to a similar formulation, which could be used instead. No automation, or even modelling, of this process has yet been published so developing this area could contribute to a new CNC forming process.

In a more general sense, the big challenges preventing models of other forming processes are threefold: mixed boundary conditions, because forming tools are typically smaller than the workpiece; the transition between sub-yield and yield, because it is rare that plastic deformation occurs everywhere in a process; and the evolution of geometry, because most processes are not continuous. None of these challenges occur when considering the inner rolling problem, hence the many advances in this area. The models presented in Chapter 6 make crude approximations about the first two challenges, and an approach for the third is presented as a suggestion for future work. More successful treatment of these challenges, such as matching the model in

Chapter 5 to a mixed boundary problem or solving the elastic-plastic transition with a free surface, could unlock modelling of numerous processes and considerably progress the field.

The modelling presented here has matured rolling models sufficiently that several new approaches are now available. It is hoped that future research can build on this work to overcome the identified challenges, since analytical models of forming processes, rather than numerical solutions, can better facilitate control systems to bring forming into a CNC world and unleash an era of bespoke, low-energy, high-quality manufacturing.

References

- Aboutorabi, A., Assempour, A., and Afrasiab, H. (Jan. 2016). “Analytical approach for calculating the sheet output curvature in asymmetrical rolling: In the case of roll axis displacement as a new asymmetry factor”. In: *International Journal of Mechanical Sciences* 105, pp. 11–22.
- Afrouz, F. and Parvizi, A. (Oct. 2015). “An analytical model of asymmetric rolling of unbounded clad sheets with shear effects”. In: *Journal of Manufacturing Processes* 20, pp. 162–171.
- Akbari Mousavi, S.A.A., Ebrahimi, S.M., and Madoliat, R. (June 2007). “Three dimensional numerical analyses of asymmetric rolling”. In: *Journal of Materials Processing Technology* 187-188, pp. 725–729.
- Akcan, M.H. (July 2009). “Analysis of profiled ring rolling”. M.Sc. Thesis. The Department of Manufacturing Engineering, Atilim University.
- Alexander, J.M. (1955). “A slip line field for the hot rolling process”. In: *Proceedings of the Institution of Mechanical Engineers* 169, p. 1021.
- Alexander, J.M. (Feb. 1972). “On the theory of rolling”. In: *Proceedings of the Royal Society A: Mathematical, Physical and Engineering Sciences* 326.1567, pp. 535–563.
- Allwood, J. M., Cullen, J. M., and Carruth, M. A. (2012). *Sustainable materials with both eyes open*. English. Cambridge, England: UIT Cambridge Ltd.
- Anders, D., Münker, T., Artel, J., and Weinberg, K. (June 2012). “A dimensional analysis of front–end bending in plate rolling applications”. In: *Journal of Materials Processing Technology* 212.6, pp. 1387–1398.
- Arthington, M. R., Cleaver, C. J., Huang, J., and Duncan, S. R. (2016). “Curvature control in radial-axial ring rolling”. In: *IFAC-PapersOnLine* 49.20, pp. 244–249.
- Berti, G.A., Quagliato, L., and Monti, M. (Aug. 2015). “Set—up of radial–axial ring—rolling process: Process worksheet and ring geometry expansion prediction”. In: *International Journal of Mechanical Sciences* 99, pp. 58–71.

- Bland, D. R. and Ford, H. (June 1948). “The calculation of roll force and torque in cold strip rolling with tensions”. In: *Proceedings of the Institution of Mechanical Engineers* 159, p. 144.
- Bland, D.R. and Ford, H. (1948). “An approximate treatment of the elastic compression of the strip in cold rolling”. In: *Journal of Iron Steel Institute* 171, pp. 245–249.
- Buxton, S. A. E. and Browning, S. C. (1972). “Turn—up and turn—down in hot rolling: a study on a model mill using plasticine”. In: *Journal of Mechanical Engineering Science* 14.4, pp. 245–254.
- Cawthorn, C. J., Minton, J. J., and Brambley, E. J. (Feb. 2016). “Asymptotic analysis of cold sandwich rolling”. In: *International Journal of Mechanical Sciences* 106, pp. 184–193.
- Chekmarev, A. P. and Nefedov, A. A. (1956). “Rolling with unequal diameter rolls (complex cases of rolling)”. In: *Obrabotka Metallov Davleniem* 4, pp. 2–15.
- Cherukuri, H.P., Johnson, R. E., and Smelser, R.E. (1997). “A rate-dependent model for hot—rolling”. In: *International Journal of Mechanical Sciences* 39.6, pp. 705–727.
- Collins, I. F. (1969). “Slipline field solutions for compression and rolling with slipping friction”. In: *International Journal of Mechanical Sciences* 11, pp. 971–978.
- Collins, I. F. and Dewhurst, P. (1975). “A slipline field analysis of asymmetrical hot rolling”. In: *International Journal of Mechanical Sciences* 17, pp. 643–651.
- Dassault Systemes (2012a). *ABAQUS 6.12*.
- Dassault Systemes (2012b). *ABAQUS 6.12 example problems manual*.
- Dassault Systemes (2012c). *ABAQUS 6.12 theory manual*.
- Dassault Systemes (2012d). *ABAQUS 6.12 user’s manual*.
- Dewhurst, P. and Collins, I. F. (1973). “A matrix technique for constructing slip-line field solutions to a class of plane strain plasticity problems”. In: *International Journal for Numerical Methods in Engineering* 7.3, pp. 357–378.
- Dewhurst, P., Collins, I. F., and Johnson, W. (June 1974). “A theoretical and experimental investigation into asymmetrical hot rolling”. In: *International Journal of Mechanical Sciences* 16.6, pp. 389–397.
- Domanti, S. A. and McElwain, D. L. S. (1995). “Two—dimensional plane strain rolling: an asymptotic approach to the estimation of inhomogeneous effects”. In: *International Journal of Mechanical Sciences* 37.2, pp. 175–196.
- Domanti, S. A. and McElwain, D. L. S. (Jan. 1998). “Cold rolling of flat metal products: contribution of mathematical modelling”. In: *Proceedings of the Institution of*

- Mechanical Engineers, Part B: Journal of Engineering Manufacture* 212.1, pp. 73–86.
- Domanti, S. A., McElwain, D. L. S., and Middleton, R. H. (1994). “Model of cold rolling of thin metal sheets between nonparallel rolls”. In: 18.July.
- Dvorkin, E.N., Goldschmit, M.B., Cavaliere, M.A., Amenta, P.M., Marini, O., and Stroppiana, W. (1997). “2D finite element parametric studies of the flat-rolling process”. In: *Journal of Materials Processing Technology* 68, pp. 99–107.
- Dyja, H., Korczak, P., Pilarczyk, J.W., and Grzybowski, J. (1994). “Theoretical and experimental-analysis of plates asymmetric rolling”. In: *Journal of Materials Processing Technology* 45.1-4, pp. 167–172.
- Eizadjou, M., Danesh Manesh, H., and Janghorban, K. (2008). “Investigation of roll bonding between aluminium alloy strips”. In: *Materials and Design* 29.4, pp. 909–913.
- Farhat-Nia, F., Salimi, M., and Movahhedy, M.R. (July 2006). “Elasto-plastic finite element simulation of asymmetrical plate rolling using an ALE approach”. In: *Journal of Materials Processing Technology* 177.1-3, pp. 525–529.
- Farhatnia, F. and Salimi, M. (2011). “Effect of entry bending moment on exit curvature in asymmetrical rolling”. In: *International Journal of Engineering, Science and Technology* 3.4, pp. 147–163.
- Fu, Y., Xie, S., Xiong, B., Huang, G., and Cheng, L. (2012). “Effect of rolling parameters on plate curvature during snake rolling”. In: *Journal Wuhan University of Technology, Materials Science Edition* 27.2, pp. 247–251.
- Gadala, M. S. and Wang, J. (2000). “Elasto—plastic finite element simulation of rolling and compression between wedge-shaped dies”. In: *Journal of Materials Processing Technology* 97.1-3, pp. 132–147.
- Ghobrial, M. I. (1989). “A photoelastic investigation on the contact stresses developed in rolls during asymmetrical flat rolling”. In: *International Journal of Mechanical Sciences* 31.10, pp. 751–764.
- Gong, W., Pang, Y., Liu, C., Yu, H., Lu, B., and Zhang, M. (Jan. 2010). “Effect of asymmetric friction on front end curvature in plate and sheet rolling process”. In: *Journal of Iron and Steel Research, International* 17.1, pp. 22–26.
- Govindarajan, R.M. and Aravas, N. (1991). “Asymptotic analysis of extrusion of porous metals”. In: *Journal of Mechanical Science* 33.7, pp. 505–527.

- Gudur, P.P., Salunkhe, M.A., and Dixit, U.S. (Feb. 2008). "A theoretical study on the application of asymmetric rolling for the estimation of friction". In: *International Journal of Mechanical Sciences* 50.2, pp. 315–327.
- Guo, L. and Yang, H. (2011). "Towards a steady forming condition for radial-axial ring rolling". In: *International Journal of Mechanical Sciences* 53.4, pp. 286–299.
- Hao, L., Di, H.S., and Gong, D.Y (May 2013). "Analysis of sheet curvature in asymmetrical cold rolling". In: *International Journal of Iron and Steel Research* 20.5, pp. 34–37.
- Harrer, O., Philipp, M., and Pokorný, I. (2003). "Numerical simulation of asymmetric effects in plate rolling". In: *Acta Metallurgica Slovaca* 9.4, pp. 306–313.
- Hartley, P., Sturgess, C.E.N, Liu, C., and Rowe, G.W. (1989). "Experimental and theoretical studies of workpiece deformation, stress, and strain during flat rolling". In: *International Materials Reviews* 34.1, pp. 19–34.
- Hawkyard, J.B., Johnson, W., Kirkland, J., and Appleton, E. (Nov. 1973). "Analyses for roll force and torque in ring rolling, with some supporting experiments". In: *International Journal of Mechanical Sciences* 15.11, pp. 873–893.
- Hua, L., Deng, J., Qian, D., Lan, J., and Long, H. (2016). "Modeling and application of ring stiffness condition for radial-axial ring rolling". In: *International Journal of Machine Tools and Manufacture* 110, pp. 66–79.
- Hwang, Y. M. and Tzou, G. Y. (1996a). "An Analytical Approach to Asymmetrical Cold- and Hot-Rolling of Clad Sheet Using the Slab Method". In: *Journal of Materials Processing Technology* 62, pp. 249–259.
- Hwang, Y. M. and Tzou, G. Y. (1996b). "Stress analysis of asymmetrical cold rolling of clad sheet using the slab method". In: *Journal of Materials Engineering and Performance* 5.October, pp. 621–631.
- Hwang, Y., Chen, D., and Tzou, G. (1999). "Study on asymmetrical sheet rolling by the finite element method". In: *The Chinese Journal of Mechanics* 15.4, pp. 149–155.
- Hwang, Y. and Chen, T. (1996a). "Analysis of asymmetrical sheet rolling by stream function method". In: *The Japan Society of Mechanical Engineers* 39.4, pp. 598–605.
- Hwang, Y., Chen, T., and Hsu, H. (1996b). "Analysis of asymmetrical clad sheet rolling by stream function method". In: *International Journal of Mechanical Sciences* 38.4, pp. 443–460.
- Hwang, Y. and Tzou, G. (1993). "An analytical approach to asymmetrical cold strip rolling using the slab method". In: *Journal of Materials Engineering and Performance* 2, pp. 597–606.

- Hwang, Y. and Tzou, G. (1997). “Analytical and experimental study on asymmetrical sheet rolling”. In: *International Journal of Mechanical Sciences* 39.3, pp. 289–303.
- Jeswiet, J. and Greene, P.G. (Dec. 1998). “Experimental measurement of curl in rolling”. In: *Journal of Materials Processing Technology* 84.1-3, pp. 202–209.
- Johnson, R. E. (1987). “Conical extrusion of a work-hardening material: an asymptotic analysis”. In: *Journal of Engineering Mathematics* 21.4, pp. 295–329.
- Johnson, R. E. (1991). “Shape forming and lateral spread in sheet rolling”. In: *International Journal of Mechanical Sciences* 33.6, pp. 449–469.
- Johnson, R. E. (1994a). “Cold sheet rolling with unequal friction at the roll-sheet interfaces”. In: *Manufacturing Science and Engineering*. Vol. 68, pp. 619–626.
- Johnson, R. E. (June 1994b). “The effect of friction and inelastic deformation on chatter in sheet rolling”. In: *Proceedings of the Royal Society A: Mathematical, Physical and Engineering Sciences* 445.1925, pp. 479–499.
- Johnson, R. E. and Keanini, R.G. (1998). “An asymptotic model of work roll heat transfer in strip rolling”. In: *International Journal of Mass Transfer* 41, pp. 871–879.
- Johnson, R. E. and Smelser, R.E. (1992). “An asymptotic formulation of shear effects in two dimensional rolling”. In: *Journal of Materials Processing Technology* 34, pp. 311–318.
- Johnson, W. and Needham, G. (1966a). “An experimental study of asymmetrical rolling”. In: *Proceedings of the Institution of Mechanical Engineers* 180.
- Johnson, W. and Needham, G. I. (June 1966b). “Further experiments in asymmetrical rolling”. In: *International Journal of Mechanical Sciences* 8, pp. 443–455.
- Jones, G. W. and Mahadevan, L. (2015). “Optimal control of plates using incompatible strains”. In: *Nonlinearity* 28.9, pp. 3153–3174. arXiv: 1412.6940.
- Karabin, M. E. and Johnson, R. E. (May 1993). “A comparison of asymptotic and numerical rolling models for quasi-three-dimensional problems”. In: *International Journal of Mechanical Sciences* 35.5, pp. 425–439.
- Karabin, M. E. and Smelser, R. E. (Jan. 1990). “A quasi-three-dimensional analysis of the deformation processing of sheets with applications”. In: *International Journal of Mechanical Sciences* 32.5, pp. 375–389.
- Karman, T. von (1925). “Beitrag zur theorie des walzvorganges”. In: *Zeitschrift fur angewandte Mathematik und Mechanik* 5, pp. 139–141.
- Kawałek, A. (Nov. 2004). “Forming of band curvature in asymmetrical rolling process”. In: *Journal of Materials Processing Technology* 155-156, pp. 2033–2038.

- Kennedy, G.E. and Slamar, F. (1958). “Turn-up and turn-down in hot rolling”. In: *Iron and Steel Engineer* 35, p. 71.
- Kiuchi, M. M. and Hsiang, S. H. (1986). “Analytical model of asymmetrical rolling process of sheets”. In: *Proceedings of the 14th NAMRC, Society of Manufacturing Engineers, Minneapolis*, p. 384.
- Kiuchi, M., Hsiang, S., and Hwang, Y. (1987). “Analytical model of asymmetrical rolling processes of sheets”. In: *4th International Steel Rolling Conference 2*.
- Knight, C. W., Hardy, S. J., Lees, A. W., and Brown, K. J. (2003). “Investigations into the influence of asymmetric factors and rolling parameters on strip curvature during hot rolling”. In: *Journal of Materials Processing Technology* 134, pp. 180–189.
- Knight, C. W., Hardy, S. J., Lees, A. W., and Brown, K. J. (Sept. 2005). “Influence of roll speed mismatch on strip curvature during the roughing stages of a hot rolling mill”. In: *Journal of Materials Processing Technology* 168.1, pp. 184–188.
- Langlands, T.A.M. and McElwain, D.L.S. (2002). “A modified Hertzian foil rolling model: approximations based on perturbation methods”. In: 44, pp. 1715–1730.
- Lee, C., Park, J., Tyne, C., and Moon, Y. (2015). “Analysis of warping during flat rolling of bimetallic slabs”. In: *Proceedings of the Institution of Mechanical Engineers, Part C: Journal of Mechanical Engineering Science* 229.17, pp. 3153–3161.
- Li, S., Qin, N., Liu, J., and Zhang, X. (2016). “Microstructure, texture and mechanical properties of AA1060 aluminum plate processed by snake rolling”. In: *Materials and Design* 90, pp. 1010–1017.
- Lin, H. and Zhi, Z. Z. (1997). “The extremum parameters in ring rolling”. In: *Materials Processing Technology* 69, pp. 273–276.
- Lu, J.-S., Harrer, O.-K., Schwenzfeier, W., and Fischer, F.D. (Jan. 2000). “Analysis of the bending of the rolling material in asymmetrical sheet rolling”. In: *International Journal of Mechanical Sciences* 42.1, pp. 49–61.
- Maleki, H., Bagherzadeh, S., Mollaei-Dariani, B., and Abrinia, K. (2013). “Analysis of bonding behaviour and critical reduction of two-layer strips in clad cold rolling process”. In: *Journal of Materials Engineering and Performance* 22.4, pp. 917–925.
- Mamalis, A. G. (1975). “Profile Ring Rolling”. PhD thesis.
- Manesh, H. Danesh and Taheri, A. Karimi (2005). “Theoretical and experimental investigation of cold rolling of tri-layer strip”. In: *Journal of Materials Processing Technology* 166.2, pp. 163–172.

- Markowski, J., Dyja, H., Knapiński, M., and Kawalek, A. (July 2003). “Theoretical analysis of the asymmetric rolling of sheets on leader and finishing stands”. In: *Journal of Materials Processing Technology* 138.1-3, pp. 183–188.
- MathWorks (2015). “MATLAB Primer R2015a”. In:
- Minton, J. J. and Brambley, E. J. (2017). “Meta-analysis of curvature trends in asymmetric rolling”. In: *Proceedings of the ICTP2017* September.
- Minton, J. J., Cawthorn, C. J., and Brambley, E. J. (2016). “Asymptotic analysis of asymmetric thin sheet rolling”. In: *International Journal of Mechanical Sciences* 113, pp. 36–48.
- Mischke, J. (1996). “Equations of Strip Equilibrium During Asymmetrical Flat Rolling”. In: *Journal of Materials Processing Technology* 61, pp. 382–394.
- Montmitonnet, P. (Oct. 2006). “Hot and cold strip rolling processes”. In: *Computer Methods in Applied Mechanics and Engineering* 195.48-49, pp. 6604–6625.
- Montmitonnet, P. and Buessler, P. (1991). “A review on theoretical analyses of rolling in europe”. In: 31.6, pp. 525–538.
- Nadai, A. (1931). ““Plasticity””. In: *Journal of Applied Mechanics* 6, A–55.
- Nakajima, K. (1980). “(Unknown)”. In: *Proceedings of the 31st Japan Society of Manufacturing Engineers (JSTP) Conference*, p. 177.
- Nakajima, K. (1984). “(Unknown)”. In: *J. Jpn. Soc. Technol. of Plasticity* 25, p. 987.
- Orowan, E. (July 1943). “The calculation of roll pressure in hot and cold flat rolling”. In: *Proceedings of the Institution of Mechanical Engineers* 150, pp. 140–167.
- Orowan, E. and Pascoe, K.J. (1946). *First Report of the Rolling-Mill Research Subcommittee*. London: Iron and Steel Institute.
- Pan, D. and Sansome, D. H. (1982). “An experimental study of the effect of roll-speed mismatch on the rolling load during the cold rolling of thin strip”. In: *Journal of Mechanical Working Technology* 6, pp. 361–377.
- Pan, S. C., Huang, M. N., Tzou, G. Y., and Syu, S. W. (2006). “Analysis of asymmetrical cold and hot bond rolling of unbounded clad sheet under constant shear friction”. In: *Journal of Materials Processing Technology* 177.1-3, pp. 114–120.
- Pan, S.C., Tzou, G., Huang, M. N., and Huang, C. W. (2008). “Analytical Model of Asymmetric Cold Bond Rolling of Two-Layer Unbonded Clad Sheet Under Coulomb Friction”. In: *Steel Research International, Special Edition Metal Forming Conference 2*, pp. 734–741.

- Parvizi, A. and Abrinia, K. (Feb. 2014). “A two dimensional upper bound analysis of the ring rolling process with experimental and FEM verifications”. In: *International Journal of Mechanical Sciences* 79, pp. 176–181.
- Parvizi, A., Abrinia, K., and Salimi, M. (Jan. 2011). “Slab analysis of ring rolling assuming constant shear friction”. In: *Journal of Materials Engineering and Performance* 20.9, pp. 1505–1511.
- Pesin, A., Pustovoytov, D., and Sverdlik, M. (2014). “Influence of Different Asymmetric Rolling Processes on Shear Strain”. In: *International Journal of Chemical, Nuclear, Metallurgical and Materials Engineering* 8.6, pp. 422–424.
- Philipp, M., Schwenzfeier, W., Fischer, F.D., Wödlinger, R., and Fischer, C. (Apr. 2007). “Front end bending in plate rolling influenced by circumferential speed mismatch and geometry”. In: *Journal of Materials Processing Technology* 184.1-3, pp. 224–232.
- Pietrzyk, M. and Lenard, J. G. (1991). *Thermal-mechanical modelling of the flat rolling process*. English. Berlin [etc.]: Springer.
- Pishbin, H., Parsa, M. H., and Dastvareh, A. (2010). “An analytical modified model of clad sheet bonding by cold rolling using upper bond theorem”. In: *Journal of Materials Engineering and Performance* 19.7, pp. 936–941.
- Pospiech, J. (1987). “A note on the influence of some factors affecting curvature in the flat rolling of strip”. In: *Journal of Mechanical Working Technology* 15, pp. 69–80.
- Quagliato, L. and Berti, G.A. (2016). “Mathematical definition of the 3D strain field of the ring in the radial-axial ring rolling process”. In: *International Journal of Mechanical Sciences* 115-116, pp. 746–759.
- Qwamizadeh, M., Kadkhodaei, M., and Salimi, M. (Nov. 2011). “Asymmetrical sheet rolling analysis and evaluation of developed curvature”. In: *The International Journal of Advanced Manufacturing Technology* 61.1-4, pp. 227–235.
- Qwamizadeh, M., Kadkhodaei, M., and Salimi, M. (2013). “Slab analysis of asymmetrical rolling of bonded two—layer sheets”. In: *ISIJ International* 53.2, pp. 265–273.
- Qwamizadeh, M., Kadkhodaei, M., and Salimi, M. (2014). “Asymmetrical rolling analysis of bonded two-layer sheets and evaluation of outgoing curvature”. In: *International Journal of Advanced Manufacturing Technology* 73.1-4, pp. 521–533.
- Richelsen, A. B. (1997). “Elastic—plastic analysis of the stress and strain distributions in asymmetric rolling”. In: *International Journal of Mechanical Sciences* 39.11, pp. 1199–1211.

- Salganik, V. M., Chikishev, D. N., Pustovoitov, D. O., Denisov, S. V., and Stekanov, P. A. (Apr. 2014). “Developing regimes for the asymmetric rolling of low-alloy steel plates to minimize bending of the ends of the plate”. In: *Metallurgist* 57.11-12, pp. 1005–1008.
- Salimi, M. and Kadkhodaei, M (July 2004). “Slab analysis of asymmetrical sheet rolling”. In: *Journal of Materials Processing Technology* 150.3, pp. 215–222.
- Salimi, M. and Sassani, F. (2002). “Modified slab analysis of asymmetrical plate rolling”. In: *International Journal of Mechanical Sciences* 44, pp. 1999–2023.
- Salunkhe, M.A. (2006). “Analysis of cold flat asymmetric rolling process”. M Tech Thesis. Indian Institute of Technology, Guwahati.
- Sauer, R. and Pawelski, O. (1987). “Theoretical study of the effect of asymmetries on the cold rolling process.” In: *Steel Res.* 58.7, pp. 319–326.
- Seffen, K. A. and Guest, S. D. (2011). “Prestressed morphing bistable and neutrally stable shells”. In: *Journal of Applied Mechanics* 78.1, p. 011002.
- Seffen, K.A. (2007). “‘Morphing’ bistable orthotropic elliptical shallow shells”. In: *Proceedings of the Royal Society A: Mathematical, Physical and Engineering Sciences* 463.2077, pp. 67–83.
- Seo, J. H., Vantyne, C. J., and Moon, Y. H. (2016). “Prediction of turn down warping during hot plate rolling based on a Gaussian function”. In: *International Journal of Material Forming*, pp. 705–713.
- Shintani, K. and Hwang, Y. (1992). “Mathematical simulation of clad sheet rolling and sandwich sheet rolling”. In: *Annals of the CIRP* 41.1, pp. 13–16.
- Shivpuri, R., Chou, P. C., and Lau, C. W. (1988). “Finite element investigation of curling in non-symmetric rolling of flat stock”. In: *International Journal of Mechanical Sciences* 30.9, pp. 625–635.
- Siebel, E. (1924). “Berichte des walzwerksausschusses”. In: *Verein deutscher Eisenhüttenleute* 37, pp. 1–4.
- Siebel, E. and Pomp, A. (1927). “Mitteilungen aus dem Kaiser”. In: *Mitteilungen aus dem Kaiser Wilhelm Institut für Eisenforschung, Dusseldorf* 9, p. 157.
- Sims, R. B. (1954). “The Calculation of Roll Force and Torque in Hot Rolling Mills”. In: *Proceedings of the Institution of Mechanical Engineers* 168, pp. 191–200.
- Smet, R. P. and Johnson, R. E. (1989). “An asymptotic analysis of cold sheet rolling”. In: *Journal of Applied Mechanics* 56.March 1989, pp. 33–39.
- Tanaka, E., Fukuda, T., Niibayashi, T., Suzuki, Y., and Nihei, Y. (1969). “Curling of cold-rolled thin strips”. In: *J Jap Inst Metals* 33.1, pp. 4–9.

- Timoshenko, S. and Lessells, J.M. (1925). *Applied Elasticity*. Westinghouse technical night school Press.
- Tzou, G., Huang, M., Chen, C. J., Chiu, Y.C., and Ian, M.H. (2003). “Study of asymmetrical cold-and-hot rolling of three-layer bounded clad sheet”. In: *Key Engineering Materials* 233, p. 359.
- Van Der Winden, M.R. (2005). *Method for processing a continuously cast metal slab or strip, and plate or strip produced in this way*.
- Venter, R. D and Abd-Rabbo, A (1980). “Modelling of the rolling process I: inhomogeneous deformation model”. In: *International Journal of Mechanical Sciences* 22.2, pp. 83–92.
- Venter, R. D. and Abd-Rabbo, A. (1980). “Modelling of the rolling process II: evaluation of the stress distribution in the rolled material”. In: 22, pp. 93–98.
- Vidoli, Stefano (Mar. 2013). “Discrete approximations of the Föppl-Von Kármán shell model: From coarse to more refined models”. In: *International Journal of Solids and Structures* 50.9, pp. 1241–1252.
- Wang, H., Zhang, D., and Zhao, D. (2015). “Analysis of asymmetrical rolling of unbonded clad sheet by slab method considering vertical shear stress”. In: *ISIJ International* 55.5, pp. 1058–1066.
- Wanheim, T. and N. Bay (1978). “A model for friction in Metal Forming Processes”. In: *CIRP Annals - Manufacturing Technology* 27.1, pp. 1–6.
- Xu, W., Yang, X., Gong, X., and Zhou, J. (Oct. 2012). “A new mathematical model for predicting the diameter expansion of flat ring in radial-axial ring rolling”. In: *International Journal of Advanced Manufacturing Technology* 60.9-12, pp. 913–921.
- Yan, F. L., Hua, L., and Wu, Y. Q. (2007). “Planning feed speed in cold ring rolling”. In: *International Journal of Machine Tools and Manufacture* 47.11, pp. 1695–1701.
- Yang, H., Guo, L., and Zhan, M. (2005). “Role of friction in cold ring rolling”. In: 21.6, pp. 914–920.
- Yang, J., Li, S., Liu, J., Li, X., and Zhang, X. (2017). “Finite element analysis of bending behavior and strain heterogeneity in snake rolling of AA7050 plates using a hyperbolic sine-type constitutive law”. In: *Journal of Materials Processing Technology* 240, pp. 274–283.
- Yong, J., Dashu, P., Dong, L., and Luoxing, L. (2000). “Analysis of clad sheet bonding by cold rolling”. In: *Journal of Materials Processing Technology* 105.1, pp. 32–37.

- Yoshii, M., Ohmori, K., Seto, T., Nikaido, H., Nishizaki, H., and Inoue, M. (1991). “Analysis of warping phenomenon in plate rolling”. In: *ISIJ International* 31.9, pp. 973–978.
- Zamani, M. R. (2014). “New method of determination for pressure and shear frictions in the ring rolling process as analytical function”. In: *Journal of Solid Mechanics* 6.3, pp. 322–333.
- Zhou, P., Zhang, L., Gu, S., Ruan, J., and Teng, L. (2014). “Mathematic modeling and FE simulation of radial-axial ring rolling large L-section ring by shape axial roll”. In: *The International Journal of Advanced Manufacturing Technology* 72.5-8, pp. 729–738.
- Zorowski, C. F. and Shutt, A. (1963). “Analysis of the load and torque characteristics of single-roll mills”. In: *International Research in Production Engineering*, pp. 380–387.

Appendix A

Asymmetric rolling asymptotic correction

It was noted in Chapter 2 that all the $O(\delta)$ terms were zero. Continuing the expansion from Section 2.3 in orders of δ , the second order governing equations are

$$-\beta \frac{\partial p^{(2)}}{\partial x} + \frac{\partial s_{xx}^{(2)}}{\partial x} + \beta \frac{\partial s_{xy}^{(2)}}{\partial y} = 0, \quad (\text{A.1})$$

$$-\beta \frac{\partial p^{(2)}}{\partial y} - \frac{\partial s_{xx}^{(2)}}{\partial y} + \beta \frac{\partial s_{xy}^{(0)}}{\partial x} = 0, \quad (\text{A.2})$$

$$\frac{\partial u^{(2)}}{\partial x} = \lambda^{(0)} s_{xx}^{(2)} + \lambda^{(2)} s_{xx}^{(0)}, \quad (\text{A.3})$$

$$\frac{\partial u^{(2)}}{\partial y} + \frac{\partial v^{(0)}}{\partial x} = 2\beta \lambda^{(0)} s_{xy}^{(0)}, \quad (\text{A.4})$$

$$\frac{\partial u^{(2)}}{\partial x} + \frac{\partial v^{(2)}}{\partial y} = 0 \quad (\text{A.5})$$

$$\text{and } 2s_{xx}^{(0)} s_{xx}^{(2)} + \beta^2 s_{xy}^{(0)2} = 0. \quad (\text{A.6})$$

Likewise, the boundary conditions are

$$\begin{aligned}
s_{xy}^{(2)}(x, h_t(x)) &= \gamma_t \left(\beta p^{(2)}(x, h_t) + s_{xx}^{(2)} \right) + \frac{2}{\beta} s_{xx}^{(2)}(x, h_t) \frac{dh_t}{dx} \\
&\quad + \gamma_t \left(\beta p^{(0)}(x, h_t) + s_{xx}^{(0)}(x, h_t) \right) \left(\frac{dh_t}{dx} \right)^2 \\
&\quad + s_{xy}^{(0)}(x, h_t) \left(\left(\frac{dh_t}{dx} \right)^2 - 2\beta\gamma_t \frac{dh_t}{dx} \right) \\
s_{xy}^{(2)}(x, h_b(x)) &= \gamma_b \left(\beta p^{(2)}(x, h_b) + s_{xx}^{(2)} \right) + \frac{2}{\beta} s_{xx}^{(2)}(x, h_b) \frac{dh_b}{dx} \\
&\quad + \gamma_b \left(\beta p^{(0)}(x, h_b) + s_{xx}^{(0)}(x, h_b) \right) \left(\frac{dh_b}{dx} \right)^2 \\
&\quad + s_{xy}^{(0)}(x, h_b) \left(\left(\frac{dh_b}{dx} \right)^2 - 2\beta\gamma_b \frac{dh_b}{dx} \right)
\end{aligned} \tag{A.7}$$

$$\begin{aligned}
\int_{h_b(0)}^{h_t(0)} -\beta p^{(2)}(0, y) + s_{xx}^{(2)}(0, y) dy &= 0, \\
\int_{h_b(1)}^{h_t(1)} -\beta p^{(2)}(1, y) + s_{xx}^{(2)}(1, y) dy &= 0,
\end{aligned} \tag{A.8}$$

$$\int_{h_b(x)}^{h_t(x)} u^{(2)}(x, y) dy = 0, \tag{A.9}$$

$$\begin{aligned}
v^{(2)}(x, h_t(x)) &= \frac{dh_t(x)}{dx} u^{(2)}(x, h_t(x)) \\
\text{and } v^{(2)}(x, h_b(x)) &= \frac{dh_b(x)}{dx} u^{(2)}(x, h_b(x)).
\end{aligned} \tag{A.10}$$

The second order correction to the horizontal velocity can be determined by integrating equation (A.4) with respect to y , which gives

$$u^{(2)} = 2\beta\lambda^{(0)} \int s_{xy}^{(0)} dy - \int \frac{\partial v^{(0)}}{\partial x} dy$$

where the constant of integration can be determined using equation (A.9). This ultimately leads to

$$\begin{aligned}
 u^{(2)}(x, y) = \frac{2}{\Delta h^2} & \left[\left(y - \frac{h_t^2 - h_b^2}{2\Delta h} \right) \left(2\beta \frac{d\Delta h}{dx} K(x) \right. \right. \\
 & \left. \left. - \left(h_t \frac{d^2 h_b}{dx^2} - h_b \frac{d^2 h_t}{dx^2} \right) \frac{2}{\Delta h} \frac{d\Delta h}{dx} \left(h_t \frac{dh_b}{dx} - h_b \frac{dh_t}{dx} \right) \right) \right. \\
 & \left. + \left(\frac{y^2}{2} - \frac{h_t^3 - h_b^3}{6\Delta h} \right) \left(2\beta \frac{d\Delta h}{dx} \frac{dp^{(0)}}{dx} - \frac{d^2 \Delta h}{dx^2} + \frac{2}{\Delta h} \left(\frac{d\Delta h}{dx} \right)^2 \right) \right] \quad (\text{A.11})
 \end{aligned}$$

where $K(x)$ is defined by equation (2.28c).

Differentiating $u^{(2)}$ with respect to x and integrating with respect to y gives the second order correction to vertical velocity from equation (A.5),

$$\begin{aligned}
v^{(2)} &= - \int \frac{\partial u^{(2)}}{\partial x} dy \\
&= \frac{4}{\Delta h^3} \frac{d\Delta h}{dx} \left[\left\{ 2\beta \frac{d\Delta h}{dx} K(x) - \left(h_t \frac{d^2 h_b}{dx^2} - h_b \frac{d^2 h_t}{dx^2} \right) \right. \right. \\
&\quad \left. \left. + \frac{2}{\Delta h} \frac{d\Delta h}{dx} \left(h_t \frac{dh_b}{dx} - h_b \frac{dh_t}{dx} \right) \right\} \left(\frac{y^2}{2} - \frac{h_t^2 - h_b^2}{2\Delta h} y \right) \right. \\
&\quad \left. + \left\{ 2\beta \frac{d\Delta h}{dx} \frac{dp^{(0)}}{dx} - \frac{d^2 \Delta h}{dx^2} + \frac{2}{\Delta h} \left(\frac{d\Delta h}{dx} \right)^2 \right\} \left(\frac{y^3}{6} - \frac{h_t^3 - h_b^3}{6\Delta h} y \right) \right] \\
&\quad - \frac{2}{\Delta h^2} \left[\left\{ 2\beta \frac{d^2 \Delta h}{dx^2} K(x) + 2\beta \frac{d\Delta h}{dx} \frac{dK}{dx} \right. \right. \\
&\quad \left. \left. - \left(h_t \frac{d^3 h_b}{dx^3} + \frac{dh_t}{dx} \frac{d^2 h_b}{dx^2} - \frac{d^2 h_t}{dx^2} \frac{dh_b}{dx} - \frac{d^3 h_t}{dx^3} h_b \right) \right. \right. \\
&\quad \left. \left. + \left(\frac{2}{\Delta h} \frac{d^2 \Delta h}{dx^2} - \frac{2}{\Delta h^2} \left(\frac{d\Delta h}{dx} \right)^2 \right) \left(h_t \frac{dh_b}{dx} - h_b \frac{dh_t}{dx} \right) \right. \right. \\
&\quad \left. \left. + \frac{2}{\Delta h} \frac{d\Delta h}{dx} \left(h_t \frac{d^2 h_b}{dx^2} - h_b \frac{d^2 h_t}{dx^2} \right) \right\} \left(\frac{y^2}{2} - \frac{h_t^2 - h_b^2}{2\Delta h} y \right) \right. \\
&\quad \left. + \left\{ 2\beta \frac{d\Delta h}{dx} K(x) - \left(h_t \frac{d^2 h_b}{dx^2} - h_b \frac{d^2 h_t}{dx^2} \right) + \frac{2}{\Delta h} \frac{d\Delta h}{dx} \left(h_t \frac{dh_b}{dx} - h_b \frac{dh_t}{dx} \right) \right\} \right. \\
&\quad \left. \left(\frac{h_t^2 - h_b^2}{2\Delta h^2} \frac{d\Delta h}{dx} - \frac{1}{\Delta h} \left(h_t \frac{dh_t}{dx} - h_b \frac{dh_b}{dx} \right) \right) y \right. \\
&\quad \left. + \left\{ 2\beta \frac{d^2 \Delta h}{dx^2} \frac{dp^{(0)}}{dx} + 2\beta \frac{d\Delta h}{dx} \frac{d^2 p^{(0)}}{dx^2} - \frac{d^3 \Delta h}{dx^3} + \frac{4}{\Delta h} \frac{d\Delta h}{dx} \frac{d^2 \Delta h}{dx^2} \right. \right. \\
&\quad \left. \left. - \frac{2}{\Delta h^2} \left(\frac{d\Delta h}{dx} \right)^3 \right\} \left(\frac{y^3}{6} - \frac{h_t^3 - h_b^3}{6\Delta h} y \right) \right. \\
&\quad \left. + \left\{ 2\beta \frac{d\Delta h}{dx} \frac{dp^{(0)}}{dx} - \frac{d^2 \Delta h}{dx^2} + \frac{2}{\Delta h} \left(\frac{d\Delta h}{dx} \right)^2 \right\} \right. \\
&\quad \left. \left(\frac{h_t^3 - h_b^3}{6\Delta h^2} \frac{d\Delta h}{dx} - \frac{1}{2\Delta h} \left(h_t^2 \frac{dh_t}{dx} - h_b^2 \frac{dh_b}{dx} \right) \right) y \right] + c_1(x). \tag{A.12}
\end{aligned}$$

The function $c_1(x)$ can be determined algebraically from the velocity boundary conditions, equation (A.10), giving

$$c_1(x) = \frac{dh_t}{dx} u^{(2)}(x, h_t) - v^{(2)-}(x, h_t) \tag{A.13}$$

where $v^{(2)-} = v^{(2)} - c_1(x)$.

The second order correction to the longitudinal deviatoric stresses follow from equation (A.6) as

$$s_{xx}^{(2)} = -s_{yy}^{(2)} = -\beta^2 \frac{s_{xy}^{(0)2}}{2s_{xx}^{(0)}} \quad (\text{A.14})$$

and the correction to the flow rate parameter is found from equation (A.3) to be

$$\lambda^{(2)} = \frac{1}{s_{xx}^{(0)}} \left(\frac{\partial u^{(2)}}{\partial x} - \lambda^{(0)} s_{xx}^{(2)} \right). \quad (\text{A.15})$$

Substituting equation (2.31) into equation (A.2) reveals the form of $p^{(2)}$ as

$$\begin{aligned} p^{(2)} &= \int \frac{\partial s_{xy}^{(0)}}{\partial x} dy - \frac{s_{xx}^{(2)}}{\beta} \\ &= \frac{d^2 p^{(0)}}{dx^2} \frac{y^2}{2} + \frac{dK}{dx} y - \frac{s_{xx}^{(2)}}{\beta} + c_2(x) \end{aligned} \quad (\text{A.16})$$

and substituting this result into equation (A.1) shows the form of $s_{xy}^{(2)}$ to be

$$\begin{aligned} s_{xy}^{(2)} &= \frac{y^3}{3} \left(\frac{1}{2} \frac{d^3 p^{(0)}}{dx^3} + \frac{2\beta}{s_{xx}^{(0)}} \frac{dp^{(0)}}{dx} \frac{d^2 p^{(0)}}{dx^2} \right) \\ &\quad + \frac{y^2}{2} \left(\frac{d^2 K}{dx^2} + \frac{2\beta}{s_{xx}^{(0)}} \left(\frac{dp^{(0)}}{dx} \frac{dK}{dx} + \frac{d^2 p^{(0)}}{dx^2} K \right) \right) \\ &\quad + y \left(\frac{dc_2}{dx} + \frac{2\beta}{s_{xx}^{(0)}} \frac{dK}{dx} K \right) + c_3(x). \end{aligned} \quad (\text{A.17})$$

It now remains to solve for the arbitrary functions $c_2(x)$ and $c_3(x)$ by applying the force boundary conditions. Applying each friction condition to equation (A.17) and eliminating $c_3(x)$ leaves a differential equation for $c_2(x)$:

$$\begin{aligned} \frac{dc_2}{dx} &= \frac{1}{\Delta h} \left(s_{xy}^{(2)}(x, h_t) - s_{xy}^{(2)}(x, h_b) \right) \\ &\quad - \frac{1}{\Delta h} \left(s_{xy}^{(2)-}(x, h_t) - s_{xy}^{(2)-}(x, h_b) \right) \end{aligned} \quad (\text{A.18})$$

where the shear terms of the first line are given by the boundary conditions, equation (A.7), and

$$s_{xy}^{(2)-}(x, y) = s_{xy}^{(0)} - y \frac{dc_2}{dx} - c_3(x). \quad (\text{A.19})$$

Like the leading order, this can be solved piecewise, ensuring continuity of horizontal stress along the centreline by adjusting the neutral points. The boundary conditions for the outer two regions are determined by the end tensions, equation (A.8), to be

$$c_2(x) = -\frac{d^2 p^{(0)}}{dx^2} \frac{h_t^3 - h_b^3}{6\Delta h} - \frac{dK}{dx} \frac{h_t^2 - h_b^2}{2\Delta h} - \frac{\beta}{\Delta h s_{xx}^{(0)}} \left(\left(\frac{dp^{(0)}}{dx} \right)^2 \frac{h_t^3 - h_b^3}{3} + \frac{dp^{(0)}}{dx} K (h_t^2 - h_b^2) + K^2 \Delta h \right) \quad (\text{A.20})$$

for $x = 0, 1$. Finally, this result is substituted back into equation (A.17) with one of the two friction conditions to yield $c_3(x)$,

$$c_3(x) = s_{xy}^{(2)}(x, h_t) - s_{xy}^{(2)-}(x, h_t) - h_t \frac{dc_2}{dx} \quad (\text{A.21})$$

where, once again, the first term is given by the boundary condition equation (A.7) and $s_{xy}^{(2)-}$ is defined by equation (A.19).

Appendix B

Clad-sheet rolling asymptotic correction

Expanding the interfacial boundary conditions shows that the first order correction is identically zero as there are no non-zero boundary contributions. This is true for the interfacial surface also. The $O(\delta^2)$ governing equations are then

$$-\beta \frac{\partial p^{(2)}}{\partial x} + \frac{\partial s_{xx}^{(2)}}{\partial x} + \beta \frac{\partial s_{xy}^{(2)}}{\partial y} = 0 \quad -\beta \frac{\partial P^{(2)}}{\partial x} + \frac{\partial S_{xx}^{(2)}}{\partial x} + \beta \frac{\partial S_{xy}^{(2)}}{\partial y} = 0, \quad (\text{B.1})$$

$$-\beta \frac{\partial p^{(2)}}{\partial y} - \frac{\partial s_{xx}^{(2)}}{\partial y} + \beta \frac{\partial s_{xy}^{(0)}}{\partial x} = 0 \quad -\beta \frac{\partial P^{(2)}}{\partial y} - \frac{\partial S_{xx}^{(2)}}{\partial y} + \beta \frac{\partial S_{xy}^{(0)}}{\partial x} = 0, \quad (\text{B.2})$$

$$\frac{\partial u^{(2)}}{\partial x} = \lambda^{(2)} s_{xx}^{(0)} + \lambda^{(0)} s_{xx}^{(2)} + \lambda^{(1)} s_{xx}^{(1)} \quad \frac{\partial U^{(2)}}{\partial x} = \Lambda^{(2)} S_{xx}^{(0)} + \Lambda^{(0)} S_{xx}^{(2)} + \Lambda^{(1)} S_{xx}^{(1)}, \quad (\text{B.3})$$

$$\frac{\partial u^{(2)}}{\partial y} + \frac{\partial v^{(0)}}{\partial x} = 2\beta \lambda^{(0)} s_{xy}^{(0)} \quad \frac{\partial U^{(2)}}{\partial y} + \frac{\partial V^{(0)}}{\partial x} = 2\beta \Lambda^{(0)} S_{xy}^{(0)}, \quad (\text{B.4})$$

$$\frac{\partial u^{(2)}}{\partial x} + \frac{\partial v^{(2)}}{\partial y} = 0 \quad \frac{\partial U^{(2)}}{\partial x} + \frac{\partial V^{(2)}}{\partial y} = 0 \quad (\text{B.5})$$

$$\text{and } 2s_{xx}^{(2)} s_{xx}^{(0)} + s_{xx}^{(1)2} + \beta^2 s_{xy}^{(0)2} = 0 \quad 2S_{xx}^{(2)} S_{xx}^{(0)} + S_{xx}^{(1)2} + \beta^2 S_{xy}^{(0)2} = 0 \quad (\text{B.6})$$

with interfacial boundary conditions

$$\begin{aligned} u^{(2)}(x, g^{(0)}) + g^{(2)} \frac{\partial u^{(0)}}{\partial y} \Big|_{y=g^{(0)}} &= U^{(2)}(x, g^{(0)}) + g^{(2)} \frac{\partial U^{(0)}}{\partial y} \Big|_{y=g^{(0)}}, \\ v^{(2)}(x, g^{(0)}) + g^{(2)} \frac{\partial v^{(0)}}{\partial y} \Big|_{y=g^{(0)}} &= V^{(2)}(x, g^{(0)}) + g^{(2)} \frac{\partial V^{(0)}}{\partial y} \Big|_{y=g^{(0)}}, \end{aligned} \quad (\text{B.7})$$

$$\begin{aligned} &- 2 \left(\frac{dg^{(2)}}{dx} s_{xx}^{(0)}(x, g^{(0)}) + \frac{dg^{(0)}}{dx} \left(s_{xx}^{(2)}(x, g^{(0)}) + g^{(2)} \frac{\partial s_{xx}^{(0)}}{\partial y} \Big|_{y=g^{(0)}} \right) \right) \\ &+ \beta \left(s_{xy}^{(2)}(x, g^{(0)}) + g^{(2)} \frac{\partial s_{xy}^{(0)}}{\partial y} \Big|_{y=g^{(0)}} - \left(\frac{dg^{(0)}}{dx} \right)^2 s_{xy}^{(0)}(x, g^{(0)}) \right) \\ &= -2 \left(\frac{dg^{(2)}}{dx} S_{xx}^{(0)}(x, g^{(0)}) + \frac{dg^{(0)}}{dx} \left(S_{xx}^{(2)}(x, g^{(0)}) + g^{(2)} \frac{\partial S_{xx}^{(0)}}{\partial y} \Big|_{y=g^{(0)}} \right) \right) \\ &+ \beta \left(S_{xy}^{(2)}(x, g^{(0)}) + g^{(2)} \frac{\partial S_{xy}^{(0)}}{\partial y} \Big|_{y=g^{(0)}} - \left(\frac{dg^{(0)}}{dx} \right)^2 S_{xy}^{(0)}(x, g^{(0)}) \right) \end{aligned} \quad (\text{B.8})$$

and

$$\begin{aligned} &\beta \left(p^{(2)}(x, g^{(0)}) + g^{(2)} \frac{\partial p^{(0)}}{\partial y} \Big|_{y=g^{(0)}} + \left(\frac{dg^{(0)}}{dx} \right)^2 p^{(0)}(x, g^{(0)}) \right) \\ &+ \left(s_{xx}^{(2)}(x, g^{(0)}) + g^{(2)} \frac{\partial s_{xx}^{(0)}}{\partial y} \Big|_{y=g^{(0)}} - \left(\frac{dg^{(0)}}{dx} \right)^2 s_{xx}^{(0)}(x, g^{(0)}) \right) + \beta s_{xy}^{(0)} \frac{\partial g^{(0)}}{\partial x} \\ &= \beta \left(P^{(2)}(x, g^{(0)}) + g^{(2)} \frac{\partial P^{(0)}}{\partial y} \Big|_{y=g^{(0)}} + \left(\frac{dg^{(0)}}{dx} \right)^2 P^{(0)}(x, g^{(0)}) \right) \\ &+ \left(S_{xx}^{(2)}(x, g^{(0)}) + g^{(2)} \frac{\partial S_{xx}^{(0)}}{\partial y} \Big|_{y=g^{(0)}} - \left(\frac{dg^{(0)}}{dx} \right)^2 S_{xx}^{(0)}(x, g^{(0)}) \right) + \beta S_{xy}^{(0)} \frac{\partial g^{(0)}}{\partial x}. \end{aligned} \quad (\text{B.9})$$

The second order correction can be solved using the same method as the leading order with additional forcing terms. The equation for shear flow gives

$$\frac{\partial u^{(2)}}{\partial y} = 2\beta \lambda^{(0)} s_{xy}^{(0)} - \frac{\partial v^{(0)}}{\partial x} \qquad \frac{\partial U^{(2)}}{\partial y} = 2\beta \Lambda^{(0)} S_{xy}^{(0)} - \frac{\partial V^{(0)}}{\partial x} \quad (\text{B.10})$$

so, with sufficient generality to capture the leading order terms, the velocity correction is defined as

$$u^{(2)} = a(x)\frac{y^2}{2} + b(x)y + c(x) \quad U^{(2)} = A(x)\frac{y^2}{2} + B(x)y + C(x). \quad (\text{B.11})$$

By performing the integration, two of the three coefficients are determined,

$$\begin{aligned} a(x) &= \left(\frac{2}{\Delta h} \frac{d\Delta h}{dx} - \frac{d^2\Delta h}{dx^2} \right) \frac{2}{\Delta h^2} + 2\beta\lambda^{(0)} \frac{dp^{(0)}}{dx} \\ b(x) &= \frac{2}{\Delta h} \left(\left(h_t \frac{d^2 h_b}{dx^2} - h_b \frac{d^2 h_t}{dx^2} \right) - \frac{2}{\Delta h} \frac{d\Delta h}{dx} \left(h_t \frac{dh_b}{dx} - h_b \frac{dh_t}{dx} \right) \right) \\ &\quad + 2\beta\lambda^{(0)} \left(-h_t \frac{dp^{(0)}}{dx} + \gamma_t (\beta p^{(0)} + s_{xx}^{(0)}) + s_{xx}^{(0)} \frac{2}{\beta} \frac{dh_t}{dx} \right) \end{aligned}$$

$$A(x) = \left(\frac{2}{\Delta h} \frac{d\Delta h}{dx} - \frac{d^2\Delta h}{dx^2} \right) \frac{2}{\Delta h^2} + 2\beta\Lambda^{(0)} \frac{dP^{(0)}}{dx} \quad (\text{B.12})$$

$$\begin{aligned} B(x) &= \frac{2}{\Delta h} \left(\left(h_t \frac{d^2 h_b}{dx^2} - h_b \frac{d^2 h_t}{dx^2} \right) - \frac{2}{\Delta h} \frac{d\Delta h}{dx} \left(h_t \frac{dh_b}{dx} - h_b \frac{dh_t}{dx} \right) \right) \\ &\quad + 2\beta\Lambda^{(0)} \left(-h_b \frac{dP^{(0)}}{dx} + \gamma_b (\beta P^{(0)} + S_{xx}^{(0)}) + S_{xx}^{(0)} \frac{2}{\beta} \frac{dh_b}{dx} \right), \end{aligned} \quad (\text{B.13})$$

and mass conservation, $\int_{h_b}^g U^{(2)} dy = 0$ and $\int_g^{h_t} u^{(2)} dy = 0$, determines the third,

$$c(x) = \frac{g^{(2)}u^{(0)} + \int_g^{h_t} \bar{u}^{(2)} dy}{g^{(0)} - h_t} \quad C(x) = \frac{g^{(2)}U^{(0)} + \int_{h_b}^g \bar{U}^{(2)} dy}{h_b - g^{(0)}}. \quad (\text{B.14})$$

Using this result and the incompressibility condition, the vertical velocities can be determined as

$$v^{(2)} = -\frac{da}{dx} \frac{y^3}{3} - \frac{db}{dx} \frac{y^2}{2} - \frac{dc}{dx} y + d(x) \quad V^{(2)} = -\frac{dA}{dx} \frac{y^3}{3} - \frac{dB}{dx} \frac{y^2}{2} - \frac{dC}{dx} y + D(x) \quad (\text{B.15})$$

where the functions $d(x)$ and $D(x)$ are determined using the no penetration boundary conditions for

$$d(x) = \frac{dh_t}{dx} u^{(2)}(h_t) + \frac{da}{dx} \frac{h_t^3}{3} + \frac{db}{dx} \frac{h_t^2}{2} + \frac{dc}{dx} h_t \quad (\text{B.16})$$

and

$$D(x) = \frac{dh_b}{dx} U^{(2)}(h_b) + \frac{dA}{dx} \frac{h_b^3}{3} + \frac{dB}{dx} \frac{h_b^2}{2} + \frac{dC}{dx} h_b. \quad (\text{B.17})$$

The yield condition gives the s_{xx} terms,

$$s_{xx}^{(2)} = \frac{\beta^2 s_{xy}^{(0)2}}{2s_{xx}^{(0)}} \quad S_{xx}^{(2)} = \frac{\beta^2 S_{xy}^{(0)2}}{2S_{xx}^{(0)}}, \quad (\text{B.18})$$

and then the vertical force balance gives

$$\frac{\partial p^{(2)}}{\partial y} = \frac{\partial s_{xy}^{(0)}}{\partial x} - \frac{1}{\beta} \frac{\partial s_{xx}^{(2)}}{\partial y} \quad (\text{B.19})$$

$$\text{and } p^{(2)} = \int \frac{\partial s_{xy}^{(0)}}{\partial x} dy - \frac{1}{\beta} s_{xx}^{(2)} \quad (\text{B.20})$$

$$= f(x, y) + c_2(x) \quad (\text{B.21})$$

where

$$\begin{aligned} f(x, y) = & \frac{d^2 p^{(0)}}{dx^2} \left(\frac{y^2}{2} - h_t(x)y \right) - \frac{dp^{(0)}}{dx} h'_t(x)y + \beta \gamma_t \left(\beta \frac{dp^{(0)}}{dx} + \frac{ds_{xx}^{(0)}}{dx} \right) y \\ & + \frac{ds_{xx}^{(0)}}{dx} \frac{2}{\beta} \frac{dh_t}{dx} y + s_{xx}^{(0)} \frac{2}{\beta} \frac{d^2 h_t}{dx^2} y - \frac{1}{\beta} s_{xx}^{(2)}. \end{aligned} \quad (\text{B.22})$$

Similarly,

$$P^{(2)} = F(x, y) + C_2(x) \quad (\text{B.23})$$

$$F(x, y) = \frac{d^2 P^{(0)}}{dx^2} \left(\frac{y^2}{2} - h_b(x)y \right) - \frac{dP^{(0)}}{dx} h'_b(x)y + \beta \gamma_b \left(\beta \frac{dP^{(0)}}{dx} + \frac{dS_{xx}^{(0)}}{dx} \right) y \quad (\text{B.24})$$

$$+ \frac{dS_{xx}^{(0)}}{dx} \frac{2}{\beta} \frac{dh_b}{dx} y + S_{xx}^{(0)} \frac{2}{\beta} \frac{d^2 h_b}{dx^2} y - \frac{1}{\beta} S_{xx}^{(2)}. \quad (\text{B.25})$$

The normal stress interfacial boundary condition, equation (B.9), relates c_2 and C_2 ,

$$\begin{aligned} C_2(x) = & c_2(x) - \left(\frac{dg^{(0)}}{dx} \right)^2 \left(p^{(0)}(x, g^{(0)}) - P^{(0)}(x, g^{(0)}) \right) + \left(f(x, g^{(0)}) - F(x, g^{(0)}) \right) \\ & + \frac{1}{\beta} \left(- \left(\frac{dg^{(0)}}{dx} \right)^2 \left(s_{xx}^{(0)} - S_{xx}^{(0)} \right) + \left(s_{xx}^{(2)} - S_{xx}^{(2)} \right) + \frac{dg^{(0)}}{dx} \left(s_{xy}^{(0)} - S_{xy}^{(0)} \right) \right), \end{aligned} \quad (\text{B.26})$$

which will be written as $C_2(x) = c_2(x) + G(x)$ for brevity. The horizontal force balance can be solved for

$$s_{xy}^{(2)}(h_t(x)) - s_{xy}^{(2)}(g^{(0)}) = \int_{g^{(0)}}^{h_t} \frac{\partial f}{\partial x} - \frac{1}{\beta} \frac{\partial s_{xx}^{(2)}}{\partial x} dy + \frac{dc_2}{dx} \left(h_t(x) - g^{(0)}(x) \right) \quad (\text{B.27})$$

and

$$S_{xy}^{(2)}(g^{(0)}) - S_{xy}^{(2)}(h_b) = \int_{h_b}^{g^{(0)}} \frac{\partial F}{\partial x} - \frac{1}{\beta} \frac{\partial S_{xx}^{(2)}}{\partial x} dy + \frac{dC_2}{dx} (g^{(0)}(x) - h_b(x)). \quad (\text{B.28})$$

Applying the tangential stress interfacial boundary condition, equation (B.8), and the previous three results, an ODE for c_2 can be found,

$$\begin{aligned} \frac{dc_2}{dx} \Delta h &= 2 \frac{dg^{(2)}}{dx} (s_{xx}^{(0)} - S_{xx}^{(0)}) + 2 \frac{dg^{(0)}}{dx} (s_{xx}^{(2)} - S_{xx}^{(2)}) \\ &\quad - \beta \left(\frac{dg^{(0)}}{dx} \right)^2 (s_{xy}^{(0)} - S_{xy}^{(0)}) + \beta g^{(2)} \left(\frac{ds_{xy}^{(0)}}{dy} - \frac{dS_{xy}^{(0)}}{dy} \right) + (s_{xy}^{(2)}(h_t) - S_{xy}^{(2)}(h_b)) \\ &\quad - \int_{g^{(0)}}^{h_t} \frac{\partial f}{\partial x} - \frac{1}{\beta} \frac{\partial s_{xx}^{(2)}}{\partial x} dy + \int_{h_b}^{g^{(0)}} \frac{\partial F}{\partial x} - \frac{1}{\beta} \frac{\partial S_{xx}^{(2)}}{\partial x} dy + (h_b - g^{(0)}) \frac{dG(x)}{dx} \end{aligned} \quad (\text{B.29})$$

Finally,

$$\begin{aligned} s_{xy}^{(2)} &= \int_{h_t}^y \frac{\partial f}{\partial x} - \frac{1}{\beta} \frac{\partial s_{xx}^{(2)}}{\partial x} dy + \frac{dc_2(x)}{dx} (y - h_t(x)) + s_{xy}^{(2)}(h_t(x)) \\ S_{xy}^{(2)} &= \int_{h_b}^y \frac{\partial F}{\partial x} - \frac{1}{\beta} \frac{\partial S_{xx}^{(2)}}{\partial x} dy + \frac{dC_2(x)}{dx} (y - h_b(x)) + S_{xy}^{(2)}(h_b(x)) \end{aligned}$$

which can be closed with the surface friction boundary conditions.

Appendix C

Statistical method

This appendix provides greater detail of the digitised data and regression models presented in Chapter 4.

C.1 Data exploration

Some initial checks of the data are conducted to ensure no unusual features exist in the dataset. A histogram and box plot of the curvature values, Figure C.1, shows that the data are almost normally distributed, with a slight left skew and heavy tails. This is verified by a Q-Q plot, Figure C.2: the flat gradient indicates heavy tails and greater deviation to the left hand end indicates a left skew. A scatter matrix, Figure C.3, shows a great deal of structure to the data but no concerning amount of correlation between the independent variables. This is expected considering the design of the experiments these data were collected from.

Both Figure C.1 and Figure C.3 show a number of outliers; however, these will be the Buxton et al. (1972) dataset, discussed in Chapter 4.

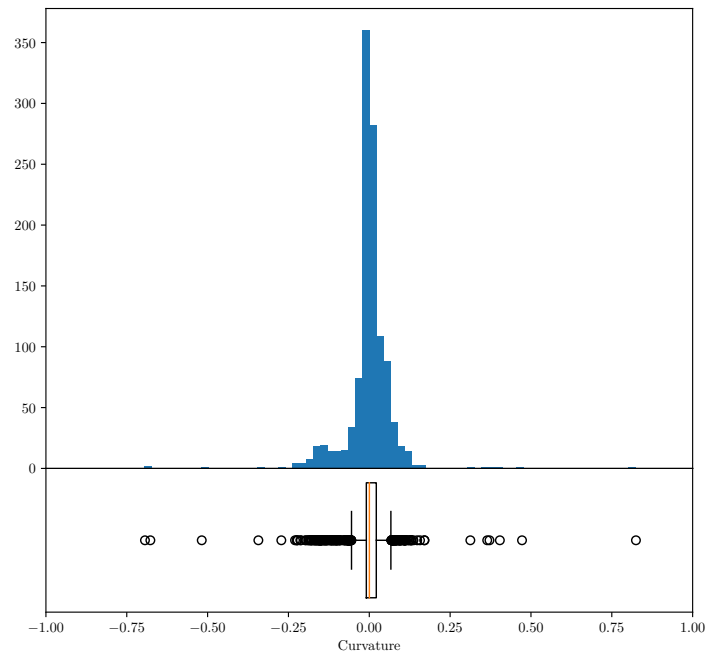


Fig. C.1 Histogram and box plot of the digitised curvature data.

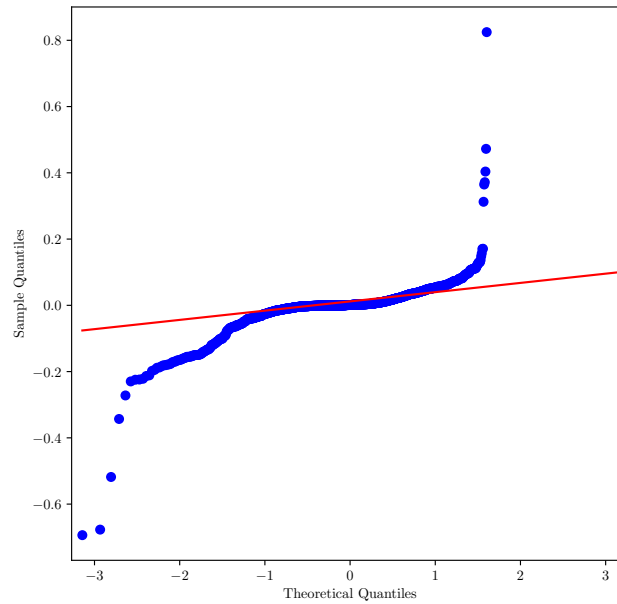


Fig. C.2 Q-Q plot of the digitised curvature data.

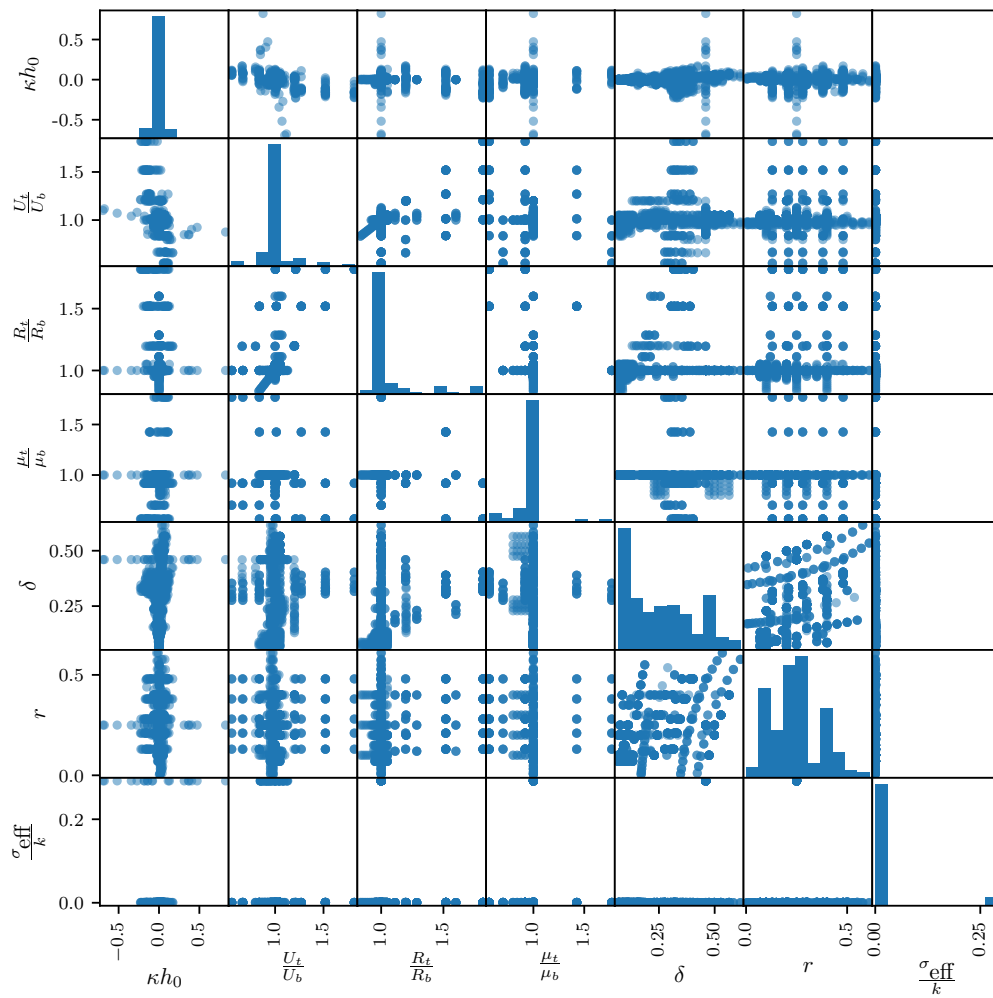


Fig. C.3 Scatter matrix of the digitised curvature data.

C.2 Linear regression

Regression over asymmetric terms

This model achieves an adjusted R-squared value of 0.40 with three variables over 1039 data. Table C.1 shows the fitted coefficients and Figure C.4 plots the distribution of the residuals against each regressor and the curvature. There is correlation with the curvature indicating higher order terms may be required.

Table C.1 Linear regression coefficients for the asymmetric terms

Regressor	Coefficient	Regressor	Coefficient
$\log\left(\frac{U_t}{U_b}\right)$	-0.192	$\log\left(\frac{R_t}{R_b}\right)$	-0.0232
$\log\left(\frac{\mu_t}{\mu_b}\right)$	0.0333		

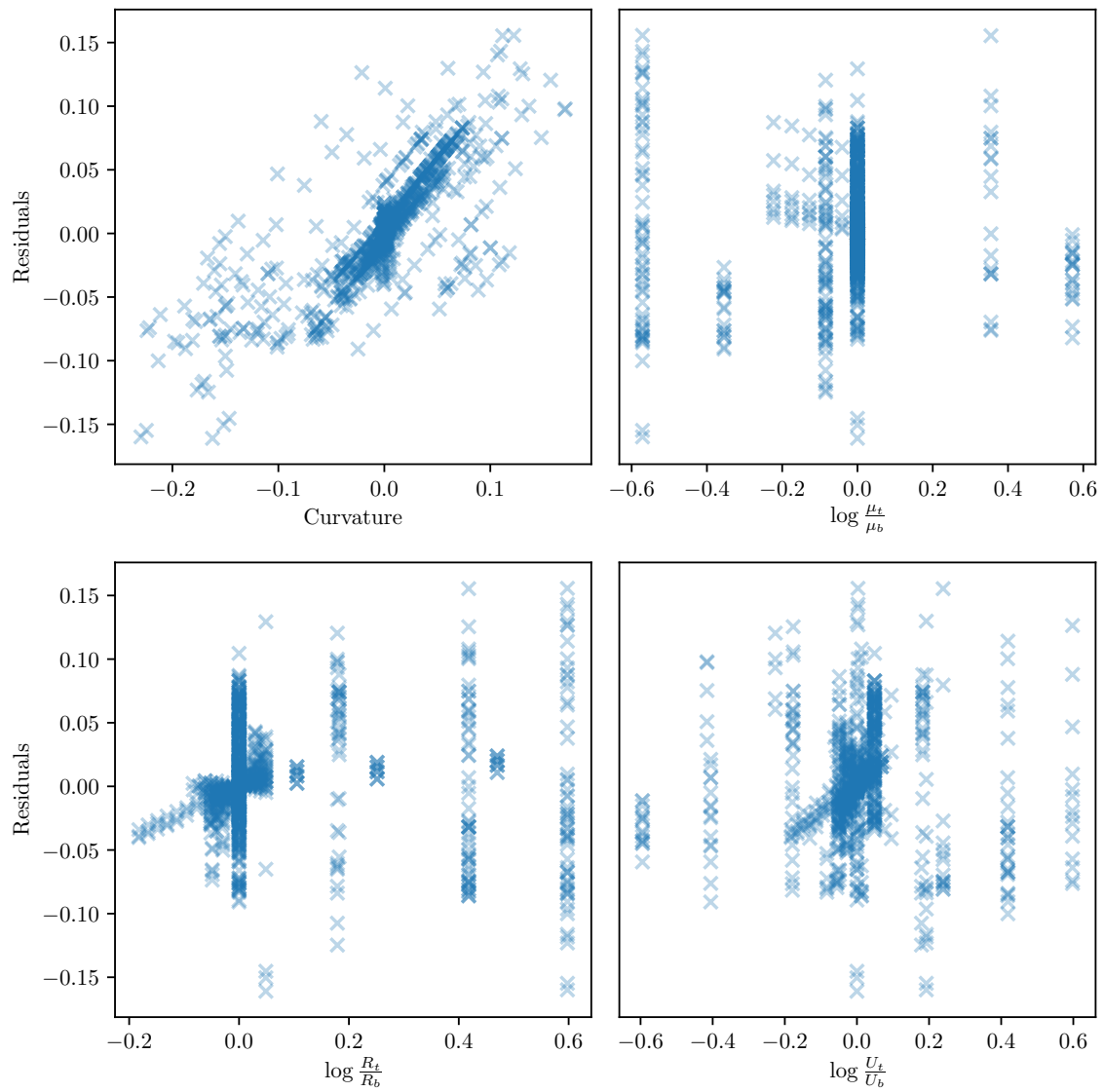


Fig. C.4 Residuals from regression over the asymmetric terms.

Regression over asymmetric by non-asymmetric terms

This model achieves an adjusted R-squared value of 0.52 with twelve variables over 1034 data. An ANOVA p-value of 2.7×10^{-50} was found with the previous model indicating that the additional variables capture significantly more of the trend. Table C.2 gives the fitted coefficients and Figure C.5 shows the distribution of residuals against each regressor and the curvature.

Table C.2 Linear regression coefficients for the asymmetric by non-asymmetric terms

Regressor	Coefficient	Regressor	Coefficient
$\log\left(\frac{R_t}{R_b}\right) \frac{\sigma_Y}{E}$	-2.32e+02	$\log\left(\frac{U_t}{U_b}\right) \frac{\sigma_Y}{E}$	-1.91e+02
$\log\left(\frac{\mu_t}{\mu_b}\right)$	-1.31	$\delta\log\left(\frac{U_t}{U_b}\right)$	-1.05
$\log\left(\frac{\mu_t}{\mu_b}\right) \delta$	-0.9	$\delta\log\left(\frac{R_t}{R_b}\right)$	-0.265
$\log\left(\frac{R_t}{R_b}\right)$	0.0218	$\log\left(\frac{\mu_t}{\mu_b}\right) r$	0.15
$\log\left(\frac{U_t}{U_b}\right) r$	0.155	$\log\left(\frac{U_t}{U_b}\right)$	0.219
$\log\left(\frac{R_t}{R_b}\right) r$	0.58	$\log\left(\frac{\mu_t}{\mu_b}\right) \frac{\sigma_Y}{E}$	2.58e+03

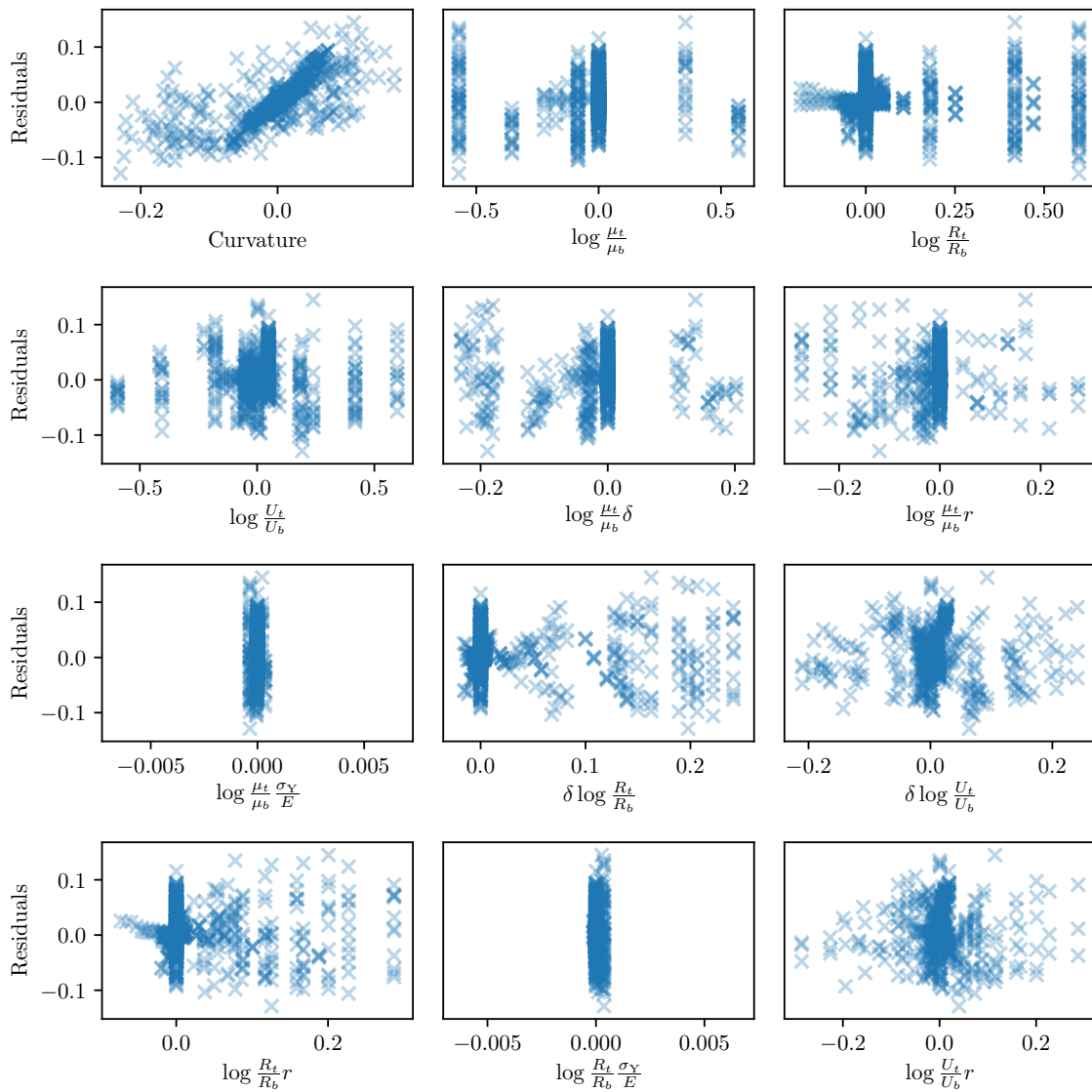


Fig. C.5 Residuals from regression over the asymmetric by non-asymmetric terms.

Regression over asymmetric and asymmetric cubed by non-asymmetric terms

This model achieves an adjusted R-squared value of 0.69 with 47 variables over 1034 data. ANOVA p-values of 8.1×10^{-78} was found with the previous model and 8.1×10^{-125} with the first model presented showing this model captures significantly more of the curvature trend than either of the previous models. Table C.3 gives the fitted coefficients; however, the residual scatter plots were omitted due the large number of variables.

Table C.3 Linear regression coefficients for the asymmetric and cubed asymmetric by non-asymmetric terms

Regressor	Coefficient	Regressor	Coefficient
$\frac{\sigma_Y}{E} \left(\log \left(\frac{\mu_t}{\mu_b} \right) \right)^3$	-5.55e+04	$\log \left(\frac{R_t}{R_b} \right) \frac{\sigma_Y}{E} \left(\log \left(\frac{U_t}{U_b} \right) \right)^2$	-1.56e+04
$\frac{\sigma_Y}{E} \left(\log \left(\frac{R_t}{R_b} \right) \right)^3$	-9.98e+03	$\log \left(\frac{U_t}{U_b} \right) \frac{\sigma_Y}{E} \left(\log \left(\frac{R_t}{R_b} \right) \right)^2$	-4.96e+03
$\log \left(\frac{R_t}{R_b} \right) \frac{\sigma_Y}{E}$	-25.0	$\delta \log \left(\frac{U_t}{U_b} \right) \left(\log \left(\frac{R_t}{R_b} \right) \right)^2$	-13.8
$\log \left(\frac{R_t}{R_b} \right) \left(\log \left(\frac{\mu_t}{\mu_b} \right) \right)^2$	-10.6	$\delta \left(\log \left(\frac{U_t}{U_b} \right) \right)^3$	-8.45
$\log \left(\frac{R_t}{R_b} \right) r \left(\log \left(\frac{U_t}{U_b} \right) \right)^2$	-7.33	$r \left(\log \left(\frac{R_t}{R_b} \right) \right)^3$	-6.73
$\log \left(\frac{\mu_t}{\mu_b} \right) \delta \left(\log \left(\frac{U_t}{U_b} \right) \right)^2$	-6.71	$\log \left(\frac{\mu_t}{\mu_b} \right) \left(\log \left(\frac{R_t}{R_b} \right) \right)^2$	-5.93
$\log \left(\frac{R_t}{R_b} \right) r \left(\log \left(\frac{\mu_t}{\mu_b} \right) \right)^2$	-5.68	$\log \left(\frac{\mu_t}{\mu_b} \right)$	-5.1
$\log \left(\frac{\mu_t}{\mu_b} \right) r \left(\log \left(\frac{R_t}{R_b} \right) \right)^2$	-4.22	$r \left(\log \left(\frac{\mu_t}{\mu_b} \right) \right)^3$	-2.78
$\delta \log \left(\frac{R_t}{R_b} \right)$	-1.94	$\log \left(\frac{\mu_t}{\mu_b} \right) \delta \log \left(\frac{R_t}{R_b} \right) \log \left(\frac{U_t}{U_b} \right)$	-1.23
$\log \left(\frac{\mu_t}{\mu_b} \right) \delta$	-1.2	$\log \left(\frac{U_t}{U_b} \right) r$	-0.863
$\log \left(\frac{U_t}{U_b} \right) \left(\log \left(\frac{\mu_t}{\mu_b} \right) \right)^2$	-0.818	$\left(\log \left(\frac{U_t}{U_b} \right) \right)^3$	-0.465
$\log \left(\frac{U_t}{U_b} \right)$	-0.3	$\delta \log \left(\frac{U_t}{U_b} \right) \left(\log \left(\frac{\mu_t}{\mu_b} \right) \right)^2$	-0.12
$\log \left(\frac{R_t}{R_b} \right) \frac{\sigma_Y}{E} \left(\log \left(\frac{\mu_t}{\mu_b} \right) \right)^2$	-0.00659	$\log \left(\frac{\mu_t}{\mu_b} \right) \frac{\sigma_Y}{E} \left(\log \left(\frac{R_t}{R_b} \right) \right)^2$	-0.00367
$\log \left(\frac{U_t}{U_b} \right) \frac{\sigma_Y}{E} \left(\log \left(\frac{\mu_t}{\mu_b} \right) \right)^2$	-0.000506	$\log \left(\frac{\mu_t}{\mu_b} \right) \log \left(\frac{R_t}{R_b} \right) \log \left(\frac{U_t}{U_b} \right) \frac{\sigma_Y}{E}$	7.06e-05
$\log \left(\frac{\mu_t}{\mu_b} \right) \frac{\sigma_Y}{E} \left(\log \left(\frac{U_t}{U_b} \right) \right)^2$	0.000829	$\log \left(\frac{\mu_t}{\mu_b} \right) \log \left(\frac{R_t}{R_b} \right) \log \left(\frac{U_t}{U_b} \right)$	0.114
$\log \left(\frac{R_t}{R_b} \right)$	0.254	$\log \left(\frac{\mu_t}{\mu_b} \right) r$	0.325
$\left(\log \left(\frac{R_t}{R_b} \right) \right)^3$	0.543	$\delta \log \left(\frac{U_t}{U_b} \right)$	0.765
$\log \left(\frac{R_t}{R_b} \right) r$	0.982	$\log \left(\frac{\mu_t}{\mu_b} \right) \left(\log \left(\frac{U_t}{U_b} \right) \right)^2$	1.34
$\log \left(\frac{\mu_t}{\mu_b} \right) r \left(\log \left(\frac{U_t}{U_b} \right) \right)^2$	2.2	$\log \left(\frac{U_t}{U_b} \right) r \left(\log \left(\frac{\mu_t}{\mu_b} \right) \right)^2$	2.24
$\log \left(\frac{\mu_t}{\mu_b} \right) \log \left(\frac{R_t}{R_b} \right) \log \left(\frac{U_t}{U_b} \right) r$	2.39	$r \left(\log \left(\frac{U_t}{U_b} \right) \right)^3$	2.82
$\log \left(\frac{U_t}{U_b} \right) \left(\log \left(\frac{R_t}{R_b} \right) \right)^2$	3.28	$\log \left(\frac{U_t}{U_b} \right) r \left(\log \left(\frac{R_t}{R_b} \right) \right)^2$	8.88
$\log \left(\frac{R_t}{R_b} \right) \left(\log \left(\frac{U_t}{U_b} \right) \right)^2$	9.22	$\delta \log \left(\frac{R_t}{R_b} \right) \left(\log \left(\frac{U_t}{U_b} \right) \right)^2$	13.5
$\delta \left(\log \left(\frac{\mu_t}{\mu_b} \right) \right)^3$	14.6	$\log \left(\frac{\mu_t}{\mu_b} \right) \delta \left(\log \left(\frac{R_t}{R_b} \right) \right)^2$	20.1
$\delta \left(\log \left(\frac{R_t}{R_b} \right) \right)^3$	22.6	$\left(\log \left(\frac{\mu_t}{\mu_b} \right) \right)^3$	29.7
$\delta \log \left(\frac{R_t}{R_b} \right) \left(\log \left(\frac{\mu_t}{\mu_b} \right) \right)^2$	36.8	$\log \left(\frac{U_t}{U_b} \right) \frac{\sigma_Y}{E}$	3.45e+02
$\frac{\sigma_Y}{E} \left(\log \left(\frac{U_t}{U_b} \right) \right)^3$	3.27e+03	$\log \left(\frac{\mu_t}{\mu_b} \right) \frac{\sigma_Y}{E}$	9.16e+03

Regression over asymmetric and asymmetric cubed by non-asymmetric terms with p-value over 1×10^{-4}

This model achieves an adjusted R-squared value of 0.66 with fifteen variables over 1034 data points. An ANOVA p-value of 3.1×10^{-13} was found with the previous model that suggests the full cubed model captures significantly more of the curvature trend than this model. Table C.4 gives the fitted coefficients and Figure C.6 shows the distribution of residuals against each regressor and the curvature.

Table C.4 Linear regression coefficients for the asymmetric and cubed asymmetric by non-asymmetric terms with p-value less than 1×10^{-4}

Regressor	Coefficient	Regressor	Coefficient
$\log\left(\frac{R_t}{R_b}\right) \frac{\sigma_Y}{E} \left(\log\left(\frac{U_t}{U_b}\right)\right)^2$	-1.42e+04	$\frac{\sigma_Y}{E} \left(\log\left(\frac{\mu_t}{\mu_b}\right)\right)^3$	-8.14e+02
$\log\left(\frac{R_t}{R_b}\right) r \left(\log\left(\frac{U_t}{U_b}\right)\right)^2$	-7.48	$\delta \log\left(\frac{U_t}{U_b}\right) \left(\log\left(\frac{R_t}{R_b}\right)\right)^2$	-7.28
$\log\left(\frac{\mu_t}{\mu_b}\right)$	-3.92	$\log\left(\frac{R_t}{R_b}\right) \left(\log\left(\frac{\mu_t}{\mu_b}\right)\right)^2$	-2.62
$\delta \left(\log\left(\frac{U_t}{U_b}\right)\right)^3$	-1.76	$\delta \log\left(\frac{R_t}{R_b}\right)$	-1.53
$\log\left(\frac{R_t}{R_b}\right) \frac{\sigma_Y}{E} \left(\log\left(\frac{\mu_t}{\mu_b}\right)\right)^2$	-0.00162	$\log\left(\frac{R_t}{R_b}\right)$	0.184
$\log\left(\frac{R_t}{R_b}\right) r$	0.49	$\delta \left(\log\left(\frac{R_t}{R_b}\right)\right)^3$	1.67
$\delta \log\left(\frac{R_t}{R_b}\right) \left(\log\left(\frac{\mu_t}{\mu_b}\right)\right)^2$	8.1	$\delta \log\left(\frac{R_t}{R_b}\right) \left(\log\left(\frac{U_t}{U_b}\right)\right)^2$	38.0
$\log\left(\frac{\mu_t}{\mu_b}\right) \frac{\sigma_Y}{E}$	6.64e+03		

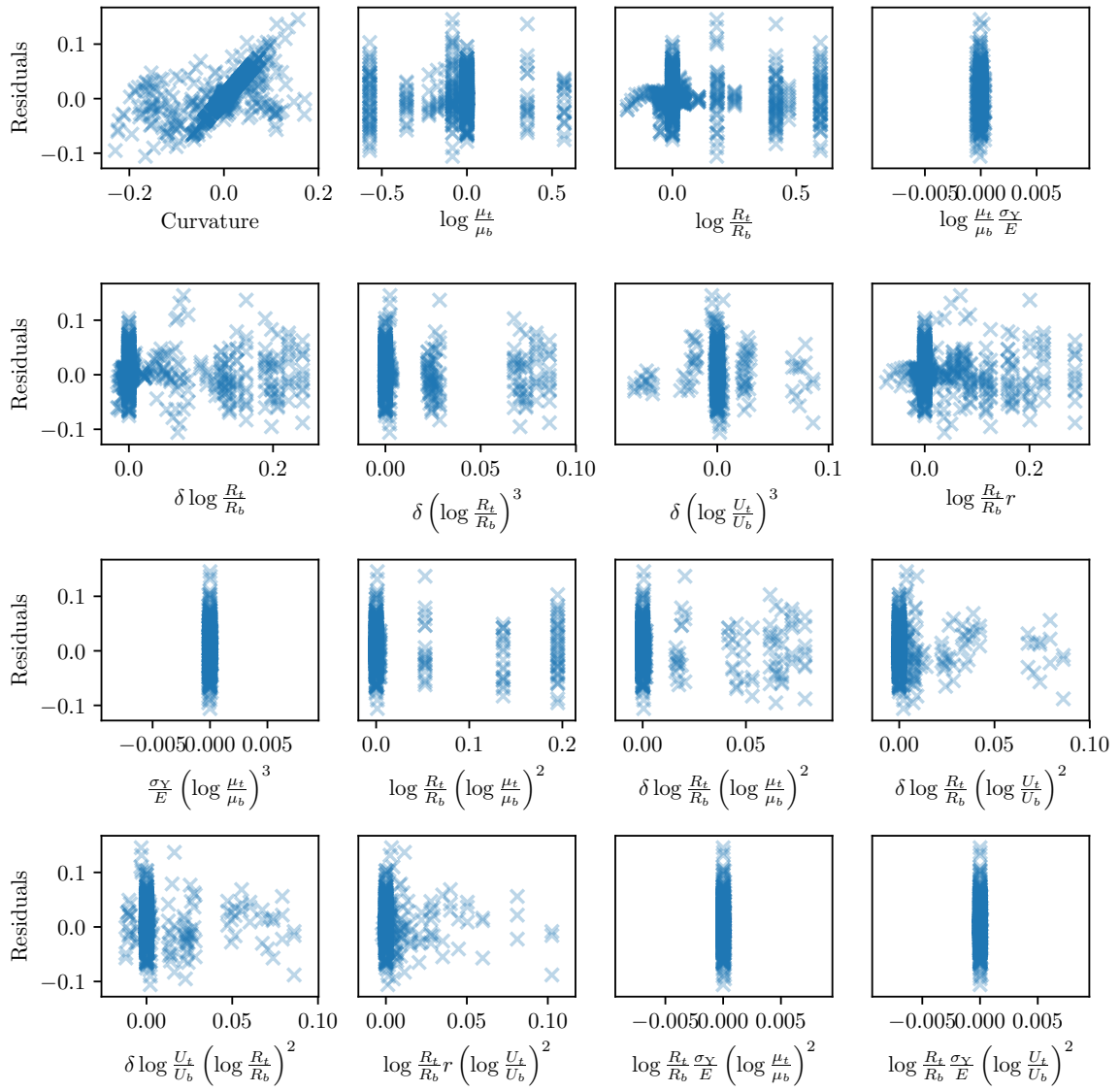


Fig. C.6 Residuals from regression over the asymmetric and cubed asymmetric by non-asymmetric terms with p-value over 1×10^{-4} .

Appendix D

ABAQUS simulations

Numerical simulations using the *ABAQUS* finite element analysis package (Dassault Systemes, 2012a) were used throughout this work for investigation and validation. The models implemented are described in Appendix D.1 along with some discussion of the objectives and challenges that motivated the design choices at each stage. Mesh convergence is demonstrated in Appendix D.2 to ensure accuracy of the numerical results used. The post-processing used is described in Appendix D.3 and a summary of the techniques applied to limit the influence of initial transients and ensure stability are described in Appendix D.4. Finally, Appendix D.5 provides some detail and discussion of the friction behaviour observed in the simulations, casting doubt on the description provided in the *ABAQUS* documentation (Dassault Systemes, 2012c).

D.1 Simulation configurations

Four main models were developed throughout this work: three-dimensional explicit sheet rolling, both symmetrical and asymmetrical; two-dimensional explicit asymmetric sheet rolling; two-dimensional implicit asymmetric composite-sheet rolling; and two-dimensional explicit ring rolling without guide rolls. These were to support preliminary investigations; Chapters 2 and 5; Chapter 3; and Chapter 6 respectively. In the following sections, each of these models are described, and modelling decisions and developments from one model to the next are discussed.

Table D.1 Parameters for three-dimensional symmetric rolling

	Size (m)	Elements
Workpiece thickness	0.04	11
Workpiece length	0.84	167
Workpiece width	0.16	10
Roll radius	1.75	analytic

D.1.1 Three-dimensional symmetric and asymmetric rolling

The first model used to simulate symmetric rolling was a parametrised version of an example provided in the *ABAQUS* Examples Manual (Dassault Systemes, 2012b). Parameterisation of workpiece geometry, workpiece material properties, roll size, roll speed and friction coefficient was achieved by generating the *ABAQUS* input text file, equivalent to that provided in the examples manual, with a *Python* script. The original version of the script was written by Dr Evripides Loukaides but was heavily modified for this and the following applications. This model was used as a test case for the *ABAQUS* workflow, to provide some direct intuition about the rolling process, and to develop some intuition about the assumptions used in the analytical models discussed in Chapter 1.

The model consisted of a single roll and a quarter workpiece about two planes of symmetry: vertically and span-wise. The physical dimensions are specified in Table D.1. Like most industrial rolling processes, these simulations were initialised with the rolls at the correct separation, rotating at speed, and the workpiece out of the roll gap. An initial velocity is imparted to the workpiece so that it moves into the roll gap. With sufficient friction and momentum the rolls will pinch the workpiece after contact and be able to continue deformation with friction alone. The roll constraints did not change throughout and the simulation was conditionally terminated on the convergence of four values: the roll force, the roll torque, the average equivalent plastic strain of a cross section, and the spread of the equivalent plastic strain over the same cross section.

The roll surface was defined as an analytical rigid surface with a central control node; rigid surfaces produce better convergence than deformable surfaces and analytical surfaces have greater accuracy than discretised surfaces. Additionally, roll deformation is known to only be significant for foil rolling, where the magnitude of roll deformation is comparable to the gauge, so a deformable mesh added unnecessary complexity for this application. The workpiece was defined using *C3D8R* elements: linear hexahedral contact elements. The mesh resolution was scaled with the workpiece thickness, the

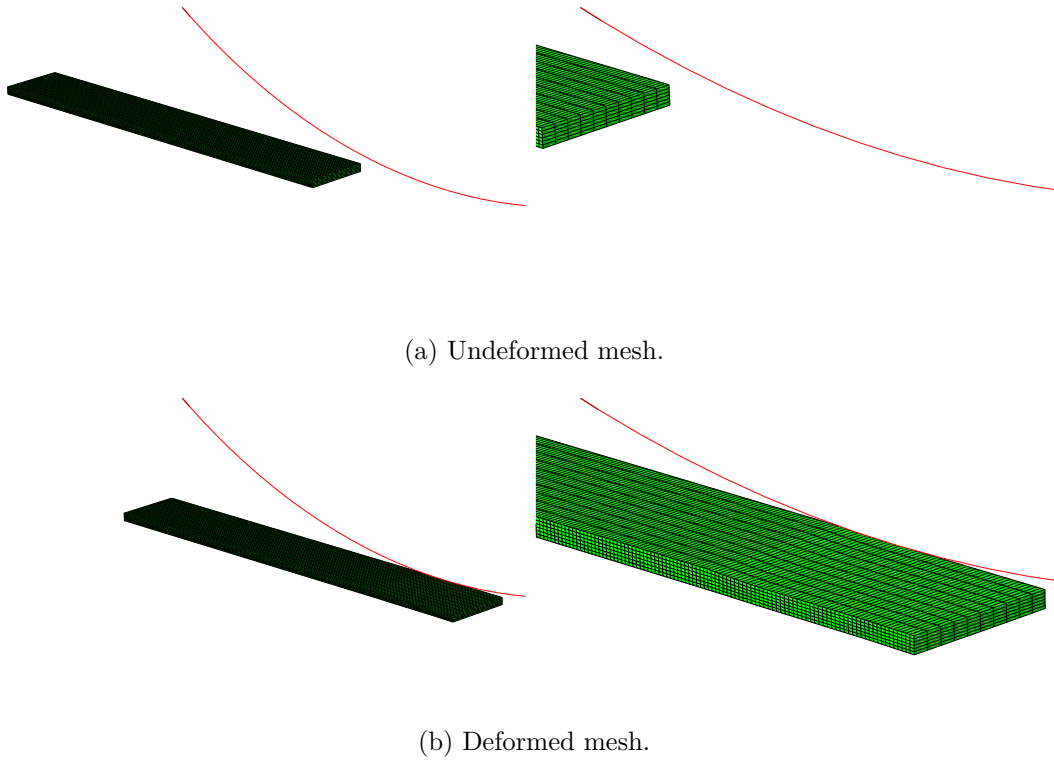


Fig. D.1 Example of symmetric rolling mesh used in simulation.

smallest dimension of the problem, to ensure through-thickness resolution was achieved and each element retained an aspect ratio of more than 0.5. The number of elements for each dimension are specified in Table D.1 and Figure D.1 illustrates an example of this mesh, both undeformed and deformed.

The workpiece material was unchanged from the material provided as part of the original *ABAQUS* example. It is defined to have a Young's modulus of 150GPa, Poisson's ratio of 0.3 and a work hardening yield stress defined with eleven experimentally determined data points. The unworked yield stress is 168.2MPa and hardens to a maximum of 448.45MPa. This material simulates the behaviour of C15 steel; a low carbon, low strength work hardening forging steel.

This model was generalised for asymmetric rolling by replacing the horizontal symmetry plane with a second roll and making the workpiece full thickness to allow the size, rotation and workpiece-roll friction conditions to be controlled independently from top to bottom. This doubled the elements in the simulation, causing noticeably longer simulation times. The plane termination conditions were also removed as the curvature induced in the workpiece by asymmetry rendered them unusable. Instead

Table D.2 Parameters for two-dimensional asymmetric rolling

	Size (m)	Elements
Workpiece thickness	0.01	20-30
Workpiece length	2.0-2.19	2000-3286
Roll radius	0.4-5.3	analytic
Reduction	0.05-0.6 %	
Roll surface speed	0.96-1.8ms ⁻¹	
Friction coefficients	0.08-0.15	
Mass scaling	2000	

the simulations were run set to twice the duration of any of the symmetric simulations observed. The simulation remained otherwise unchanged.

D.1.2 Two-dimensional asymmetric rolling

More modifications were made to the finite element model for use in validating the asymptotic model developed in Chapter 2. To study the effects of each asymmetry, the roll gap aspect ratio, the reduction and the magnitude of friction, shorter computation times were required. The previous finite element model was reduced to two-dimensions to achieve this. This also eliminated one more difference of modelling assumptions between the simulations and the asymptotic model: specifically, plane-strain; the validity of which has been studied elsewhere (Sims, 1954). Like the asymmetric three-dimensional simulations, these simulations were run for a fixed duration: sufficient to roll approximately half the work piece in these cases. Given the increased speed of two-dimensional simulations, this more conservative duration was feasible and provided the opportunity for making curvature predictions. *CPE4R*, linear quadrilateral plane-strain, elements were used for these simulations. Table D.2 specifies the parameters, including number of elements, defining the set-up and Figure D.2 illustrates an example of the asymmetric rolling mesh used, both undeformed and deformed.

Three different materials were used with this model; two are approximations to rigid-perfect plasticity to match the material model used in the asymptotic analysis of Chapter 2 and the third having the same hardening curve as the C15 material used previously but with lower yield stress. *ABAQUS* is unable to model rigid-plastic or incompressible materials as this leads to under-determined stress states in sub-yield areas. Alternatively, the computational problem can be observed by considering the

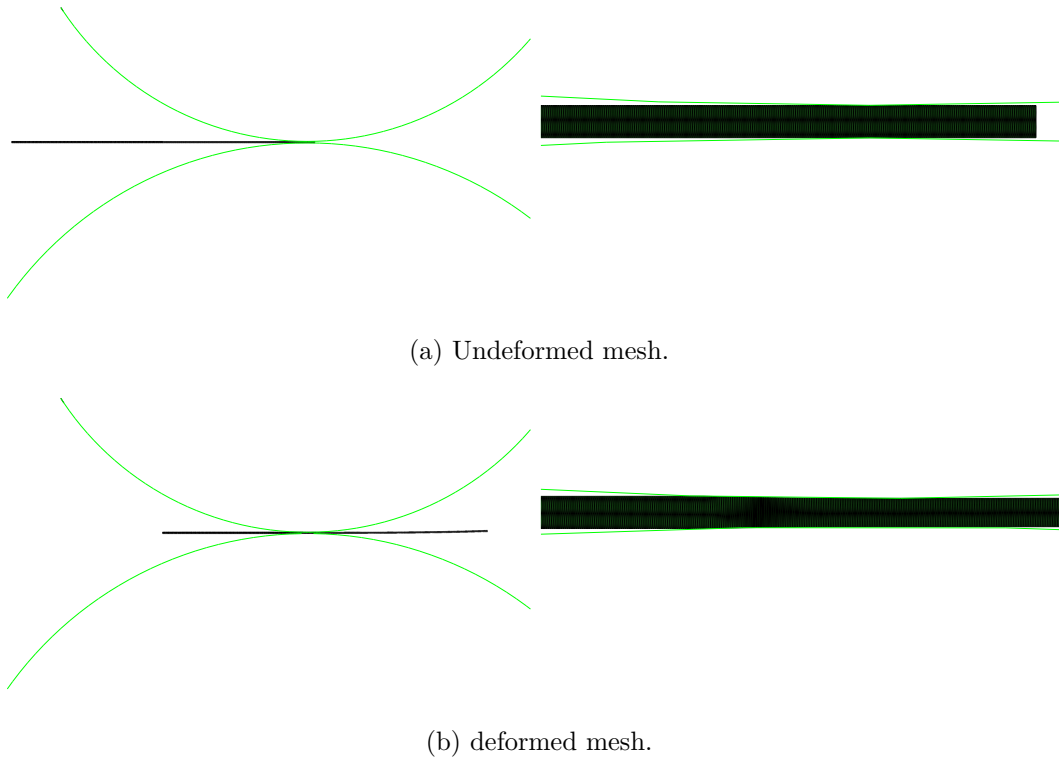


Fig. D.2 Example of asymmetric rolling mesh used in simulation.

elastic wave speed,

$$c = \sqrt{\frac{E}{3\rho(1-2\nu)}}$$

where E , ρ and ν are the Young's modulus, density and Poisson's ratio respectively. A rigid material can be described as the limit of Young's modulus tending to infinity and incompressibility as Poisson's ratio equalling half. Either of these conditions leads to the elastic wave speed tending to infinity which would require an infinitesimally small time step to resolve. Obviously this is impossible and so some compromise is required. The first approximation to rigid-perfect plasticity assumes a Young's modulus of 200GPa, a Poisson's ratio of 0.45 and a yield shear stress of 173.2MPa. The Young's modulus and Poisson's ratio were chosen to be at the limits of feasible computational times to provide the best possible approximation to rigid plasticity¹. The second approximation assumes a Young's modulus reduced to 100GPa, a Poisson's ratio reduced to 0.35 and a yield shear stress of 100MPa. Sufficiently similar results to the first approximation were observed with these changes, while the improved computation times made it feasible to run more comprehensive parameter validations. The material density was taken as

¹Simulations run on an Intel i5 3.4GHz quad-core with 32Gb RAM.

2700kg/m³, although, the effect of this depends directly on the mass scaling, discussed below. The final material, to provide a comparison with a realistic material, has a hardening profile based on the material used in the previous models. The yield shear stress curve starts at 186MPa and hardens to 496MPa; it is presented in Figure 2.11. The Young's modulus, Poisson's ratio and material density are assumed to be 180GPa, 0.27, and 7850kg/m³ respectively.

One of the key challenges encountered running these simulations was ensuring that transients are suppressed quickly to simulate the steady state phase of the process. While a mean solution tended to a steady state quickly, a high frequency oscillation persisted in many of the time history outputs, particularly roll force and torque. It is hypothesised that vertical vibrations in the workpiece, which would have been suppressed by the horizontal plane of symmetry in the symmetrical case, caused this. Further changes intended to replace the stability provided by this plane of symmetry were made.

First, initialisation was modified so both rolls pinch a stationary workpiece close to one end before the rolls begin to rotate. This was to reduce the effect of impact between the rolls and workpiece on first contact as the corners of the workpiece produce high stresses and strains when contacting the rigid analytic surfaces of the rolls. Further, the new initialisation allows vertical inertia of the workpiece to dissipate before rolling begins.

Secondly, greater simulation durations allowed transients to dissipate more completely. Increasing simulation durations required longer workpieces, and consequently more elements, which meant computation time practically scaled worse than linearly with simulation duration.

Thirdly, smaller mass scalings minimised vibrations. Mass scaling, as the name suggests, scales the density of all materials within the simulation. Higher densities means slower wave speed, which allows for larger time steps; however, higher densities also means more inertial effects, including vibrations. Ultimately a mass scaling of 2000 was selected, that is 2000 times the density defined as the material property.

Two other failure modes were observed with this simulation set-up. Insufficient friction or an overly aggressive workpiece reduction meant the rolls could not exert sufficient traction to form the workpiece. In the original initialisation, the workpiece bounced off the rolls and began to climb the exterior of one of the rolls. In the modified initialisation, the rolls slipped entirely and the workpiece remained undeformed after the initial squeeze step. This is a physical failure mode and, as predicted by the

Table D.3 Parameters for two-dimensional asymmetric rolling

	Size (m)	Elements
Workpiece thickness	0.01	18
Workpiece length	20.0	3600
Roll radius	12.5	analytic
Reduction	0.2 %	
Roll surface speed	1.2ms ⁻¹	
Friction coefficients	0.1	

analytical models, would require external forcing to overcome. For this work it was simply considered a failure and these simulations were discarded.

The second failure mode was less predictable and non-physical. Large deformation of each element collapsed the mesh in contact with the rolls. High reductions, high frictions and high mass scaling each seem to increase the likelihood of this occurring. It is possible that these simulations could have been recovered by choosing different mass scalings or limiting the time stepping; however, given how infrequently this occurred, these simulations were discarded as well.

D.1.3 Clad-sheet rolling

The simulations were further generalised to model composite workpieces. Independent materials were applied to element sets so the workpiece was comprised of any number of bonded horizontal sheets with different material properties. The meshing was controlled such that a row of nodes would be generated along the interface of bonded sheets. This meant that any element was wholly part of a single material sheet.

The mesh and model dimensions are specified in Table D.3 and an illustrative example of the mesh is shown in Figure D.3. The second, computationally faster, material without hardening from the asymmetric simulations is used for these simulations: a Young's modulus of 100GPa, a Poisson's ratio of 0.35 and a yield shear stress chosen for each independent material, specifically 100MPa for the top material and 65MPa to 155MPa for the bottom material to achieve the desired yield stress ratios.

The second significant change from the asymmetric simulations was to use an implicit solver, after a suggestion from Dr Adam Nagy. This is the *ABAQUS/Standard* package compared to the *ABAQUS/Explicit* package.

Functionally, explicit solvers use the current system state to determine updates to the geometry and material properties at each time step. *ABAQUS/Explicit* uses

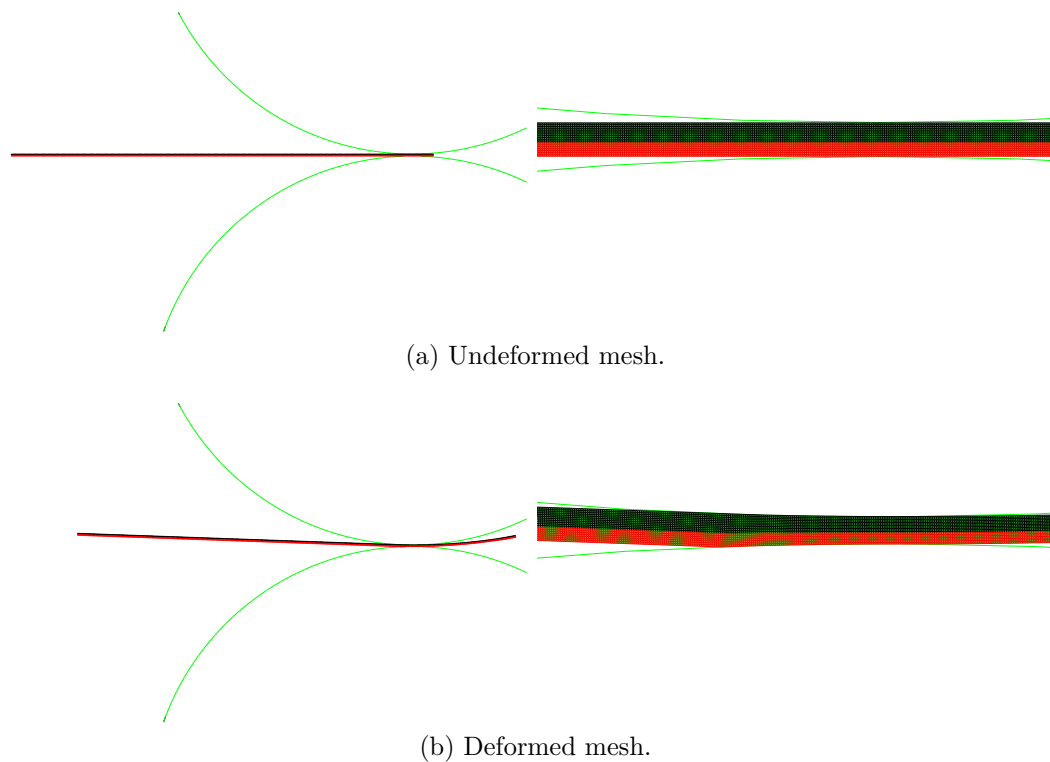


Fig. D.3 Example of clad-sheet rolling mesh used in simulation.

a central difference scheme and a diagonal lumped mass matrix to achieve this form. Implicit solvers use the current and new state of the system to determine the update, which requires a matrix inversion at each time step. *ABAQUS/Standard* uses the Hilber-Hughes-Taylor method to form the update and Newton-Raphson method to iteratively perform the inversion. Solving the matrix inversion at each time step is slower but numerically more stable, so larger time steps can be taken. Implicit solvers are generally considered to be slower and do not scale as effectively as explicit solvers as the larger time steps do not fully account for the slower solve time at each time step.

The appropriate choice of solver is dependent on the problem being solved. Implicit solvers are more appropriate for static problems with significant residual stresses such as cyclic loading, snap through and snap back. Explicit solvers are more appropriate for complex and dynamic problems such as impact problems. It is not immediately obvious which of these solution methods are more appropriate to simulate rolling but it was suggested by Dr Nagy that if the spring back and residual stresses observed in the explicit simulations were significant then an implicit solver would capture these more accurately. This would be particularly relevant for curvature prediction.

A weak, 1Nm^{-1} , spring was attached to one of the central nodes on the trailing edge of the workpiece. This improves conditioning for the implicit solver with a negligible effect on the results.

In addition to using an implicit solver, three more techniques were suggested by Dr Nagy to further minimise transient oscillations observed in the explicit asymmetric simulations. First, static time steps neglect inertia in the solution process, which quickly dissipates waves that may be caused by shocks or other start up effects. Second, pressure over-closure provides a continuous relationship between the normal surface force and the distance between the contact surfaces, which prevents discontinuities when contact first occurs. Exponential pressure over-closure was used here. Finally, smooth displacement and velocity transitions prevent infinite accelerations and the associated forces. While this is most relevant for explicit solvers as implicit solvers handle these discontinuities well, it was included regardless. These were applied to the roll displacement, when the workpiece is initially squeezed, and to the roll rotational velocity, when the rolls begin to rotate and accelerate the workpiece. This new analysis successfully eliminated the unwanted oscillations in all the observed cases.

D.1.4 Ring rolling

The final finite element model developed was of a simple ring rolling configuration: a work roll, mandrel and workpiece without axial or guide rolls. Like the previous two simulations, the rolls initially close on a segment of the workpiece before they begin rotating. The same plane-strain workpiece elements, analytic roll surfaces and contact definitions are all used.

Although the design decisions made are mostly the same as the previous simulations, the scripting used is substantially different. The *ABAQUS Python API* was used to construct the model within *ABAQUS CAE* from which the input file was saved, as opposed to generating the input files directly from *Python* as a text file. The complexity of defining the nodes and elements of a circular workpiece made this approach favourable and it transpired that *ABAQUS* records the actions of a *CAE* session as *Python* commands in an ‘abaqus.rpy’ file. This can be examined for prompts of appropriate *ABAQUS Python API* commands to use in a script.

The inner and outer edge of the workpiece are seeded with a fixed number of nodes each so that the auto generated mesh is regular with annular sectors. An example of the mesh is shown in Figure D.4.

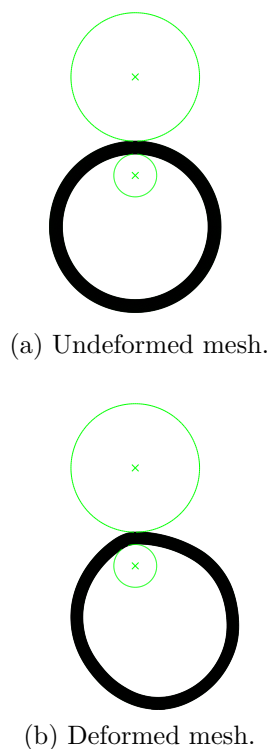


Fig. D.4 Example of the ring rolling mesh used in simulation.

A configuration that converges using the *ABAQUS/Standard*, implicit, solver could not be found so the *ABAQUS/Explicit* solver was used for these simulations. The second, computationally faster, perfectly plastic material without hardening from the asymmetric simulations and clad-sheet simulations is used again here.

Without guide rolls, the stability of the physical process is poor. Further, without active control of the work rolls, a rolling process which maintains a circular and uniformly thick workpiece is impossible. Configurations that remain sufficiently circular for sufficiently long were used to gain qualitative and quantitative insight about the process. This had limited success so more components or a more sophisticated control mechanism could provide useful validation to progress the ring rolling model presented in Chapter 6.

D.2 Mesh convergence

Mesh convergence studies have been conducted on the simulation models described in the previous sections. The results of these studies are presented in Figures D.5 to D.7 where the relative error of the roll force and torque is plotted against the element size.

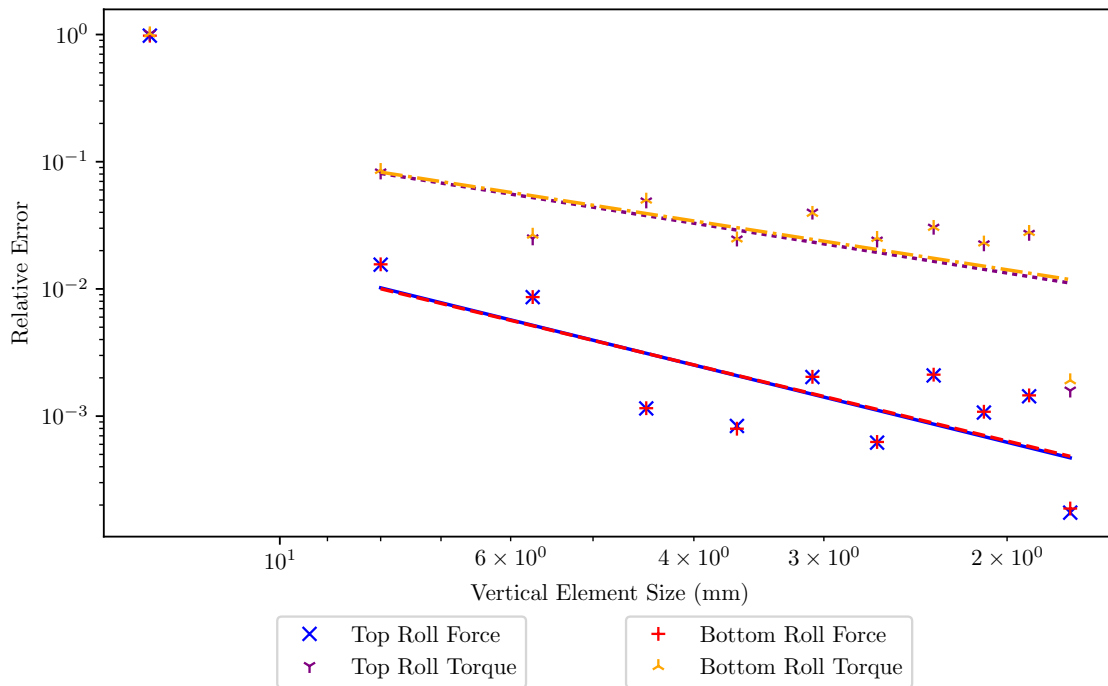


Fig. D.5 Convergence study for the explicit, three-dimensional asymmetric rolling finite element model.

The results from a simulation with finer meshing than those included in the plots was used to calculate the relative error. An experimental or analytical solution would have been preferred but no such data are available for the desired configurations.

The implicitly solved simulations show much less variation from a linear convergence than both explicit solutions. It is hypothesised that the undamped transients, causing high frequency oscillations in the solutions, are the cause of this variation. This and measures to limit the impact are discussed in the previous section and summarised in Appendix D.4. Regardless of these transients, a convergent trend is observed and the errors remain of comparable size to the implicit solution.

Early termination of finely meshed models was observed for the implicit solver and refining the meshes further resulted in fewer increments being completed. This may be a memory throttling mechanism of *ABAQUS/Standard* and so more advanced configuration of the software may reveal a solution; however, sufficient accuracy was achieved so this was not investigated further.

Finer meshed models of course require greater computational time so the final choice of mesh resolution was a compromise between accuracy and computational cost.

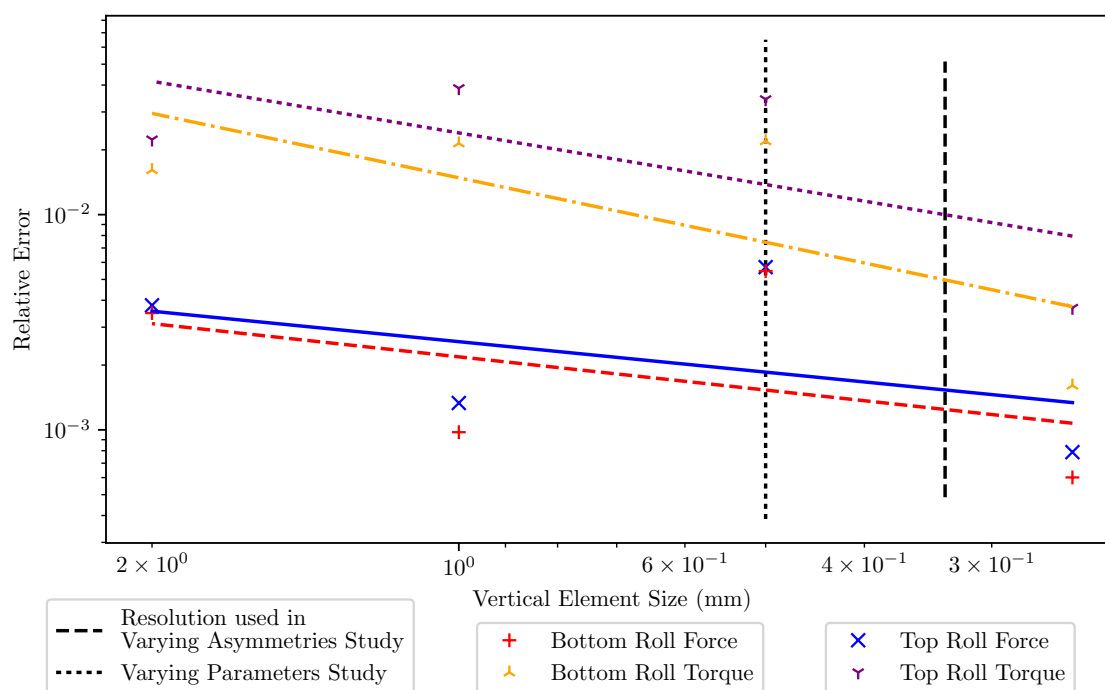


Fig. D.6 Convergence study for the explicit, two-dimensional asymmetric rolling finite element model used in Chapter 2. The discretisation used for the varying asymmetries study and non-dimensional parameters study are marked as vertical long dashed and short dashed lines respectively.

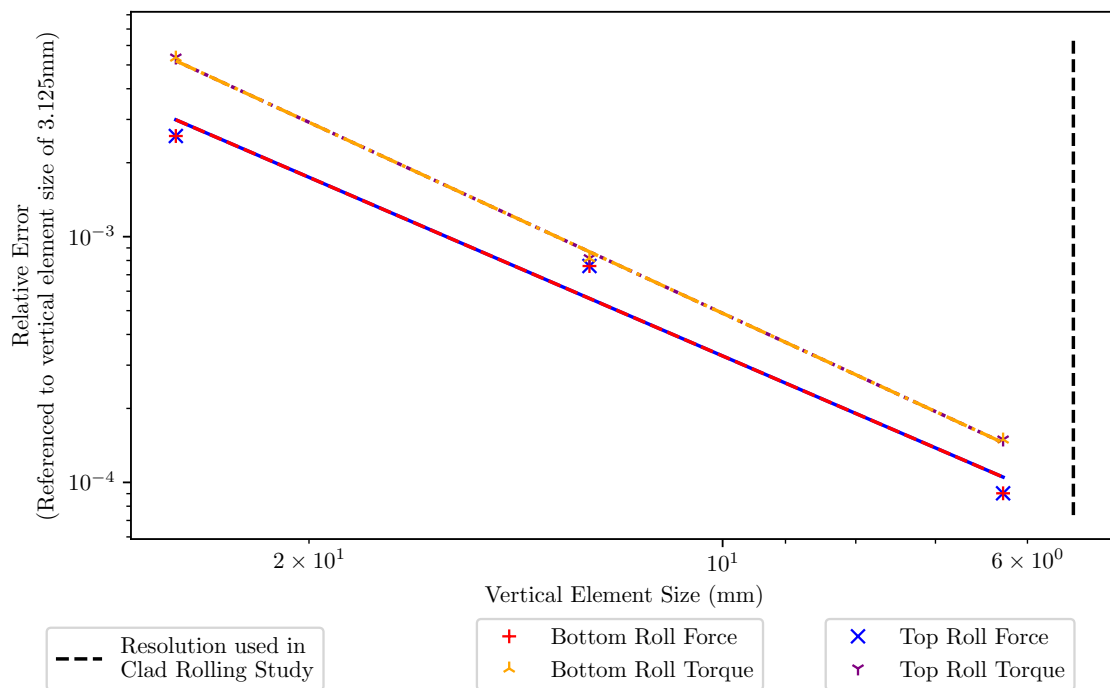


Fig. D.7 Convergence studies for the implicit, clad-sheet rolling finite element model used in Chapter 3. The discretisation used for the study in that chapter is marked with a dashed line.

The resolutions used for parametric studies throughout this work have been marked as vertical black lines on the appropriate figures.

D.3 Post-processing

ABAQUS simulation results are stored in database files, ‘.odb’ files, which can be accessed through the *ABAQUS CAE* graphical user interface or using the *Python API* provided by *ABAQUS*. The former was used to generate the images of deformed and undeformed meshes in Appendix D.1 and the latter for batch post-processing of the results presented throughout this document. As part of post-processing, calculations are made of the roll force and torque; surface and interfacial stresses; effective friction coefficients; neutral point locations; curvature; curvature approximations; and stress and strain fields. A description of each follow.

Roll force and torque Roll force and torque values are determined as the force and torque acting on the control node for each roll. The simulations were configured to record these values at every increment of the simulation. An average over the final .5 seconds of simulation time is taken to estimate the steady state of these values as only the vibrational transients discussed previously remained in this time period.

Surface/interfacial stresses and relative-slip The simulations were configured to save velocity data, stress data and surface stress data at twenty points during the rolling step. A path, defined by a list of edge nodes, is constructed along the roll-workpiece surfaces and material interfaces, if any exist. Values for the saved data can be generated along this path and saved with the associated position along the path. The relative-slip is simply the workpiece surface speed along this path less the roll surface speed.

Effective friction coefficients The local Coulomb friction coefficient is determined by dividing the normal force with the roll shear at any point. Similarly, the local relative-slip coefficient or local friction factor coefficient is determined by dividing the normal force with the relative-slip or yield stress respectively. An average of these local coefficients is taken over the workpiece surface in contact with the roll for the effective friction coefficients.

Neutral points The neutral points are taken to be where no relative-slip occurs. Often this is a region, not a single point, and checks to discard regions of no-slip at the entry or exit are also performed.

Curvature prediction The middle nine-tenths of the nodes that have completely undergone rolling are used to calculate curvature. This is to eliminate leading edge transients and regions around the exit of the roll gap in which residual stresses may not have been relaxed. The curvature of each row of nodes is calculated using a circle that is fitted by least squares. The workpiece curvature is taken as the average of these curvatures. Although computationally slow, this approach produces values that are robust to through-thickness variation and inclusion of limited end transients.

Stress and strain fields Field data, including position, is calculated for each node. Displacements are defined on nodes so can be read directly. Velocities can also be read directly for *ABAQUS/Explicit* simulations but must be calculated from the displacement change between the final two frames for *ABAQUS/Standard* simulations. The position of each node is calculated from its initial position plus its displacement. Finally, stresses are defined on elements so the stress state at a node must be computed by averaging the stress state of each element the node is a vertex of.

D.4 Transients control

As discussed in Appendix D.1, minimising the contribution to the solution by transient effects was a major consideration of the finite element models. The techniques employed to limit these effects are summarised here for reference.

Mass scaling The maximum convergent time increment for explicit solvers is proportional to the minimum element size and inversely proportional to the wave speed of the medium. Increasing the material density decreases the wave speed and allows larger time steps to be taken. Mass scaling uniformly scales the density of every material within the simulation to facilitate longer time steps and, hence, reduce computational time. Mass scalings also increases inertia so must be kept sufficiently small for this not to influence the result of interest. One way of determining the significance of inertia is to compare the kinetic and

internal energies over time; the kinetic energy should be small throughout the simulation. In the current application, higher mass scalings did not affect the averaged force and torque predictions; however, oscillation in these values and oscillating residual stresses grew in magnitude with greater mass scaling and were minimal when no mass scaling was used.

Simulation duration Simply increasing the simulation duration allows more transients to pass before considering the result as steady state. While the simulation duration is linearly related to the computation time, longer simulations form more of the workpiece so a longer workpiece is required to accommodate this. This increases the complexity of every time increment so ultimately the computational time scales worse than linearly with simulation duration. It was also observed that oscillations would not necessarily dissipate quickly enough to make longer durations a feasible approach to eliminating transients.

Static time stepping Static time steps, an option for simulation *steps* in *ABAQUS*, neglect inertia in the finite element calculations. This eliminates the dynamic component of oscillations and produces very strong damping of shocks and initial transients.

Pressure over-closure Pressure over-closure smooths the relationship between the normal contact pressure and clearance distance of the contact surfaces. This eliminates the discontinuity at initial contact which can lead to shocks within the system. An exponential over-closure relationship was used in this work but others are available.

Smooth amplitude transitions Using smooth displacement or velocity profiles can prevent discontinuities in velocity which produce infinite accelerations, and hence forces. Smooth transitions were employed to reduce shocks when the rolls squeeze the workpiece and when the rolls begin to rotate.

Artificial damping Artificial damping can be incorporated into *ABAQUS* in several ways depending on the solver being used. While it was not explored for these models it could be used to reduce the simulation required to achieve steady state.

D.5 Friction behaviour

It is specified in the *ABAQUS* users manual (Dassault Systemes, 2012d) that Coulomb friction is available by default for simulations and hence used here. Figure D.8 shows that this is not the case in regions around the neutral point, marked roughly in the figure by the vertical dashed lines, as the normal stress is at a maximum but the magnitude of shear reduces smoothly around the change of shear direction. The final plot in Figure D.8 shows that these smooth transitions coincide with regions of no-slip.

Figure D.9 illustrates the departure from Coulomb friction more clearly by plotting the roll surface shear stress against the roll surface pressure. The dashed lines in the first plot of Figure D.9 denote the Coulomb friction relationship between the workpiece and the top and bottom rolls. Clearly the points above 300MPa pressure depart from this relationship. Plotting the roll surface shear stress against the relative-slip shows that these points coincide with a region of no-slip, as observed in the last plot of Figure D.9 around the dashed vertical line.

This suggests that an alternative friction model is used for sticking contact; however, it is not clear what this alternative model might be. It is possible it is designed to smooth discontinuities that would otherwise occur, like the analytical solutions presented in Chapter 2 or Chapter 3, or that some other phenomenon, perhaps associated with elasticity, is influencing the surface shear.

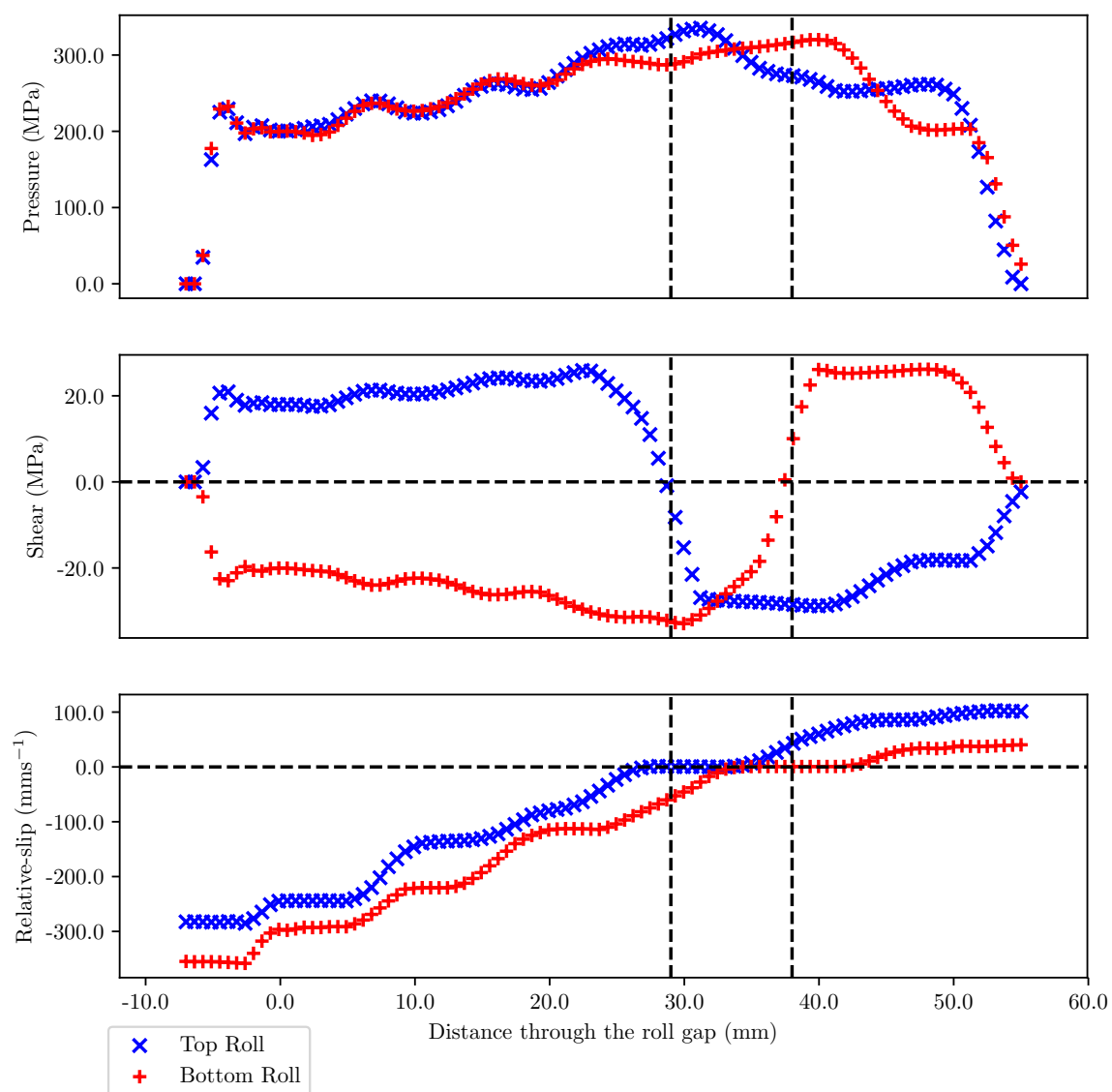


Fig. D.8 Surface normal stress (top), tangential stress (middle) and relative-slip (bottom) throughout the roll gap for an example asymmetric simulation.

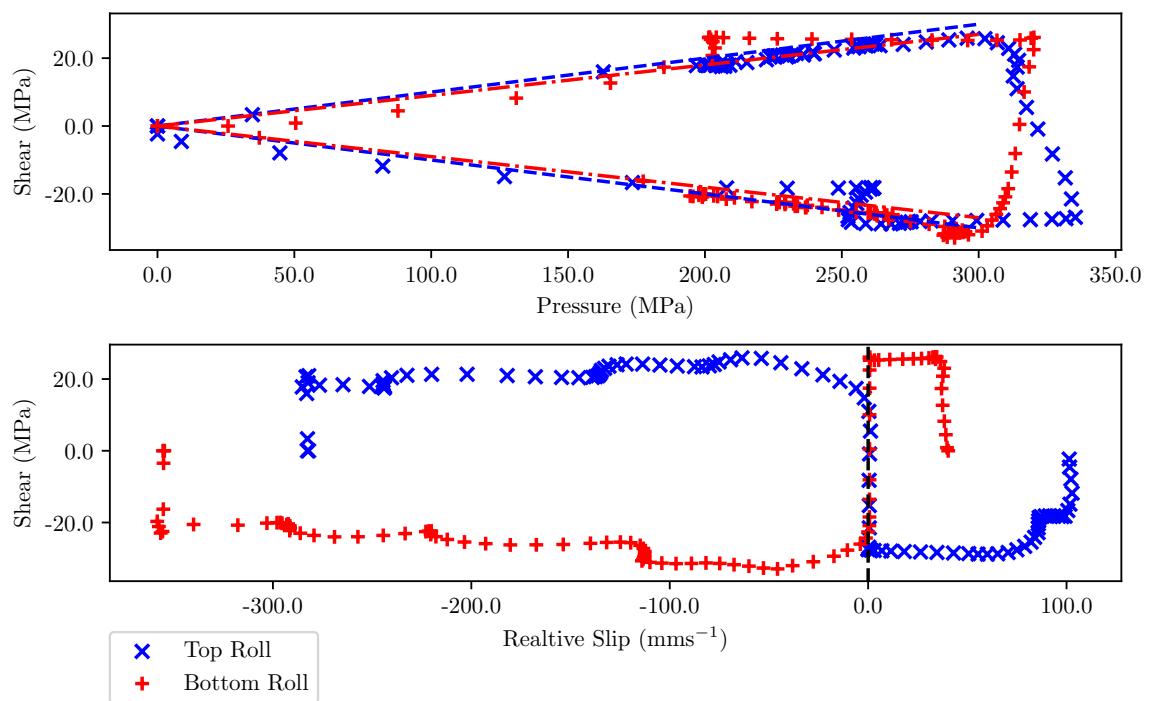


Fig. D.9 Surface tangential stress against surface normal stress (top) and relative-slip (bottom) for an example asymmetric simulation.